Design of a Defocused Transducer for Targeted Cancer Drug Delivery by Ultrasound-Mediated Hyperthermia



Brian Tze Chuen Chu

St Cross College

Supervised by:

Prof. Constantin Coussios & **Prof. Robin Cleveland**

This dissertation is submitted for the degree of

DPhil in Engineering Science

Michaelmas Term 2018

Acknowledgements

Firstly I would like to thank Research Councils UK for funding my studies and giving me the opportunity to pursue a PhD in the field that I am most passionate about.

I am incredibly thankful to my two supervisors, Prof. Constantin Coussios and Prof. Robin Cleveland for their guidance, support, and mentorship throughout my journey into biomedical acoustics. I am also very grateful for the technical support from Dr Michael Gray, and for his incredible patience during the experiments with the clinical HIFU system, which were incredibly tedious at times. I am also very thankful to James Fisk and David Salisbury who have helped me with their expertise in the mechanical workshop, and for many entertaining conversations.

I would like to thank my friends from the CDT, BUBBL, St Cross College, and elsewhere for enriching my time in Oxford. In particular, I would like to thank Steve, Lee, Yao and Lok for being good friends who encouraged me on and off the court. I am very grateful for the friendship and company of my old housemates: Kirubin, Navin, Nicolas, and Oliver, who really made me feel at home. I would like to thank Stephen and Louisa Passey for their generous hospitality and understanding of my situation during my write-up period, and to their incredibly well-fed cat, Minnaloushe, who would keep me company if I decided to burn the midnight oil. I am also incredibly thankful to Helen for her loving support and encouragement from across the world, despite the distance and time difference.

Finally, I would like to thank my parents and my sister for their unconditional love, encouragement, and support. This thesis is dedicated to them.

Abstract

A major challenge in chemotherapy is that the systemic delivery of drugs to both healthy tissue as well as the tumour results in unwanted side effects. Thermosensitive liposomal carriers are designed to release their payload when they are exposed to mild hyperthermia (a few degrees above body temperature). If a tumour can be locally heated, thermosensitive liposomes can provide triggered and localised delivery of the drug which should reduce systemic toxicity. Ultrasound is a noninvasive modality which can be used to produce localised heating at depth. However, most clinically approved high-intensity focused ultrasound (HIFU) systems are designed for tumour ablation and exhibit a focal volume which typically spans 1-3mm in width and 10-15mm in length, generating temperatures in excess of 50°C for a few seconds to directly kill tissue within the focal volume. Hyperthermia-triggered drug release usually requires maintaining a tumour volume which often spans several centimetres in size at a consistent therapeutic temperature of 39.5-42°C for durations up to an hour. This is difficult to achieve for most current HIFU transducers due to their small focal volume. The approach employed here is to design an acoustic lens that retrofits onto a clinical HIFU system to produce a focal volume better suited for mild hyperthermia. 3D printing is employed in this work to produce the lenses, and sectored lenses which enable a single-element transducer to produce acoustic fields with multiple foci in an annular pattern are investigated. Experimental measurements of the pressure and temperature using a small therapeutic transducer are consistent with simulations, and the simulated -3dB free-field focal volume of the transducer was increased from 9.6mm^3 to 90.9mm^3. Finite element software is used to perform 3D linear full-wave simulations of an acoustic lens

in a human liver target derived from a segmented CT dataset. The computational challenges with performing large 3D finite element simulations are addressed by dividing the simulation domain into several subregions. A phase-conjugate lens combined with masking transducer locations associated with ribs is explored as a solution to address aberrations in the acoustic field caused by tissue inhomogeneity. Experiments with a sectored acoustic lens on a clinical HIFU system showed the radial location of the free-field focus was shifted from 0mm to $\pm$2.8mm in an annular pattern. This work shows that retrofitting a HIFU system with an acoustic lens is a practical approach to broadening the focal spot.

Table of contents

List of figures viii

List of tables xiii

1 Introduction 1

1.1 Motivation . . . 1

1.2 Aims and Objectives . . . 2

1.3 Summary of the Current Work . . . 3

2 Background 5

2.1 Cancer and Controlled Drug Release . . . 5

2.2 Therapeutic Hyperthermia . . . 6

2.2.1 Background . . . 6

2.2.2 Ultrasound-Mediated Hyperthermia . . . 8

2.2.3 Therapeutic Ultrasound Transducers for Hyperthermia . . . 11

2.3 Modelling Ultrasound in Tissue . . . 15

2.3.1 Linear Sound Propagation . . . 15

2.3.2 Nonlinear Sound Propagation . . . 16

2.3.3 Acoustic Beam Models . . . 21

2.3.4 Full-wave Models . . . 23

2.3.5 PZFlex . . . 24

2.3.6 Tissue Models Used in Hyperthermia . . . 27

2.3.7 Acoustic and Thermal Parameters of Biological Tissues . . . 30

3 Sectored Transducer Investigation 38

3.1 Current Transducer Designs and Strategies for Mild Hyperthermia . . . 38

3.2 Optimisation of a Sectored Transducer . . . 42

3.2.1 Fresnel Approximation of the Rayleigh Integral . . . 43

3.2.2 Manual Optimisation . . . 54

3.2.3 Automated Optimisation Routine . . . 59

4 Acoustic Lenses for Mild Hyperthermia 68

4.1 Introduction . . . 68

4.2 Acoustic Lens Design Process . . . 69

4.3 Heat Generation in an Agar Phantom with an Acoustic Lens . . . 80

5 Simulation of a Patient-Specific Acoustic Lens 89

5.1 Introduction . . . 89

5.2 CT Dataset Preparation and PZFlex Model Setup . . . 91

5.2.1 Phase-Conjugate Lens Approach . . . 93

5.2.2 Thermal Simulation Scenarios . . . 97

5.3 PZFlex Simulations Results . . . 99

5.3.1 Heating Scenario 1 . . . 100

5.3.2 Heating Scenario 2 . . . 104

5.3.3 Heating Scenario 3 . . . 106

5.3.4 Sensitivity to Translational or Rotational Misalignment . . . 111

5.4 Discussion . . . 115

5.5 Conclusion . . . 119

6 Application to the JC200 Clinical Device 120

6.1 Introduction . . . 120

6.2 3D Printed Acoustic Lenses for the JC200 Clinical Transducer . . . 121

6.2.1 Acoustic Lens Design 121
6.2.2 Generation of Mild Hyperthermia in an Agar Phantom 130
6.2.3 Spot Heating Results 131
6.2.4 Repeated Line Scan Results 136
6.3 Simulation of the JC200 in PZFlex 140
6.3.1 Model Reduction Strategy to Simulate a Larger Transducer . . 140
6.3.2 Forward Simulation Model in a Segmented CT Dataset 142
6.3.3 Virtual Point Source Simulation Model 155
6.3.4 Phase-Conjugate Lens and Model Simulation 158
6.4 Conclusions 166

7 Summary and Future Directions 170
7.1 Summary 170
7.2 Future Directions 174

References 179

Appendix A 195

List of figures

2.1 Two examples of an extracorporeal single-element spherically focused transducer . . . 12

2.2 Phased-array focused ultrasound transducer capabilities . . . 14

2.3 Nonlinear wave steepening . . . 18

2.4 Simulated axial and radial normalised pressure profiles for the H101 transducer . . . 26

2.5 Tissue model examples . . . 28

2.6 Reported acoustic attenuation coefficient and blood flow values for human liver . . . 32

2.7 Reported acoustic attenuation coefficient and blood flow values for human adipose tissue . . . 33

2.8 Reported acoustic attenuation coefficient and blood flow values for human skeletal muscle tissue . . . 34

2.9 Reported blood flow values for human and dog bone . . . 36

3.1 Illustration of a sectored transducer surface. . . . 40

3.2 Simulated acoustic fields for a sectored transducer operating in modes 0, 1, 2 and 4 . . . 41

3.3 Simulated axial and radial pressure profiles for the H101 transducer in water using the Fresnel approximation. . . . 48

3.4 Simulated axial and radial pressure fields of the H101 transducer in water by PZFlex and the Fresnel approximation . . . 50

3.5 PZFlex and Fresnel approximation simulations of the H101 transducer targeted into an attenuating medium 51
3.6 Simulated temperature rise in a homogeneous attenuating medium using PZFlex and the Fresnel approximation 53
3.7 Simulate steady-state temperature fields in a perfused homogeneous attenuating medium 58
3.8 $RMSE$ and T_{max} as a function of acoustic power. 59
3.9 Simulated steady-state temperature fields produced by a sectored transducer operating in modes 0, 2 and 4 60
3.10 Illustrative flowchart of the optimisation process for a sectored transducer. 62
3.11 Variation of $RMSE$, acoustic power, and standard deviation of the surface phase distribution as a function of iteration number. 63
3.12 Surface phase and pressure fields produced by three independent optimisation runs. 64
3.13 Simulated steady-state temperature fields produced by the final iteration of optimisation runs 1, 2 and 3. 66

4.1 Illustration of pressure transmission through a three-layer model. . . . 70
4.2 Cross-sectional illustration of a curved acoustic lens with two distinct thickness steps 72
4.3 Pressure transmission coefficients for a two-thickness clear resin acoustic lens as a function of lens base thickness. 73
4.4 AutoCAD rendering of an eight-sector mode 4 acoustic lens for the H102 therapeutic transducer. 74
4.5 Image of the H102 transducer submerged in a large tank of degassed water with an eight-sector mode 4 acoustic lens. 75

4.6 Pre-focal and focal plane hydrophone scans of a H102 transducer in water with and without an acoustic lens. 77
4.7 Focal plane scans of the H102 transducer alone, and with a mode 2 or mode 4 acoustic lens. 79
4.8 Illustration of the through-transmission setup. 81
4.9 Attenuation coefficient measurements of agar-silica phantoms as a function of frequency. 83
4.10 Image of the lensed H102 transducer targeted into an agar-silica phantom. 84
4.11 Recorded and simulated temperature profiles produced in an agar-silica phantom. 87

5.1 Volume rendering of the segmented CT dataset and acoustic window. . 92
5.2 Cross-sectional illustration of the virtual point source simulation and phase-conjugate lens approach. 94
5.3 Graphical illustration of the surface amplitude thresholding process. . . 96
5.4 Graphical illustration of the surface phase and generation of the final acoustic lens profile. 98
5.5 Simulated -6dB pressure contours simulated in the liver for operational modes 0, 2 and 4. 101
5.6 Maximum simulated temperature curves from heating scenario 1 103
5.7 Simulated 39.5°C thermal contours produced in heating scenario 1. . . 103
5.8 Simulated 39.5°C thermal contours produced in heating scenario 2 . . . 106
5.9 Simulated 39.5°C thermal contours produced in heating scenario 3 . . . 109
5.10 Simulated 39.5°C thermal contours for the M2 PS case from heating scenario 3 with varying translational shift 112
5.11 Simulated 39.5°C thermal contours for the M2 PS case from heating scenario 3 with varying rotational offset. 114

6.1 Image of a 3D printed eight-sector mode 4 acoustic lens mounted onto the JC200 clinical transducer. 122
6.2 Image of the 2D positioning system setup on the JC200 device with acoustic hydrophone placement prior to water filling. 124
6.3 Two typical source waveforms recorded by an acoustic hydrophone situated in the nearfield of the JC200 transducer 126
6.4 Free-field radial line pressure measurements in the focal plane of the JC200 system with the T60, M2, and M4 lenses. 128
6.5 Schematic cross-sectional view of the JC200 agar-heating experiment setup. 132
6.6 Image of the phantom placement setup above the JC200 system. 133
6.7 Measured and simulated temperature curves in an agar-silica phantom produced by the JC200 using the T60, M2 and M4 lenses 134
6.8 Measured and simulated temperature curves produced in an agar-silica phantom by repeated line scans with the JC200 using the T60, M2, and M4 lenses. 138
6.9 Illustration of the multi-model finite element simulation approach with three example divisions 143
6.10 Axisymmetric acoustic simulations of the JC200 transducer in water compared with an equivalent free-field boundary source 144
6.11 CT volume renderings of two target locations in the liver 145
6.12 Simulated acoustic pressure volume contours produced in the liver by the JC200 transducer in case 1 and case 2 148
6.13 Simulated acoustic pressure volume contours produced in the liver by the JC200 transducer with a mode 4 acoustic lens in case 1 and case 2 149

6.14 Simulated 39.5°C thermal contours for cases 1 and 2 produced by the JC200 152
6.15 Simulated 39.5°C thermal contours for cases 1 and 2 produced by the JC200 with the M4 lens 153
6.16 Recorded peak acoustic pressure amplitude at the plane $x = 84$mm. . . 157
6.17 Recorded arrival time and relative phase at the plane $x = 84$mm 159
6.18 Projected amplitude and phase maps on the JC200 surface 160
6.19 Illustration of the amplitude threshold process for the JC200 162
6.20 Illustration of the surface phase and phase-conjugate lens thickness . . 163
6.21 Acoustic pressure and phase produced by a phase-conjugate lens on the plane $x = 84$mm approximated by the RS-integral. 165
6.22 Simulated pressure contours in the CT dataset produced by the phase-conjugate lens 167

List of tables

2.1 Nonlinearity parameter values for human tissues. 20
2.2 Comparison of the RS-integral and PZFlex at various simulation resolution 27
2.3 Table of average acoustic and thermal properties of human tissue and other materials. 37

5.1 Insonation parameters and simulated thermal contour volumes from heating scenario 1. 104
5.2 Insonation parameters and simulated thermal contour volumes for heating scenario 2. 107
5.3 Insonation parameters and simulated thermal contour volumes from heating scenario 3 110
5.4 Insonation parameters and simulated thermal contour volumes for the M2 PS case in heating scenario 3 with varying positional offset 115
5.5 Insonation parameters and simulated thermal contour volumes for the M2 PS case in heating scenario 3 with varying rotational offset 116

6.1 Insonation parameters and simulated thermal contour volumes produced by the JC200 151
6.2 Insonation parameters and simulated thermal contour volumes produced by the JC200 with the M4 lens. 154

1 Introduction

1.1 Motivation

Minimising the systemic toxicity of cancer drug therapies whilst delivering an effective dosage to the target site is a fundamental challenge in the treatment of cancer. Traditional chemotherapy drugs are systemically administered; affecting both healthy and unhealthy cells throughout the entire body, and cleared by the liver and kidneys. Liposomal encapsulation of chemotherapy drugs is a technique used to extend the circulation time of the drug in the body [1], and lyso-thermosensitive liposomes (LTSLs) in particular, show preferrential drug release when subjected to a threshold temperature [2]. Hyperthermia-triggered drug release from LTSLs using a localised heat source can reduce systemic toxicity yet deliver standard therapeutic drugs at locally higher doses, significantly enhancing drug delivery to tumours [3–6].

Ultrasound-mediated hyperthermia is a promising approach for this type of targeted drug release since it provides an entirely extracorporeal and non-invasive method of localised tissue heating at depth in the body, an advantage over conventional hyperthermia methods such as radiofrequency ablation and microwave radiation [7]. The recently completed TARDOX clinical trial in Oxford (UK) has successfully demonstrated, for the first time in humans, the safety and feasibility of targeted release of doxorubicin in the liver from thermosensitive liposomes using non-invasive ultrasound-mediated hyperthermia. The initial findings are promising, with tissue samples showing intra-

tumoural doxorubicin concentrations between two and ten times greater than that achieved through standard chemotherapy alone [8].

Existing clinically approved therapeutic ultrasound devices have tight focal regions and are designed to achieve tumour ablation, generating temperatures of over 50°C for a few seconds in order to directly kill cells by thermal necrosis [9]. In contrast, targeted drug release from LTSLs requires maintaining therapeutic levels of mild-hyperthermia in the range of $39.5 - 42$°C throughout the target volume for durations of up to one hour. This can be difficult to achieve using highly focused transducers since treatment volumes are often significantly larger than the focal volume of the device. In comparison, weakly focused transducers either lack the acoustic gain or produce a focal volume with poor axial resolution. Strategies for therapeutic ultrasound transducers to generate larger focal volumes which maintain an adequate axial resolution have been investigated for several decades, however an approved transducer for the purpose of mild hyperthermia-triggered drug release in large target volumes has yet to emerge in the clinic.

1.2 Aims and Objectives

It has been established that ultrasound-mediated hyperthermia is a promising technique for improving tumour drug delivery from thermosensitive carriers. The use of existing clinically approved therapeutic ultrasound devices (originally designed for tumour ablation) may not be an optimal solution for large volume mild hyperthermia therapy. The aims for this thesis are therefore to:

- Investigate existing therapeutic ultrasound strategies suitable for large volume mild hyperthermia.

- Implement a strategy for existing clinically approved therapeutic transducers in order to improve the performance of current ultrasound-mediated mild hyperthermia techniques.
- Verify the proposed strategy through simulation with experimental results to support simulation credibility.

1.3 Summary of the Current Work

Chapter 2 of this thesis provides a rough overview of the biological and clinical relevance of hyperthermia in the context of cancer therapy. This chapter also lays the groundwork and foundation for the underlying physics behind ultrasound-mediated heat generation in the body, and some approaches to modelling ultrasound-mediated mild hyperthermia are discussed.

Chapter 3 begins with an insight into existing ultrasound transducer strategies used to generate large volume mild hyperthermia. The acoustic fields produced by a sectored array are explored through simulation, and the optimisation of a sectored transducer to produce and maintain a therapeutic volume of hyperthermia in a homogeneous attenuating medium with fixed perfusion is explored.

In Chapter 4, 3D printed sectored acoustic lenses are explored as an affordable and practical method to generate mild hyperthermia from a preclinical spherically-focused single-element transducer, building upon existing strategies from previous researchers in the field and verifying the reproducibility of the work with simulations and experimental validation. Acoustic and thermal simulations were performed using both numerical and finite element approaches, and the increase in volumetric heating is verified through thermocouple measurements within a tissue-mimicking phantom.

Chapter 5 explores the use of PZFlex (a commercial finite element package) to simulate the performance of a lensed preclinical therapeutic transducer to generate mild hyperthermia in a single patient-specific liver target. The finite element approach in combination with a segmented patient-specific CT dataset enabled the investigation of intercostal targeting challenges such as rib obstruction and tissue inhomogeneity. The simulation of a virtual point source located in the liver is used to determine the acoustic aberration caused by tissue inhomogeneity, and a phase-conjugate acoustic lens with masking of transducer locations associated with the ribs is proposed. Several hyperthermia insonation strategies are simulated in order to explore the therapeutic performance of the modified lens, and the effect of positional or rotational alignment error relative to the patient target location is also reported.

Chapter 6 describes the challenges of translating the current work to a larger clinical transducer. 3D printed sectored acoustic lenses are designed and verified with simulations and experimental measurements in a tissue-mimicking phantom. For PZFlex simulations, the significant increase in size of the transducer makes finite element simulations very challenging, and strategies to minimise the computational requirements of modelling a larger transducer are presented. Simulations of acoustic propagation into two intercostal liver target sites are presented, and the predicted therapeutic volumes produced by the clinical transducer for various insonation parameters are shown. The simulation of a virtual point source situated in the liver is performed in order to derive a phase-conjugate acoustic lens and determine transducer locations affected by ribs, and a modelling strategy to simulate a patient-specific lens is proposed.

Finally, Chapter 7 concludes the findings of this thesis in the greater context of the field, the limitations and challenges involved in producing this work are discussed, and several directions for possible future work are presented.

2 Background

2.1 Cancer and Controlled Drug Release

Cancer describes a group of diseases caused by unregulated cell division, which in 2016, contributed to 28% of all UK mortalities [10]. Depending on the type and severity of the disease, the three main medical interventions to treat cancer include surgery, chemotherapy, and radiotherapy [11]. Conventional cancer treatments all come with some degree of adverse side effects; radiotherapy inflicts ionising radiation to healthy cells in the process of treatment, surgery is often very invasive, and chemotherapy introduces systemic toxicity.

Traditional chemotherapy drugs operate through the inhibition of cell division, affecting all rapidly replicating cells whether cancerous or healthy [12]. Systemic toxicity is one of the major limitations in achieving an effective tumour response with chemotherapeutic drugs, pushing drug development towards methods that preferentially target cancer cells and tumours [12–16].

Encapsulating chemotherapeutic drugs in vehicles such as PEGylated liposomes has been shown to increase the systemic circulation time of the drug in the body, and reduce systemic toxicity [17]. However, the slow diffusion of the drug out of the carrier hinders the antitumour effect [18]. Techniques pairing drug encapsulation with release or activation mechanisms from external sources have therefore been explored in order to improve drug delivery and tumour response. Examples of external stimuli for the

activation or release of drugs include strong local magnetic fields [19], temperature [4], light [20], and ultrasound [21].

Amongst the aforementioned modalities, ultrasound has the greatest therapeutic depth of penetration in soft tissues, and the ability for ultrasound to be focused and consequently generate localised heating is what makes it a suitable modality for drug release at depth. Coupled with thermosensitive liposomes as discussed in section 1.1, ultrasound-mediated hyperthermia has been shown to be a promising approach for non-invasive localised drug release in tumours [8, 22–24] - an advantage over conventional hyperthermia methods such as radiofrequency ablation and microave radiation, which are either invasive or limited to shallow treatment depths [7].

2.2 Therapeutic Hyperthermia

2.2.1 Background

Therapeutic hyperthermia is the elevation in temperature of body tissue to treat disease; often performed through radiofrequency waves, microwaves, and ultrasound [7]. Mild hyperthermia in the range of $41-45°C$ has been shown to have synergistic effects in cancer treatment, notably increasing the sensitivity of cancer cells to radiotherapy and also chemotherapy [7, 24, 25].

The synergistic effects of mild hyperthermia and cancer therapy in the tumour environment are complex. Temperatures up to 42°C haven been shown to improve blood perfusion and oxygenation in tumours, increase cell sensitivity to radiotherapy, and improve drug circulation around the tumour. However, at temperatures above 42°C, cellular death due to hyperthermia is enhanced, and tumour perfusion drops due to blood vessel damage [26, 27]. A reduction in tumour perfusion also leads to a

hypoxic and acidic cellular environment, consequently making cells more resistant to radiotherapy [28].

Exposing target tissues such as tumours to extreme levels of hyperthermia (typically above 50°C) is often referred to as thermal ablation [29]. Thermal ablation has been used as a method to treat tumours unsuitable for resection by directly inducing cell death through protein denaturation and thermal necrosis. The two main methods of implementing thermal ablation are radiofrequency ablation (RFA) and high intensity focused ultrasound (HIFU) [9]. RFA requires invasive insertion of a needle into the tumour mass in order to heat tissue regions in contact with the tip of the RF needle by applying a radiofrequency alternating current [30]. HIFU on the other hand is a non-invasive ablation technique which induces tissue heating by externally focusing ultrasound into the tumour mass, generating heat due to the high acoustic intensity within the focal volume [31].

In order to quantify the detrimental effects of temperature elevation in biological tissues, the concept of a thermal dose was introduced in 1984 by Sapareto and Dewey [32]. Thermal dose is measured in terms of cumulative equivalent minutes required to achieve the same amount of cell death at a temperature of 43°C, denoted as CEM_{43} in Equation 2.1 below

$$CEM_{43} = \int_0^t R^{(43-T)} dt \tag{2.1}$$

where T is the temperature in degrees Celsius, t is the duration in minutes, $R = 0.5$ for $T > 43$°C, and $R = 0.25$ for $T < 43$°C in order to capture the accelerated rate of observed cell death at higher temperatures.

The threshold required to induce thermal damage varies depending on the tissue type, where initial thermal damage is observed in cat and dog brain tissue after $CEM_{43} = 25$ minutes [33], and for pig liver tissue minor thermal damage was observed between $CEM_{43} = 41 - 80$ minutes [34]. The most commonly cited thermal dose

value used to indicate complete thermal ablation is established to be at $CEM_{43} = 240$ minutes [35, 36], and this definition is used as a reference to determine the presence of thermal ablation in the simulations shown in this thesis.

Knowledge of thermal dose throughout the treatment volume would be a useful tool to determine the localisation of hyperthermia treatment, and in the case for mild-hyperthermia, provide a monitoring guideline to minimise the risk of causing excessive thermal damage [37]. Thermometry of deep regions in the body is currently performed by inserting an invasive needle thermocouple, or by magnetic resonance imaging which is relatively expensive in comparison. The lack of an easily accessible non-invasive thermometry technique is thought to be one of the defining factors limiting the widespread use of hyperthermia in cancer therapy [28].

2.2.2 Ultrasound-Mediated Hyperthermia

Ultrasound describes acoustic waves with a frequency above the threshold of hearing in humans (~20kHz). In diagnostic imaging, frequencies of $1 - 20$MHz are commonly used, while therapeutic ultrasound applications typically operate in the lower frequency range of $0.8 - 3.5$MHz; often with larger peak acoustic pressures in comparison to conventional ultrasound imaging [31].

Depending on the acoustic wave properties (e.g. peak compression and rarefaction pressure, duty cycle, centre frequency) and physical properties of the medium, ultrasound can generate mechanical effects such as shockwaves [38], cavitation [39], microstreaming [40], radiation force [41], cavitation enhanced heating [42], as well as mechanically induced bioeffects such as histotripsy [43], boiling histotripsy [44], mild hyperthermia [45] and thermal ablation [46]. Some examples of therapeutic ultrasound applications which utilise one or more of the aforementioned effects include gene therapy [47], chemotherapy [48, 49], drug delivery [50, 42], lithotripsy [38, 51],

hemostatis [52], thrombolysis [53, 54], neuromodulation [55], mild hyperthermia [56], and thermal ablation of tumours [57, 58].

The acoustic energy delivered from an ultrasound wave into a target medium is commonly expressed in terms of acoustic intensity I [W.m^{-2}]. When the pressure amplitude and particle velocity are in phase, which is a reasonable approximation even for a focused nonlinear beam [59], then the temporal average acoustic intensity I at a particular location can be described by Equation 2.2 [60]

$$I = \frac{(p_{\text{rms}})^2}{\rho_0 c_0} \tag{2.2}$$

where p_{rms} is the root mean square pressure, ρ_0 is the density of the medium, and c_0 is the speed of sound in the medium.

Attenuation describes the reduction in energy from a propagating wave as it travels through a medium due to absorption and scattering [61]. For acoustic plane wave propagation in a homogeneous attenuating medium, the amplitude will decrease as a function of distance due to energy loss as expressed by Equation 2.3 [60]

$$p(x) = p_0 e^{-\alpha x} \tag{2.3}$$

where $p(x)$ is the pressure amplitude at a distance x travelled in the medium, p_0 is the incident pressure amplitude at $x = 0$, and α is the attenuation coefficient[1].

In most soft biological tissues, acoustic attenuation can be described by

$$\alpha = \alpha_a + \alpha_s \tag{2.4}$$

[1]expressed in nepers per metre [Np.m^{-1}], however in biomedical ultrasound α is commonly found expressed in [dB.cm^{-1}], where 1Np $= 20/log_e(10) = 8.686$dB.

where α is the attenuation coefficient, α_a is the attenuation due to absorption, and α_s is the attenuation due to scattering [62].

Most studies model tissue as a homogeneous medium and therefore assume that attenuation is entirely due to absorption, where the attenuation coefficient is often approximated with a power law dependency as shown in Equation 2.5 [62]

$$\alpha_a = \alpha_0 \left(\frac{f}{f_0} \right)^n \tag{2.5}$$

where α_0 is the attenuation coefficient at f_0 (typically 1MHz in biomedical applications), f is the frequency, and n typically being between 1 and 1.5 for most soft tissues [63].

Assuming that the energy lost by an acoustic plane wave travelling in a homogeneous medium due to attenuation is entirely converted into heat, the rate of heat generation at a particular location in the medium can be described by Equation 2.6 [64]

$$\dot{q} = 2\alpha I \tag{2.6}$$

where $\dot{q}$ is the rate of heat generation per unit volume due to ultrasound.

The most widely adopted model used to describe the temperature rise generated by ultrasound in biological tissue is the Pennes bioheat transfer equation [65] as described by Equation 2.7

$$\rho_0 C \frac{\partial T}{\partial t} = \dot{q} + \nabla \cdot (k \nabla T) - \rho_b C_b W_b (T - T_A) \tag{2.7}$$

where ρ_0 is the density of the tissue, C is the specific heat capacity of the tissue, $\partial T/\partial t$ is the rate of change of temperature over time, $\dot{q}$ is the rate of heat generation due to ultrasound, k is the thermal conductivity of the tissue, ρ_b is the density of blood, C_b is the specific heat capacity of blood, W_b is the perfusion rate of blood, and T_A is the arterial blood temperature.

One caveat with the Pennes bioheat transfer model is that blood perfusion is assumed to act as a uniform heat sink, where blood enters the control volume at a uniform fixed temperature (often assumed to be 37°C) and leaves the control volume at the local volume temperature. Although alternative bioheat models exist which take into account the impact of blood vessel networks [66–69], the Pennes bioheat model remains the most widely accepted method due to small blood vessels being difficult to image and validate experimentally in vivo [70].

In the case for sufficiently short insonations such that heat loss via conduction and convection can be neglected, the temperature rise due to ultrasound can be reduced to Equation 2.8

$$\Delta T = \frac{\dot{q}\Delta t}{\rho_0 C} \tag{2.8}$$

where ΔT is the rise in temperature, and Δt is the duration in time [71].

2.2.3 Therapeutic Ultrasound Transducers for Hyperthermia

Therapeutic ultrasound-mediated hyperthermia is often achieved through the use of a single-element spherically focused transducer, or a transducer comprising of multiple smaller elements known as a phased array [72]. Both transducer types can be extracorporeal or intracavitary, and are usually geometrically focused since this enables the transducer to naturally produce a region of higher acoustic gain. Flat transducers can also be focused through the use of an acoustic lens [73], and flat phased arrays can be focused through the adjustment of the phase and amplitude of each element [74].

The use of ultrasound as a source of hyperthermia can be broadly categorised into two applications, namely HIFU and therapeutic mild hyperthermia. HIFU transducers are highly focused in order to maximise the acoustic intensity at the target site while minimising the intensity elsewhere, with typical single spot lesions (regions of tissue necrosis) typically spanning $1-3$mm in width and $8-15$mm in length [31]. In order

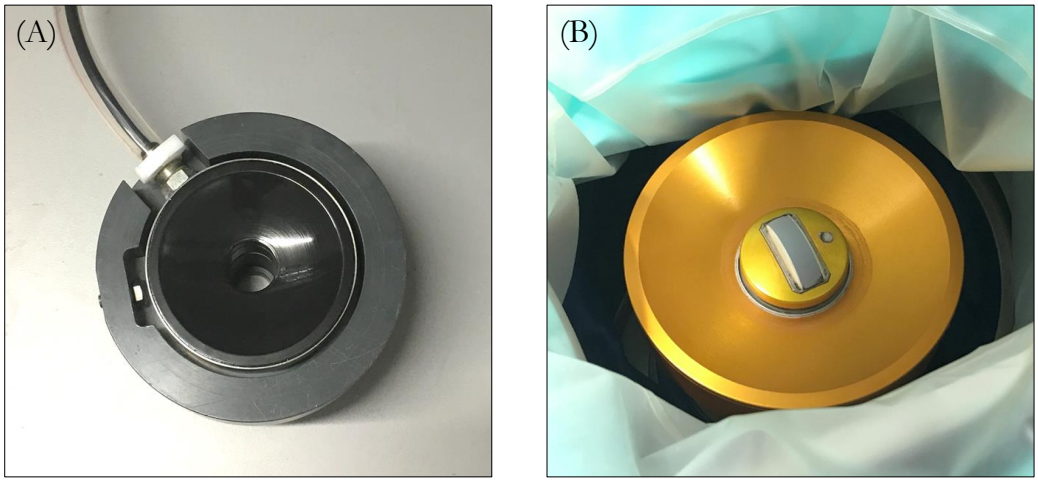


Fig. 2.1 Two examples of an extracorporeal single-element spherically focused transducer. (A) A 64mm diameter therapeutic transducer (H102, Sonic Concepts, Inc.) used in research and small animal experiments, (B) a larger 200mm diameter clinically approved focused ultrasound transducer with a central imaging transducer (JC200, Chongqing Haifu Medical Technology Co., Ltd.).

to treat a larger volume, the focus of single element HIFU transducers are often mechanically scanned, or electronically steered in the case for phased arrays [75–77]. Some examples of treatment applications for extracorporeally applied HIFU include soft tissue sarcomas, and cancers of the liver, kidney, brain, breast, and bone [78, 79]. Two extracorporeal single-element focused transducers that are used in research and clinical applications as well as the work presented in this thesis are shown in Figure 2.1.

For therapeutic mild hyperthermia applications, typical temperatures of $39.5-42°C$ need to be sustained across large target volumes for durations ranging from tens of minutes to hours [27]. Maintaining an even temperature distribution using such highly focused transducers is difficult since the focus of the transducer is often much smaller than the treatment volume. Early approaches to achieve uniform mild hyperthermia across a large treatment volume involved the use of multiple transducers with overlapping acoustic fields [80, 81]. Alternative proposed methods

include modification of the acoustic field of flat or focused transducers through the use of acoustic lenses, which created a broad annular focus or produced acoustic fields exhibiting multiple foci [73, 82, 83].

Investigations into multi-foci acoustic fields became more accessible with the development of phased arrays with increasingly higher number of elements [75–77, 84]. Some capabilities of phased arrays are illustrated in Figure 2.2, which include multi-foci acoustic field synthesis (2.2A), electronic beam steering (2.2B), and the ability to correct for acoustic field aberrations caused by refraction and reflections from acoustic propagation through inhomogeneous media (2.2C) [78]. Another notable method which utilises the capability of phased arrays is an acoustic field synthesis technique using the pseudo-inverse approach, which is a numerical method to calculate the driving signals of an array for a desired acoustic field by arranging a discretised form of the Rayleigh-Sommerfeld integral into a system of linear equations and determining a least-squares solution [85, 86].

Most clinically approved extracorporeal focused ultrasound transducers are often supported by magnetic resonance (MR) [87] or diagnostic ultrasound imaging guidance [88]. In particular, MR thermometry is a technique which enables real-time spatial localisation and estimation of temperature rises generated by focused ultrasound [89–91]. Ultrasound-based thermal imaging techniques on the other hand have yet to reach the stage of routine clinical use due to inconsistencies in temeprature estimation [88, 92, 93]. In general, the lack of a thermometry technique which is affordable, reliable, and non-invasive is thought to be one of the major factors limiting the uptake of focused ultrasound therapy as a routine clinical procedure [94, 95].

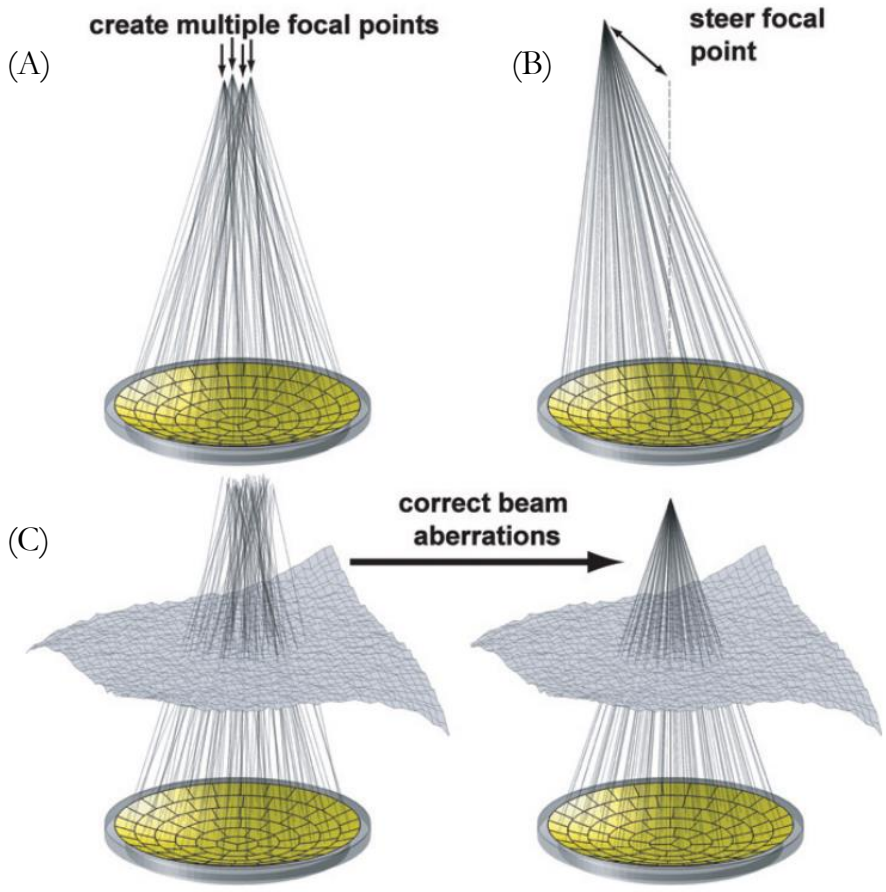


Fig. 2.2 Capabilities of phased-array focused ultrasound transducers include: (A) multi-point focal volume generation, (B) electronic beam steering, and (C) phase aberration correction. (Image reproduced from [78])

2.3 Modelling Ultrasound in Tissue

2.3.1 Linear Sound Propagation

Sound propagation in a homogeneous isotropic fluid can be described by perturbations in pressure and density [60]

$$\widetilde{p}(\mathbf{r},t) = p_0 + p(\mathbf{r},t) \tag{2.9}$$

$$\widetilde{\rho}(\mathbf{r},t) = \rho_0 + \rho(\mathbf{r},t) \tag{2.10}$$

where $\widetilde{p}(\mathbf{r},t)$ and $\widetilde{\rho}(\mathbf{r},t)$ are the total pressure and density at a particular location $\mathbf{r}$ at time t, p_0 and ρ_0 are the ambient pressure and density values, and $p(\mathbf{r},t)$ and $\rho(\mathbf{r},t)$ are the perturbations in pressure and density.

Neglecting second order terms as well as viscous losses, the corresponding governing equations which describe linear acoustic wave behaviour are the conservation of mass, conservation of momentum, and the pressure-density relationship shown in Equations 2.11, 2.12, and 2.13

$$\frac{\partial \rho}{\partial t} = -\rho_0 \nabla \cdot \mathbf{u} \tag{2.11}$$

$$\frac{\partial \mathbf{u}}{\partial t} = -\frac{1}{\rho_0}\nabla p \tag{2.12}$$

$$p = c_0^2 \rho \tag{2.13}$$

where $\mathbf{u}$ is the particle velocity, ρ is the perturbation density of the medium, p is the perturbation pressure, c_0 is the small signal sound speed, t is time, and ∇ is the gradient operator. Equations 2.11-2.13 can be combined to yield the well known

linearised wave equation as shown in Equation 2.14.

$$\nabla^2 p \;-\; \frac{1}{c_0^2}\frac{\partial^2 p}{\partial t^2} \;=\; 0 \tag{2.14}$$

In order for linear acoustic behaviour to hold true, the requirements for perturbations in pressure and density can be found by dividing Equation 2.13 by $\rho_0 c_0^2$, which results in the the two conditions below shown by Equations 2.15 and 2.16.

$$|\rho| \ll \rho_0 \tag{2.15}$$

$$|p| \ll \rho_0 c_0^2 \tag{2.16}$$

2.3.2 Nonlinear Sound Propagation

Nonlinear acoustic effects become significant when the perturbations in pressure and density no longer follow the conditions described by Equations 2.15 and 2.16. In this case, the local phase speed of an acoustic wave (in one dimension) is described by Equation 2.17 [60]

$$\frac{dx}{dt} = c_0 + \beta u \tag{2.17}$$

where x is the particle position, t is time, u is the particle displacement velocity (equal to $p/\rho_0 c_0$), and β is the coefficient of nonlinearity defined by Equation 2.18

$$[60]\beta = 1 + \frac{B}{2A} \tag{2.18}$$

where B/A is known as the nonlinearity parameter of the medium.

Taking the most simple case based on the Poisson's solution (1808) to the second order nonlinear wave equation (known as the Westervelt Equation in literature) and ignoring attenuation [96], a forward propagating nonlinear monochromatic wave in one

dimension can be approximated as

$$p(x,\tau) = p_0 \ \sin\left(\omega\tau + \left(\frac{\beta\omega p}{\rho_0 c_0^3}\right)x\right) \tag{2.19}$$

where $p(x,\tau)$ is the time dependent acoustic pressure at an observation distance x with retarded time frame $\tau = t - x/c_0$, p_0 is the source pressure amplitude, β is the coefficient of nonlinearity, ω is the angular frequency, ρ_0 is the ambient density, and c_0 is the small signal sound speed.

As a plane progressive acoustic wave propagates through a medium, regions of high acoustic pressure will result in a local particle velocity greater than the small signal sound speed. Similarly, rarefactional pressures result in a lower local particle velocity, and the phenomena of the resulting distortion of the shape of the acoustic wave is known as wave steepening [96]. To illustrate this phenomena, the Poisson's solution described by Equation 2.19 was solved numerically using MATLAB (2017b, The MathWorks, Inc.) for various propagation distances relative to the shock formation distance $\bar{x}$ as shown in Figure 2.3. The MATLAB script used to produce the curves shown in Figure 2.3 can be found in Appendix A.

The shock front is defined at the location where the slope of the pressure curve in Figure 2.3 becomes infinite, and the propagation distance at which the shock front occurs is known in literature as the shock formation distance $\bar{x}$. For a uniform plane wave of fixed amplitude in a non-attenuating homogeneous isotropic medium, the shock formation distance is defined as

$$\bar{x} = \frac{\rho_0 c_0^3}{\beta p_0 \omega} \tag{2.20}$$

where ρ_0 is the density, c_0 is the small signal sound speed, p_0 is the source pressure amplitude, ω is the angular frequency, and β is the coefficient of nonlinearity.

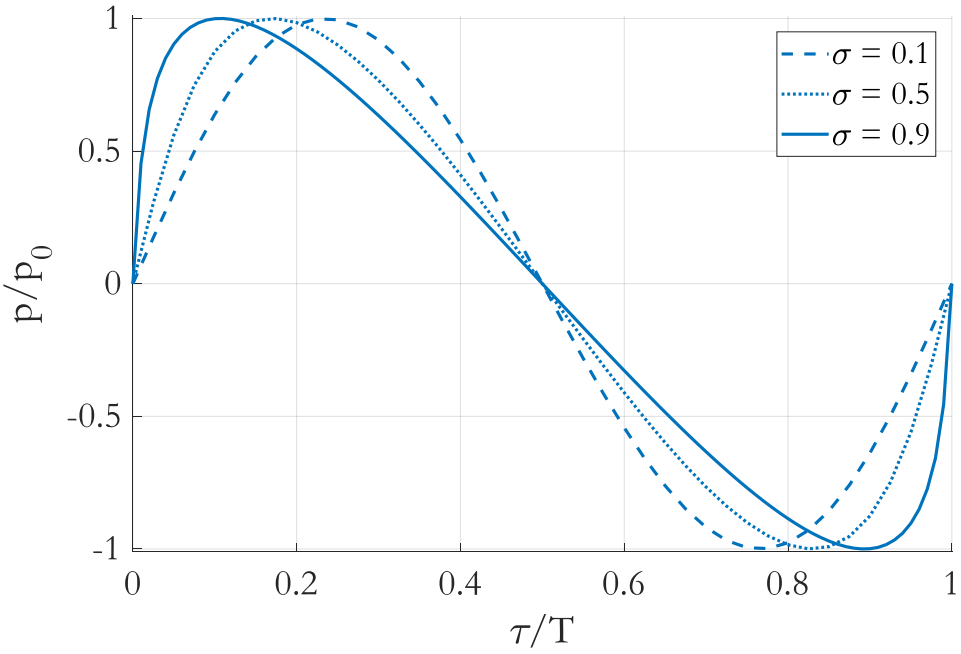


Fig. 2.3 An illustration of the acoustic wave steepening of a sinusoidal wave propagating in a homogeneous non-attenuating medium at different propagation distances relative to the shock formation distance using a retarded time frame. Waveforms were generated by numerical interpretation of the Poisson's solution (Equation 2.19) in MATLAB, where the pressure amplitude of the wave is normalised to the surface pressure p_0, $\tau = t - x/c_0$ is the retarded time frame for the forward propagating wave, T is the period, $\sigma = x/\bar{x}$ is the shock parameter, x is the propagation distance, and $\bar{x}$ is the shock formation distance as described in Equation 2.20.

The ratio of the observation distance relative to the shock formation distance is known as the shock parameter σ, defined as

$$\sigma = x/\bar{x} \tag{2.21}$$

where x is the observation location, and $\bar{x}$ is the shock formation distance. The shock parameter provides a measure of nonlinearity, where nonlinearity can be safely ignored if $\sigma \ll 1$. The physical meaning of the shock parameter is illustrated in Figure 2.3, where a low value of $\sigma = 0.1$ corresponds to a sinusoidal wave which has propagated a short distance relative to the shock formation distance, showing minimal distortion to the shape of the waveform. A larger value of $\sigma = 0.9$ corresponds to a wave which has propagated a significant distance relative to the shock formation distance. This is reflected in the significant presence of wave steepening, where the location of the peak and trough of the pressure waveform have shifted significantly.

For acoustic simulations in this thesis, it is assumed that nonlinear effects can be safely avoided if the shock formation distance (calculated using the peak focal pressure as the plane wave source pressure) is significantly far away from the focus (i.e. for small values of σ). The coefficient of nonlinearity β found in the expression for $\bar{x}$ will vary depending on the tissue type, and the values used for estimations in this thesis are based on the experimental measurements of the nonlinearity parameter B/A reported in the literature, as listed in Table 2.1.

The presence of harmonic components of an acoustic wave increases with the nonlinearity caused by wave steepening, and since the attenuation in tissue increases with frequency as described by Equation 2.5, this can result in an increased rate of heat generation [97]. Other nonlinear effects which can occur in tissue are local changes in physical tissue properties such as speed of sound, perfusion rate, and specific heat capacity as a function of local tissue temperature [98]. This can have a significant effect

Table 2.1 Reported nonlinearity parameter values for various human tissues sourced from F. A. Duck, 1990 [62].

Medium	**B/A**	**Reference**
Blood	6.05	Gong et al, 1989
Brain	6.55	Sun Yongchen et al, 1986
Fat	9.63	Sehgal et al, 1984
Kidney	8.98	Sun Yongchen et al, 1986
Liver	6.75	Sehgal et al, 1986
Muscle	7.43	Sun Yongchen et al, 1986
Water (20°C)	5.00	[96]

for very large temperature rises such as those produced in thermal ablation, however for mild hyperthermia where temperature rises of no more than 6°C are expected, the temperature dependence of tissue properties are assumed to be insignificant [98].

Another possible nonlinear effect is acoustic cavitation, which broadly describes the nucleation, growth and collapse of bubbles in the medium, often caused by significant rarefactional pressure [99]. The effects of acoustic cavitation will vary depending on whether cavitation is stable (growth and oscillation of a microbubble) or inertial (growth followed by violent collapse) [42]. The probability of producing acoustic cavitation increases with rarefactional pressure amplitude, and increases with decreasing frequency, with example reported threshold values (for a single 1.1MHz pulse) of -13.5MPa in unfiltered water (90% O_2), -16.1MPa in kidney tissue, and -9.8MPa in adipose (fat) tissue [100].

The main cavitation-related phenomena in tissue include acoustic shielding (due to the large difference in acoustic impedance at the bubble boundary) [101], tissue homogenisation (histotripsy, caused by the violent collapse of microbubbles in inertial cavitation) [102], and cavitation-enhanced heating (arising from the generation of harmonics by the presence of the microbubble, and viscous friction in the surrounding

media) [39]. Although acoustic cavitation has been shown to be beneficial for the release and extravasation of drugs [39, 103], enhance the formation of lesions [104], and aid in therapy treatment monitoring [105], it is generally undesired for mild-hyperthermia therapy since it could disrupt the acoustic field and result in an excessive delivery of thermal dose.

2.3.3 Acoustic Beam Models

Acoustic modelling approaches can be broadly categorised into acoustic beam models or full-wave models, where suitability for each technique depends on the nature of the application. Examples of modelling considerations include the required model domain size, field symmetry, whether linear or non-linear wave behaviour is expected, and if complex inhomogeneous media modelling is necessary.

Acoustic beam models tend to be faster and less computationally demanding than full-wave solvers since assumptions such as numerical approximations, ignoring refraction and reflections, or assuming a homogeneous medium with time-harmonic sources often make numerical and analytical implementation more convenient [106]. A comprehensive list of commercial and open-source acoustic modelling packages can be found from sources [106–108].

A general analytical solution to calculate the pressure field produced by a transducer of arbitrary shape in a homogeneous medium is the Rayleigh-Sommerfeld (RS) integral [109] as shown in Equation 2.22

$$p(\mathbf{r}) = -\frac{i\rho_0 c_0 k}{2\pi} \int_S \mathbf{A}(\mathbf{r}_0) \frac{e^{ik|\mathbf{r}-\mathbf{r}_0|}}{|\mathbf{r}-\mathbf{r}_0|} dS \tag{2.22}$$

where $p(\mathbf{r})$ is the pressure at the point of interest $\mathbf{r}$, $i = \sqrt{-1}$, ρ_0 is the density of the medium, c_0 is the speed of sound in the medium, k is the wave number, $A(\mathbf{r}_0)$ is the

excitation function of the source located at $\mathbf{r}_0$, and dS is the elemental surface area of the source.

Physically, Equation 2.22 states that the pressure at a particular observation point $p(\mathbf{r})$ is the result of integrating the individual contributions of each elemental point source with surface area dS from the transducer surface S. Assumptions made by the RS integral are that all point sources are strictly hemispherical waves that propagate with linear behaviour into a homogeneous medium, and the transducer surface is assumed to be surrounded by an infinite rigid baffle.

A basic attenuation model for an ultrasound source in water and propagating into a homogeneous attenuating medium can be incorporated into the RS integral through the addition of an exponential term as shown in Equation 2.23

$$p(\mathbf{r}) = -\frac{i\rho_0 c_0 k}{2\pi} \int_S \mathbf{A}(\mathbf{r}_0) \frac{e^{ik|\mathbf{r}-\mathbf{r}_0|} e^{-\alpha d}}{|\mathbf{r}-\mathbf{r}_0|} dS \tag{2.23}$$

where α is the attenuation coefficient of the lossy homogeneous medium, and d is the ray distance travelled within the lossy medium from each source location [76].

Although the RS integral is able to evaluate the acoustic field from sources of arbitrary shape and size, caveats are that reflections, refraction, nonlinearity, and scattering effects in the attenuating medium are ignored, which limits this approach to linear homogeneous propagation models. In addition, if very fine spatial sampling of the acoustic field is required, repeated evaluation of the RS integral quickly becomes very computationally demanding.

An alternative acoustic beam modelling approach is the spatial impulse response method developed by Tupholme and Stepanishen [110–112]. This method calculates the pressure at a particular location by convolving an input function with the spatial impulse response of the source rather than directly implementing the surface integral described by the RS method. Another notable beam modelling approach is the angular

spectrum method [113, 114], which calculates the acoustic field from one parallel plane to another using the 2D Fourier transform to decompose the acoustic field into a summation of plane waves at various angles (forming the angular spectrum) multiplied by a propagation term. The Fresnel approximation [115] which is explored in Chapter 3 is also another beam modelling approach, where geometrical approximations enable the simplification of the surface integral described by the RS approach to be converted into the form of a 2D Fourier transform, which can be evaluated to calculate the acoustic pressure over an entire plane at a given propagation depth.

Although these methods are faster techniques to calculate the acoustic field from arbitrary sources compared to direct numerical evaluation of the RS integral, they are often bound by the same modelling assumptions which limits their use to modelling acoustic propagation in homogeneous media. However, more recent developments to the RS integral and angular spectrum methods have since extended their application to take into account layer-based inhomogeneity [116–118].

2.3.4 Full-wave Models

Full-wave acoustic simulation methods include finite difference time domain (FDTD), finite element analysis (FEA) and pseudospectral approaches, which involve solving the linear or nonlinear wave equations in some shape or form [106–108, 119–122]. Full-wave solvers are usually more computationally demanding in comparison to the acoustic beam methods mentioned in the previous section, however they have the capability to model acoustic interactions in inhomogeneous media such as reflection and refraction, which makes them more suitable for modelling ultrasound propagation in the body [106].

In most acoustic FDTD and FEA methods, the acoustic wave equation is indirectly solved through coupling of the individual governing equations (e.g. Equations

2.11-2.13) since this enables convenient implementation of boundary conditions, the incorporation of acoustic sources into the discretised governing equations, and the convenient calculation of acoustic intensity which is necessary for modelling thermal effects [123]. An example of two open-source full-wave solver packages are SimSonic (FDTD) [122, 124], and k-Wave, which is an alternative full-wave solver which does not fall under FDTD or FEA, rather using a k-space technique that implements a pseudo-spectral method for calculating spatial derivatives [125]. Alternative commercial finite element modelling packages are PZFlex (OnScale Inc, CA, formerly PZFlex LLC) and COMSOL Multiphysics (COMSOL Inc.), which are both used in industry and in biomedical ultrasound research [126, 127].

The full-wave simulation method of choice for this thesis will be the commercial package PZFlex due to it being an optimised solver which can perform acoustic and thermal simulations in inhomogeneous media on a single high-performance workstation (given sufficient RAM to support the simulation domain size), rather than requiring access to a cluster network or computational cloud. A full comparison between different full-wave solvers is out of the scope of this thesis, however a more comprehensive list of both free and commerically available acoustical software packages can be found from [108] and [107].

2.3.5 PZFlex

PZFlex (OnScale Inc, formerly PZFlex LLC) can be used to model mechanical-piezoelectric and acoustic problems, utilising regularly spaced hexahedron elements for 3D simulations as opposed to irregular complex geometries in favour for fast computation of arrays and matrices. The main advantage and motivation of using PZFlex is the ability to model acoustic propagation in inhomogeneous media. Phenomena such as reflection, refraction, and shear wave formation in structures such as

bone are inherently taken into account, and the ability to incorporate patient-specific segmented datasets enables the modelling of ultrasound-mediated hyperthermia in clinically relevant scenarios.

Wave propagation in PZFlex is captured in the time domain by directly calculating the force-balance relationships experienced by elements with respect to an external driving force, where the general relationship between damping, mass, and stiffness is described by Equation 2.24

$$F_{ext} = M\ddot{\boldsymbol{x}} + C\dot{\boldsymbol{x}} + K\boldsymbol{x} \tag{2.24}$$

where F_{ext} is the external force experienced by an element, M is the element mass, $\ddot{\boldsymbol{x}}$ is the acceleration vector, C is a damping constant, $\dot{\boldsymbol{x}}$ is the velocity vector, K is the stiffness, and $\boldsymbol{x}$ is the displacement vector [128].

Acoustic and thermal simulations in PZFlex are conveniently decoupled since the time scales between the two simulations differ greatly. In PZFlex, mechanical energy losses on an element by element basis are recorded from the acoustic simulation, and subsequently imported into thermal simulations as the external heat source $\dot{q}$ as described in the Pennes bioheat transfer equation (Eq. 2.7).

As with all finite element approaches, there is a trade-off between simulation accuracy and the demand for computational resources. In PZFlex, the size of the model is limited to the available physical RAM of the operating system, with 3D simulations requiring approximately 1GB of RAM per 4×10^6 elements. If the minimum recommended resolution of 15 elements per wavelength is used, this corresponds to a volume spanning approximately $(10.6\lambda)^3$ where λ is the wavelength. The simulation domain size can be significantly reduced for models which exhibit half symmetry, quarter symmetry, or axisymmetry through the use of symmetric boundary conditions. Coupling symmetric simulations to full-3D models is a strategy which is explored in

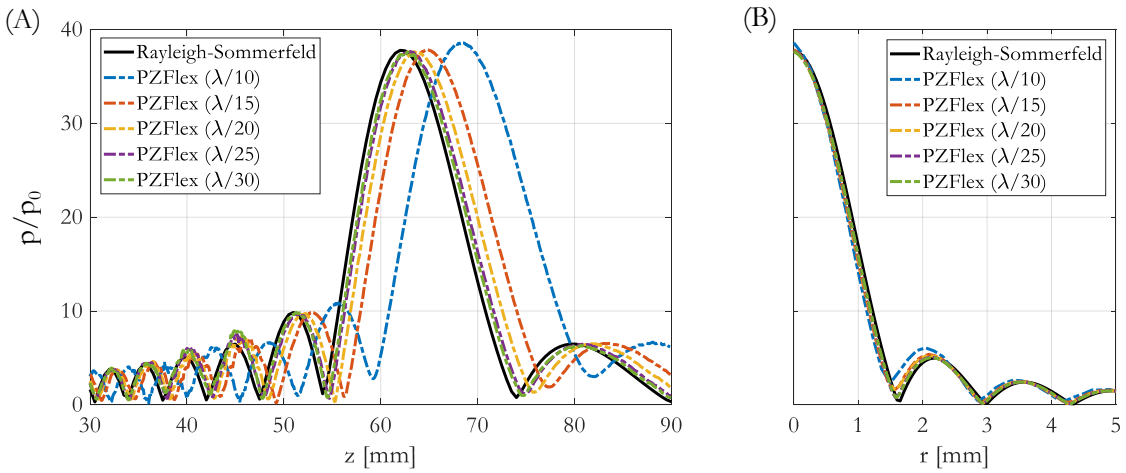


Fig. 2.4 Simulated axial (A) and radial (B) normalised pressure profiles for the H101 spherically focused transducer in water using a numerical implementation of the RS-integral (black solid line) and PZFlex (dashed lines) with varying grid resolution. The radial pressure profiles were taken at the location of the peak axial pressure, and in all simulations, the speed of sound in water was defined as $c_w = 1482 \text{m.s}^{-1}$, and the wavelength is calculated as $\lambda = c_w/f = 1.35\text{mm}$ where $f = 1.1\text{MHz}$ is the centre frequency of the transducer.

this thesis to minimise simulation times and to process models which otherwise would be too large to perform in a single attempt.

To illustrate and validate the performance of PZFlex, the acoustic field produced by an existing single-element spherically focused therapeutic ultrasound transducer (H101, Sonic Concepts, outer diameter of 64mm, centre frequency of 1.1MHz) in water was modelled with a 2D axisymmetric simulation using linear wave propagation, and compared with the numerical implementation of the RS integral in MATLAB as shown in Figure 2.4. The RS integral solution for the central axis and radial pressure profiles are shown by the black solid lines in Figures 2.4A and 2.4B, and the equivalent simulation results from PZFlex at various element resolutions are shown in comparison by the dotted lines where λ is the wavelength in water.

Simulated maximum peak axial pressure locations z_{pk} and the first radial sidelobe locations r_1 at $z = z_{pk}$ are documented in Table 2.2, along with their respective

Table 2.2 Comparison of the amplitude and location of the simulated peak axial pressure and first radial sidelobe from PZFlex at various element resolution with the RS integral solution for the H101 focused transducer in water.

	z_{pk} [mm]	% err	$\frac{p(z_{pk})}{p_0}$	% err	r_1 [mm]	% err	$\frac{p(r_1)}{p_0}$	% err
RS Integral	62.00	-	37.78	-	2.20	-	4.98	-
PZFlex ($\lambda/10$)	68.33	10.21	38.58	2.12	2.04	−7.14	6.08	22.25
PZFlex ($\lambda/15$)	64.81	4.53	37.86	0.21	2.09	−4.95	5.38	8.12
PZFlex ($\lambda/20$)	63.54	2.48	37.64	−0.37	2.12	−3.86	5.22	4.90
PZFlex ($\lambda/25$)	63.05	1.69	37.68	−0.26	2.13	−3.36	5.07	1.85
PZFlex ($\lambda/30$)	62.82	1.32	37.69	−0.24	2.14	−2.91	5.03	1.11

z_{pk} is the peak axial pressure location, $p(z_{pk})$ is the peak axial pressure, r_1 is the first radial sidelobe peak location, $p(r_1)$ is the first radial sidelobe peak pressure, p_0 is the source pressure amplitude, and % err is the percentage error between the PZFlex value relative to the RS integral solution.

amplitude values and the percentage error relative to the RS integral solution. At higher element resolutions the PZFlex simulation converged to the RS integral solution, where the highest simulated grid resolution of $\lambda/30$ resulted in peak and first radial sidelobe amplitudes which agreed to 0.24% and 1.1%, with peak location agreement to 1.3% and 2.1% respectively. The recommended minimum simulation resolution in PZFlex is stated as $\lambda/15$, which in this case resulted in simulated peak and first radial sidelobe amplitudes which agreed to 0.2% and 8.1%, with peak location agreement to 4.5% and 4.2% respectively.

2.3.6 Tissue Models Used in Hyperthermia

Figure 2.5 illustrates the three main tissue models found in literature for acoustic simulations in tissue, which include a homogeneous tissue model (2.5A), a multi-layer tissue model (2.5B), and multi-layer tissue models with patient-specific geometry (2.5C).

Early ultrasound simulation studies began with modelling ultrasound tissue propagation by assuming a homogeneous attenuating material (Fig. 2.5A) with a fixed attenuation, density, speed of sound, thermal conductivity, specific heat, and perfusion

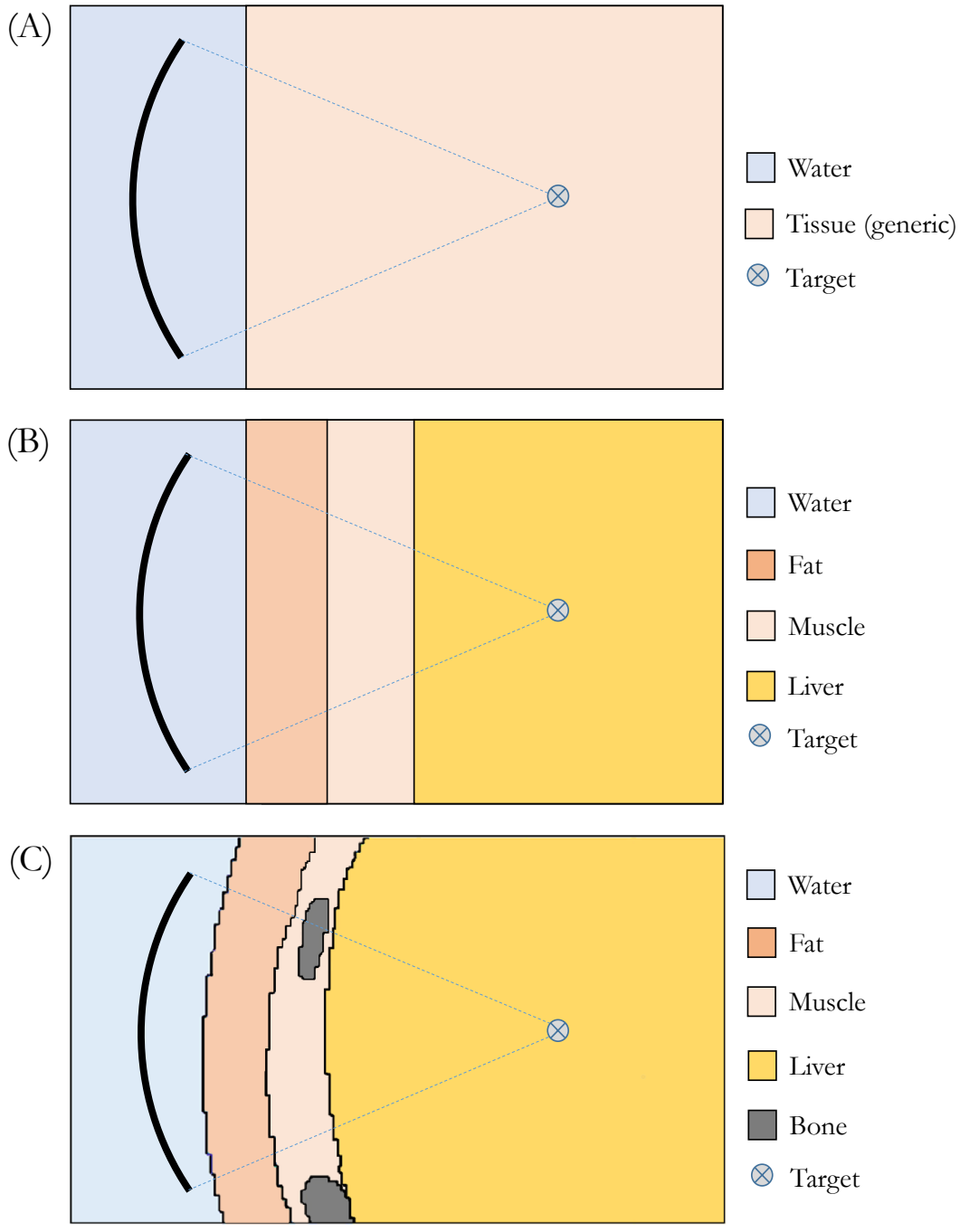


Fig. 2.5 Illustrations of a focused ultrasound transducer targeted into a (A) homogeneous tissue model, (B) simple multi-layer tissue model, and (C) a patient-specific segmented tissue model.

[129, 130]. Without perfusion, this model is also analogous to modelling a tissue-mimicking phantom, assuming that the phantom is homogeneous and has a fixed attenuation coefficient.

It is known that different tissues have characteristic speeds of sound, attenuation, and density - all of which can alter the pressure field as it propagates into the body. Some studies have therefore considered separating the homogeneous tissue medium into four major layers (Fig. 2.5B) such as skin, fat, muscle, and viscera [131–133]. In a similar manner, one study has investigated further dividing the skin region into the epidermis and dermis layers [134, 135], and another study assigned different blood perfusion values to the outer and inner regions of a tumour model on the biological basis that the inner centre of the tumour is often necrotic and thus will have a lower rate of perfusion compared to the well-vascularised periphery [136]. The multi-layered tissue model is more realistic in the context of being able to capture the effect of pre-focal layers with high attenuation or low perfusion, however this model assumes that each layer has a defined consistent thickness and lies exactly perpendicular to the transducer, which is never the case in reality.

The ability to model inhomogeneous media is where full-wave approaches such as PZFlex or k-Wave can be advantageous, since spatial variation in acoustic and thermal material properties can be taken into account. The use of CT or MRI imaging to construct segmented and labelled 3D tissue geometry maps is a step towards modelling patient-specific ultrasound propagation in the body, where Figure 2.5C illustrates a cross-section of an anonymised segmented CT dataset (provided by Prof. Robin Cleveland, University of Oxford, UK) which is used in the subsequent acoustic and thermal simulations presented in this thesis. It is necessary to point out that due to the limited soft-tissue contrast of CT imaging, the skin layer is absent in this dataset

as it has been incorporated into the fat layer, and the three remaining major tissue labels are muscle, liver, and bone.

Although imaging can give geometrical information, it is also necessary to know the acoustic and thermal properties for each major tissue type of interest on a patient-specific basis. The most accurate way of modelling ultrasound propagation in tissue would be to use an empirical relationship between tissue properties within each tissue type [137, 138], however obtaining such data for each major tissue type is difficult since some parameters may require invasive sampling. In addition, parameters such as blood perfusion rate may have significant variation between patients, between regions of the same tissue depending on the diameter and location of major vessels, and may also vary with exposure to heat [37]. Therefore in this work, patient-specific considerations are restricted to geometrical tissue segmentation through CT and MRI imaging, and then average bulk tissue properties from the literature are employed.

2.3.7 Acoustic and Thermal Parameters of Biological Tissues

Standard diagnostic ultrasound imaging techniques use an average speed of sound of 1540m.s^{-1} in soft tissue in order to calculate the time of flight of acoustic waves [139]. For focused ultrasound applications, the variation in material property values between differing tissue types can result in aberration of the acoustic field, which can significantly affect focusing [140–143]. Similarly, the variation in blood perfusion rate for different tissue types will also affect the ability to predict and induce mild hyperthermia generation in patients.

The anonymised segmented CT dataset provided for acoustic simulations in this thesis is segmented into four major tissue types: fat, muscle, bone, and other soft tissue (CT imaging has limited soft-tissue contrast in comparison to MRI), where the liver was segmented through an additional semi-automated MATLAB script (Prof.

Robin Cleveland, University of Oxford, UK). In order to select suitable bulk tissue properties, relevant reported literature values for each tissue type were reviewed, and the parameters which exhibited the greatest variation in literature (acoustic attenuation and blood perfusion) are subsequently presented in Figures 2.6-2.9 below[2].

Figure 2.6A shows a summary of some reported values in literature for the acoustic attenuation coefficient of healthy human liver tissue, where the average reported value was found to be $0.71\pm0.39\text{dB.cm}^{-1}$ (1SD) which was calculated from acoustically relevant measurements listed in [62, 144, 145]. Figure 2.6B shows the reported blood flow through the liver from the literature, where the average value was determined by averaging the experimentally measured values from [146–153], and was found to be $838\pm293\text{ml.kg}^{-1}\text{.min}^{-1}$ (1SD). An average male human liver weight of 1.561kg was used to normalise reported values where necessary [154].

The previously reported acoustic attenuation coefficient values for human adipose (fat) tissue are shown in Figure 2.7A, with an average value of $0.55\pm0.23\text{dB.cm}^{-1}$ (1SD) obtained from averaging the relevant values listed in [62, 144, 155, 156]. The reported values for blood flow for human adipose tissue are shown in Figure 2.7B with an average value of $26\pm3.3\text{ml.kg}^{-1}\text{.min}^{-1}$ (1SD) obtained from averaging the relevant values listed in [147, 157–159].

For human skeletal muscle, the reported values for attenuation coefficient and blood flow are shown in Figure 2.8, where an average attenuation coefficient value of $1.03\pm0.49\text{dB.cm}^{-1}$ (1SD) was obtained by averaging the relevant values listed in [62, 144, 155, 160]. Similarly, an average blood flow value of $26\pm5.6\text{ml.kg}^{-1}\text{.min}^{-1}$ (1SD) was obtained by averaging the relevant values listed in [147, 161, 162] as shown in Figure 2.8B.

[2]The sources shown are by no means an extensive review of all the documented studies reported in the literature.

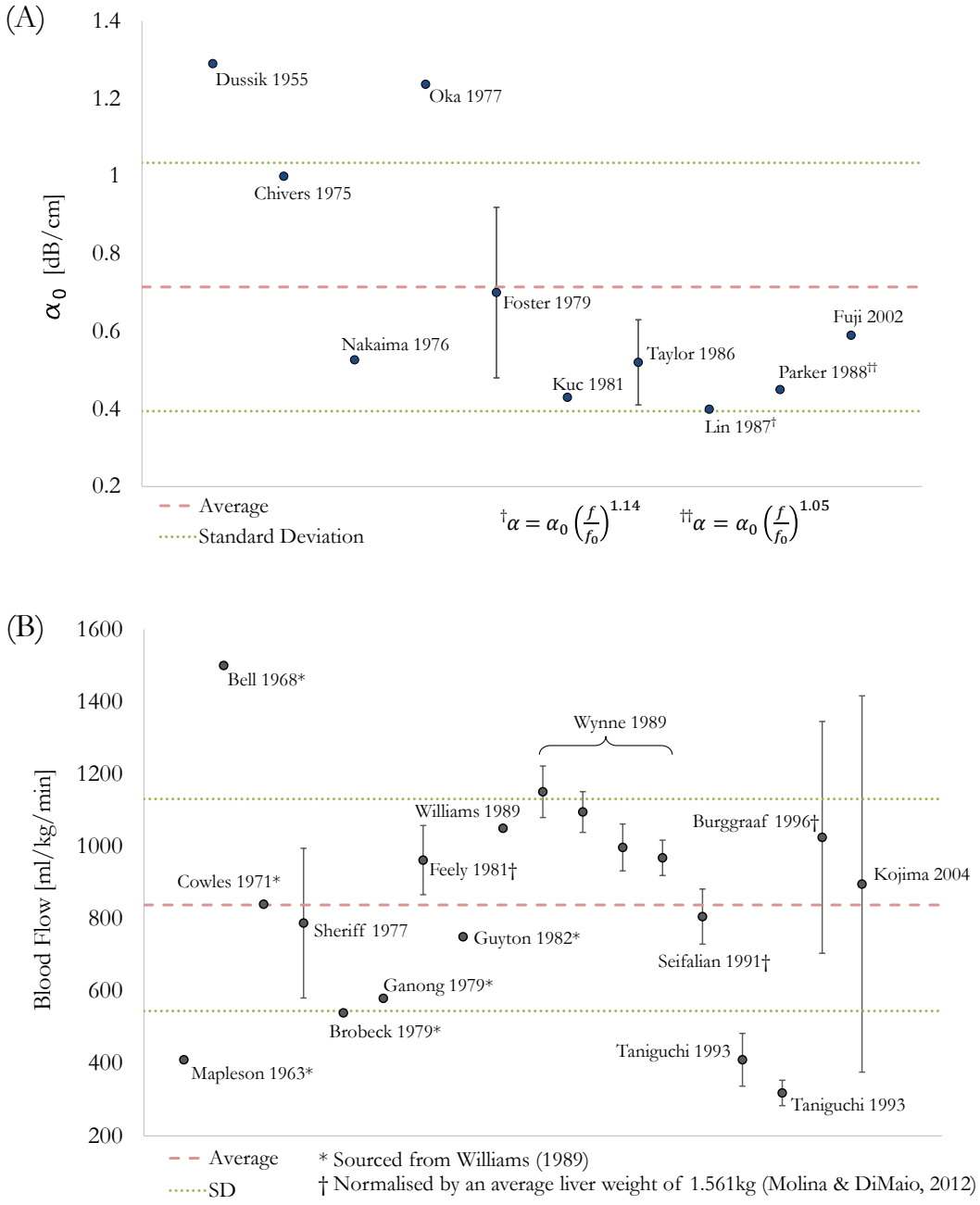


Fig. 2.6 Reported acoustic attenuation coefficient (A) and blood flow values (B) for human liver. The average reported attenuation value sourced from relevant measurements in [62, 144, 145] was found to be $0.71 \pm 0.39 \text{dB.cm}^{-1}$ (1SD). Unless stated otherwise, attenuation α is assumed to follow the model $\alpha = \alpha_0 (f/f_0)^1$ where f_0 is equal to 1MHz. The average blood flow value obtained from [146–153] was reported to be $838 \pm 293 \text{ml.kg}^{-1}.\text{min}^{-1}$ (1SD). Where necessary, liver blood flow values were normalised by the weight of an average male human liver [154].

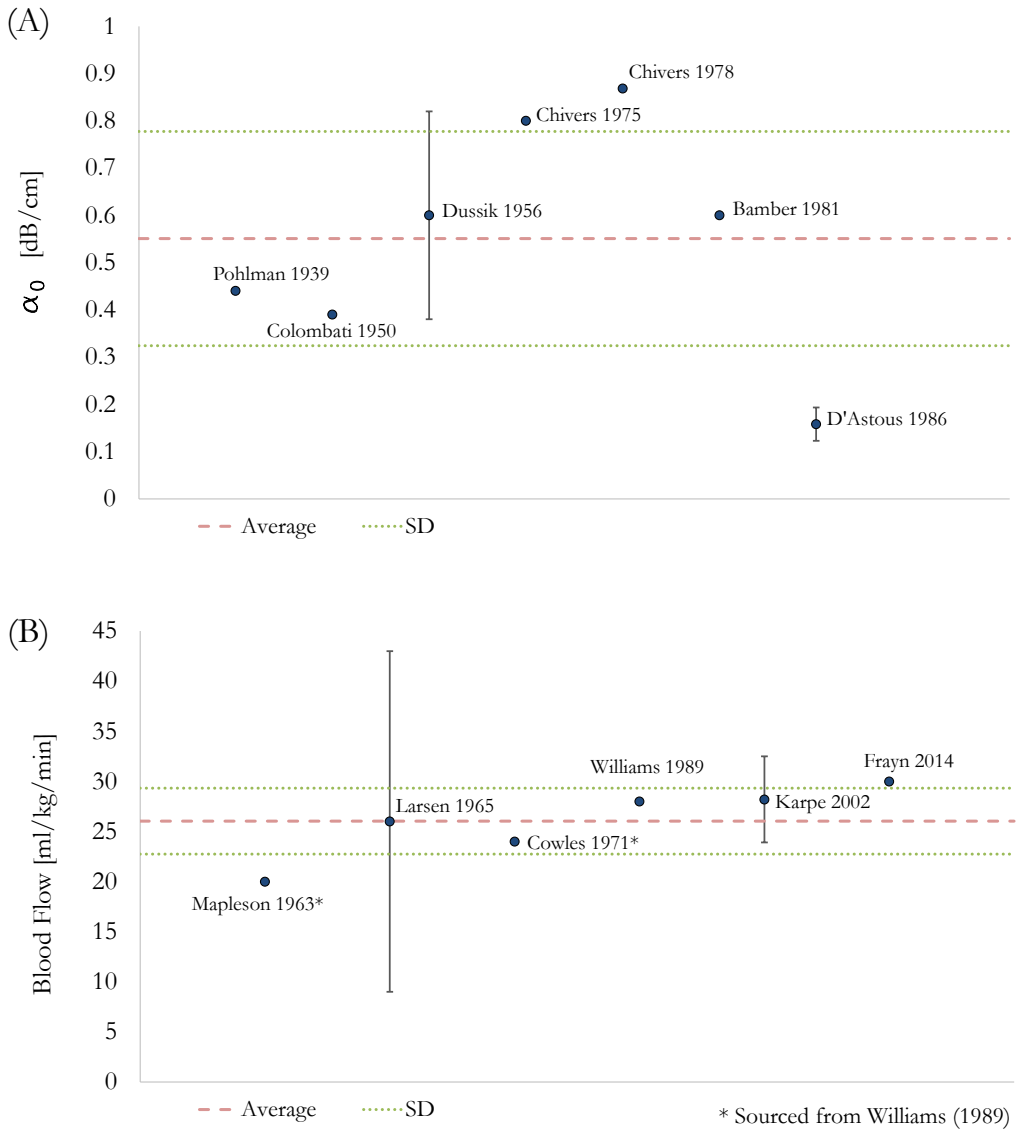


Fig. 2.7 Reported acoustic attenuation coefficient (A) and blood flow values (B) for human adipose (fat) tissue. The average reported attenuation coefficient value was found to be $0.55\pm0.23\text{dB.cm}^{-1}$ (1SD) obtained from sources listed in [62, 144, 155, 156]. Unless stated otherwise, attenuation α is assumed to follow the model $\alpha = \alpha_0(f/f_0)^1$ where f_0 is equal to 1MHz. The average blood flow rate was found to be $26\pm3.3\text{ml.kg}^{-1}\text{.min}^{-1}$ (1SD) based on the values listed in [147, 157–159].

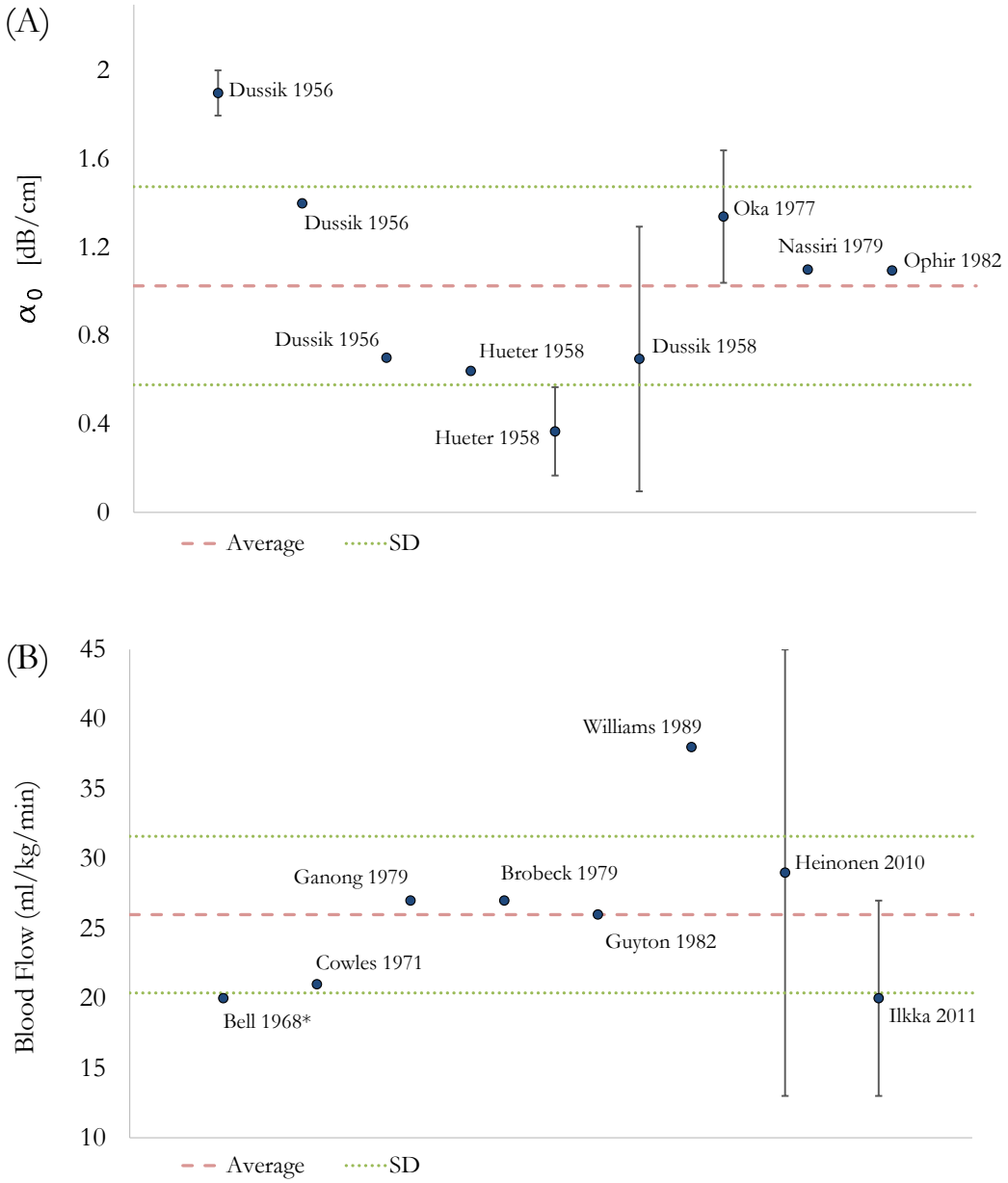


Fig. 2.8 Reported acoustic attenuation coefficient (A) and blood flow values (B) for human skeletal muscle tissue. The average reported attenuation coefficient value was found to be 1.03±0.49dB.cm^{-1} (1SD) based on the average relevant values listed in [62, 144, 155, 160]. Unless stated otherwise, attenuation α is assumed to follow the model $\alpha = \alpha_0(f/f_0)^1$ where f_0 is equal to 1MHz. The average blood flow was found to be 26±5.6ml.kg^{-1}.min^{-1} (1SD) obtained from averaging the relevant values listed in [147, 161, 162].

Finding reliable sources for the longitudinal and shear attenuation of rib bone was challenging since there were no values reported for the rib in particular, with a limited number of sources in literature focusing on the study of skull and long bones. It would not be unreasonable to compare the attenuation of the rib to the skull since the structure of the rib comprises of a thin outer shell of compact (cortical) bone with a trabecular (spongy) bone centre, rather than long bones which have a much thicker cortical shell with marrow in the centre. Some studies have treated the ribs as perfect absorbers [97, 163], while other studies have used acoustic attenuation values for skull bone instead [164–167]. In this work, the acoustic properties of rib bone were approximated by the longitudinal and shear wave speeds measured in skull bone which were 2820m.s^{-1} and 1500m.s^{-1} respectively [168], with longitudinal and shear acosutic attenuation coefficients of $\alpha = 7.75(f/f_0)^{1.37}$dB.cm^{-1} and $\alpha_s = 16.7(f/f_0)^{1.37}$dB.cm^{-1} respectively [168, 169].

Obtaining reliable sources for blood flow rate in rib bone was also very challenging due to the lack of studies looking at human ribs. In order to obtain an approximation for rib blood flow, studies from dog bone were also included to supplement the existing data for human bone as shown in Figure 2.9. An average blood flow rate of 114±80ml.kg^{-1}.min^{-1} (1SD) was obtained from the average of relevant sources listed in [147, 170–176].

Overall, parameters such as speed of sound and density were found to be quite well established and consistent, while parameters such as thermal conductivity, specific heat capacity, rib bone attenuation, and bone shear wave speed were found to be very sparse with very few sources to reference. Where possible, the average of several primary sources were used to produce a representable bulk tissue value. A summary of the finalised acoustic and thermal properties for the tissue types simulated in PZFlex can

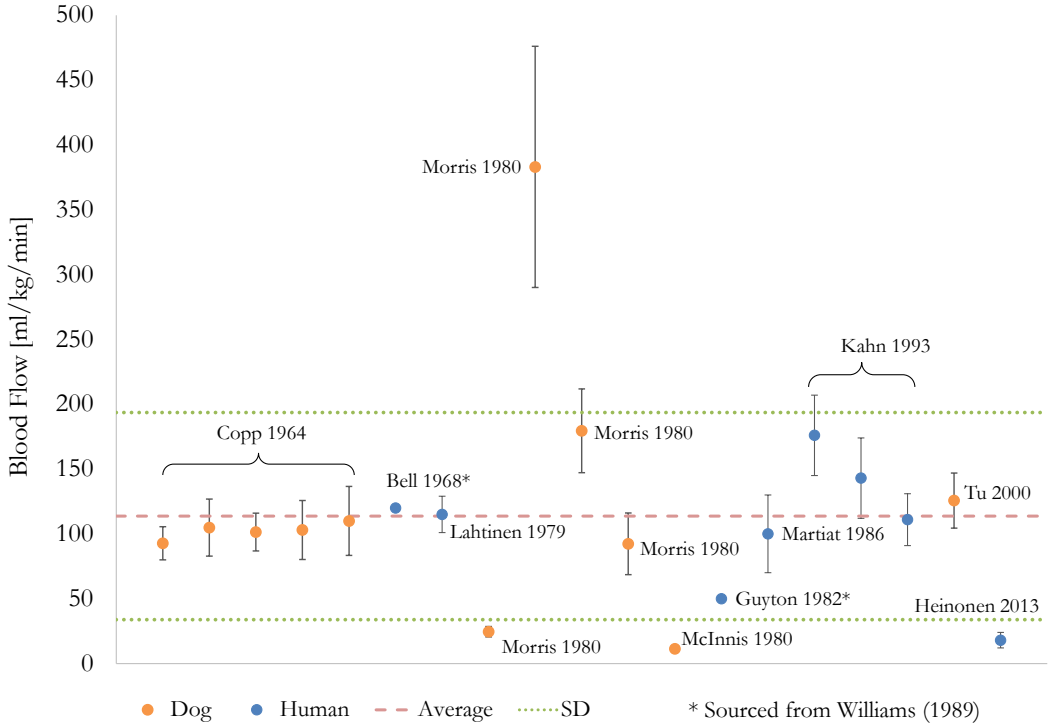


Fig. 2.9 Reported blood flow values measured in human and dog bone. An average blood flow value of 114±80ml.kg^{-1}.min^{-1} (1SD) was obtained by averaging the relevant values from [147, 170–176].

be found in Table 2.3, where average tissue blood flow values have been converted into average tissue perfusion rates with units of kg.m^{-3}.s^{-1}.

Table 2.3 Table of average acoustic and thermal properties of human tissue and other simulated materials. Unless specified, the frequency dependence of longitudinal and shear attenuation are assumed to be of the form $\alpha = \alpha_0(f/f_0)^1$ and $\alpha_s = \alpha_{s,0}(f/f_0)^1$ where $f_0 = 1\text{MHz}$.

Medium	c [m/s]	ρ [kg/m^3]	α_0 [dB/cm]	k [W/m/K]	C [J/kg/K]	c_s [m/s]	$\alpha_{s,0}$ [dB/cm]	W_b [kg/m^3/s]
Ribs	2820	1465	$7.75(f/f_0)^{1.37}$	0.435	1700	1500	$16.7(f/f_0)^{1.37}$	2.94
Liver	1584	1050	0.79	0.47	3600	-	-	15.54
Fat	1476	928	0.63	0.25	2325	-	-	0.43
Muscle	1568	1058	1.276	0.4975	3720	-	-	0.49
Water	1497	997	0.002	0.61	4182	-	-	-
Blood	-	1060	-	0.53	3600	-	-	-
Clear Resin (GPCL04)	2630	1170	5.1	0.2*	1500*	1193	18.7	-
VeroClear	2424	1185	2.25	0.2*	1500*	1193	18.7	-

*Average values for acrylic used as an approximation [177]. Sources: Ribs [62, 168, 169, 178], liver [62, 146, 145, 179], fat [62, 155, 180], muscle [62, 180, 181], blood [62]. Clear resin (GPCL04, FormLabs Inc.) acoustic properties were measured experimentally, VeroClear (Stratasys Ltd.) acosutic properties were obtained from [182], and water properties were obtained from standard reference tables at 25°C [62].

3 Investigation of Sectored Transducers for Mild Hyperthermia

3.1 Current Transducer Designs and Strategies for Mild Hyperthermia

As discussed in section 2.2.3, most existing extracorporeal clinically approved therapeutic ultrasound devices are highly focused and designed for tumour ablation, targeting very small precise volumes and inducing temperatures typically above 50°C for several seconds in order to directly kill tissue through thermal necrosis [9]. Mechanical or electronic scanning of the focal volume is often performed in order to cover a larger area, however it is difficult for such highly focused transducers to generate consistent and prolonged mild hyperthermia in large target volumes where temperatures ideally do not exceed 43°C.

In comparison, multi-foci acoustic fields have been shown to be able to generate mild hyperthermia with a more uniform and predictable heat distribution [183]. Generation of multi-foci acoustic fields often involve the use of multiple transducers [184, 185] or transducers that are comprised of many elements (known as phased arrays) which have the additional ability of electronic beam steering and independent control of the phase and amplitude of each element [74, 76, 129, 186–189].

Independent control of amplitude and phase enables the generation of optimised thermal and acoustic fields through numerical approaches such as the pseudoinverse

field synthesis technique [76, 86, 186, 190–194], or by making phase and amplitude corrections based on time-reversal approaches [141, 166, 195, 196]. However, one common disadvantage associated with transducers which have many independently driven elements are that these systems are often expensive and complex [83].

Acoustic fields produced by the sector-vortex transducer design are investigated in this chapter due to their ability to generate multi-foci acoustic fields suitable for large volume mild hyperthermia with minimal additional complexity [197–199]. Studies have investigated the ability of sector-vortex transducers to generate multi-foci acoustic fields for hyperthermia, including: theoretical simulations in a homogeneous or multi-layered perfused tissue model [197, 129, 200], experimental measurements in excised kidneys [84], and the generation of hyperthermia in small animal models [76, 83].

The principle of the sector-vortex array is illustrated in Fig. 3.1 where a spherically focused transducer surface is divided into N equal sectors. The location of the pressure maximum in the focal plane can be shifted in the radial direction away from the central axis when driven with a phase distribution whose phase rotates m times per full revolution around the transducer surface, where N is even, and m is an integer number not greater than $N/2$. The vortex mode m is directly related to the specific phase of each sector through Equation 3.1

$$\theta_n = mn\left(\frac{2\pi}{N}\right) \tag{3.1}$$

where n is the sector number of the transducer starting from 0, and θ_n is the phase of the n^{th} sector in radians. The greatest radial shift in the focal plane occurs when the transducer is driven in the highest vortex mode ($m = N/2$). It can be seen from Equation 3.1 that this results in neighbouring sectors being driven exactly out of phase with a phase difference of π radians.

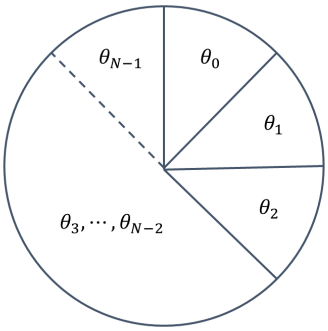


Fig. 3.1 Illustration of a sectored spherically focused transducer with N equally spaced sectors. The relative driving phase of the n^{th} sector is labelled with the notation θ_n.

The effect of varying the operational mode on the acoustic field of a spherically focused transducer with $N = 8$ equal sectors is shown in Figure 3.2, where the transducer geometry and centre frequency are based on an existing therapeutic transducer (H101, Sonic Concepts, Inc.), and simulations of the acoustic fields produced in water were performed using the Fresnel approximation (described in section 3.2.1). Column 1 of Fig. 3.2 shows the surface phase distribution, where operational modes 0, 1, 2 and 4 are shown in rows A, B, C and D respectively. The corresponding radial and axial pressure fields for each operational mode are shown in columns 2 and 3 respectively, where radial pressure fields (column 2) were taken at the geometric focus of the transducer ($z = 62.6$mm), and axial pressure fields (column 3) were taken at the plane $x = 0$mm, with the exception of D3 which was taken at $x = 1.1$mm since the plane at $x = 0$mm for $m = 4$ is a pressure null. The transducer is centred at the origin, and the amplitude of the simulated pressure fields were normalised to the surface pressure p_0.

The simulated acoustic fields in Fig. 3.2 indicate a clear increase in radial spreading of the focus with increasing operational mode, where the radial location of the peak pressure relative to the central axis for modes 1, 2, and 4 are ±1mm, ±1.6mm, and ±2.8mm respectively. The increase in radial spreading is also accompanied by a reduction in peak pressure, where the acoustic gain for modes 0, 1, 2 and 4 were 37.7,

18.8, 13.3 and 12.9 respectively. The size of the -3dB focal volume (relative to the peak pressure within each case) for modes 0, 1, 2 and 4 were 9.41mm^3, 58.30mm^3, 112.68mm^3 and 94.21mm^3 respectively. Furthermore, there is a transition in acoustic field shape from $m = 2$ to $m = 4$ where the annular ring focus (C2) is divided into eight separate radial peaks (D2) resulting from the antiphase driving pattern of the source.

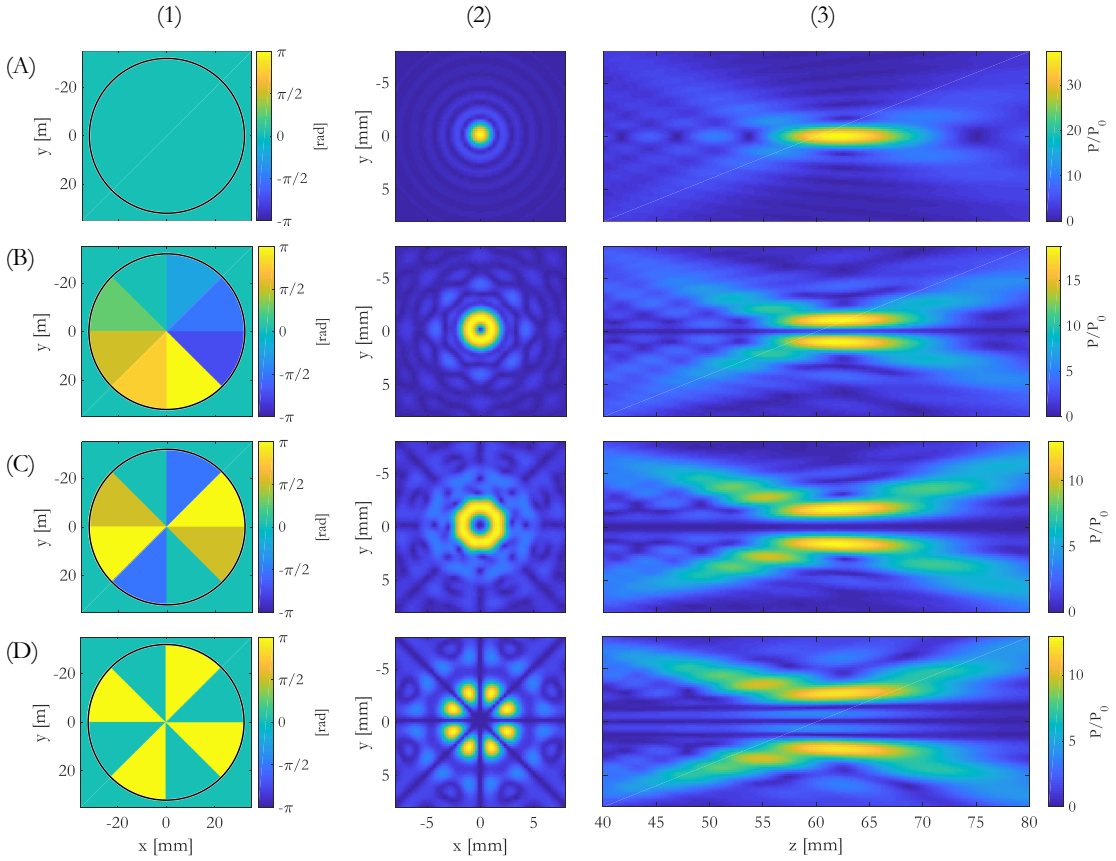


Fig. 3.2 Surface phase (column 1) and simulated pressure fields (columns 2 and 3) produced by a 64mm diameter 1.1MHz spherically focused transducer with eight equal sectors in water using the Fresnel approximation (described in section 3.2.1). Operational modes 0, 1, 2, and 4 are indicated by rows A, B, C and D respectively. The transducer is centred at the origin, with pressure field amplitudes normalised to the surface pressure p_0. Radial pressure fields (column 2) were taken at the geometric focus of the transducer ($z = 62.6$mm), and axial pressure fields (column 3) were taken at the plane $x = 0$mm, with the exception of D3 which was taken at $x = 1.1$mm since the plane $x = 0$mm for this operational mode is a pressure null.

It is also possible to further increase the radial location of the focal volume by using a transducer with a greater number of sectors and operating in a higher mode. However, simulations of 16 and 32-sector transducers operating in modes 8 and 16 respectively resulted in acoustic fields which displayed significantly lower acoustic gain. Therefore, the range of defocusing that could be achieved using eight sectors was established as being adequate for the purposes of exploring a sectored transducer with geometrical and acoustical properties based on the H101 transducer.

3.2 Optimisation Approach for a Sectored Focused Transducer for Mild Hyperthermia

In this section, an optimisation approach will be investigated to determine the performance of a sector-vortex transducer design for the purpose of large volume mild hyperthermia. Simulations of 3D temperature fields generated by focused ultrasound transducers with source conditions that have asymmetric spatial phase variation often require a finite difference or finite element strategy in order to model these characteristics. An optimisation approach which relies on numerous iterations of a finite difference forward model would be very computationally intensive and time consuming.

Techniques to solve the inverse problem have been explored in several studies, where the pseudoinverse method was used to calculate the exact source requirements to generate specific pressure field patterns of interest from an array [76, 85, 86, 186, 190–193, 201]. Although this approach is an elegant solution to determining the source condition for a well characterised predetermined field of interest, there may be other unexplored alternative acoustic field patterns which are also suitable to achieve large volume mild hyperthermia.

The optimisation approach described in this chapter addresses the forward problem; making use of the Fresnel approximation in order to solve a modified version of the Rayleigh-Sommerfeld integral to quickly calculate the acoustic field [109], followed by a 3D numerical implementation of the Pennes bioheat transfer equation to evaluate the corresponding thermal field. The Fresnel approximation, as described by Mast [115], results in a faster method of evaluating 3D acoustic fields from transducers with non-axisymmetric surface apodisation in comparison to directly solving the Rayleigh-Sommerfeld integral or finite difference techniques, enabling the forward model to be solved iteratively within a reasonable amount of time.

3.2.1 Fresnel Approximation of the Rayleigh Integral

The Rayleigh-Sommerfeld integral [109] for a time-harmonic radiating surface velocity source with $e^{-i\omega t}$ time dependence is given by Equation 3.2

$$p(\mathbf{r},t) = -\frac{i\rho_0 c_0 k}{2\pi} e^{-i\omega t} \int_S \mathbf{u}(\mathbf{r}_0) \frac{e^{ik|\mathbf{r}-\mathbf{r}_0|}}{|\mathbf{r}-\mathbf{r}_0|} dS \tag{3.2}$$

where t is time, ω is angular frequency, $i = \sqrt{-1}$, ρ_0 is the density of the medium, c_0 is the speed of sound in the medium, $k = \omega/c_0$ is the wavenumber, $\mathbf{u}$ is the particle velocity normal to the surface of the source, $\mathbf{r}$ and $\mathbf{r}_0$ are the observation and source points respectively, and S is the surface of the source. Physically, Equation 3.2 states that the pressure at a particular observation point $p(\mathbf{r},t)$ is the result of integrating the individual contribution from each elemental point source with surface area dS over the entire transducer surface S. We solve Equation 3.2 using the Fresnel approximation by extending a previous method [115] to incorporate geometric focusing and surface apodisation.

For a rectangular planar source located at $z = 0$ with surface velocity $\mathbf{u}(x_0, y_0) = u_0 A(x_0, y_0)$, Equation 3.2 becomes:

$$p(\mathbf{r}, t) = -\frac{ik\rho_0 c_0 u_0}{2\pi} e^{-i\omega t} \int_{-\infty}^{\infty} \int_{-\infty}^{\infty} A(x_0, y_0) \frac{e^{ik|\mathbf{r}-\mathbf{r}_0|}}{|\mathbf{r}-\mathbf{r}_0|} dx_0 dy_0 \tag{3.3}$$

where $A(x_0, y_0)$ is a complex dimensionless apodisation function. The Fresnel approximation makes the assumption that

$$(x - x_0)^2 + (y - y_0)^2 \ll z^2 \tag{3.4}$$

where z is the propagation axis and x and y are lateral axes, in which case the distance $|\mathbf{r} - \mathbf{r}_0|$ in the exponential term can be approximated with the first two leading terms of the binomial expansion:

$$|\mathbf{r} - \mathbf{r}_0| = \sqrt{(x - x_0)^2 + (y - y_0)^2 + z^2} \tag{3.5}$$

$$= \sqrt{(x^2 + y^2 + z^2) + (x_0^2 + y_0^2 - 2xx_0 - 2yy_0)} \tag{3.6}$$

$$\approx \quad r + \frac{x_0^2 + y_0^2 - 2xx_0 - 2yy_0}{2r} \tag{3.7}$$

Substituting Equation 3.7 as the exponential term in Equation 3.3 and approximating the nominal propagation distance from the source to an observation point $\mathbf{r} - \mathbf{r}_0$ as r from the Fresnel approximation in Equation 3.4 yields

$$\frac{e^{ik|\mathbf{r}-\mathbf{r}_0|}}{|\mathbf{r}-\mathbf{r}_0|} \approx \frac{e^{ik\left(r + \frac{x_0^2 + y_0^2 - 2xx_0 - 2yy_0}{2r}\right)}}{r} \tag{3.8}$$

giving the new expression of Equation 3.3 as shown in Equation 3.9.

$$p(\mathbf{r},t) = -\frac{ik\rho_0 c_0 u_0}{2\pi r} e^{-i\omega t} \int_{-\infty}^{\infty}\int_{-\infty}^{\infty} A(x_0,y_0) e^{ik\left(r+\frac{x_0^2+y_0^2-2xx_0-2yy_0}{2r}\right)} dx_0 dy_0 \tag{3.9}$$

Introducing the approximation of $r \approx z$ and rearranging terms, Equation 3.9 can be rewritten in the form of a 2D Fourier transform as shown in Equation 3.10 below.

$$p(r,t)_z = -\frac{ik\rho_0 c_0 u_0}{2\pi z} e^{i(kz-\omega t)} \int_{-\infty}^{\infty}\int_{-\infty}^{\infty} A(x_0,y_0) e^{\left(\frac{ik(x_0^2+y_0^2)}{2z}\right)} e^{(-ikxx_0/z)} e^{(-ikyy_0/z)} dx_0 dy_0 \tag{3.10}$$

Using the definition of the 2D Fourier transform as shown in Equation 3.11

$$F(\beta,\gamma) = \int_{-\infty}^{\infty}\int_{-\infty}^{\infty} f(x,y) e^{-i2\pi(\beta x+\gamma y)} dx dy \tag{3.11}$$

and applying the substitution $k = 2\pi/\lambda$, it can be seen that β is analogous to $x/\lambda z$, similarly γ with $y/\lambda z$, and $f(x,y)$ with $A(x_0,y_0)e^{ik(x_0^2+y_0^2)/2z}$.

To take into account phase, amplitude, and focusing from each individual sector, we let $A(x_0,y_0)$ take the form

$$A(x_0,y_0) = M(x_0,y_0) e^{i\theta(x_0,y_0)} e^{-ik(x_0^2+y_0^2)/2F_c} \tag{3.12}$$

where $M(x_0,y_0)$ and $\theta(x_0,y_0)$ account for the magnitude and phase of each source location (x_0,y_0) respectively, and the last term effects focusing at $z = F_c$. The final expression to approximate the pressure field of a focused transducer with source amplitude distribution M, surface phase distribution θ, and focusing length F_c in a

homogeneous non-attenuating medium is therefore

$$p(\mathbf{r},t)_z = -\frac{ik\rho_0 c_0 u_0}{2\pi z} e^{i(kz-\omega t)} \int_{-\infty}^{\infty}\int_{-\infty}^{\infty} M e^{i\left(\theta + \frac{k(x_0^2+y_0^2)}{2}\left(\frac{1}{z}-\frac{1}{Fc}\right)\right)} e^{i2\pi\beta x_0} e^{i2\pi\gamma y_0} dx_0 dy_0 \tag{3.13}$$

where $\beta = x/\lambda z$ and $\gamma = y/\lambda z$.

Caveats to consider when implementing a discretised form of Equation 3.13 are that this expression is only an approximation for observation points which are far away from the source and close to the central axis ($|\mathbf{r}-\mathbf{r}_0| \approx z$), and that for a given observation depth in z, the resolution of the frequency domain variables β and γ will vary due to the inverse dependence on z. To produce a consistent grid size, the resulting frequency spatial domain images were resampled to a fixed image resolution and range using cubic interpolation for every calculation depth in z.

To evaluate Equation 3.13 numerically, the 2D fast Fourier transform function in MATLAB (*fft2*, R2017b, The MathWorks Inc., Natick, MA) was employed on a Windows desktop computer (Dell Precision T1700, 3.50GHz, 16GB RAM), and simulations of an existing single-element focused transducer in water using the Fresnel approximation were compared to the Rayleigh-Sommerfeld integral and PZFlex. Ultrasound parameters were based on an available existing therapeutic transducer (H101, Sonic Concepts, Inc.) which has a geometric focus of 62.6mm, aperture radius of 32mm, and an operating frequency of 1.1MHz. The simulated acoustic fields were normalised to the effective surface pressure $p_0 = \rho_0 c_0 u_0$ for each case, and simulations were assumed to be in water with a sound speed $c_0 = 1482\text{m.s}^{-1}$ and density $\rho_0 = 997\text{kg.m}^{-3}$ with no attenuation. The Fresnel approximation script written to evaluate Equation 3.13 can be found in Appendix A.

Figure 3.3 shows a comparison of the simulated axial and radial pressure profiles at the focus obtained from numerical implementation of the Rayleigh-Sommerfeld integral

(black solid line) and the Fresnel approximation (dashed lines) with varying element resolution dx and discrete Fourier transform (DFT) length. Figures 3.3A and 3.3B show the effect of varying the DFT length on the acoustic field given a fixed element resolution of $dx = \lambda/10$ where λ is the wavelength, and convergence is seen at a DFT length of $L = 4r_0$ where r_0 is the transducer radius. Figs. 3.3C and 3.3D show the effect of element resolution on the acoustic field given a fixed DFT length ($L = 4r_0$), where convergence is seen at $dx = \lambda/6$. Figure 3.3 shows that there is good agreement between the Fresnel approximation and the RS integral, with slight misalignment of the axial pressure nulls at locations further away from the focus, with the first axial null past the focus showing greater positional error in comparison to the pre-focal nulls. The location of the radial nulls show good agreement, and the first radial null in the Fresnel approximation solution is non-zero most likely due to interpolation error between sampling points.

Figure 3.4 shows a comparison of the simulated 2D axial (A) and radial (B) pressure fields produced by the Fresnel approximation ($L = 4$, $dx = \lambda/6$) and PZFlex ($dx = \lambda/30$), where white lines indicate the -3dB, -6dB, and -10dB normalised pressure contours for each case, and a black dashed line indicates the -20dB normalised pressure contour for each case. Comparing the axial pressure contours in Figure 3.4A, there is good agreement with the shape of the focal region between the two methods, with the Fresnel approximation showing greater divergence from the PZFlex solution in the axial direction at spatial locations further away from the focus, as would be expected from the paraxial approximation. There is no significant difference between the two radial pressure fields for the simulated region shown in Figure 3.4B. The peak normalised pressure values simulated by PZFlex and the Fresnel approximation were 37.99 and 37.61 respectively, which suggests that the Fresnel approximation amplitude agrees to 1% of the PZFlex value. The axial length of the PZFlex -3dB and -6dB pressure contours

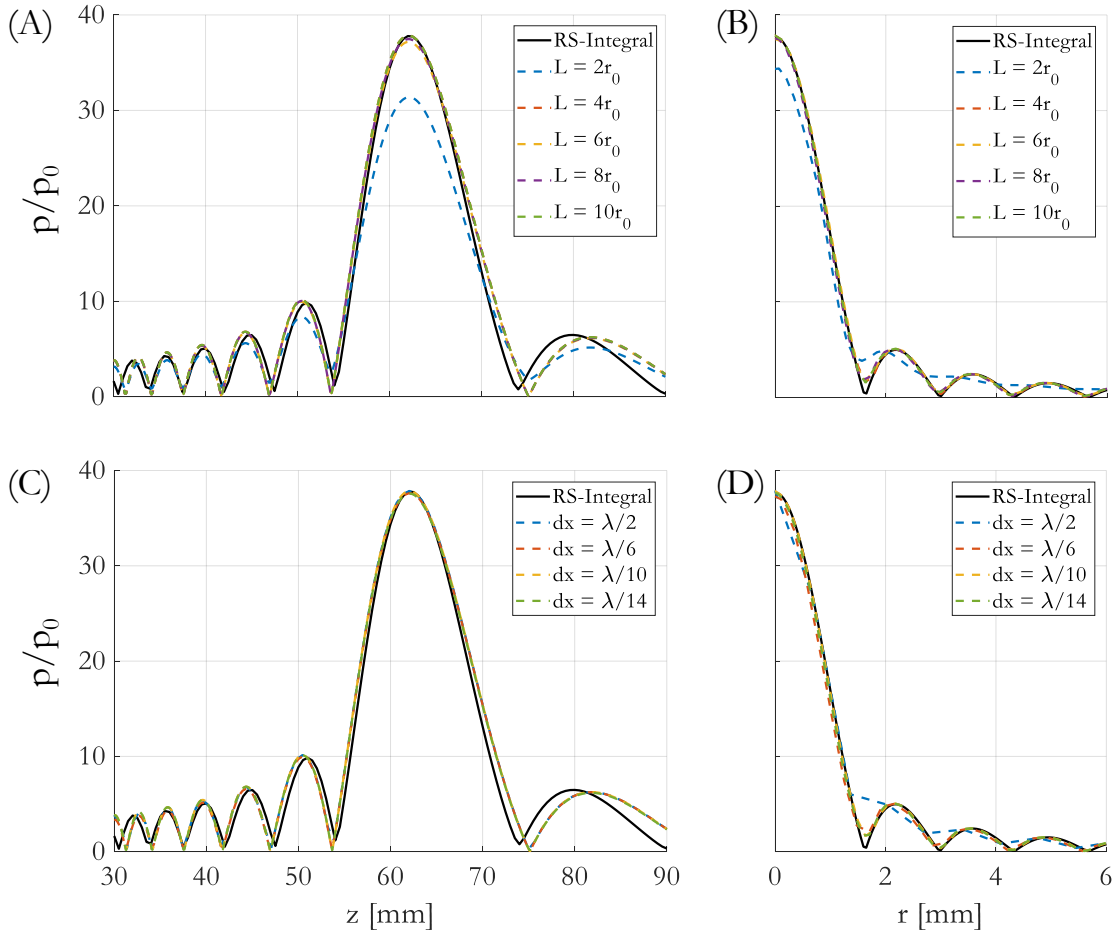


Fig. 3.3 Simulated axial and radial pressure profiles for the H101 spherically focused transducer in water (normalised to the surface pressure p_0) using the Rayleigh-Sommerfeld (RS) integral and the Fresnel Approximation at various grid resolution and DFT length. (A) and (B) show the effect of varying the DFT length L at a fixed grid resolution of $dx = \lambda/10$. (C) and (D) show the effect of varying the mesh grid resolution dx where the DFT length is fixed at $L = 4r_0$. The reference black solid lines indicate the exact solution from numerical implementation of the Rayleigh-Sommerfeld integral at a grid resolution of $dx = \lambda/10$. The H101 transducer (Sonic Concepts, Inc.) has an outer diameter of 32mm, centre frequency of 1.1MHz, and a geometrical focus of 62.6mm.

were 8.68mm and 11.77mm respectively, and 8.98mm and 12.41mm for the Fresnel approximation, which suggests that the Fresnel approximation has overestimated by 3.5% and 5.4% respectively.

The difference in simulation time for each method was notable, with the Fresnel approximation taking no more than 5 minutes for the full 3D field, and the PZFlex 2D axisymmetric model taking at least 56 minutes. The axisymmetric PZFlex simulation was performed at a relatively high resolution of 30 elements per wavelength ($dx =$ 0.09mm) to ensure convergence, while the Fresnel approximation method showed convergence with a source and field grid resolution of 6 elements per wavelength ($dx = 0.22$mm).

To incorporate attenuation due to wave propagation from water into a homogeneous attenuating medium, the Fresnel approximation expression $p(\mathbf{r}, t)_z$ in Equation 3.13 can be multiplied by an additional exponential decay term $e^{-2\alpha z_a}$ where the distance z_a[m] is the ray distance travelled in the attenuating medium, and α[Np.m^{-1}] is the attenuation coefficient of the medium at a given frequency f[MHz] with the form

$$\alpha = \alpha_0 \left(\frac{f}{f_0} \right)^n \tag{3.14}$$

where $f_0 = 1$MHz and n is typically between 1 and 1.5 for most soft tissues [125].

The assumptions required for this method to be valid are that the attenuating medium is homogeneous with identical sound speed and density as the coupling medium (water in this case). Given the attenuation as described by Equation 3.14, the resulting time-harmonic pressure fields calculated from the Fresnel approximation method can be used to simulate theoretical heat generation in a homogeneous attenuating medium. The rate of heat generation $\dot{q}$ is calculated from Equations 2.2 and 2.6, and subsequently entered into the Pennes bio-heat transfer equation as described in Equation 2.7.

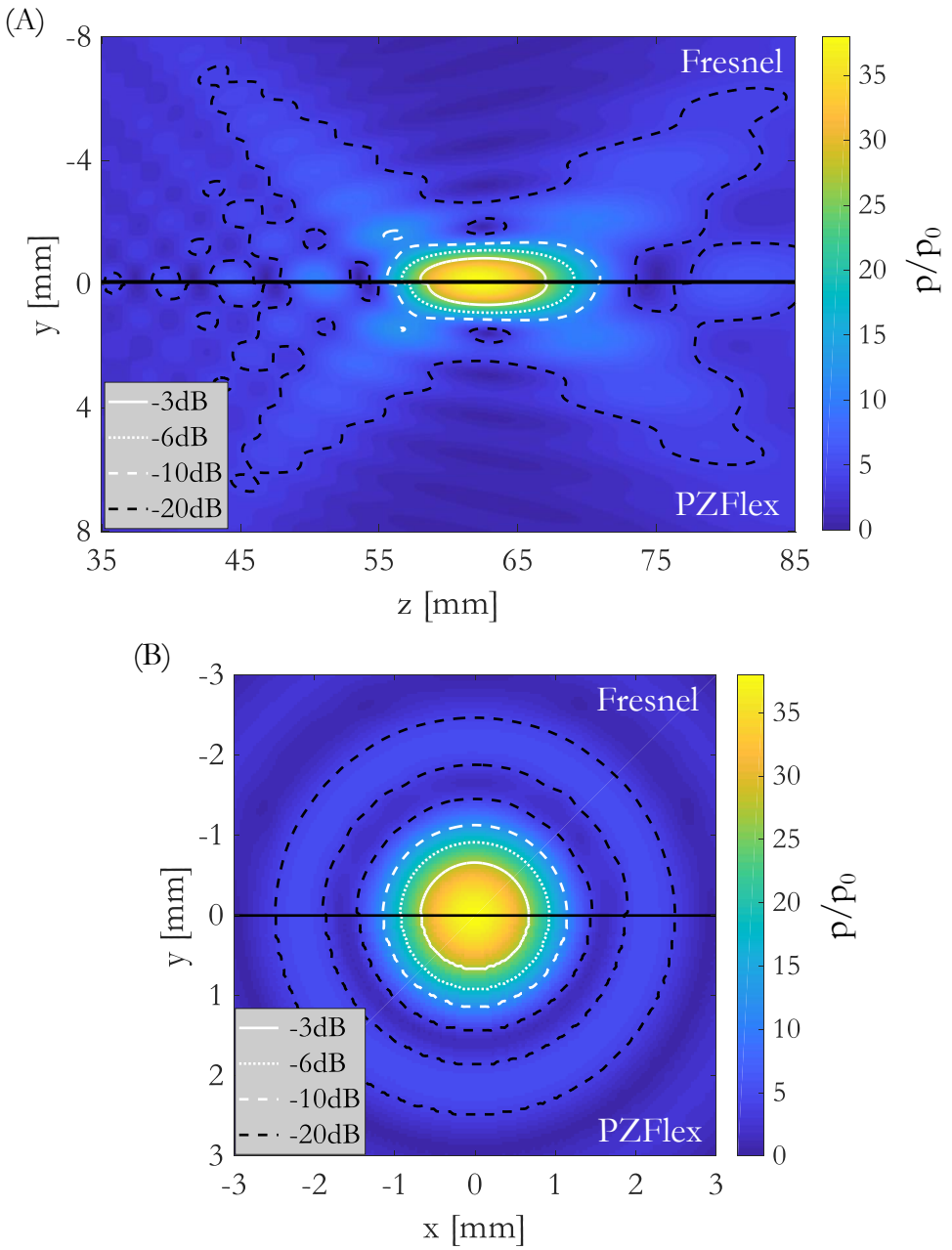


Fig. 3.4 2D axial (A) and radial (B) pressure fields of the H101 spherically focused transducer in water simulated with PZFlex and the Fresnel approximation (normalised to the surface pressure p_0). White contour lines indicate the -3dB, -6dB and -10dB pressure contours, and the black dashed line indicates the -20dB pressure contour. The z-axis location of the radial pressure field was taken at the location of the pressure maximum along the central axis in each respective case. The PZFlex simulation was performed at a grid resolution of $dx = \lambda/30$, and the Fresnel approximation was performed with a grid resolution of $dx = \lambda/6$ and a DFT length of $L = 4r_0$. The H101 transducer (Sonic Concepts, Inc.) has an outer diameter of 32mm, centre frequency of 1.1MHz, and a geometrical focus of 62.6mm.

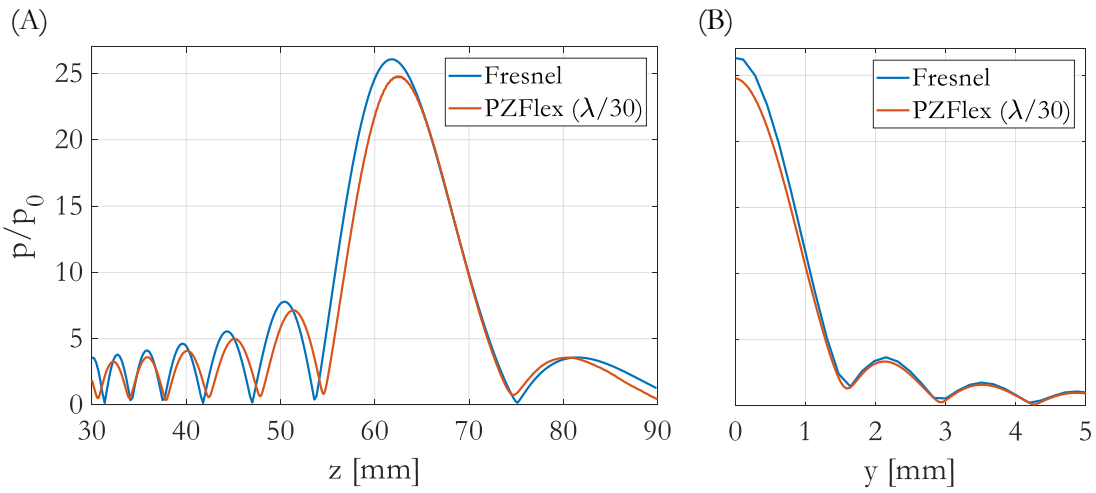


Fig. 3.5 Comparison of the simulated axial (A) and radial (B) pressure profiles for the H101 transducer focused 40mm into a homogeneous attenuating medium using PZFlex (red) and the Fresnel approximation (blue). The attenuating medium begins at the location $z = 22.6$mm, and has a fixed attenuation of 0.79dB.cm^{-1} with an identical sound speed and density to water. The H101 transducer (Sonic Concepts, Inc.) has an outer diameter of 32mm, centre frequency of 1.1MHz, and a geometrical focus of 62.6mm.

Thermal simulations based on the acoustic field simulated by the Fresnel approximation were carried out using an existing 3D alternating direction implicit (ADI) thermal solver in MATLAB (Prof. R. Cleveland, University of Oxford, May 2016) and compared to equivalent pressure and thermal simulations in PZFlex. Figure 3.5 shows the simulated axial and radial pressure profiles produced by a H101 focused transducer in water with the focus set at a depth of 40mm in a homogeneous attenuating medium with acoustic and thermal properties identical to water, except for an attenuation coefficient of 0.79dB.cm^{-1} (average attenuation value for liver as listed in Table 2.3). The shape and amplitude of the two traces shows good agreement, with a 5% overestimation in the normalised peak focal pressure from the Fresnel approximation ($p_{max}/p_0 = 26.07$) compared to PZFlex ($p_{max}/p_0 = 24.79$), where p_0 is the peak surface pressure amplitude.

The simulated temperature rise generated within the homogeneous attenuating medium due to 15 seconds of continuous wave insonation at an acoustic power of 1W are compared in Figure 3.6, where traces show the temperature observed in the focal plane at radial locations 0mm, 1mm, 2.5mm and 5mm away from the central axis. The simulated temperature rise from the combined Fresnel-ADI method shows good agreement with PZFlex for radial positions 2.5mm and 5mm away from the central axis, with a 12% and 9.4% overestimation in the temperature rise recorded at radial positions 0mm and 1mm respectively, as expected based on the slight focal pressure overestimation by the Fresnel approximation shown previously in Figure 3.5. The PZFlex thermal simulation was performed with a grid resolution of 12 elements per wavelength ($dx = 0.15$mm), executed with a time step of 0.2 seconds, and required the initial input from an axisymmetric linear pressure simulation evaluated at a resolution of 30 elements per wavelength ($dx = 0.09$mm) taking approximately one hour to perform in total. The ADI thermal simulation used the same grid resolution as the Fresnel pressure simulation ($dx = \lambda/6$), executed with a time step of 0.2 seconds, and required a total simulation time of approximately 20 minutes.

In summary, it has been shown that the Fresnel approximation can be used to simulate sectored transducers in 3D with calculation times on the order of minutes, in comparison to a full 3D finite element solver which can take hours to days depending on the size and resolution of the simulation domain. The Fresnel approximation is unable to model effects of inhomogeneous media, and simulation accuracy is reduced in the nearfield and in regions far away from the focus. However, for the application at hand where it is the focal patterns that are important, the Fresnel approximation can be reliably employed.

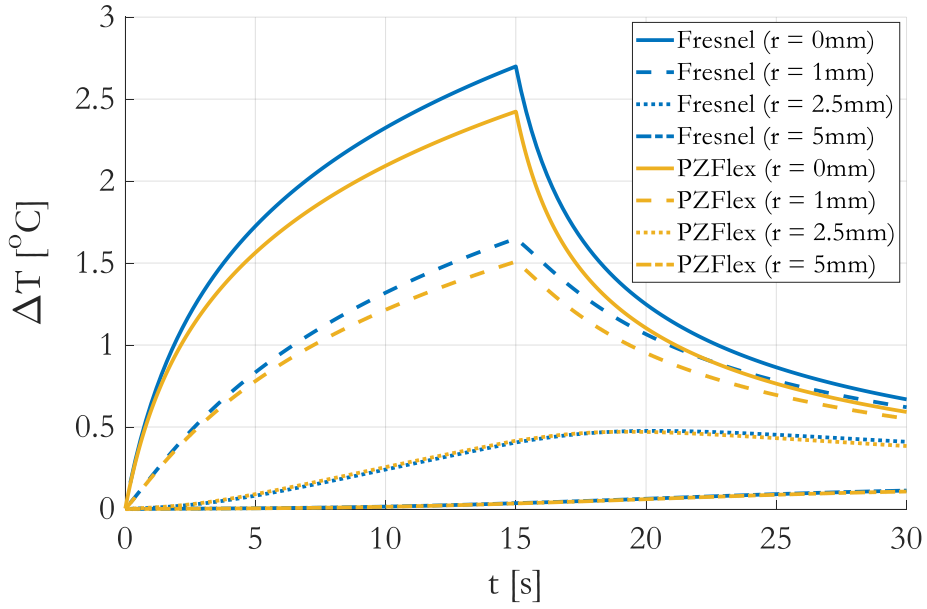


Fig. 3.6 Simulated temperature rise at four radial positions in the focal plane of a H101 transducer in water focused 40mm into a homogeneous attenuating medium in the absence of perfusion. Blue traces are generated by the Fresnel approximation, and yellow traces are generated by PZFlex. Both simulations modelled 15 seconds of continuous wave excitation at an acoustic power of 1W, and the radial positions recorded were at 0mm, 1mm, 2.5mm and 5mm away from the central axis. The acoustic and thermal properties of the attenuating medium were set to be the same as water as listed in Table 2.3, with an attenuation coefficient of 0.79dB.cm^{-1}. The peak simulated pressures produced by an acoustic power of 1W by the Fresnel approximation and PZFlex were 0.76MPa and 0.73MPa respectively. The H101 transducer (Sonic Concepts, Inc.) has an outer diameter of 32mm, centre frequency of 1.1MHz, and a geometrical focus of 62.6mm.

3.2.2 Manual Optimisation

As discussed in Chapter 2, the use of therapeutic mild hyperthermia for thermosensitive drug release requires sustaining a target volume at temperatures between 39.5-42°C for durations up to an hour. A hypothetical ideal therapeutic scenario would be a steady-state thermal profile where the entire target volume is elevated to a minimum therapeutic temperature of 39.5°C, with a maximum temperature of no more than 42°C and minimal heating outside of the target volume to ensure that the drug is not released elsewhere and thermal damage to tissue is avoided.

Whether it is possible to achieve this scenario with an ultrasound-mediated hyperthermia source will depend on numerous factors such as the size and depth of the target volume, acoustic and thermal properties of the medium, drug-related properties and kinetics, as well as the experimental ultrasound parameters used such as transducer surface apodisation, radius of curvature, diameter, operating frequency, duty cycle, and whether mechanical/electrical scanning strategies are employed. An extensive study of all the aforementioned parameters would be out of the scope of this thesis, therefore, the main variables of interest were restricted to acoustic power, and variation in the operational mode of a spherically focused sector-vortex transducer which directly influences the radial pressure distribution of the focus.

In order to explore the effect of acoustic power and operational mode on the generation of therapeutic mild hyperthermia, simulations of a stationary $N = 8$ sector-vortex transducer operating with continuous wave excitation in modes $m = 0$, 2, and 4 were compared for a range of acoustic powers between 1 and 8W. The focus of the transducer was positioned at a depth of 40mm into a homogeneous attenuating medium layer with fixed perfusion, and the transducer geometry and centre frequency were based on an existing single-element spherically focused transducer (H101, Sonic Concepts Inc.) which has a centre frequency of 1.1MHz, outer diameter of 64mm, and radius

of curvature of 62.6mm. Due to modelling constraints in the Fresnel approximation, the speed of sound and density of the attenuating medium were set to be identical to water, while the acoustic attenuation coefficient, perfusion, and thermal properties were assigned the bulk tissue values for liver as listed in Table 2.3. Fresnel approximation and thermal ADI simulations were performed at a grid resolution of $dx = \lambda/6$, with a thermal simulation time step of $dt = 0.25$s.

The effect of varying the operational mode on the resulting thermal field was determined by calculating the root mean squared error (RMSE) between the simulated 3D temperature field and a reference target temperature field across the entire thermal simulation domain ($60 \times 60 \times 60$mm centred about the focus). To ensure that a consistent peak temperature was reached, thermal simulations were executed until a steady-state temperature field was established within the attenuating medium, where steady-state was defined as a temperature change of no more than 0.05°C.min^{-1} averaged over the most recent simulation second. A hypothetical maximum temperature of 42°C would enable the largest therapeutic volume to reach the threshold of 39.5°C for drug release while ensuring thermal damage to tissue is minimised, therefore the reference thermal field for comparison consisted of a 20mm diameter spherical target volume centred at the geometrical focus of the transducer with a uniform temperature rise of 5°C (using a baseline temperature of 37°C), surrounded by a spherical exclusion volume extending 10mm outside of the target volume, with the rest of the field set to a reference temperature rise of 0°C. Since the length of the focal volume of the H101 transducer is 10.2mm [202], a spherical target volume with a diameter of 20mm was chosen to ensure the entire focus of the transducer was enclosed.

The function to be minimised for this manual optimisation approach is described by Equation 3.15

$$RMSE_{P,\theta} = \sqrt{\frac{\sum \left(\mathbf{T}_{P,\theta} - \mathbf{T}_{ref}\right)^2}{N_v}} \tag{3.15}$$

where $RMSE_{P,\theta}$ is the root mean squared error between the reference and simulated 3D steady-state temperature fields for a given acoustic power P and transducer surface phase distribution θ, $\mathbf{T}_{P,\theta}$ is the simulated 3D steady-state temperature field, $\mathbf{T}_{ref}$ is the reference target temperature field, N_v is the total number of compared volume elements in the simulation domain, and the relationship between operational mode m and surface phase distribution θ is described by Equation 3.1.

An example of the steady-state temperature fields produced by the $m = 2$ case with acoustic powers of 1W, 4W and 7W are shown in Figures 3.7A, 3.7B and 3.7C respectively. Column 1 of Figure 3.7 shows the radial temperature profiles in the focal plane at $z = 62.6$mm, and column 2 shows the axial temperature profiles at the plane $x = 0$mm, where reference temperature contours of 43°C and 39.5°C have been indicated by solid and dotted white lines. When driven with 1W (row A), a maximum steady-state temperature rise of 1.7°C was observed with no therapeutic volume ($T_{P,\theta} > 39.5$°C) produced within the target (indicated by the red dashed circle). At 4W (row B), a maximum steady-state temperature rise of 7.1°C was observed, along with a total therapeutic volume of 1.95cm^3 indicated by the elongated dotted white contour, and a therapeutic volume of 1.17cm^3 was produced within the target sphere. The volume which met or exceeded 43°C was found to be 0.10cm^3 and is shown centred within the target sphere (indicated by the solid white line). At 7W (row C), a maximum steady-state temperature rise of 12.4°C was observed, and a significantly larger total therapeutic volume of 6.52cm^3 as indicated by the dashed white line can be seen, with 2.03cm^3 occurring within the target. A significantly larger 43°C volume of 0.87cm^3 was produced, mainly centred about the target and extending towards the transducer source. The resulting $RMSE$ values for 1W, 4W and 7W were 0.67°C, 0.59°C and 0.70°C respectively, where the larger $RMSE$ values for 1W and 7W are most likely due to the the low temperature rise produced within the target volume for

the 1W case, and an excessive temperature rise within the target volume as well as a significant amount of pre-focal heating outside of the target volume in the 7W case.

Figure 3.8A displays $RMSE$ as a function of acoustic power for steady-state temperature fields produced by operational modes 0 (blue), 2 (orange) and 4 (yellow) at acoustic powers between 1W and 8W, with maximum simulated temperature as a function of power shown adjacent in Figure 3.8B for each mode respectively. Comparing the $RMSE$ curves in Figure 3.8A, the minimum $RMSE$ values for modes 0, 2 and 4 were found to be 0.61°C, 0.59°C and 0.58°C, and occur at 3W, 4W and 4.5W respectively, with corresponding maximum temperature rises of 11.8°C, 7.1°C and 5.0°C respectively. The corresponding steady state temperature fields for the minimum $RMSE$ cases for $m = 0$, 2 and 4 are shown in Figure 3.9 rows A, B and C, with on-target therapeutic volumes of 0.82cm^3, 1.13cm^3 and 1.19cm^3, total therapeutic volumes of 1.10cm^3, 1.95cm^3 and 1.90cm^3, and total volumes exceeding 43°C of 0.08cm^3, 0.10cm^3 and 0.00cm^3 respectively.

The largest on-target therapeutic volume of 1.19cm^3 was produced by the $m = 4$ case, which had a maximum temperature rise of exactly 5.0°C. The $m = 0$ case produced a very highly focused acoustic field which resulted in an excessive temperature rise of 11.8°C, while producing the smallest on-target therapeutic volume of 0.82cm^3. The $m = 2$ case resulted in very similar total and on-target therapeutic volumes to the $m = 4$ scenario, however the peak temperature rise was slightly higher at 7.1°C. The three temperature fields in Figure 3.9 show that radial defocusing of the acoustic field increases the therapeutic volume by enabling heat to diffuse in the radial direction both towards and away from the annular ring focal pattern. For a static transducer driven by continuous wave excitation, defocusing of the acoustic field by operating in a higher operational mode consequently lowers the acoustic gain and reduces the

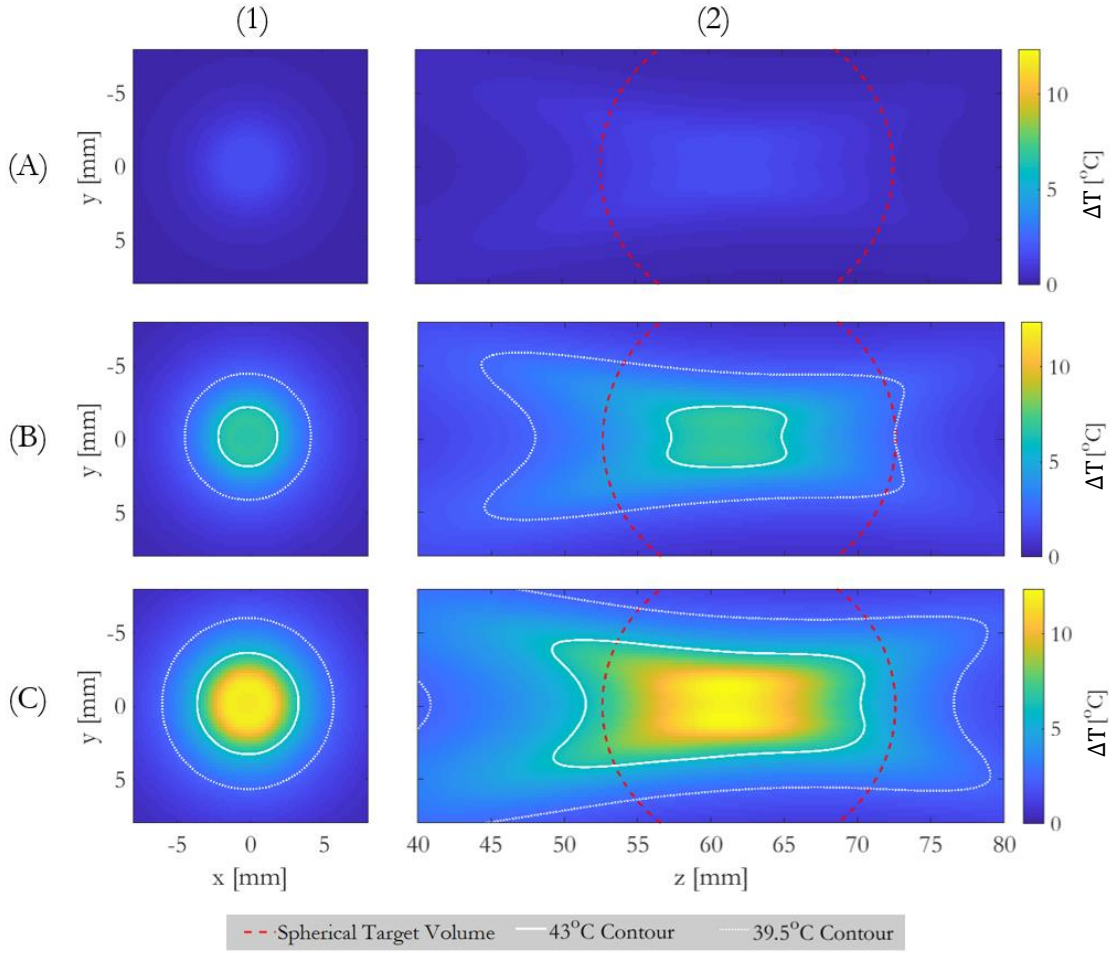


Fig. 3.7 Steady-state thermal fields generated in a perfused homogeneous attenuating medium by a sector-vortex transducer ($N = 8, m = 2$) when driven in continuous wave at 1W (row A), 4W (row B) and 7W (row C). Column 1 shows the temperature profile in the focal plane ($z = 62.6$mm), and column 2 shows the axial temperature profile at the plane $x = 0$mm. Peak simulated temperature rises for 1W, 4W and 7W were 1.7°C, 7.1°C and 12.4°C respectively. Where possible, solid and dotted white contour lines indicate the 43°C and 39.5°C thermal contours, and the boundary of the spherical target volume is indicated by the red dashed line. The base temperature was set to 37°C at the start of the simulation.

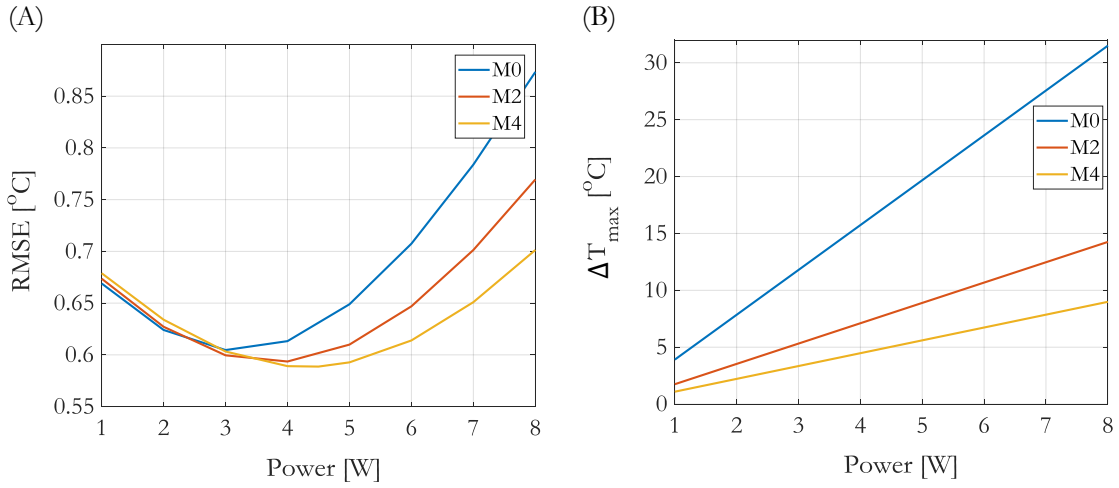


Fig. 3.8 (A) *RMSE* and (B) maximum simulated temperature rise as a function of acoustic power for steady-state temperature fields produced by an $N = 8$ sector-vortex transducer operating in modes 0 (blue), 2 (orange) and 4 (yellow).

peak temperature rise, resulting in a more favourable temperature profile suitable for mild-hyperthermia therapy in comparison to the completely focused ($m = 0$) case.

3.2.3 Automated Optimisation Routine

The presented manual optimisation results for pure operational modes 0, 2 and 4 have shown that the annular focusing patterns produced by a sector-vortex transducer can result in therapeutic temperature fields more suitable for mild hyperthermia in comparison to those produced by an equivalent spherically focused transducer. However, this approach has only explored three operational modes, and the performance of alternative phase distributions not limited to a specific operational mode have yet to be considered. Performing multiple manual optimisation iterations for each possible combination of surface phase conditions for an eight-sector array would require a significant amount of time, therefore the move towards an automated optimisation approach would be advantageous.

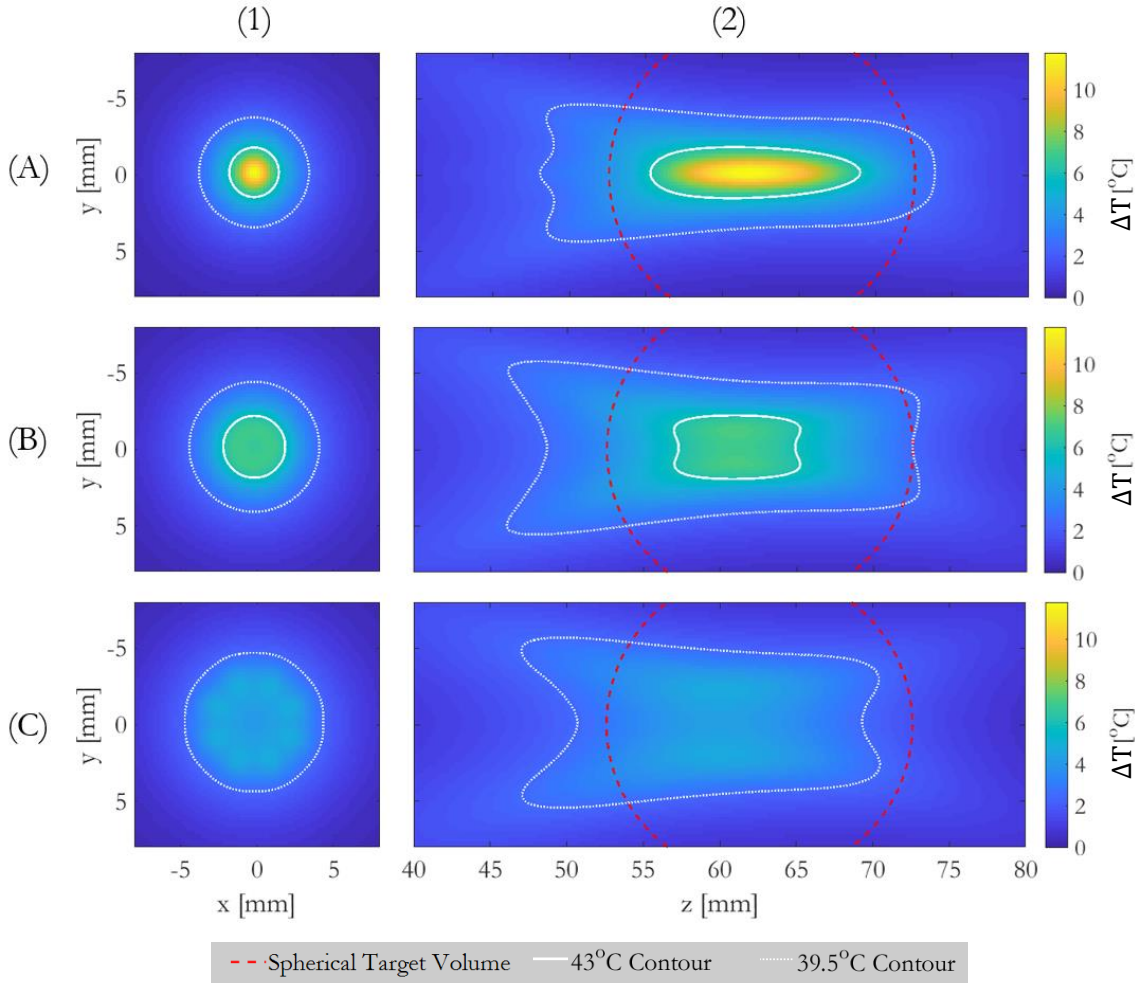


Fig. 3.9 Steady-state temperature fields generated in a perfused homogeneous attenuating medium by a sector-vortex transducer ($N = 8$) driven in continuous wave and operating in mode 0 at 3W (row A), mode 2 at 4W (row B) and mode 4 at 4.5W (row C). Column 1 shows the temperature profile in the focal plane ($z = 62.6$mm), and column 2 shows the axial temperature profile at the plane $x = 0$mm. Peak simulated temperature rises for each case were 11.8°C, 7.1°C and 5.0°C respectively. Where possible, solid and dotted white contour lines indicate the 43°C and 39.5°C thermal contours, and the boundary of the spherical target volume is indicated by the red dashed line.

An automated optimisation approach was performed by incorporating the Fresnel-ADI simulation method into an existing constrained optimisation solver (*fmincon*, MATLAB Optimisation Toolbox), where surface phase distribution θ and acoustic power P were variables that could be controlled. The transducer geometry and acoustic field model were kept the same as described in the manual optimisation approach, and similarly the function supplied to *fmincon* to be minimised is described by Equation 3.15, where lower and upper bounds for P and θ were defined to be between 0 and 15W, and $-\pi$ to π radians respectively.

Acoustic power P and phase distribution θ for an $N = 8$ sector-vortex array were randomly initialised using a random number generator in MATLAB, and an illustrative flowchart of the described optimisation process is shown in Figure 3.10, where the MATLAB scripts and functions used to implement the constrained optimisation process are included in Appendix A. Figure 3.11 shows how the optimisation variables varied with the first 300 iterations for three independently initialised optimisation procedures where Figures 3.11A, 3.11B and 3.11C show the $RMSE$, acoustic power, and standard deviation σ of the surface phase distribution respectively. Looking at Figure 3.11A, the $RMSE$ for all three optimisation runs have converged to a minimum value of 0.58°C, and in Figure 3.11B the three runs converged to an acoustic power of approximately 3.6W. In Figure 3.11C, the standard deviation of the surface phase distribution shows greater variation with values ranging from 1.2 to 1.9 radians, yet from iteration 230 to 300, Figures 3.11A-C show that when driven at approximately the same acoustic power of 3.6W, variations in θ made by the optimisation function did not have a significant effect on $RMSE$.

The surface phase and corresponding acoustic fields produced by the final iteration of the three independent optimisation runs are shown in Figure 3.12, where optimisation runs 1, 2 and 3 are represented by rows A, B and C respectively. The surface phase

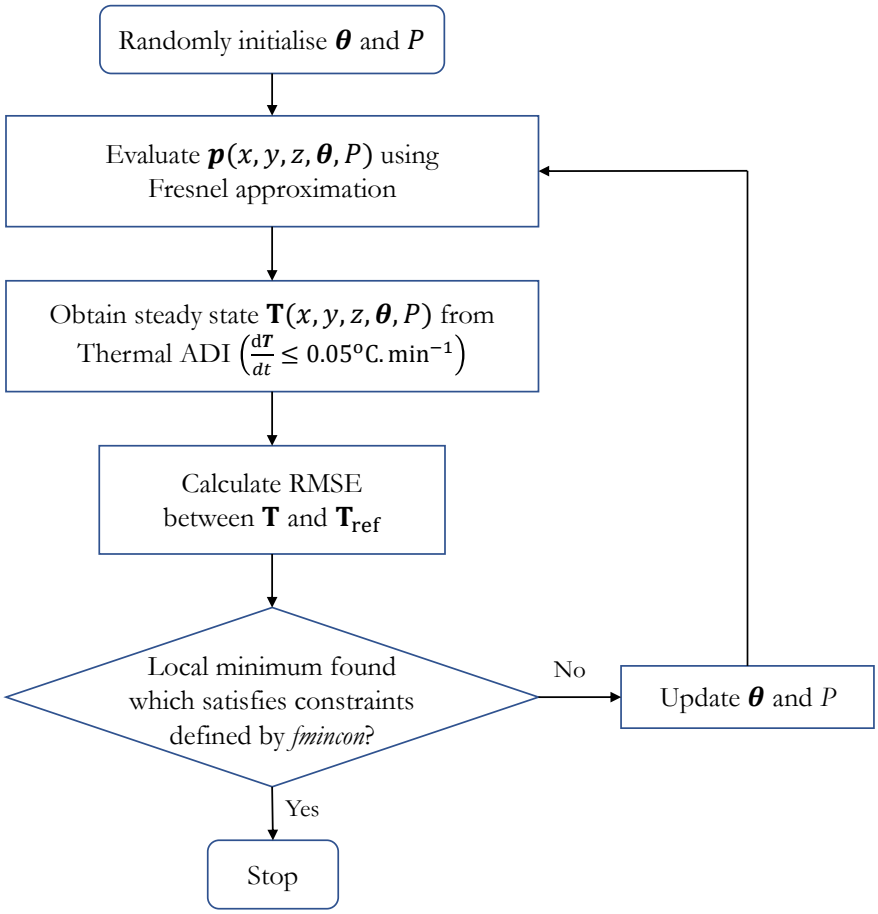


Fig. 3.10 Illustrative flowchart of the automated optimisation procedure for an $N = 8$ sector-vortex transducer focused into a homogeneous attenuating medium with fixed perfusion. The acoustic power P and sector phase distribution θ are optimisation variables which are randomly initialised and controlled by the optimisation function *fmincon*. The Fresnel-ADI method is used to perform acoustic and thermal simulations for given values of P and θ, and the resulting steady-state temperature field is compared with the reference temperature field to calculate the RMSE. P and θ are automatically varied in an iterative process by *fmincon* until the RMSE is deemed to be situated at a satisfactory local minimum.

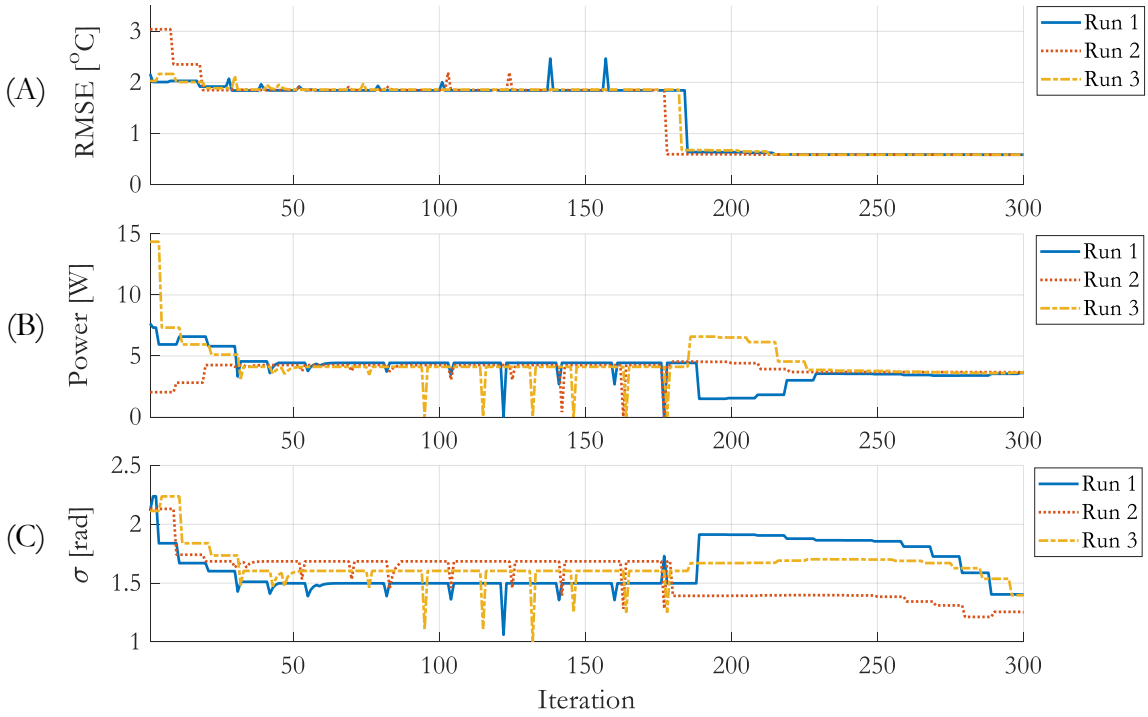


Fig. 3.11 Variation in $RMSE$ (A), acoustic power (B) and standard deviation of the surface phase distribution (C) as a function of iteration number performed by the automated optimisation process for an $N = 8$ sector-vortex transducer. Three independent optimisation runs are shown by the traces in blue, orange, and yellow, each with randomly initialised values of P and θ, where σ is the standard deviation of the surface phase distribution θ.

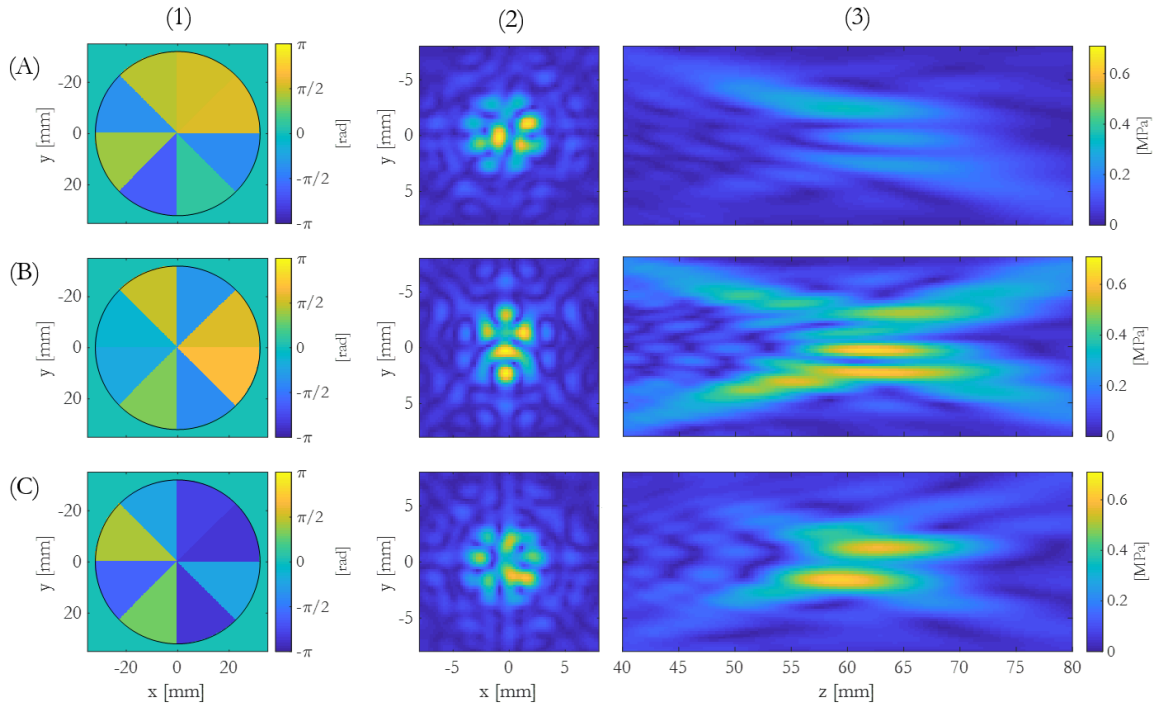


Fig. 3.12 Surface phase distribution (column 1) and resulting pressure fields produced by the final values of θ and P from optimisation runs 1 (row A), 2 (row B) and 3 (row C). Column 2 shows the pressure field in the focal plane ($z = 62.6$mm), and column 3 shows the axial pressure field at the plane $x = 0$mm. The peak simulated pressures for optimisation runs 1, 2 and 3 were 0.71MPa, 0.67MPa and 0.64MPa respectively.

is shown in column 1, with corresponding radial pressure fields (column 2) taken at the geometric focus of the transducer ($z = 62.6$mm), and axial pressure fields (column 3) taken at the plane $x = 0$mm. The acoustic power for cases 1, 2 and 3 were 3.70W, 3.67W, and 3.76W, and the peak acoustic pressure in each case were also found to be very similar, with values of 0.71MPa, 0.67MPa and 0.63MPa respectively. All three acoustic fields appear to be rather asymmetric in comparison to the fields produced by the pure operational modes of an eight-sector array shown in Figure 3.2.

The corresponding steady state thermal fields produced by iteration 300 of optimisation runs 1, 2 and 3 are shown in Figure 3.13 rows A, B and C respectively. The temperature field in the focal plane of the transducer is shown in column 1, while the axial temperature field in the plane $x = 0$mm is shown in column 2. Solid and dotted

white contour lines indicate the 43°C and 39.5°C thermal contours respectively, and the outline of the spherical target is shown by the red dashed line. The total therapeutic volume produced by optimisation runs 1, 2 and 3 were found to be 1.37cm^3, 1.36cm^3 and 1.34cm^3, with on-target therapeutic volumes of 0.96cm^3, 0.95cm^3 and 0.97cm^3, and total volumes above 43°C of 0.015cm^3, 0.013cm^3 and 0.002cm^3 respectively. The maximum temperature rise observed in runs 1, 2 and 3 were found to be 6.83°C, 6.69°C, and 6.20°C respectively.

In each automated optimisation run shown in Figure 3.12, an asymmetric multi-foci acoustic field was established, featuring up to five main foci in the focal plane. Comparing the resulting steady-state temperature fields in Figure 3.13, although the location of the hottest regions are not the same, the total and on-target therapeutic volumes are very similar. In comparison to the total and on-target therapeutic volumes produced by the pure mode 2 (1.95cm^3, 1.13cm^3) and mode 4 (1.90cm^3, 1.19cm^3) cases, the automated optimisation runs resulted in smaller total and on-target therapeutic volumes. The three optimisation runs also resulted in an RMSE value of 0.58°C, which is similar to the values observed from the manual optimisation results for mode 2 (0.59°C) and mode 4 (0.58°C). Comparing both manual and automated optimisation results, the manual optimisation with operational mode 4 resulted in the largest on-target therapeutic volume of 1.19cm^3 with the lowest peak temperature rise of exactly 5.0°C, however it also resulted in the largest total therapeutic volume of 1.95cm^3, which means there is more pre-focal heating occurring outside of the target volume. The automated optimisation runs resulted in less radially defocused acoustic fields compared to the mode 4 case, which resulted in temperature fields which slightly overshot the maximum ideal temperature rise of 5°C, however the amount of heating occurring outside of the target volume is reduced, resulting in an equivalent RMSE value overall.

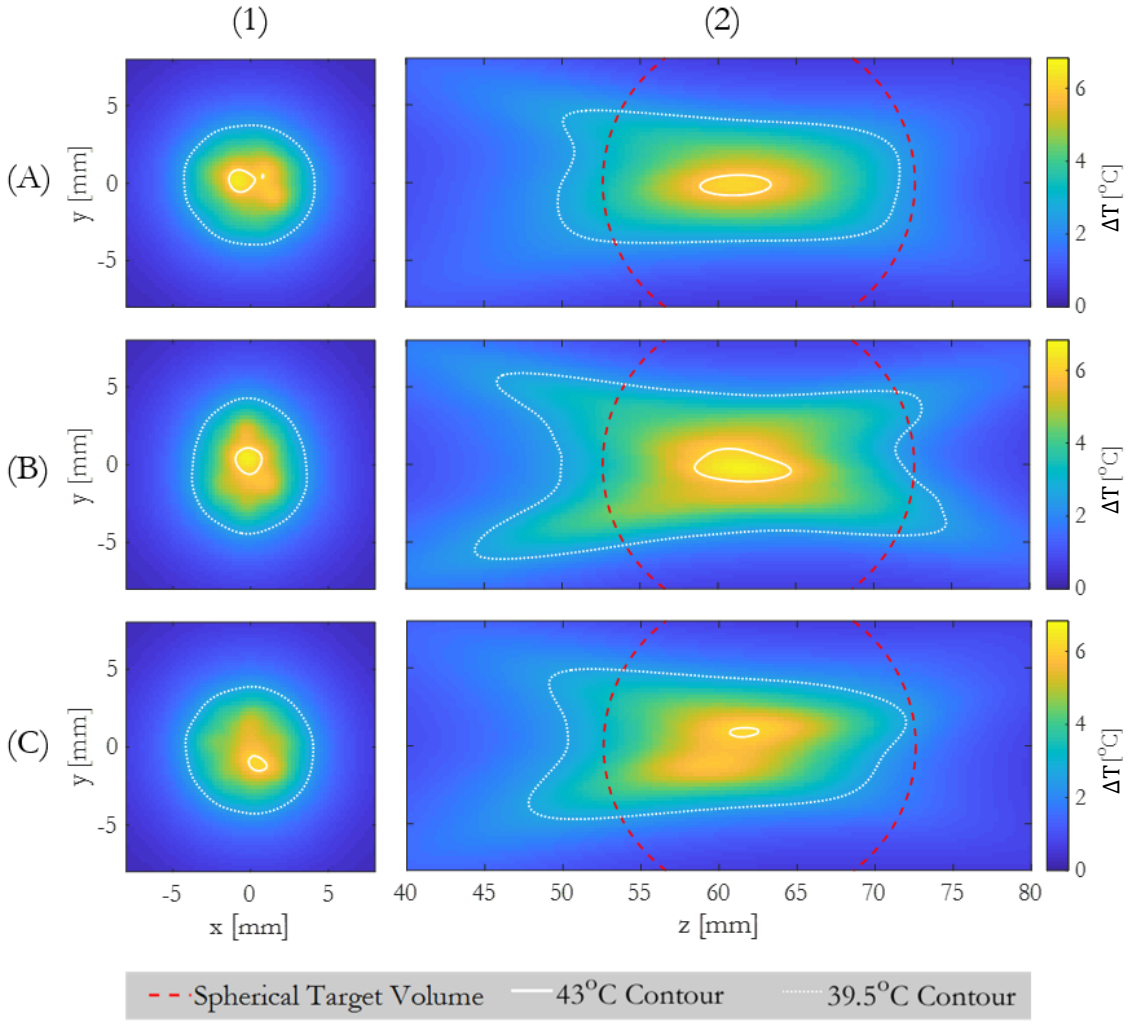


Fig. 3.13 Simulated steady-state temperature fields produced by the acoustic fields shown in Figure 3.12. Optimisation runs 1, 2 and 3 are represented by rows A, B and C, where column 1 shows the temperature field in the focal plane ($z = 62.6$mm), and column 2 shows the axial temperature field at the plane $x = 0$mm. The maximum temperature rise produced in optimisation runs 1, 2 and 3 were found to be 6.83°C, 6.69°C and 6.20°C respectively. Solid and dotted white contour lines indicate the 43°C and 39.5°C thermal contours, and the boundary of the spherical target volume is shown by the red dashed line.

The conclusions which can be made from the results of the manual and automated optimisation methods are that the problem presented has more than one optimum solution. Whether a higher peak temperature rise with less pre-focal heating, or lower peak temperature with greater pre-focal heating is more suitable depends on the application at hand. If the target volume is a tumour, slightly overheating the target tissue for the increased accuracy of localised heating for drug release would not be of much concern (automated optimisation case). However, if the target volume is near a sensitive tissue structure such as nerves for example, the situation may require that thermal safety play a greater role where the peak temperature is reduced, at the cost of reduction in accuracy of the heated volume for drug release (manual mode 4 optimisation case). In both scenarios, the therapeutic volumes produced by multi-focal acoustic fields outperformed that produced by the original focused transducer, which suggests that multi-focal acoustic fields should be explored. Since both optimisation results produced similar RMSE values, pure-mode acoustic fields will be explored due to their ability to produce thermal fields with axisymmetry.

4 Design and Verification of a Sectored Acoustic Lens for Mild Hyperthermia

4.1 Introduction

As discussed in Chapters 2 and 3, multi-foci acoustic fields usually involve the use of multiple transducers or a multi-element array. An alternative method to adjust the phase of a pressure wave generated from a single-element transducer source is to use an acoustic lens [182]. Early studies explored the use of an acoustic lens to broaden the focal volume of a single-element planar transducer to create annular focal regions in a small rodent model [73], while more recent approaches include techniques to design lenses for specific focal shapes a particular plane of depth [182, 203]. Previous studies have also demonstrated the ability for acoustic lenses recreate the pressure fields of transducers such as the sector-vortex transducer [83], and produce sustained large volume mild hyperthermia in a rodent model [204]. The design of acoustic lenses to optimally heat up predefined target volumes in simple theoretical scenarios have also been considered [205].

Acoustic lenses are an affordable and less complex alternative to using phased arrays but not without drawbacks. Firstly, the impedance mismatches at the transducer-lens and lens-water interfaces will result in the amplitude loss of waves travelling through the lens, and secondly the attenuation in the lens material will result in further amplitude reduction, with possible heating of the lens if a significant amount of energy

is absorbed. 3D printed sectored acoustic lenses will be explored in this chapter as an affordable and simple technique to enable existing focused transducers to produce multifoci pressure fields to generate large volume mild hyperthermia with increased uniformity and consistency.

In order to investigate whether sufficient acoustic gain is retained while maintaining some degree of radial spreading of the focal volume, both a four-sector mode 2 and an eight-sector mode 4 acoustic lens were explored. A four-sector mode 2 acoustic lens was chosen instead of an eight-sector mode 2 lens because simulations of the four-sector case for a sector-vortex transducer in water resulted in a higher acoustic gain. The more radially dispersed field produced by an eight sector mode 4 transducer will also be investigated in order to compare the mode 0 (focused) and mode 2 cases with a more defocused acoustic field.

4.2 Acoustic Lens Design Process

The phase and amplitude of a wavefront can be adjusted by using an acoustic lens which exhibits a difference in sound speed and density to the propagating medium. Assuming that the surface layer of an ultrasound transducer has an impedance which matches closely to that of water and emits a normally incident plane wave, an acoustic lens can be modelled as a three-layer transmission problem [60], as illustrated in Figure 4.1. Beginning from the left, the first layer is the surface coating of the transducer (approximated as water given that most transducers use matching layers that are impedance matched to water), the second layer is the acoustic lens with known acoustic properties, and the third layer is water.

The complex pressure p_n in medium n can be expressed as a combination of forward and backward travelling waves with amplitudes A and B respectively, as shown in

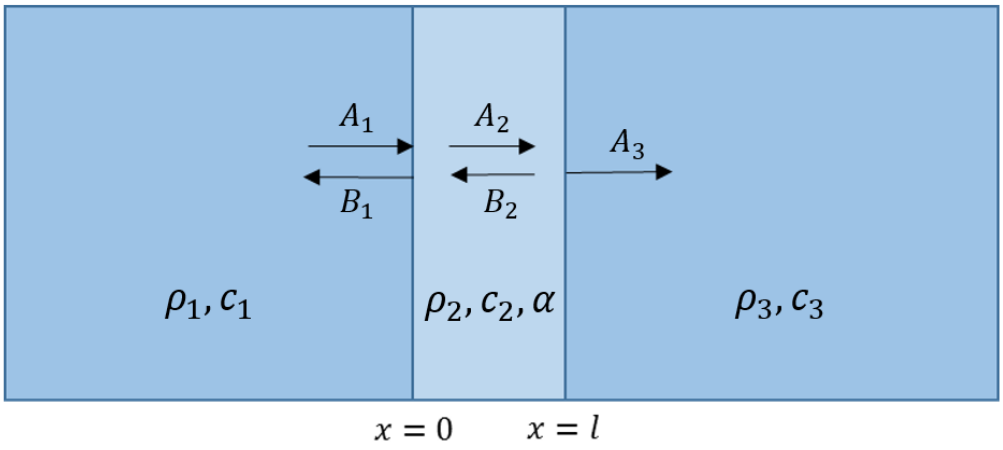


Fig. 4.1 Illustration of pressure transmission through a three-layer model where ρ is the density, c is the speed of sound, α is the acoustic attenuation coefficient, A is the amplitude of the forward travelling plane wave, B is the amplitude of the backwards travelling plane wave, and l is the thickness of the central attenuating layer.

Equations 4.1-4.3

$$p_1 = A_1 e^{-ik_1 x} + B_1 e^{ik_1 x} \tag{4.1}$$

$$p_2 = A_2 e^{-i(k_2 - i\alpha)x} + B_2 e^{i(k_2 - i\alpha)x} \tag{4.2}$$

$$p_3 = A_3 e^{-ik_3(x-l)} \tag{4.3}$$

where l is the thickness of the lens layer and α is the attenuation coefficient of the lens material. Combining Equations 4.1-4.3, the pressure transmission coefficient T for the three layer model is given by Equation 4.4

$$T = \frac{A_3}{A_1} = \frac{2}{\cos\left((k_2 - i\alpha)l\right)\left(1 + \frac{Z_1}{Z_3}\right) + i\sin\left((k_2 - i\alpha)l\right)\left(\frac{Z_1}{Z_2} + \frac{Z_2}{Z_3}\right)} \tag{4.4}$$

where A_1 and A_3 are the amplitudes of the forward propagating waves before and after the lens interfaces, and $Z_n = \rho_n c_n$ is the acoustic impedance of medium n, where ρ_n and c_n are the density and speed of sound in medium n [60].

As shown in Chapter 3, useful multi-foci acoustic fields can be generated by operating a spherically focused sectored transducer in a higher mode. Taking the eight sector transducer as an example, the highest mode ($m = 4$) occurs when neighbouring sectors are driven exactly out of phase, resulting in an alternating phase difference of π radians as shown in Figure 3.2(D1). The relationship between the phase difference $\Delta\phi$ and the difference in lens sector thickness l to achieve this is given by Equation 4.5

$$\Delta\phi = 2\pi f l \left(\frac{1}{c_w} - \frac{1}{c_l} \right) \tag{4.5}$$

where c_w is the speed of sound in water, c_l is the speed of sound in the acoustic lens, and f is the frequency [204].

A 3D printable clear resin material (GPCL04, Formlabs Inc.) was explored to create an acoustic lens for an existing single-element spherically focused transducer (H102, Sonic Concepts, Inc.) which has an outer diameter of 64mm, inner diameter of 20mm, geometrical focus of 62.6mm, and a centre frequency of 1.1MHz. Properties of the clear resin at room temperature when cured were provided courtesy of Dr. Jason Raymond (University of Oxford), with reported values for speed of sound of 2630m.s^{-1}, density of 1.17kg.m^{-3}, and an attenuation coefficient value of 5.1dB.cm^{-1}.MHz^{-1} with linear dependence on frequency.

Using the surface phase pattern of an eight sector transducer operating in mode 4 as an example (illustrated in Chapter 3, Figure 3.2), the alternating phase difference of π radians could be achieved by using an acoustic lens with two fixed thickness steps. From Equation 4.5, the minimum thickness required for an acoustic lens made from GPCL04 clear resin to induce a phase difference of π radians relative to water is

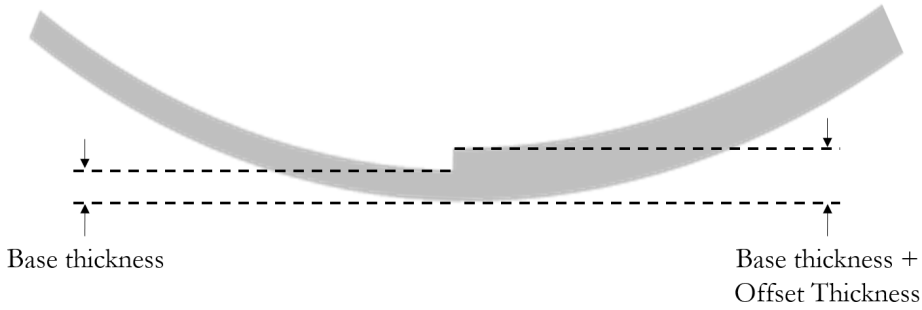


Fig. 4.2 Cross-sectional illustration of a curved acoustic lens with two distinct thickness steps comprising of a base thickness and an additional offset thickness for phase alteration.

calculated to be 1.57mm at room temperature, and an example illustration of a curved acoustic lens comprising of a base thickness and an additional offset thickness for phase alteration is shown in Figure 4.2.

The acoustic transmission through the curved lens is approximated by the three layer transmission model described by Equation 4.4 since the transducer source is situated flush and normally incident to the lens surface, and the distance travelled through the lens is short (on the order or several wavelengths at most) which minimises the effect of curvature on the acoustic field. Figure 4.3 shows the transmission coefficient for a water-lens-water model as a function of lens thickness. The blue curve indicates the predicted transmission coefficient through the base lens layer as a function of thickness, and the yellow curve indicates the transmission coefficient through sectors which have an additional thickness of 1.57mm required for a phase shift of π radians. Comparing the two curves, the transmission amplitudes oscillate with peaks occurring at multiples of $\lambda_l/2$ where $\lambda_l = 2.39$mm is the wavelength in the lens material. Locations where the two curves intersect are base thickness solutions which yield equal transmission through both thick and thin lensed regions, and the mutual maximum transmission coefficient of 0.83 is situated at a base thickness of 0.89mm as indicated by the red circle.

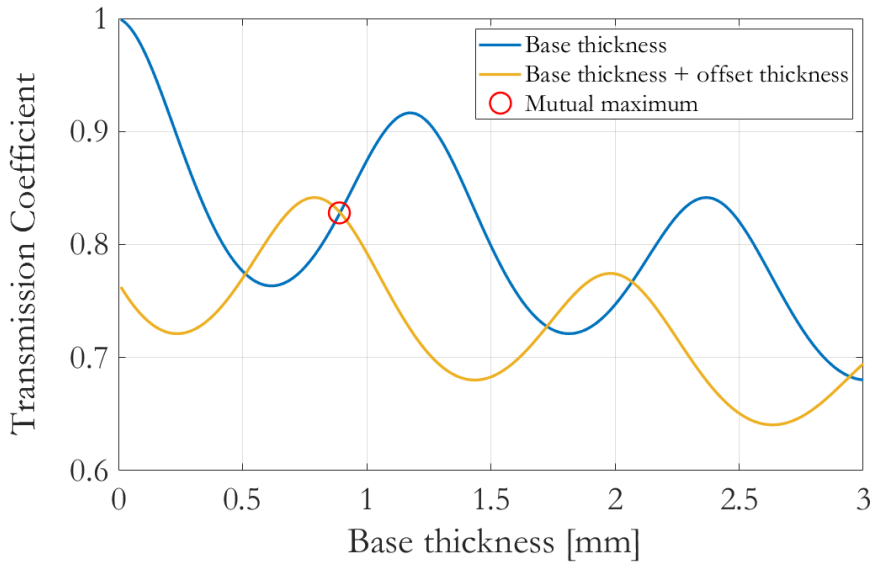


Fig. 4.3 Pressure transmission coefficients for a two-thickness clear resin acoustic lens as a function of lens base thickness. The additional thickness of 1.57mm has been calculated to induce a phase shift of π radians and the location of the mutual maximum for acoustic transmission is indicated by the red circle.

Computer-aided design software (AutoCAD 2016, Autodesk Inc.) was used to generate two acoustic lenses for the H102 transducer. The diameter and curvature of the lenses were designed to match that of the H102 such that the lens would sit flush with the transducer surface, and additional overhanging material was added to secure the lens in place as shown in Figure 4.4. Each lens comprised of eight equally spaced sectors with two alternating thickness levels in order to produce the surface phase distribution of an eight sector transducer operating in mode 4. Two values for base thickness were explored, with one lens designed with a base thickness of 0.79mm to grant maximum acoustic transmission through the thickest lensed regions, and a second lens with a base thickness of 0.89mm to produce a uniform surface amplitude. The acoustic lenses were manufactured using a 3D printer (Form 2, Formlabs Inc.) and printed in clear resin at the highest available resolution of 0.025mm.

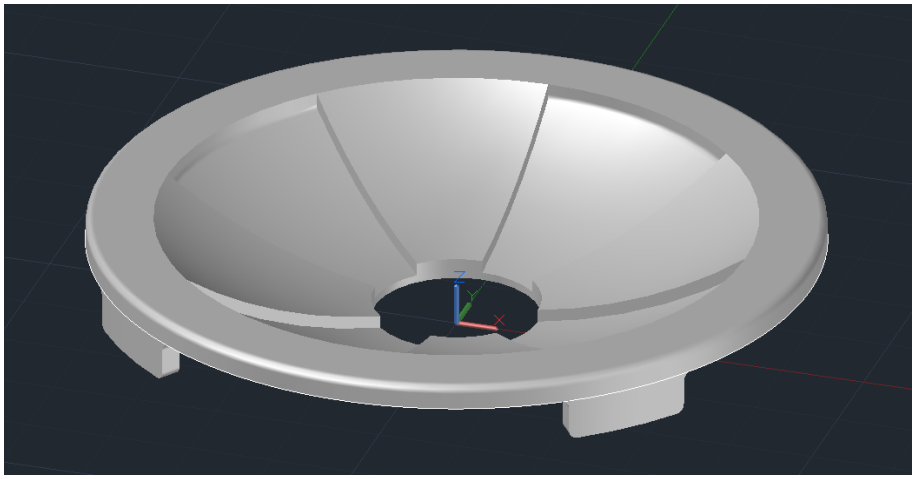


Fig. 4.4 AutoCAD rendering of an eight-sector mode 4 acoustic lens for the H102 therapeutic transducer.

The acoustic field generated by the 3D printed lenses were characterised by securing them to the surface of a H102 transducer which was submerged in a large tank of degassed water. The H102 transducer was powered by a 400W 55dB linear amplifier (1040L, Electronics & Innovation, Ltd.), and a signal generator (Agilent 33220A, Keysight Technologies) was used to provide a 25 cycle sinusoidal burst waveform. Pressure measurements were obtained using a 0.2mm diameter needle hydrophone and preamplifier (Precision Acoustics Ltd.) connected to an oscilloscope (LeCroy WaveSurfer, Teledyne Technologies Inc.), and a computer controlled three axis positioning system (UMS, Precision Acoustics Ltd.) as shown in Figure 4.5. The calibration uncertainty of the needle hydrophone at 1.1MHz was documented to be ±14% with a sensitivity of 58mV.MPa^{-1}, and the uncertainty of the three axis positioning system is documented to be ±0.006mm. Lenses were degassed in deionised water for at least 30 minutes prior to placement onto the transducer surface to minimise the chance of bubble formation at the transducer-lens interface.

Figure 4.6 shows the measured peak pressure scans of the H102 transducer in the free-field and with the two mode 4 acoustic lenses when driven at an acoustic power

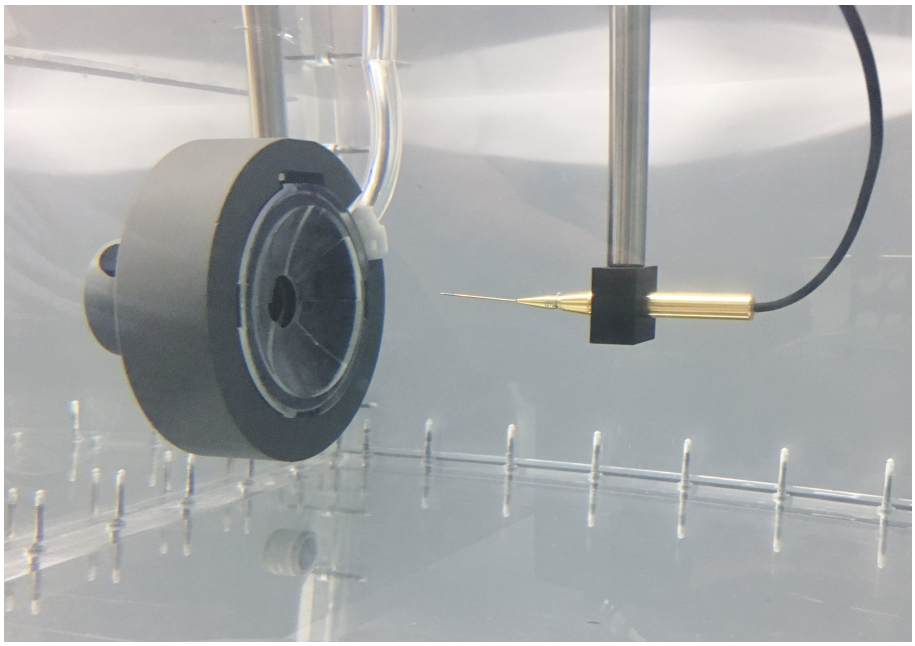


Fig. 4.5 Image of the H102 transducer submerged in a large tank of degassed water with an eight-sector mode 4 acoustic lens secured flush to the surface. A needle hydrophone is shown attached to a metal rod which in turn is mounted onto a three-axis positioning system, where mechanical scanning of the hydrophone is performed in order to provide measurements at multiple locations.

such that the peak focal pressure without the lens was measured to be 1MPa. The location of the peak focal pressure was determined to the nearest 0.1mm by performing multiple positional scans and observing the peak hydrophone signal. Focal plane scans for the H102, H102 with the 0.79mm base thickness lens, and H102 with the 0.89mm base thickness lens were obtained at a spatial sampling resolution of 0.4mm and are shown in Figures 4.6B, 4.6D and 4.6F respectively. Nearfield scans for the three cases were obtained at a spatial resolution of 2mm at an axial plane 40mm away from the focal plane towards the transducer surface, and are shown in Figures 4.6A, 4.6C and 4.6E respectively. In Figure 4.6A with no lens, the nearfield map shows a relatively uniform axisymmetric beam with a dip in the middle due to the central hole, and a tight axial focus is seen in Figure 4.6B. For the 0.79mm lens, the outline of the sectors in the nearfield (Figure 4.6C) can be seen and the difference in amplitude between

adjacent sectors is clear, with the expected eight foci pattern in the focal plane (Figure 4.6D). For the 0.89mm lens, the sector amplitudes in the nearfield (Figure 4.6E) are much closer and the foci in the focal plane (Figure 4.6F) are now larger in extent. This suggests that the three-layer transmission model described by Equation 4.4 can be reliably employed.

Using the optimum base thickness of 0.89mm for the clear resin lens, a four-sector mode 2 lens was produced and hydrophone measurements of the acoustic fields from the H102 alone, with the mode 2 lens, and with the 0.89mm base thickness mode 4 lens were compared to equivalent acoustic simulations in PZFlex (material properties listed in Table 2.3). Simulations of the lensed H102 transducer were performed on a high performance computer (Dell Precision T910 Workstation, 32 Cores, 192GB RAM) at a grid resolution of $dx = \lambda_w/15$, where λ_w is the wavelength in water. The source was modelled as a pressure[1] load boundary condition between elements located on the surface of the transducer and the acoustic lens, which was flush with the transducer surface. The applied source condition was a continuous 1.1MHz sinusoidal wave with a linear 5 cycle ramp up, and the simulation was executed until acoustic waves had travelled 1.5 times the geometric focus of the transducer in order to ensure a steady state field had been established. Quarter symmetry boundary conditions were applied at $y = 0$mm and $z = 0$mm in order to reduce computational demand, and absorbing boundary conditions were applied to the remaining boundaries. The source pressure amplitude was calculated such that the transducer surface emitted an acoustic power

[1]No significant difference was observed between pressure and velocity loaded boundary conditions in PZFlex, where surface pressure p_0 is related to surface velocity u_0 with the relationship $p_0 = \rho_0 c_0 u_0$. Note: the source pressure amplitude applied to a boundary element surface was equal to $2p_0$ due to the fact that this will produce two acoustic waves which propagate in the forwards and backwards directions with an amplitude equal to half of the source amplitude.

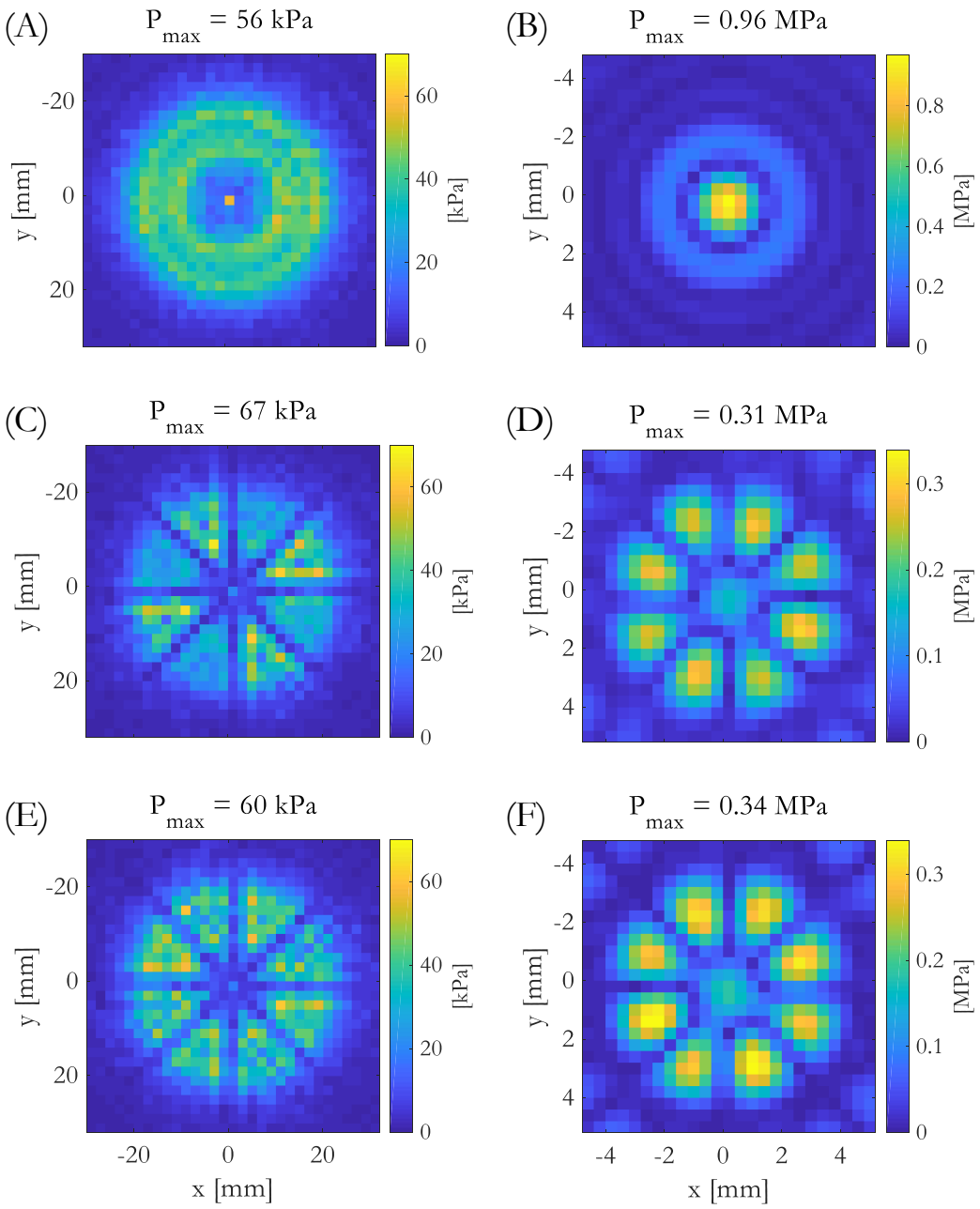


Fig. 4.6 Recorded peak pressure scans of a H102 transducer in water with and without an acoustic lens at the focal plane (right column) and at a nearfield plane located 40mm in front of the focus, approximately 20mm from the surface of the transducer (left column). (A) Nearfield and (B) focal plane scan with no lens, (C) nearfield and (D) focal plane scan with a 0.79mm base thickness eight sector mode 4 lens (maximum transmission through the thickest sectors), (E) nearfield and (F) focal plane scan with a 0.89mm base thickness lens (maximum uniform surface amplitude). Images (A), (C) and (E) are scaled to a maximum pressure of 0.07MPa, while images (D) and (F) are scaled to a maximum of 0.34MPa.

of 1W using the relations shown in Equations 4.6 and 4.7

$$I_0 = \frac{(p_0)^2}{2\rho_0 c_0} \tag{4.6}$$

$$P = I_0 A_s \tag{4.7}$$

where p_0 is the surface pressure, I_0 is the temporal average acoustic intensity, P is the acoustic power, and A_s is the surface area of the transducer.

Figure 4.7 displays the comparison between measured and simulated focal planes for the three cases, where images of the H102, with a mode 2 lens, and with a mode 4 lens are shown by A1, B1 and C1, where white dotted lines indicate the location of the lens sector separations relative to the transducer surface. Row 2 shows the experimentally measured focal planes for each respective case (normalised to the peak pressure within each image), and row 3 shows the equivalent simulated normalised focal fields. Care was taken to make sure that the position of the transducer relative to the hydrophone was kept constant as the acoustic lenses were applied or removed.

A comparison between the measured pressure fields (Figs. 4.7 A2, B2, and C2) and the theoretical linear simulations (Figs. 4.7 A3, B3, and C3) show good agreement, where the measured peak pressures in water for the focused H102 alone, with a mode 2 lens, and with a mode 4 lens were 0.96MPa, 0.45MPa, 0.34MPa, and the simulated peak pressures were 1.00MPa, 0.43MPa, and 0.31MPa respectively. The uncertainty of the acoustic hydrophone at 1.1MHz is ±14%, which verifies that the the discrepancy between simulated and measured values lie within the accuracy of the hydrophone. The simulated -3dB focal volumes (relative to the peak pressure in each simulation) over the entire simulation domain for cases A, B and C were found to be 9.60mm^3, 40.74mm^3 and 90.87mm^3 respectively.

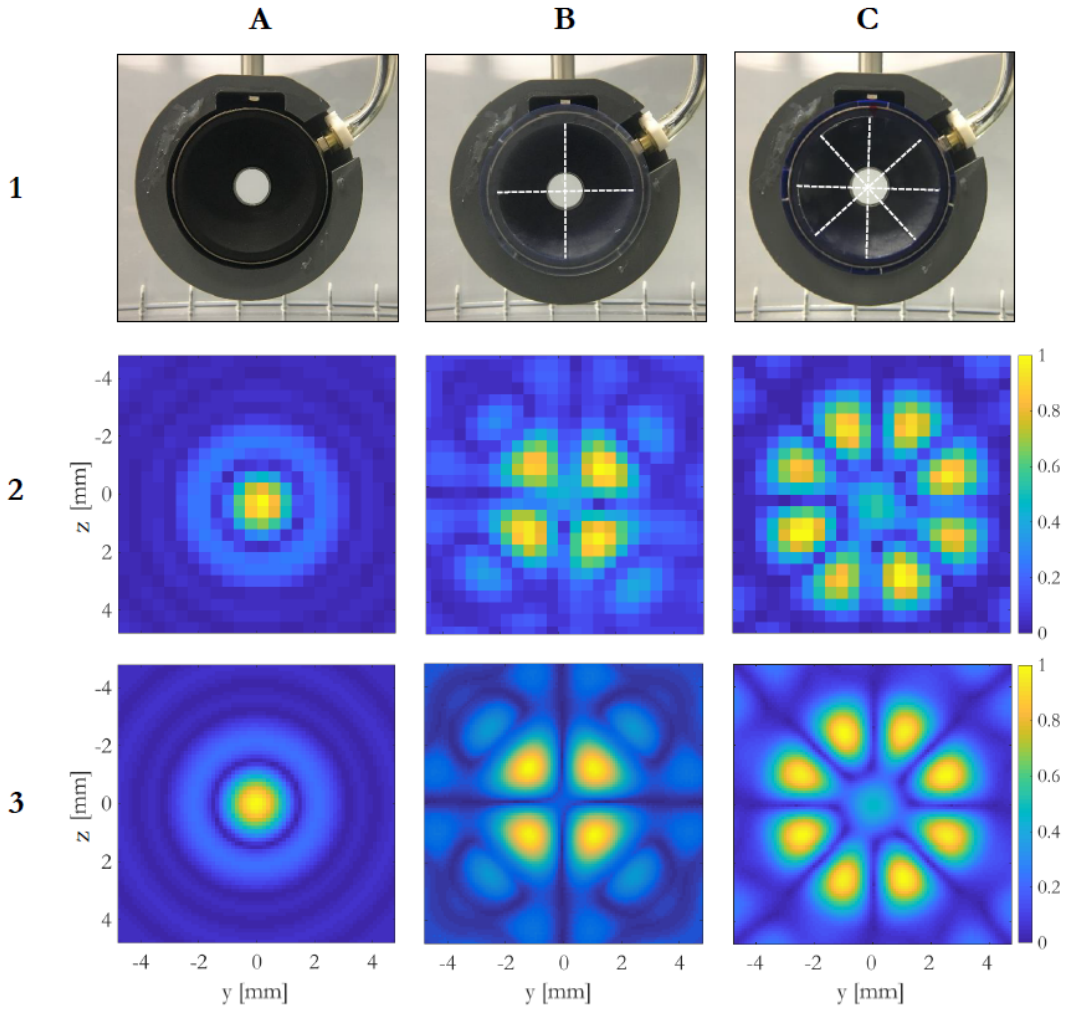


Fig. 4.7 Frontal view of the H102 transducer in water (A1), with the mode 2 lens (B1), and the mode 4 lens (C1), where white dashed lines have been added to indicate the location of the lens sector separations. Focal plane hydrophone measurements generated in a degassed water tank by the H102 transducer alone, with the mode 2 lens, and with the mode 4 lens are shown in A2, B2 and C2 respectively. The axial depth for all three measured scans were obtained at the peak axial pressure location of the H102 transducer (A2) and are normalised by the maximum pressure within each image. Simulated radial pressure fields of the H102 transducer alone, with the mode 2 lens, and with the mode 4 lens are shown in A3, B3 and C3 respectively. Measured peak pressures from left to right were 0.96MPa, 0.45MPa and 0.34MPa with a hydrophone measurement uncertainty of ±14%, and simulated peak pressures from left to right were 1.00MPa, 0.43MPa, and 0.31MPa. The transducer is centred at the origin with the axial direction orientated along the x-axis.

4.3 Heat Generation in an Agar Phantom with an Acoustic Lens

To investigate the effect of the 3D printed acoustic lens on heat generation in an attenuating medium, an agar-based tissue mimicking phantom [206] was employed and the temperature rise generated by a short insonation from the H102 transducer (with and without a lens) was recorded at several radial positions in the focal plane using an embedded 0.15mm diameter fibre-optic hydrophone (FOH) (Precision Acoustics Ltd., UK). A FOH was used in order to acquire both pressure and temperature data simultaneously [207], and to minimise the viscous heating artefact commonly associated with metal needle thermocouples [208, 209].

To produce the phantom, 1.5%w/v powdered agar (Agar Fine Powder, Sigma-Aldrich Co.) and 3%w/v silica microspheres in the size range of $9-13\mu m$ in diameter (Sigma-Aldrich Co.) were mixed with distilled water and degassed for a minimum of one hour using a vacuum pump (MZ 2 NT, Vacuubrand). The mixture was heated to 95°C in a microwave to ensure the agar powder was completely dissolved and then left to cool on a workbench until the temperature of the mixture reached 45°C. At this point the solution was gently stirred to prevent sedimentation, and slowly poured into a rectangular perspex mould to prevent the entrapment of gas bubbles. Moulds were made with dimensions of $80 \times 80 \times 40$mm in order to provide two acoustic windows of different length where attenuation and speed of sound could be measured experimentally using the same sample.

The acoustic properties of the phantom were determined using a through-transmission setup as shown in Figure 4.8, where two identical broadband unfocused piston transducers (Panametrics NDT V306, Olympus NDT Inc.) with a diameter of 13mm and a centre frequency of 2.25MHz were axially aligned and spaced 100mm apart using

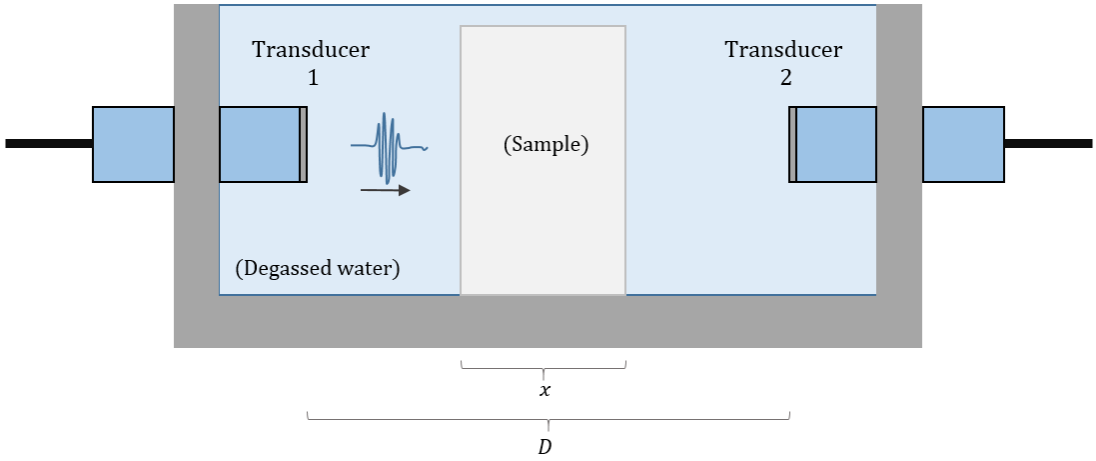


Fig. 4.8 Setup of the through-transmission technique using a custom rig to axially align two unfocused piston transducers with a sample inserted in between.

a customised rig. The transducers and rig were submerged in a tank of degassed water with a phantom sample of fixed width x placed in the acoustic path between the two transducers. One transducer was driven by a signal generator (Agilent 33220A, Keysight Technologies) using a 25 cycle burst at frequency values ranging from 1MHz to 3.5MHz in steps of 0.25MHz with a peak to peak voltage amplitude of 10V, and the second transducer was used to receive the transmitted signal which was recorded and saved using a digital oscilloscope (Waverunner, Teledyne LeCroy). Altering the frequency of the input pulse enabled the frequency-dependent attenuation response of the sample to be measured, so long as there was sufficient signal amplitude from the receive transducer.

The acoustic attenuation coefficient was determined by taking the ratio of the two measured voltage signals from the receive transducer when samples of different thickness had been inserted. Keeping the distance D between the transducers the same in each case and assuming the effect of diffraction is small, the attenuation coefficient is given by Equation 4.8 where Δx is the difference in thickness between the two samples, V_1 is the amplitude of the peak located at the driving frequency in the frequency

spectrum of the received voltage signal when the first sample is present, and V_2 is the amplitude when the second sample is present.

$$\alpha = \frac{20\log_{10}(V_2/V_1)}{\Delta x} \tag{4.8}$$

Figure 4.9 shows the calculated attenuation at each frequency step for agar-silica phantoms comprised of 2%, 3%, and 4%w/v silica microspheres ($n = 3$). A line of best fit has been drawn through the data which follows the power law attenuation model described in Equation 3.14.

Typically, the frequency dependence of attenuation in most soft tissues is in the range of 1 to 1.5 [125] which is significantly higher than the measured values shown in Figure 4.9. However, as long as the phantom is exposed to an acoustic field where pressure amplitudes exhibit predominantly linear behaviour, then choosing a phantom with the correct attenuation at that frequency will capture the acoustical and thermal fields as there will be no nonlinearly generated harmonics. For 1.1MHz, the acoustic phantom which most closely matched the attenuation of human liver was the one comprising of 3%w/v silica microspheres. The density and speed of sound at room temperature (23°C) for the 3%w/v silica phantom were measured to be $1017 \pm 27\text{kg.m}^{-3}$ and $1510 \pm 2\text{m.s}^{-1}$ respectively.

In order to record the temperature rise produced in a 3%w/v silica phantom due to ultrasound exposure, a 0.15mm diameter FOH was inserted into the centre of an $80 \times 80 \times 60$mm phantom. The FOH was guided by a 1mm diameter coaxial needle, and the insertion was performed with the phantom submerged in degassed water in order to minimise the entrapment of air. The coaxial needle was retracted once the FOH was in position in order to expose the tip of the FOH to the phantom, being careful not to disturb the position of the FOH relative to the phantom. Both the front and back mould walls (80×80mm) perpendicular to the ultrasound propagation

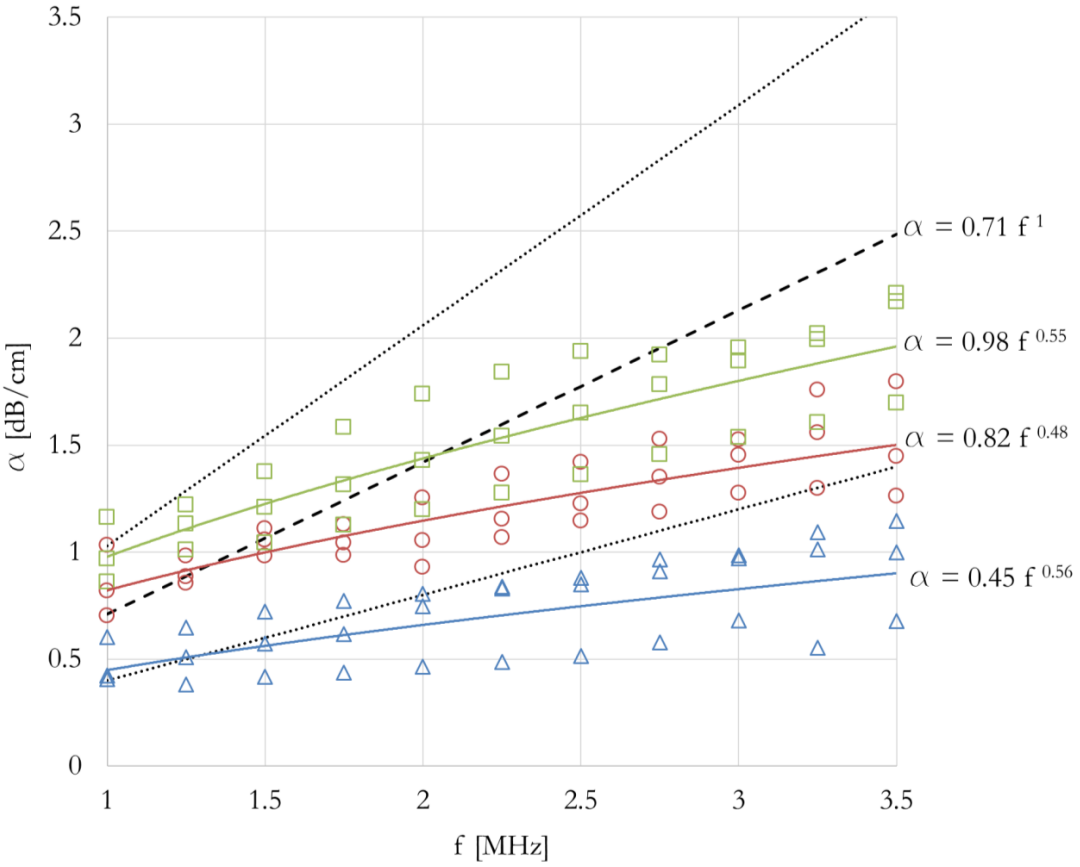


Fig. 4.9 Measured attenuation coefficient for phantoms made of 1.5%w/v agar powder and 2%w/v silica (blue triangles), 3%w/v silica (red circles) and 4%w/v silica (green squares) microspheres of $9-13\mu m$ in diameter in distilled degassed water (n = 3). The solid traces show the line of best fit using the formula $\alpha = \alpha_0(f/f_0)^b$ where f is the frequency of interest, and f_0 is equal to 1MHz. The black dashed line shows the average attenuation value for human liver as reported in Table 2.3, and the two dotted black lines indicate ± 1 standard deviation.

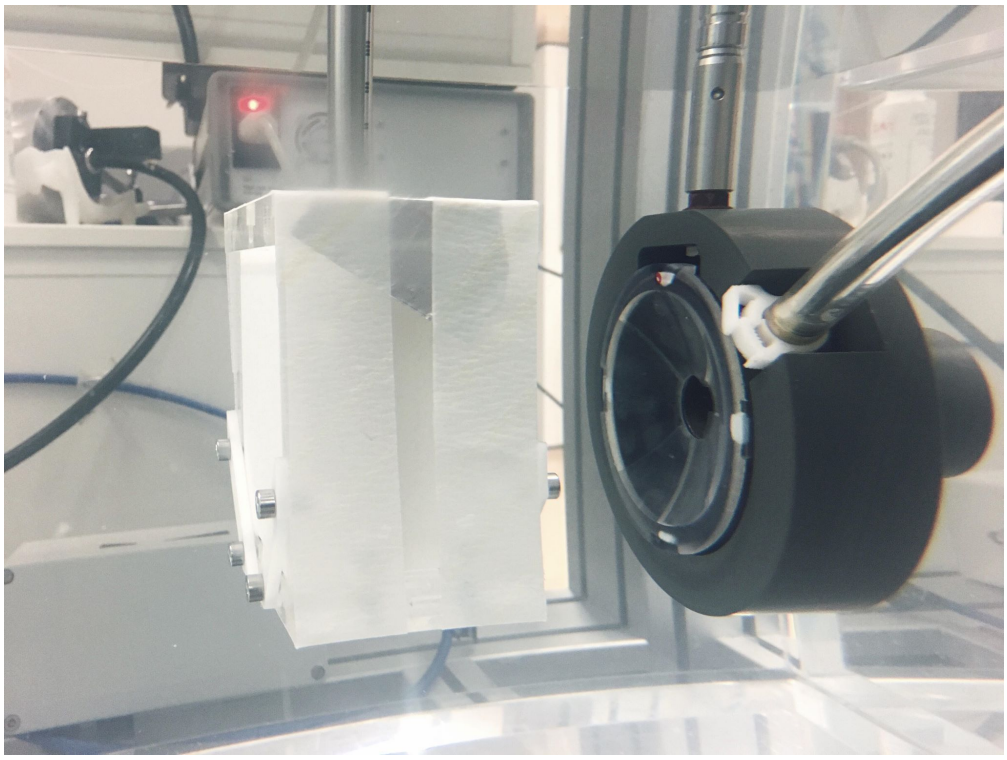


Fig. 4.10 Setup of the H102 transducer with a mode 4 acoustic lens secured in place. An agar-silica phantom with a FOH embedded in the centre is placed in the focal field of the transducer using a 3-axis positioning stage.

direction were removed in order to provide an acoustic window for sound to enter and exit the phantom. The phantom mould was mounted onto a 3-axis positioning stage, submerged in a large tank of degassed water, and positioned into the focal field of the H102 transducer as shown in Figure 4.10. The phantom was repositioned until the location of the focus within the phantom was determined to the nearest 0.1mm by looking at the observed peak acoustic pressure.

The function generator source amplitude was varied from 10mV (peak) in steps of 10mV (corresponding to peak pressure increments of approximately 0.1MPa) until a peak temperature rise of approximately 5°C was generated after 30 seconds of continuous wave insonation. A cooling time of at least 5 minutes between recordings ensured that the temperature of the phantom returned to a reasonable steady state level ($|d\mathrm{T}/d\mathrm{t}| < 0.25°\mathrm{C.min}^{-1}$) before each new insonation. Signal generator amplitude

was converted to acoustic power by comparing against a previous calibration of peak focal pressure in water as a function of input voltage, and using Equations 4.6, 4.7 and 4.9

$$p_0 = p_{max}/G \tag{4.9}$$

where p_{max} is the peak pressure at the focus, G is the documented gain of the transducer, and p_0 is the estimated peak pressure at the surface of the transducer.

To obtain temperature measurements from several locations in the focal plane using a single embedded FOH, repeated insonations were performed with the phantom repositioned 1mm, 2.5mm and 5mm in the x (radial) direction in order to achieve a relative displacement between the FOH and the acoustic focus. The acoustic power which generated a 5 ± 0.5°C peak temperature rise at the focus after 30s continuous wave insonation was found to be approximately 1.4W by extrapolation from the peak acoustic pressure. Taking into account the ±14% uncertainty in peak focal pressure measured by the FOH, the minimum and maximum predicted temperature range corresponded to acoustic powers of 1.04W and 1.81W respectively. Simulations were performed in PZFlex using a grid resolution of 0.091mm ($\lambda/15$) using an axisymmetric model for the H102 transducer, and a quarter symmetry model for the mode 4 acoustic lens. The acoustic properties of the phantom were set to be the average measured values for 3%w/v silica, and thermal properties of the phantom were assumed to be the same as water (listed in Table 2.3). When securing the 3D printed mode 4 lens to the front face of the transducer, care was taken not to disturb the transducer or phantom in order to maintain the same alignment between the focus and the FOH.

Figure 4.11A displays the measured (lines) and predicted temperature profiles (shaded regions) produced by the H102 transducer from 30s continuous wave insonation at radial locations 0mm (blue), 1mm (yellow), 2.5mm (green) and 5mm (red) away from the central axis. Dashed lines indicate the standard deviation of the measurements

for repeated insonations (n = 3). The shaded temperature ranges are produced by PZFlex simulations evaluated at 1.04W and 1.81W to account for the uncertainty in measurement of the peak focal pressure. All recorded temperature curves show good agreement with theoretical simulations, with the peak temperature rise of 5.4°C located at the focus as expected (shown by the blue solid line).

The resulting temperature profile produced by the same insonation parameters with the mode 4 acoustic lens secured in place are shown by the solid lines in Figure 4.11B, where shaded regions indicate the predicted temperature range based on equivalent quarter symmetry PZFlex simulations. Due to the annular focusing pattern caused by the lens, the temperature rise is relatively uniform for radial positions 0mm, 1mm and 2.5mm away from the focus, where both simulated and measured curves show that the observed peak temperature rise after 30s of insonation remain within 0.2°C of each other. The measured peak temperature rises at radial positions 0mm, 1mm, 2.5mm and 5mm after 30s were 0.88°C, 0.82°C, 0.88°C and 0.33°C respectively, with the 0mm and 5mm curves continuing to rise to peak temperature rises of 0.93°C and 0.37°C respectively after the source was turned off due to thermal conduction. All measured curves fell within the bounds of the predicted temperature rise from simulations, which suggests good agreement with measured and simulated cases.

For temperature measurements obtained in an ultrasonic field using metal thermocouples, the often large difference in density between the thermocouple and the surrounding medium may lead to an artificially high recorded temperature rise due to viscous heating, known in literature as a viscous heating artefact [209]. For the FOH used in this study, the very thin diameter (0.15mm) and lower density of the glass hydrophone in comparison to most metals means that this is largely minimised, and is supported by the good agreement between the simulated and measured temperature rises shown in Figures 4.11A and 4.11B. Figures 4.11A and 4.11B have also verified

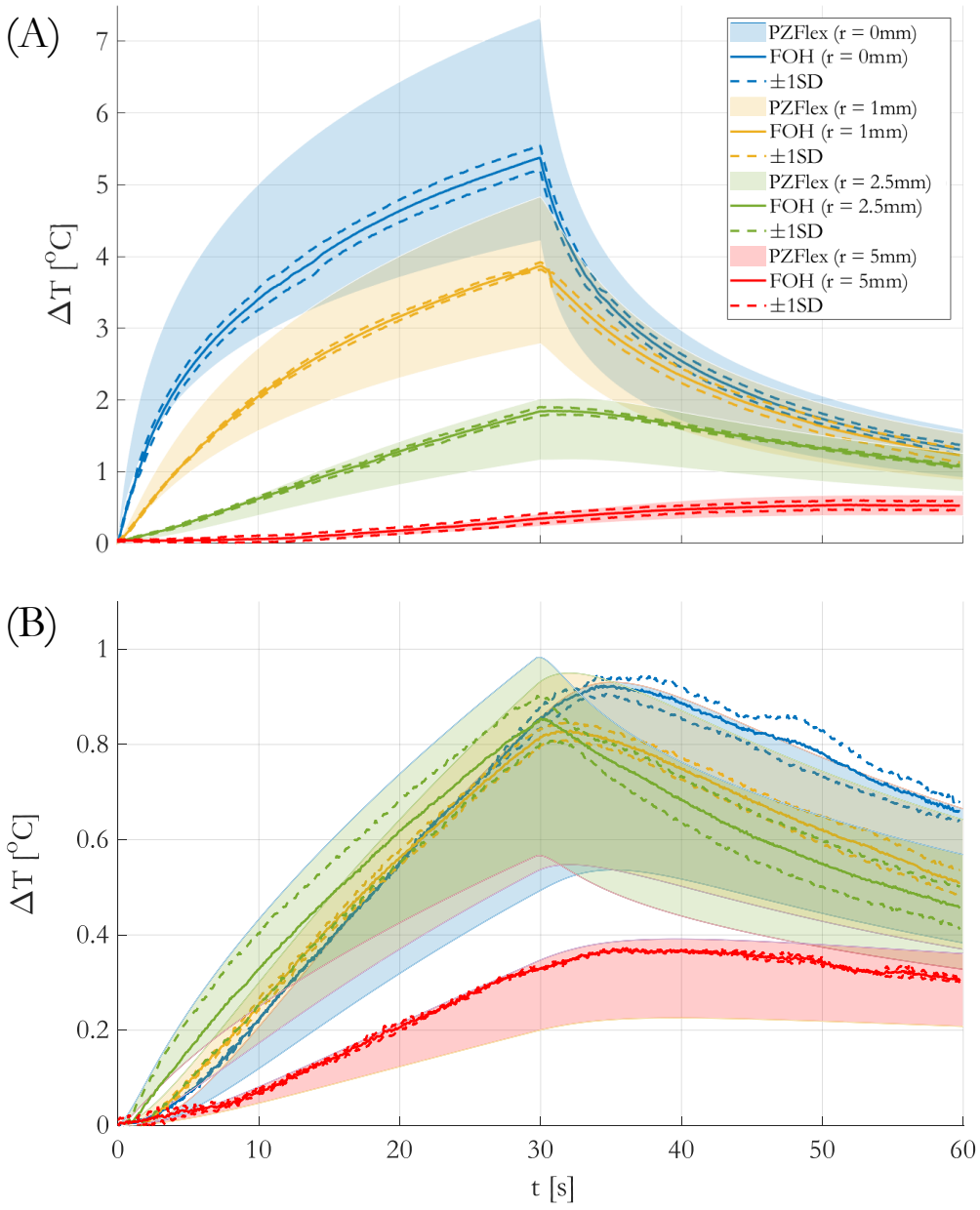


Fig. 4.11 Measured temperature profile (solid lines, dashed lines ±1 standard deviation) in a 3%w/v silica phantom caused by 30s of continuous wave insonation from a H102 transducer driven at an acoustic power of 1.4W (A) and with the addition of a mode 4 acoustic lens (B). Measurements were recorded with an embedded FOH at a propagation depth of 30mm into the phantom at the focus (blue), and radial positions 1mm (yellow), 2.5mm (green) and 5mm (red) away. Shaded regions indicate the minimum and maximum predicted temperature rise from PZFlex simulations for acoustic powers of 1.04W and 1.81W (estimated from the ±14% uncertainty in acoustic pressure measured at the focus by the FOH).

that the introduction of a 3D printed sectored acoustic lens can enable a single-element focused transducer to generate mild hyperthermia across a larger volume, in a more uniform manner without the use of mechanical scanning, and that this can be modelled accurately using PZFlex. The performance of a 3D printed sectored acoustic lens will be investigated in the next chapter through PZFlex simulations in a patient-specific liver target.

5 Simulation of a Patient-Specific Acoustic Lens for Large Volume Mild Hyperthermia

5.1 Introduction

The acoustic and thermal simulations presented so far have only considered heat generation in a homogeneous attenuating medium. In clinical applications, therapeutic ultrasound encounters multiple tissue interfaces, curved boundaries, and tissue-dependent variation in acoustic and thermal properties as discussed in Chapter 2 (summarised in Table 2.3). Depending on the degree of variation, these factors may result in a significant difference compared to the pressure and temperature fields produced in a homogeneous attenuating medium. Full-wave 3D simulations in the body have recently become more accessible through the advancement of computing technology [106, 210], and is explored in this chapter in order to model these effects.

Continuing from section 2.3.6, early uses of a patient-specific dataset with focused ultrasound explored geometrical ray tracing as a method to select an appropriate acoustic window for optimal transducer placement, which was subsequently coupled with acoustic and thermal simulations that assumed a homogeneous attenuating medium [211]. More recent studies have been driven towards modelling patient-specific scenarios in targets such as the abdominal wall [166, 212–214], and more specifically in breast tissue [141], kidney [140], liver [165], prostate [215], and the skull [216, 217].

The principle effect on ultrasound propagation by inhomogeneities in the body is the distortion of the acoustic field due to reflection and refraction. Although refraction has been shown to be small for low angles of incidence in soft tissues [117], for highly focused sources such as those used in tumour ablation, these tissue interfaces play a more significant role, resulting in shifting of the focal point, as well as splitting of the focus [140]. In transcostal focused ultrasound scenarios, pre-focal heating due to the high reflectivity of the tissue-bone interface at the ribs poses a significant challenge to treatment safety. For transducers with many multiple elements, the natural approach to minimise rib heating would be to switch off obstructed elements [164, 211, 218–221], however this is not feasible for single-element focused ultrasound sources and alternative methods include placing sound absorbing structures in front of the affected ribs [222], or invasive surgical resection of ribs lying in the acoustic window [223].

One strategy to undo the acoustic field abberations caused by tissue inhomogeneity is through the use of the time reversal technique [142, 224, 225], which involves recording the pressure history emitted by an acoustic source situated at the intended target location using an array of transducers positioned at the desired source location, with the intention of re-emitting the recorded waves in reverse so that the acoustic waves self-correct by the time they reach the target. In the case for phased arrays, this is performed by providing appropriate amplitude and phase corrections to each acoustic source element to mirror the received acoustic waves [141, 142, 166].

Phase correction (conjugation) has recently been incorporated into an acoustic lens for a spherically focused single-element transducer, where the simulation of a virtual point source located at the intended target location was used in the design and production of an acoustic lens to undo the aberrations caused by the skull [217]. Similarly, a phase-conjugate acoustic lens is designed in this chapter by first simulating a virtual spherical point source at the geometrical focus of the transducer in the liver

using PZFlex, and subsequently recording the pressure time history at locations outside of the body coinciding with the transducer surface. As long as the amplitude of the source wave is not entirely attenuated by the tissue before it exits the body, the recorded pressure time histories can provide useful amplitude and phase information to generate an appropriate acoustic lens for a single-element spherically focused transducer, as well as determine which regions of the transducer surface may be obstructed by the ribs. The resulting phase-conjugate lens is simulated in PZFlex in order to determine the performance of a hypothetical 3D printed acoustic lens in a patient-specific scenario, in combination with the masking of obstructed source locations for rib-sparing.

5.2 CT Dataset Preparation and PZFlex Model Setup

To compare the two acoustic lenses shown in Fig. 4.7 with the unmodified H102 focused transducer at generating useful therapeutic volumes of mild hyperthermia in the liver, 3D PZFlex simulations in a segmented tissue model derived from an anonymised CT data set were carried out. The anonymised segmented CT dataset was provided by Prof. Robin Cleveland (University of Oxford, UK) and featured a spatial resolution of 0.79mm with the major tissue types labelled as fat, bone, liver and other soft tissue. The acoustic and thermal properties for the generic soft tissue regions were assigned to be the same as skeletal muscle since this layer predominantly occupied the intercostal spacing between the ribs and in the region directly behind the fat. A computer visualisation of the segmented CT dataset is shown in Figure 5.1A, and in this study, one focal target in the liver is explored (Fig. 5.1B) which features partial obstruction of the acoustic field as indicated by the overlapping acoustic beam width

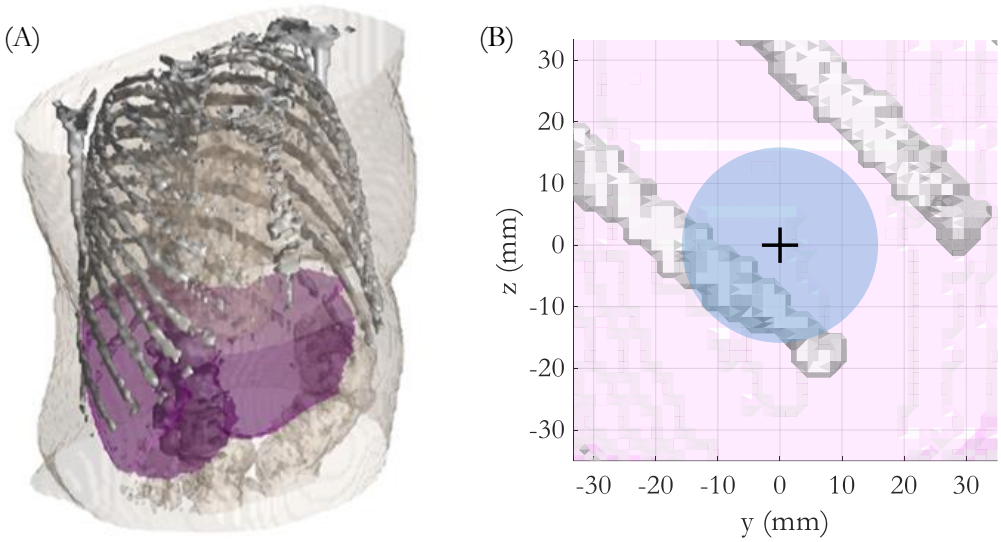


Fig. 5.1 (A) Volume rendering of the segmented CT dataset used in acoustic and thermal simulations. Contours shown indicate bone, liver (purple), and the tissue surface. (B) The location of the geometric focus of the transducer relative to the rib is shown by the black cross, where the degree of obstruction from the rib on the acoustic field can be seen by the overlap of the approximated focal beam (blue circle) at the rib depth.

(blue circle) with the 9^{th} rib. The simulation domain consisted of a 95×70×70mm volume which encompassed both the transducer and the CT target region of interest.

3D linear full-wave pressure simulations of the transducer-CT model were performed using PZFlex at a grid resolution of 0.089mm (15 elements per wavelength in water) and required approximately 150GB RAM. Simulations were executed on a high-performance computer (Dell Precision T910 Workstation, 32 Cores, 192GB RAM) with a simulation time step of 0.048μs (determined by the Courant-Friedrichs-Lewy limit for convergence) and the acoustic simulation required up to 10 hours to complete. The water and soft-tissue were modelled as a fluid, and the bone and the acoustic lens as an elastic solid. To provide a domain grid resolution suitable for pressure simulations, the CT dataset was up-sampled to the pressure simulation resolution using nearest neighbour interpolation. In all simulations, the ultrasound source was centred about the origin

and modelled by a continuous-wave sinusoidal pressure boundary condition at elements corresponding to locations on the transducer surface. The source pressure amplitude was adjusted such that a total acoustic power of 1W was emitted from the transducer surface for linear scaling convenience in thermal simulations. Acoustic simulations were executed until source waves had travelled 1.5 times the geometrical focal length of the transducer in order to establish a steady state acoustic field, and absorbing boundary conditions were applied to all model boundaries to minimise reflections. An equivalent model using a velocity boundary condition showed comparable results with a difference in peak pressure of less than 1%. Once the acoustic field was established, the temporal average intensity over the duration of one period was saved and used to calculate the acoustic heat source in separate thermal simulations. Since all simulations were linear, changes in the acoustic power of the source were accounted for by scaling the intensity appropriately. The thermal model performed by PZFlex is a 3D FDTD implementation of the Pennes bioheat transfer equation described earlier in Equation 2.7. Thermal simulations do not need the same spatial resolution as pressure simulations to reach convergence, therefore simulations were interpolated to a lower grid resolution of 0.337mm (4 elements per wavelength in water), which required approximately 45GB RAM and were processed within two hours for the insonation durations investigated in this study.

5.2.1 Phase-Conjugate Lens Approach

In order to investigate the effect of rib obstruction and tissue inhomogeneity on the acoustic field, an inverse approach as illustrated in Figure 5.2 was implemented. Firstly, a virtual continuous-wave point source with a peak amplitude of 1MPa and centre frequency of 1.1MHz located at the geometric focus of the H102 transducer in the liver was simulated, and the acoustic pressure history at locations coinciding with

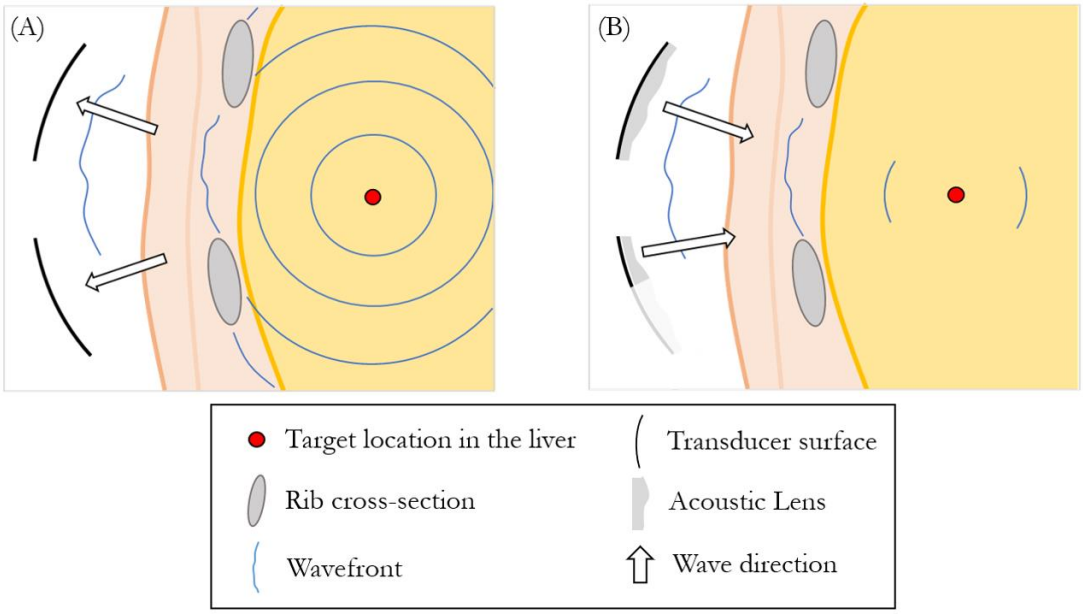


Fig. 5.2 Cross-sectional illustration of the virtual point source simulation method. (A) Illustration of a point source in the liver (red circle) with wavefronts (shown in blue) being distorted as they encounter the ribs and tissue inhomogeneity. (B) Forward simulation of the transducer with an acoustic lens where aberrated wavefronts self-correct as they propagate through inhomogeneous media and reach the liver target. The faded region on the transducer indicates source locations which are masked in order to avoid rib heating.

the transducer surface were recorded (Fig. 5.2A). The phase and amplitude of the fundamental frequency from the pressure history recordings were used to produce a phase-conjugate acoustic lens to undo aberrations caused by tissue inhomogeneity, and the surface amplitude distribution was used to determine the source locations obstructed by ribs, which were subsequently masked in the following forward simulation in order to minimise rib heating (Fig. 5.2B). Masking was implemented by setting the source amplitude at these locations to zero.

Figure 5.3A shows the 2D projection of the recorded pressure history amplitude across the transducer surface (obtained by plotting the amplitude of the centre frequency (1.1MHz) from the pressure history signal at each location), and the corresponding histogram of the surface amplitude distribution is shown in Fig. 5.3B. It is assumed

that regions of low amplitude correlate with the presence of rib obstruction, however, thresholding of the original amplitude distribution results in regions of false positives and false negatives as shown in Fig. 5.3E, where blue areas indicate regions which are labelled as obstructed. In order to obtain a clearly defined region of rib obstruction (known to only occur at the bottom-left region of the transducer for the CT liver target shown in Figure 5.1), the surface pressure amplitude distribution was convolved with a 2D Gaussian smoothing filter ($\sigma = 3$mm) using the function *fspecial* in MATLAB (The MathWorks, Inc.) to produce Fig. 5.3C, with a corresponding surface pressure histogram shown in Fig. 5.3D. A threshold value of 2.85kPa was used to determine rib-obstruction based on the histogram of the surface pressure distribution shown in Fig. 5.3D, and the difference in thresholded regions without and with Gaussian smoothing are shown by comparing the blue shaded regions in Figs. 5.3E and 5.3F respectively. The rib-obstructed region indicated in Fig. 5.3F is more clearly defined in comparison to Fig. 5.3E and the source regions occupying these locations were subsequently masked in PZFlex simulations.

Fig. 5.4A shows the 2D projection of the phase distribution on the transducer surface obtained from the centre frequency of the recorded acoustic pressure time history. In order to correct for large jumps in phase between neighbouring locations, phase-unwrapping was performed by comparing the phase at each location relative to the local surrounding average phase. If the difference in phase could be reduced by adding or subtracting 2π, then the phase value with least difference to the mean value was adopted, which resulted in Fig. 5.4B (rib obstructed regions masked). The lens thickness needed to provide phase correction was directly calculated using Equation 4.5 and is shown by Fig. 5.4C, and a 2D Gaussian smoothing filter was applied to the raw lens thickness map in order to minimise large jumps on the lens surface as shown in Fig. 5.4D. A comparison of the lens surface profile obtained along a single line

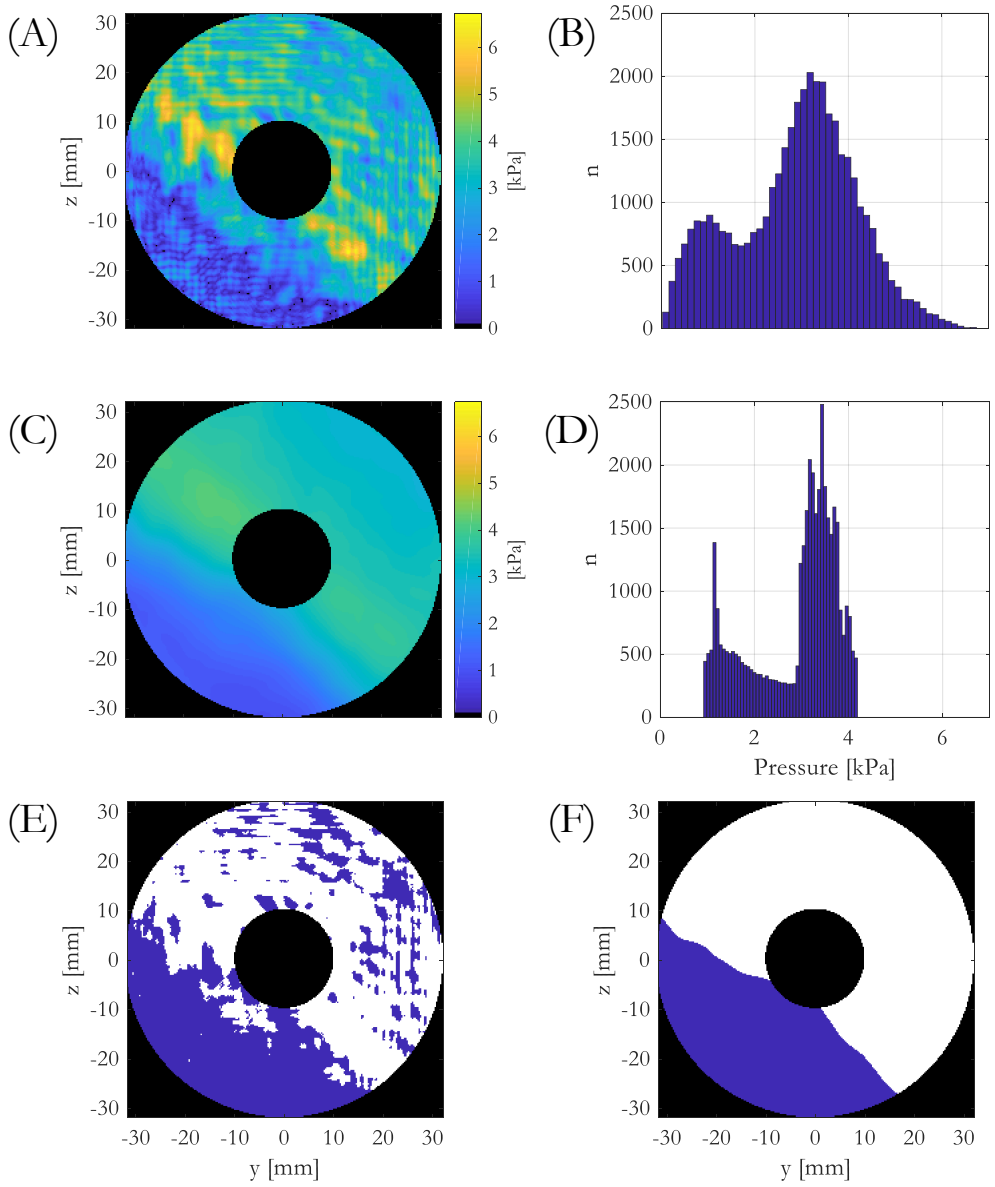


Fig. 5.3 (A) 2D projection of the recorded peak pressure history amplitude on the transducer surface and (B) histogram of the surface pressure amplitude distribution. (C) 2D projection of the surface pressure amplitude after Gaussian filtering ($\sigma = 3$mm) and (D) corresponding histogram. (E) Rib-obstructed regions (blue) resulting from thresholding (A) at a pressure value of 2.85kPa (based on the histogram shown in (D)). (F) Rib-obstructed regions (blue) resulting from thresholding (C) at a pressure value of 2.85kPa.

(indicated by the white dashed lines in Figs. 5.4C and D) are compared in Fig. 5.4E. Since the printing resolution of the 3D printer is fixed at 0.025mm, the value of σ defined in the Gaussian smoothing filter used to produce Fig. 5.4D was increased until the largest difference between adjacent lens regions did not change by more than 0.025mm in order to minimise large discontinuities on the lens surface.

To incorporate the appropriate phase correction modifications to the mode 2 and mode 4 lenses, the additional lens thickness distribution shown in Fig. 5.4D was added to the phase difference thickness of the mode 2 and mode 4 lenses, and the base lens thickness was adjusted to match the average phase correction thickness with the optimum minimum lens thickness (described in Figure 4.3). Finally, regions deemed obstructed by the ribs were masked in simulations to emulate the presence of an acoustic absorber.

5.2.2 Thermal Simulation Scenarios

To compare the effect of the mode 2 (M2) and mode 4 (M4) acoustic lenses to the focused H102 transducer alone (M0) on the generation of useful volumes of therapeutic mild hyperthermia in the liver, three insonation scenarios were compared, taking note of the simulated 39.5°C thermal contour volumes which coincided with a 10.2mm diameter spherical target centred at the geometrical focus of the transducer in the liver. The diameter of the target sphere was chosen to be 10.2mm due to this being the documented free-field focal length of the H102 transducer, and a reference temperature of 39.5°C was selected due to this being the reported threshold temperature for drug release from thermosensitive liposomes [226].

The first heating scenario modelled a low-power continuous-wave insonation in order to minimise thermal damage to tissue. The acoustic powers for each simulation were manually adjusted to produce a maximum steady state temperature of 43±0.1°C

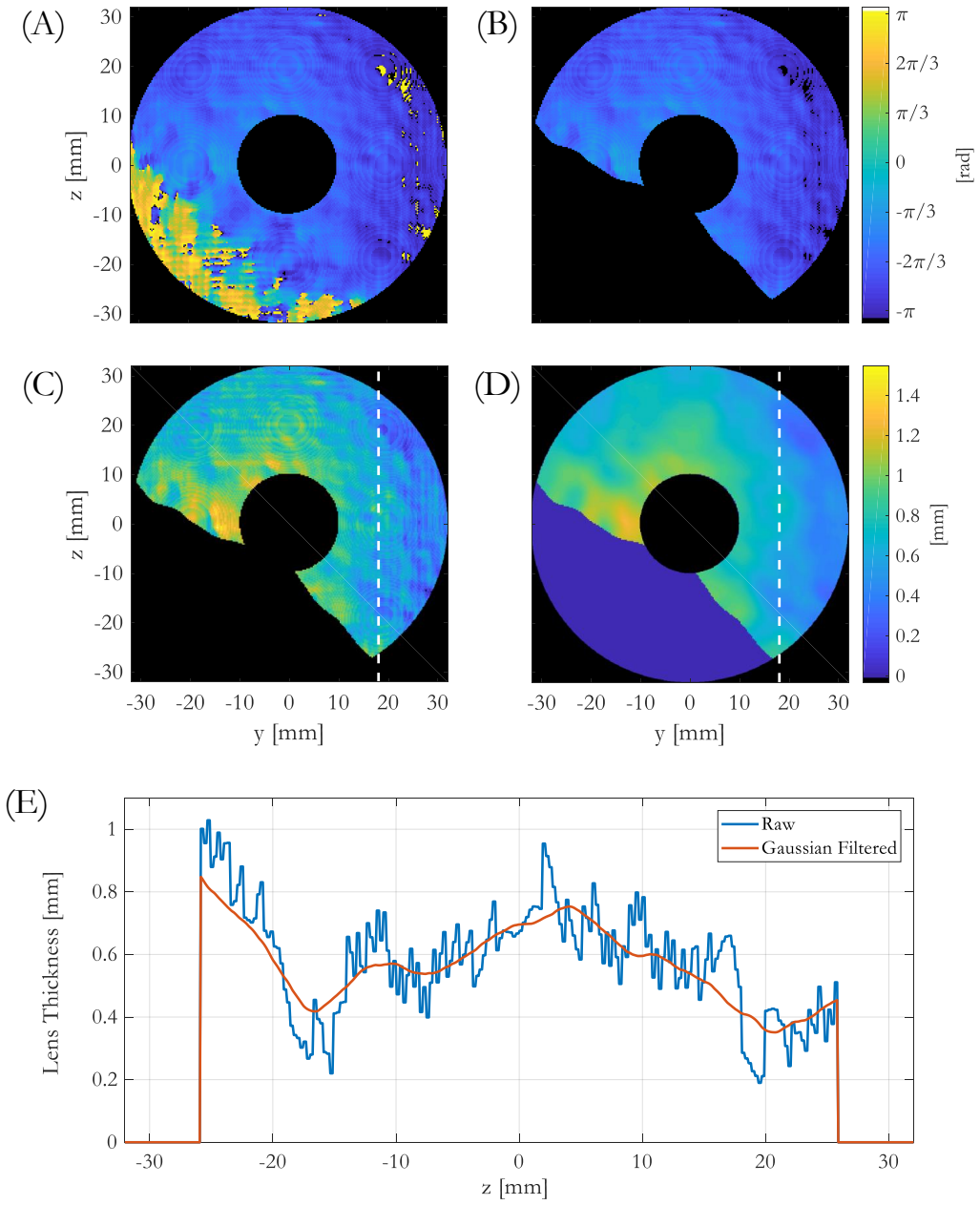


Fig. 5.4 (A) Phase distribution on the transducer surface extracted from the centre frequency of the pressure time history signal at each recorded location. (B) Unwrapped surface phase distribution (rib-obstructed locations masked). (C) Phase correction lens thickness obtained by direct conversion from the unwrapped phase distribution shown in (B). (D) Surface lens thickness after the application of a Gaussian smoothing filter. (E) Comparison of the lens surface profile obtained along the dotted white lines located at $y = 18$mm in (C) and (D).

anywhere within the simulation domain, with a final rate of change in temperature of $0.5°C.min^{-1}$ (averaged across the last simulation second).

The second heating scenario investigated the effect of operating at a fixed peak focal pressure (chosen to be 1.5MPa) in order to model a therapeutic temperature rise generated in shorter insonation times compared to scenario 1. The acoustic powers for each simulation were manually adjusted so that the maximum peak pressure was 1.5MPa, and thermal simulations were executed until a maximum temperature of 43±0.1°C had been reached. The observed on-target therapeutic contour volumes and the insonation durations in this heating scenario were also linearly extrapolated to estimate the hypothetical minimum therapy duration and required energy to raise a target volume of $1cm^3$ to a therapeutic temperature of 39.5°C.

Using the optimal insonation parameters from the second heating scenario, the third heating scenario compares all simulation cases with the same amount of delivered energy (keeping the acoustic power and duration of insonation constant) in order to investigate the differences in peak temperature rise, therapeutic volume, and to check for regions of ablation - defined here as a critical thermal dose (CEM_{43}) of 240 minutes [32].

5.3 PZFlex Simulations Results

The -6dB simulated pressure contours generated in the CT dataset for the focused transducer alone (M0), with a mode two lens (M2), and with a mode four lens (M4) are shown in blue in Figs. 5.5A, 5.5B, and 5.5C respectively, and the effect of incorporating a patient-specific (PS) lens with rib masking for the three cases is shown in Fig. 5.5D, 5.5E, and 5.5F respectively. For reference, a green spherical target volume with a diameter of 10.2mm is shown centred at the geometrical focus of the transducer. A diameter of 10.2mm was chosen since this was equal to the focal length of the H102

transducer in water [227], and earlier thermal simulations presented in Chapter 3 show an optimal thermal field which does not exceed 5mm in the radial direction. Both the M0 and M0 PS cases show a tight localised focal volume, and as the operational mode is increased from M0 to M4, the -6dB contour volumes increase, indicating successful defocusing of the acoustic field. The incorporation of patient-specific modifications to the sectored lenses also show successful defocusing in the liver, with notable absence of blue contour in front of the rib in the M4 PS case (Fig. 5.5F) compared to M4 (Fig. 5.5C). However for both the M2 and M4 cases, the four and eight foci radial pressure field patterns previously observed in water appear slightly skewed and distorted due to tissue inhomogeneity and the presence of the rib.

5.3.1 Heating Scenario 1

The maximum temperature curves for thermal simulations in heating scenario 1 (termination criteria: $T_{max} = 43 \pm 0.1°C$ with $dT/dt = 0.5 \pm 0.05°C.min^{-1}$ averaged over the last simulation second) for the focused transducer and the two lensed cases with and without patient-specific modifications (solid and dashed lines respectively) are shown in Fig. 5.6. Three distinct curve groups can be seen, with the M4 PS case taking approximately 300 seconds to reach the termination criteria (solid green), the M2 and M4 cases taking around 190 seconds (dashed orange and green), and the M0, M0 PS and M2 PS cases taking under 100 seconds (dashed and solid blue, solid orange). The termination time reflects the perfusion value of the tissue situated at the maximum temperature location, where liver has the highest perfusion rate, followed by bone, and then finally fat and muscle (see Table 2.3 for tissue perfusion coefficients). A higher perfusion rate enables the termination criteria to be achieved sooner, which suggests that the M0, M0 PS and M2 PS cases have successfully generated a peak temperature rise in the liver, while the M2 and M4 cases generated a peak temperature rise in

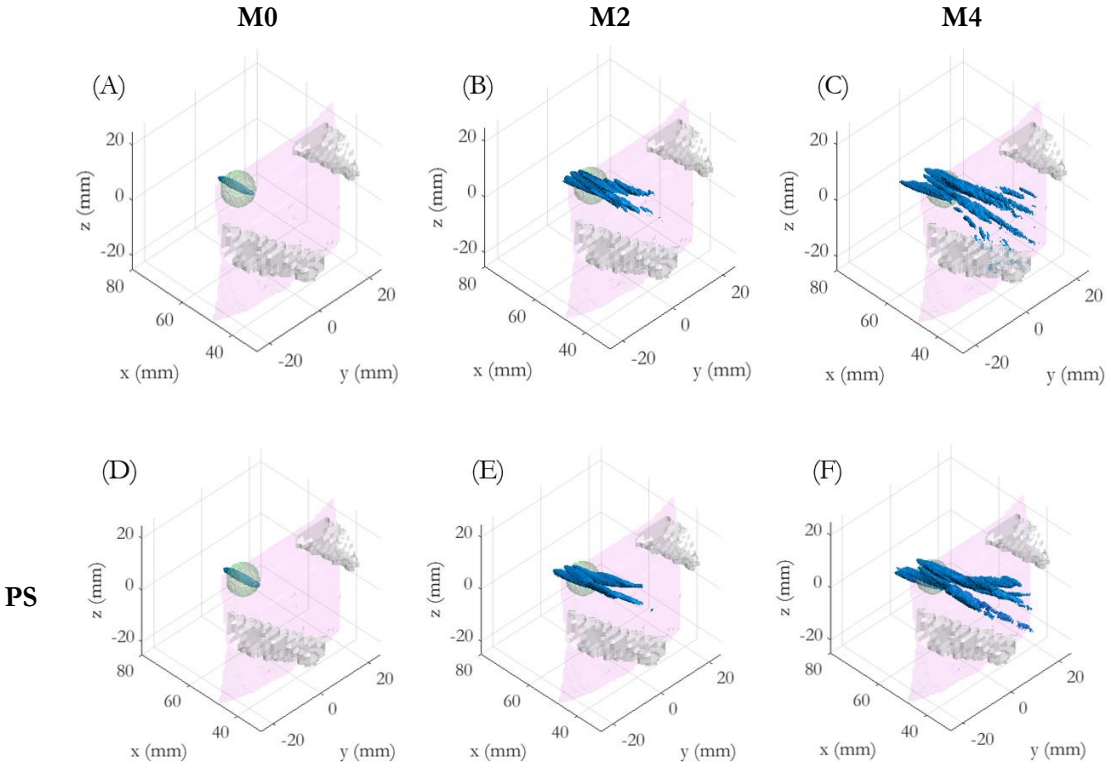


Fig. 5.5 Simulated -6dB pressure contours (blue) generated in the CT dataset from the M0 (A), M2 (B), and M4 (C) cases, and with the addition of patient-specific modifications (D, E and F respectively). The outline of the liver is shown by the pink surface located at approximately $x = 50$mm, the 8^{th} and 9^{th} ribs are indicated by the two diagonal grey isosurfaces, and the transducer source is centred at the origin propagating in the x direction. The outline of the spherical target volume is indicated by a green sphere centred at the geometrical focus of the transducer in the liver.

the rib, and the M4 PS case has avoided rib heating but resulted in pre-focal heating primarily in the muscle or fat.

The location of the maximum temperature curves for heating scenario 1 can also be confirmed by comparing the corresponding 39.5°C therapeutic temperature contours shown in red in Fig. 5.7, where Figs. 5.7A, 5.7B, and 5.7C are generated by the M0, M2 and M4 cases respectively, and Figs. 5.7D, 5.7E and 5.7F are generated by their patient-specific counterparts. For the M0 and M0 PS cases (Figs. 5.7A and 5.7D), there is a small elongated red contour coinciding with the green spherical target volume which indicates localised focusing into the liver. A noticeable portion of the thermal contour is also situated at the rib in M0, which is avoided in M0 PS. In M2 and M4 (Figs. 5.7B and 5.7C), the thermal contour is situated only around the rib with no significant heating observed in the liver. In the M2 PS and M4 PS cases (Figs. 5.7E and 5.7F) rib heating is successfully avoided, with significantly greater thermal contour overlap in the target volume for M2 PS compared to M4 PS. However, in both the M2 PS and M4 PS cases, the reduction in focal gain from defocusing the acoustic field has also resulted in a significant volume of pre-focal heating in the muscle and fat tissue layers.

A summary of contour volumes and insonation parameters in each simulation for heating scenario 1 can be found in Table 5.1. The volume of the 39.5°C contour coinciding with the green spherical target volume in the M2 PS case is 332mm^3, which is considerably larger compared to the M0 (123mm^3), M0 PS (164mm^3) and M4 PS (8mm^3) cases. Comparing M2 PS with the next best case (M0 PS), M2 PS used 608J delivered in 98 seconds, while M0 PS used 292J delivered in 81 seconds.

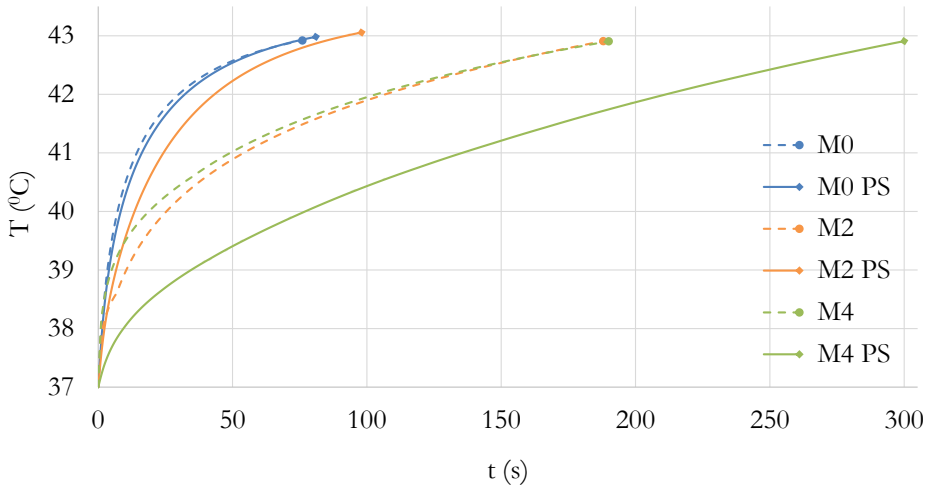


Fig. 5.6 Maximum simulated temperature curves from heating scenario 1 (T_{max} = 43±0.1°C, dT/dt = 0.5°C.min^{-1}) for the M0, M2 and M4 cases as well as their patient-specific counterparts (denoted by the abbreviation 'PS'). Case by case insonation parameters are listed in Table 5.1.

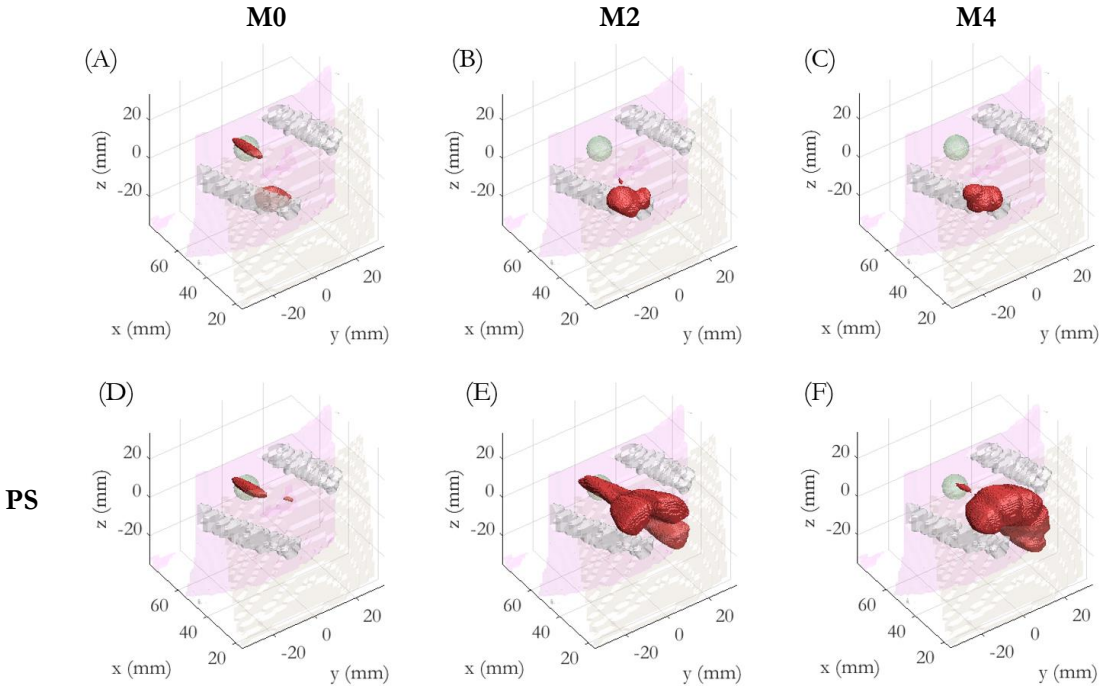


Fig. 5.7 Simulated 39.5°C volume contours (red) produced by heating scenario 1 (T_{max} = 43 ± 0.1°C, dT/dt = 0.5°C) where Figures (A), (B) and (C) are produced by the M0, M2 and M4 cases, and (D), (E) and (F) are produced by their patient-specific counterparts. A green spherical target volume is shown centred at the geometrical focus of the transducer in the liver, the outline of the liver is shown by the pink surface, and the two grey rectangular contours indicate the location of the ribs.

Table 5.1 Insonation parameters for heating scenario 1 (termination criteria: $T_{max} = 43 \pm 0.1°C$ with $dT/dt = 0.5 \pm 0.05°C.min^{-1}$). *Based on a 10.2mm diameter spherical target volume in the liver, centred at the geometrical focus of the transducer.

	M0		M2		M4	
	Normal	Patient specific	Normal	Patient specific	Normal	Patient specific
Power [W]	1.35	3.60	1.90	6.20	1.45	3.80
t [s]	76	81	188	98	173	300
P_{max} [MPa]	0.88	0.79	0.39	0.67	0.32	0.41
Energy [J]	102.6	291.6	357.2	607.6	250.9	1140.0
39.5°C Contour						
Vol. on target* [mm^3]	123	164	0	332	0	8
Vol. in bone [mm^3]	339	0	402	0	369	0
Total vol. [mm^3]	882	288	1327	7799	1086	10512

5.3.2 Heating Scenario 2

For the second heating scenario, the acoustic power was adjusted in each simulation so that the maximum peak pressure was scaled to 1.50MPa, and thermal simulations were executed until a maximum temperature of 43±0.1°C was achieved. The resulting 39.5°C therapeutic volume contours generated at the end of the second heating scenario are shown in Fig. 5.8, where Figs. 5.8A, 5.8B, and 5.8C are generated by the M0, M2 and M4 cases respectively, and Figs. 5.8D, 5.8E, and 5.8F are produced by their patient-specific counterparts. Most thermal simulations required an insonation time between 2.7s and 3.4s, with the exception of M2 and M4 which achieved a maximum temperature of 43°C in 0.29s and 0.12s respectively, see Table 5.2 for thermal volumes and insonation parameters for heating scenario 2. This short insonation duration is due to the location of the peak pressure occurring at the rib (which exhibits the largest attenuation values for absorption and shear), and is reflected in the very small temperature contour volumes shown in Figs. 5.8B and 5.8C respectively (indicated by

black arrows). The thermal contours produced by the M0 case are shown in Fig. 5.8A, where the majority of the contour is situated within the target volume, with some small contour volumes shown at the edge of the rib. Comparing M0 with M0 PS (Figs. 5.8A and 5.8D), the thermal contours located near the rib are avoided in M0 PS, and the heated region is localised in the liver entirely. For the M2 PS and M4 PS cases (Figs. 5.8E and 5.8F respectively), the shorter insonation time has resulted in less pre-focal heating compared to heating scenario 1, with a larger thermal contour volume coinciding with the target in the liver (1050mm^3 and 1100mm^3 respectively) compared to the M0 and M0 PS cases (32mm^3 and 35mm^3 respectively). The total energy delivered in the M2 PS and M4 PS cases were 90J and 138J, while the M0 and M0 PS cases required 14J and 39J respectively.

Using the target volumes and insonation durations listed in Table 5.2 from heating scenario 2, linear numerical extrapolations of the required energy and insonation duration for each case to cover a 1cm^3 target volume are shown at the bottom of Table 5.2 (ignoring the contribution of temperature field changes from one insonation to the next, and assuming that the energy and time required to produce the reported volume on target in heating scenario 2 remains the same for repeated insonations). The numerical extrapolation resulted in predicted total insonation times of 107.9s and 85.7s for M0 and M0 PS, 27.7s for M2 PS, and 24.6s for M4 PS (the M2 and M4 cases were unable to be extrapolated since no therapeutic volumes were produced in the liver target). The M4 PS case required the most energy (1262J) compared to M0 (428J), M0 PS (1111J), and M2 PS (855J), and is estimated to produce the largest therapeutic volume outside of the target region (5cm^3 compared to 0.9cm^3 for M0, 0.1cm^3 for M0 PS and 1.1cm^3 for M2 PS). Based on the simulations from heating scenario 2 and the numerical extrapolation, the M2 PS case is able to generate a larger therapeutic

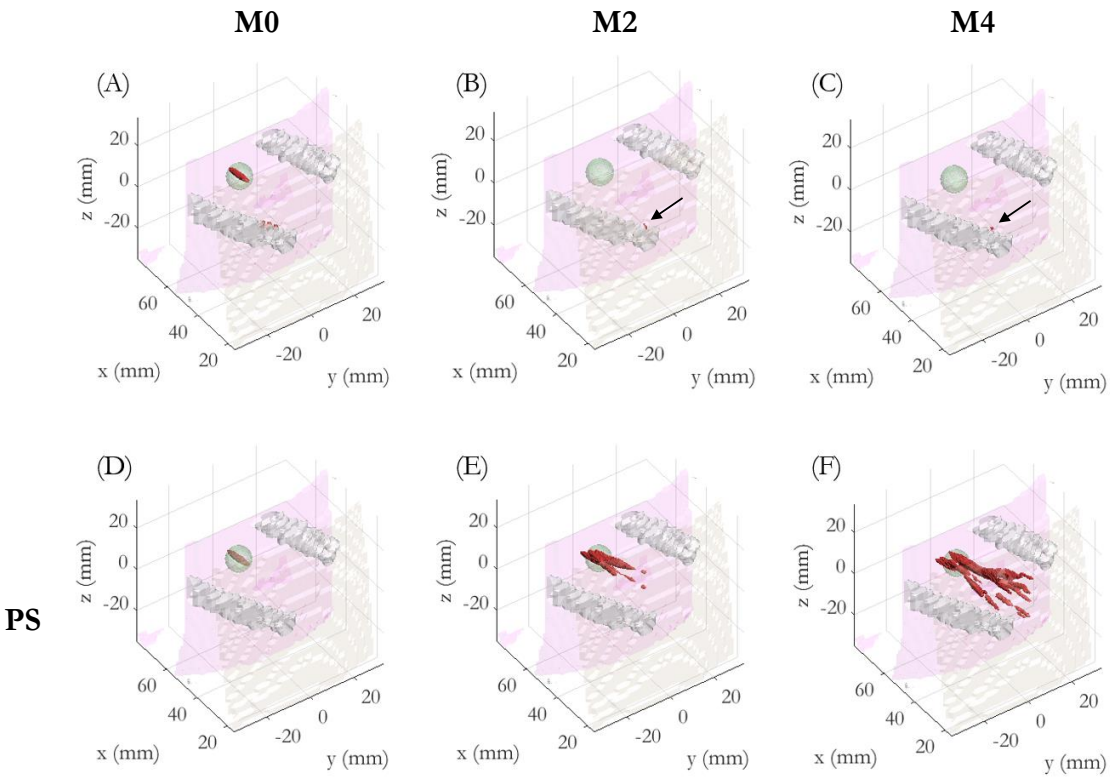


Fig. 5.8 Simulated 39.5°C thermal contours produced by heating scenario 2 (P_{max} = 1.50MPa, $T_{max} = 43 \pm 0.1$°C). The contours shown in (A), (B) and (C) are produced by the M0, M2 and M4 cases respectively (contour locations in (B) and (C) are indicated by black arrows), while (D), (E) and (F) are produced by their patient-specific counterparts respectively. A green spherical target volume is centred at the geometrical focus of the transducer in the liver, the outline of the liver is shown by the surface contour located at approximately $x = 50$mm, and the two rectangular grey contours indicate the location of the ribs.

volume in the liver compared to M0 and M0 PS, and is more energy efficient than M4 and M4 PS, making it the optimal case out of the six explored.

5.3.3 Heating Scenario 3

For the third heating scenario, the same acoustic power and insonation duration for the M2 PS case in heating scenario 2 (30.88W, 2.90s) is applied to the other five simulation cases for comparison. The final 39.5°C therapeutic volume contours generated from the third heating scenario are shown by the red isosurfaces in Fig. 5.9, with ablated regions

Table 5.2 Insonation parameters and thermal contour volumes for heating scenario 2 ($P_{max} = 1.50$MPa, termination criteria: $T_{max} = 43 \pm 0.1$°C) and numerical extrapolation to accumulate a therapeutic target volume of 1cm^3. *Based on a 10.2mm diameter spherical target volume in the liver, centred at the geometrical focus of the transducer. †Numerical linear extrapolation to accumulate a target volume of 1cm^3 based on the insonation durations and therapeutic contour volumes produced from heating scenario 2. Extrapolation was not possible for the normal M2 and M4 cases due to no therapeutic contour volume occurring in the liver target.

	M0		M2		M4	
	Normal	Patient specific	Normal	Patient specific	Normal	Patient specific
Power [W]	3.96	12.97	27.91	30.88	32.21	51.23
t [s]	3.40	3.00	0.29	2.90	0.12	2.70
P_{max} [MPa]	1.50	1.50	1.50	1.50	1.50	1.50
Energy [J]	13.5	38.9	8.1	89.5	3.9	138.3
39.5°C Contour						
Vol. on target* [mm^3]	32	35	0	105	0	110
Vol. in bone [mm^3]	22	0	1	0	1	0
Total vol. [mm^3]	59	38	1	217	1	661
Numerical extrapolation†						
t [s]	107.9	85.7	-	27.7	-	24.6
Energy delivered [J]	427.6	1111.3	-	855.3	-	1261.9
Vol. in bone [cm^3]	0.7	0.0	-	0.0	-	0.0
Total therapeutic vol. [cm^3]	1.9	1.1	-	2.1	-	6.0

($CEM_{43} \geq 240$) shown by black isosurfaces. Figs. 5.9A, 5.9B and 5.9C are generated by the M0, M2 and M4 cases respectively, and Figs. 5.9D, 5.9E and 5.9F are generated by their patient-specific counterparts. For M0 (Fig. 5.9A), a large elongated thermal contour can be seen passing through the target volume in the liver, accompanied by significant heating in the rib, where black contours indicate the presence of tissue ablation in both the edge of the rib and at the focus. For M2 and M4 (Figs. 5.9B and 5.9C respectively), heat generation in the liver is also accompanied by significant rib heating, with M4 also showing a small region of ablation at the rib edge. The thermal contour coinciding with the target volume in the liver for the M2 case ($135mm^3$) is greater than that for the M4 case ($39mm^3$) due to the M4 acoustic field being more defocused. Comparing M0 PS with M0 (Figs. 5.9D and 5.9A respectively), the thermal contour is mostly situated in the liver target, and rib heating and tissue ablation are both avoided due to a reduction in focal gain caused by acoustic transmission loss through the lens. Similarly for M2 PS and M4 PS (Figs. 5.9E and 5.9F respectively), rib heating and tissue ablation are avoided in both cases, with M2 PS showing greater therapeutic contour volume overlap with the liver target compared to M4 PS due to M4 PS having a focus with lower acoustic gain and consequently lower peak pressure (P_{max} = 1.16MPa compared to 1.50MPa for M2 PS). The 43°C thermal contour volumes noted in Table 5.3 indicate the proportion of the thermal volume situated at a tolerable temperature for tissue, with the M2 PS and M4 PS cases generating no therapeutic temperatures greater than 43°C in the third heating scenario. The thermal contour volumes and insonation parameters for all simulations in the third heating scenario are summarised in Table 5.3.

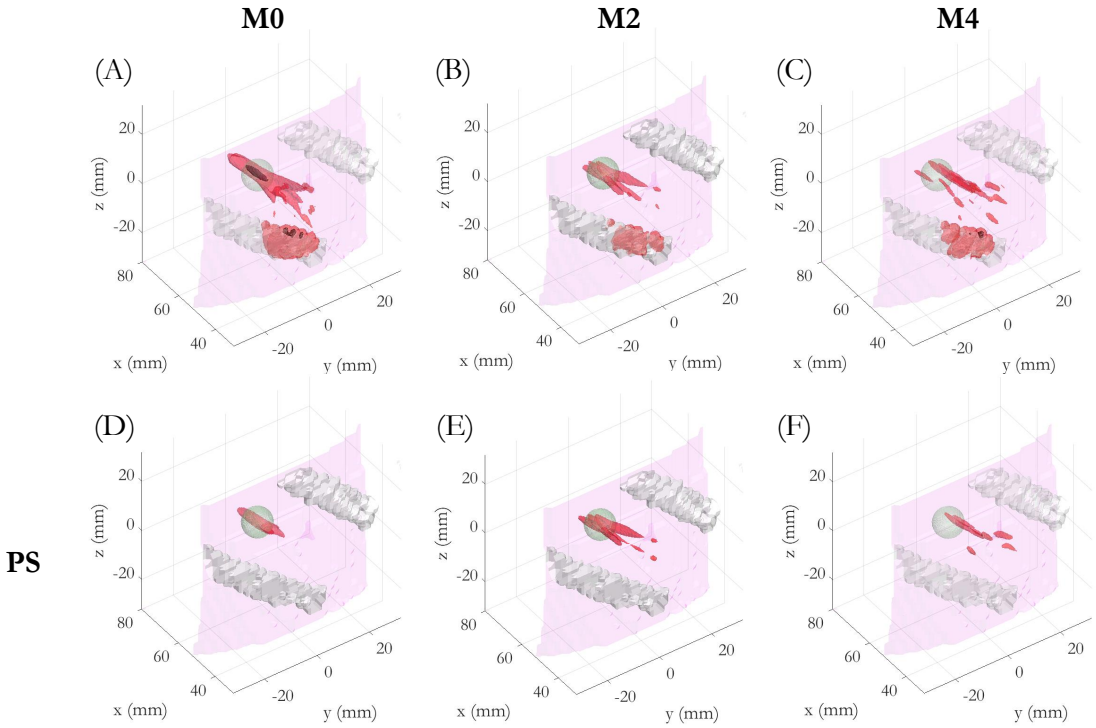


Fig. 5.9 Simulated 39.5°C thermal contours (red) from heating scenario 3 (fixed energy: 30.88W, t = 2.9s) where Figures (A), (B) and (C) are produced by the M0, M2 and M4 cases, and (D), (E) and (F) are produced by their patient-specific counterparts. Regions of thermal ablation ($CEM_{43} \geq 240$ minutes) are shown by the black contours, the large grey contours indicate the position of the ribs, and the green spherical target volume is shown at the geometrical focus of the transducer in the liver.

Table 5.3 Insonation parameters and thermal contour volumes for heating scenario 3 (Power = 30.88W, t = 2.9s). $^{\dagger}CEM_{43} \geq 240$ minutes. *Based on a 10.2mm diameter spherical target volume centred at the geometrical focus.

	M0		M2		M4	
	Normal	Patient specific	Normal	Patient specific	Normal	Patient specific
Power [W]	30.88	30.88	30.88	30.88	30.88	30.88
t [s]	2.90	2.90	2.90	2.90	2.90	2.90
P_{max} [MPa]	4.19	2.31	1.58	1.50	1.47	1.16
Energy [J]	89.6	89.6	89.6	89.6	89.6	89.6
T_{max} [°C]	79.1	50.9	57.2	43.0	73.9	40.8
39.5°C Contour						
Vol. on target* [mm^3]	175	105	135	105	39	11
Vol. in bone [mm^3]	475	0	310	0	362	0
Total vol. [mm^3]	1507	191	681	217	720	82
43°C Contour						
Vol. on target* [mm^3]	98	33	1	0	0	0
Vol. in bone [mm^3]	279	0	122	0	160	0
Total Vol. [mm^3]	535	36	134	0	199	0
Ablation Contour†						
Vol. on target* [mm^3]	24	0	0	0	0	0
Vol. in bone [mm^3]	12	0	0	0	7	0
Total vol. [mm^3]	39	0	0	0	8	0

5.3.4 Sensitivity to Translational or Rotational Misalignment

The simulations presented so far are dependent on maintaining the exact position of the transducer and lens relative to the CT dataset. In clinical practice, the extent to which this can be achieved is dependent on the ability to register the transducer with the patient, and if the position of the patient during ultrasound therapy does not exactly match the contour from their CT scan, the acoustic field and therefore predicted therapy results may differ significantly from simulations.

The sensitivity of the modified lens approach to translation and rotational errors is investigated through PZFlex simulations, focusing on the M2 PS case in particular. Simulations were compared for positional shifts in the CT dataset of ±1mm, ±3mm and ±5mm in the y-axis with the transducer source remaining centred at the origin, as well as rotational shifts of ±5°, ±10° and ±15° about the original location. Thermal simulations were performed with the insonation parameters described in heating scenario 3 for all cases (2.9s continuous-wave insonation at 30.88W).

The resulting 39.5°C thermal contours shown in Figs. 5.10A, 5.10B, and 5.10C indicate the 1mm, 3mm and 5mm offsets in the y-direction respectively, and Figs. 5.10D, 5.10E, and 5.10F indicate the -1mm, -3mm and -5mm offsets respectively. Comparing Figs. 5.10A, 5.10B and 5.10C, increasing positional shift results in reduced therapeutic volume coinciding with the target as expected. The shape of the thermal contour does not change significantly with positional offset, nor is there significant bone heating, which suggests that the acoustic field has not significantly clipped the next rib. Comparing Figs. 5.10D, 5.10E and 5.10F, the presence of the rib is immediately noticed by the appearance of a red thermal contour at the edge of the rib, and the volume of the thermal contour at the rib increases with increasing offset due to progressive overlap with the acoustic field.

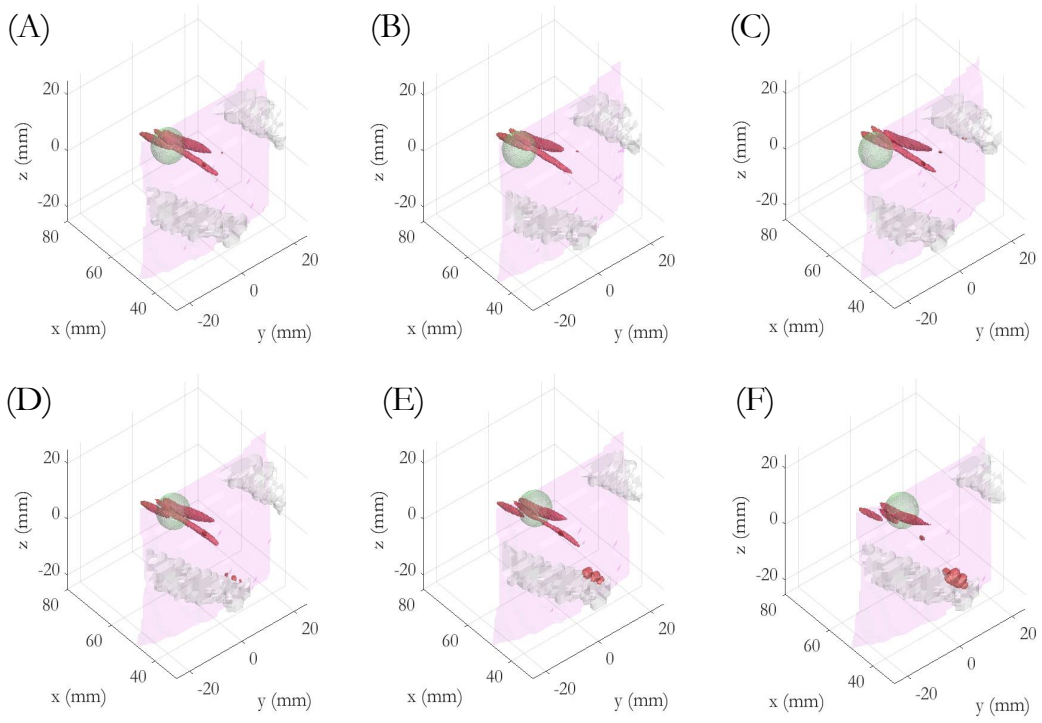


Fig. 5.10 Simulated 39.5°C thermal contours (red) for the M2 PS case in heating scenario 3 (fixed energy: 30.88W, t = 2.9s) where Figures (A), (B) and (C) are produced by a y-shift of 1mm, 3mm, and 5mm respectively, and (D), (E) and (F) are produced by a y-shift of -1mm, -3mm and -5mm respectively. The transducer source is centred at the origin, large grey contours indicate the position of the ribs, and the green spherical target volume is shown centred at the intended geometrical focus location of the transducer in the liver without the positional offset.

The thermal contour volumes from each positional offset simulation are reported in Table 5.4. Comparing the six positional offset cases with the original, a shift in CT alignment has shown to result in a decrease in total therapeutic volume between 19.4% to 26.3%. For positive y-shifts, rib clipping was not significant and the shape and total therapeutic volume generated did not change greatly (average total therapeutic volume of 172.3±2.3mm^3), however the therapeutic volume which remained on-target dropped significantly, where 1mm, 3mm and 5mm shifts resulted in on-target therapeutic volumes of 79%, 72% and 30% relative to the original case respectively. For the negative shift scenarios, overlap with the rib can immediately be seen from a -1mm shift by the appearance of the red thermal contour near the rib edge, and reduced on-target therapeutic volumes of 66%, 34% and 9% for shifts of -1mm, -3mm and -5mm respectively. For the -5mm case, simulations show that a small volume of 0.3mm^3 in the rib achieves ablation (see Table 5.4 for the summary of thermal contour volumes and insonation parameters).

Figure 5.11 shows the simulated 39.5°C temperature contours produced from varying rotational offset, where Figs. 5.11A, 5.11B, and 5.11C indicate the 5°, 10° and 15° rotational offsets respectively, and Figs. 5.11D, 5.11E, and 5.11F indicate the -5°, -10° and -15° rotational offsets respectively. For the 5°, 10° and 15° cases, no rib heating is observed which suggests that the previously defined source regions to be masked had exceeded the region clipped by the ribs. For the -5°, -10° and -15° cases, rib clipping is seem immediately from -5° and increases with rotational offset, which suggests that the masked region is much closer to the rib obstructed regions towards the negative rotational edge.

Looking at the corresponding therapeutic volumes reported in Table 5.5, the 5°, 10° and 15° offset cases yield on-target 39.5°C contour volumes of 80%, 84% and 87% relative to the on-target volume produced in the original case. The total 39.5° volume

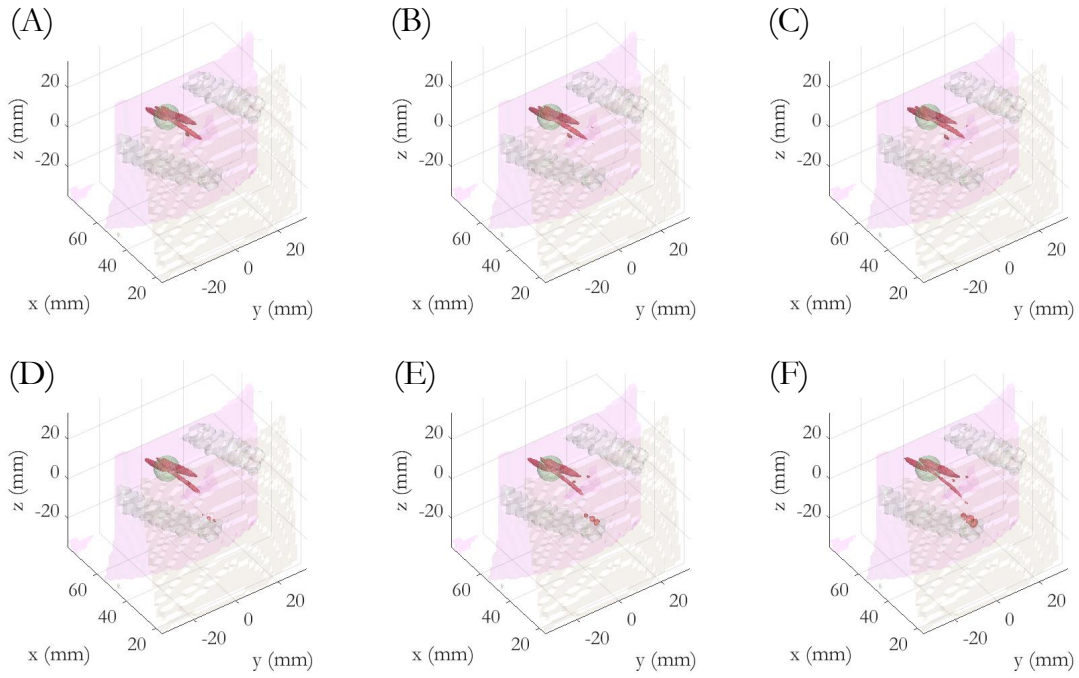


Fig. 5.11 Simulated 39.5°C thermal contours (red) for the M2 PS case in heating scenario 3 (fixed energy: 30.88W, t = 2.9s) where Figures (A), (B) and (C) are produced by a rotational offset of 5°, 10° and 15° respectively, and (D), (E) and (F) are produced by rotational offset of -5°, -10° and -15° respectively (positive counter-clockwise looking along the x-axis). The large grey contours indicate the position of the ribs, and the green spherical target volume is shown at the geometrical focus of the transducer in the liver.

Table 5.4 Thermal contour volumes and insonation parameters for the M2 PS case in heating scenario 3 with varying positional offset. †$CEM_{43} \geq 240$ minutes. *Based on a 10.2mm diameter spherical target volume centred at the original geometrical focus of the transducer.

Offset [mm]	-5	-3	-1	0	1	3	5
Tmax [°C]	60.5	51.5	42.6	43.0	42.5	42.5	42.2
39.5°C Contour							
Vol. on target* [mm^3]	9.1	35.7	69.8	105	82.8	75.6	31.2
Vol. in bone [mm^3]	47.8	18.8	2.6	0	0	0	0.2
Total vol. [mm^3]	169	160	164	217	171	175	171
43°C Contour							
Vol. on target* [mm^3]	0	0	0	0	0	0	0
Vol. in bone [mm^3]	13.1	3.6	0	0	0	0	0
Total vol. [mm^3]	18.3	5.4	0	0	0	0	0
Ablation Contour†							
Vol. on target* [mm^3]	0	0	0	0	0	0	0
Vol. in bone [mm^3]	0.3	0	0	0	0	0	0
Total vol. [mm^3]	0.3	0	0	0	0	0	0

for these three rotational offset cases is also reduced, with values of 82%, 85% and 86% respectively relative to the total 39.5° volume produced by the original case. Similarly for rotational offsets of -5°, -10° and -15°, the total 39.5°C therapeutic contour volumes relative to the original case were found to be 76%, 78%, and 84% respectively, and for the on-target volumes this was found to be 70%, 66% and 59% respectively.

5.4 Discussion

The simulations in a CT dataset have shown that the volume of mild hyperthermia generated in the liver by a single-element focused transducer can be increased without mechanical scanning by using an acoustic lens, however the increase in therapeutic volume is dependent on several major parameters such as local tissue perfusion rate, insonation time, acoustic power, and degree of defocusing.

Table 5.5 Thermal contour volumes and insonation parameters for the M2 PS case in heating scenario 3 with varying rotational offset. $^{\dagger}CEM_{43} \geq 240$ minutes. *Based on a 10.2mm diameter spherical target volume centred at the original geometrical focus of the transducer.

Rotational Offset [°]	-15	-10	-5	0	5	10	15
Tmax [°C]	51.3	46.1	43.0	43.0	42.6	42.7	42.7
39.5°C Contour							
Vol. on target* [mm^3]	61.8	69.2	73.9	105.0	84.1	88.6	91.7
Vol. in bone [mm^3]	27.1	11.7	2.4	0	0	0	0
Total vol. [mm^3]	181.8	169.6	164.5	217.0	178.0	185.1	187.6
43°C Contour							
Vol. on target* [mm^3]	0.1	0	0	0	0	0	0
Vol. in bone [mm^3]	3.3	0.5	0	0	0	0	0
Total vol. [mm^3]	4.3	0.6	0	0	0	0	0
Ablation Contour†							
Vol. on target* [mm^3]	0	0	0	0	0	0	0
Vol. in bone [mm^3]	0	0	0	0	0	0	0
Total vol. [mm^3]	0	0	0	0	0	0	0

Increasing the acoustic power enabled the rate of heat generation by ultrasound to overcome the fast rate of cooling due to high blood perfusion in the liver, and reducing the insonation time helps minimise the accumulation of pre-focal heating in the muscle and fat. Masking source regions of the transducer surface obstructed by the ribs reduced the amount of rib heating, and the incorporation of patient-specific modifications to the acoustic lens improves the retention of acoustic gain in the liver.

Thermal simulations suggest that the mode 2 acoustic lens achieves an acceptable balance between retaining focal gain while defocusing the acoustic field to increase the focal volume. The mode 4 lens was found to defocus the acoustic field too much, and the sacrifice in acoustic gain resulted in tendency towards pre-focal heating. The mode 4 lens generated the greatest therapeutic volume in the liver target when the acoustic power was increased and the insonation time was shortened, however a greater amount

of energy was required compared to the mode 2 case, and the excess therapeutic volume generated outside of the liver target was also notably larger.

Several major limitations to current work are that the simulations presented only take into account one specific acoustic window from a single patient model, and do not take into account patient deformation between scanning position and the patient position when lying down on the ultrasound therapy bed. Our simulations show that mechanical repositioning of the transducer relative to the predefined target location can significantly change the acoustic field since structures such as the ribs are highly reflective and absorbing. The simulations of rotational and positional offsets for the patient-specific lenses have verified that this method is indeed sensitive to geometrical alignment of the ribs, which places great emphasis on the reliance of accurate image registration and knowledge of transducer orientation relative to the patient throughout the procedure. Simulation of a positional offset of -1mm in the y-direction revealed a reduction in total predicted therapeutic volume of 25% compared to the original orientation, and similarly for a rotational offset of $-5°$, the total predicted therapeutic volume fell by 30%.

In this study, the method used to account for rib sparing is to mask the obstructed source locations in the acoustic simulation. To achieve this in physical practice, one implementation could be the introduction of a material which exhibits high acoustic absorption [222]. Placement of sound absorbing structures fixed relative to the geometry of the patient would enable greater flexibility than placement on the transducer surface, since this would enable the transducer to be repositioned without constantly readjusting the location of the acoustic absorbers. However issues to consider would be possible distortion of the acoustic field due to the physical presence of the acoustic absorbers, as well as possible heat generation within the absorbing material which could conduct to the patient. Suggestions to minimise the risk of heating would be the use of active

water cooling, and to maintain a small water gap between the acoustic absorber and the patient to enable convection.

Each virtual point source simulation required up to 150GB RAM and between 6 and 8 hours to process, and the time required to manufacture a single acoustic lens was approximately 10 hours. Based on these values, the estimated time required to produce a patient-specific acoustic lens upon receiving an already segmented CT dataset would be approximately 1 day per simulated acoustic window and lens. Existing simulation results could be improved by performing simulations with a finer mesh (currently limited by physical RAM). The spatial resolution of the segmented CT dataset presented is typical of routine clinical scans, further work would be required to determine whether the accuracy of simulations can be significantly improved by using tissue maps with higher spatial resolution. Furthermore, the use of a virtual acoustic source with an ellipsoidal or more complex shape which represents the intended focal volume may produce a better effect in comparison to simply using a spherical point source, since the unique propagation paths from multiple source locations will also contribute to the subsequent pressure amplitude and phase distributions recorded at the source locations.

The H102 therapeutic transducer is simulated here as initial proof of concept since the full 3D model can be processed in one sitting on a 192GB RAM workstation. From a therapy point of view, a larger transducer with higher focal gain would be more a promising option since the pre-focal acoustic pressure can me minimised, and the increase in acoustic gain may enable the use of higher operational mode lenses which further distribute the focal pressure to generate greater therapeutic volumes and may shorten therapy times.

5.5 Conclusion

Advances in computing power have shown that desktop computers, as used in this study, are able to simulate ultrasound in the body. Simulations have shown that it is possible to produce semi-focused pressure distributions in the liver using a sectored acoustic lens, and the incorporation of patient-specific phase correction into the lens enables the problem of tissue inhomogeneity to be addressed. Thermal simulations have also shown that rib heating can be minimised by maintaining a high acoustic gain (minimising pre-focal pressure amplitudes), operating at a higher acoustic power for a relatively short insonation time, and entirely prevented by masking acoustic source locations with propagation paths which coincide with bone.

The use of 3D printing technology is presented as a feasible low-cost implementation method for single-element transducers to produce larger therapeutic volumes without the use of mechanical scanning, however the introduction of an acoustic lens comes with the cost of some transmission loss, as well as a reduction in focal gain depending on the magnitude of defocusing. The effect of this on the generation of hyperthermia in the liver was explored in three heating scenarios, with the mode 2 acoustic lens reaching an acceptable compromise between retention of focal gain and defocusing of the acoustic field to increase the focal volume.

The challenges faced by high-intensity focused ultrasound as a therapy are no longer due to computational or technological limitations, rather the physical and logistical challenges of implementing this technology in clinical practice, such as tissue deformation and accurate thermal monitoring during the procedure.

6 Application to the JC200 Clinical Device

6.1 Introduction

The investigation of 3D printed acoustic lenses so far have been based on the H102 therapeutic transducer, and the simulations presented in Chapter 5 suggest that the application of a sectored phase-conjugate acoustic lens on the H102 transducer is able to defocus the acoustic field and increase focal volume generated within the liver. However, excessive defocusing as shown by the mode 4 lens, failed to provide sufficient localisation to the target site and resulted in significant pre-focal heating. Clinical single-element extracorporeal transducers typically exhibit a larger aperture and acoustic gain than the H102. Therefore, it would be of clinical interest to upscale the current methods to model larger transducers for further investigation.

The transducer of interest for the work presented in this chapter is the JC200 (Chongqing Haifu Medical Technology Co., China) as previously shown in Figure 2.1B. The JC200 is originally designed for tumour ablation, and comprises of a diagnostic ultrasound probe in the centre, surrounded by a single-element spherically focused therapeutic transducer which has an outer diameter of 200mm, inner diameter of 80mm, centre frequency of 0.96MHz, geometrical focus of 164mm, and a simulated acoustic gain in water of approximately 103 based on the Fresnel approximation.

This chapter explores the translation of the work shown in Chapters 4 and 5 to the JC200, beginning with the design and production of 3D printed lenses, experimental verification of the lenses through measurement of ultrasound-mediated heat generation

in an agar-silica tissue-mimicking phantom, followed by the task of scaling up acoustic and thermal PZFlex simulations to model the generation of mild hyperthermia in a segmented CT liver target.

6.2 3D Printed Acoustic Lenses for the JC200 Clinical Transducer

6.2.1 Acoustic Lens Design

The 3D printed acoustic lenses shown in Chapter 4 for the H102 transducer were manufactured in-house using a Formlabs Form 2 printer, which has a maximum printing voume of 145×145×175mm. In order to produce a single piece lens for the JC200 transducer, a 3D printer with a larger build volume (Objet Eden 500V, Stratasys Ltd.) was outsourced (3D Creation Lab, Worcestershire, UK), and acoustic lenses were printed using a translucent ultraviolet light-cured resin (VeroClear, Stratasys Ltd.). VeroClear was chosen since a previous study had characterised the speed of sound in the material to be 2424m.s^{-1} with an attenuation of 5.5dB.cm^{-1} at 2MHz [182], which is assumed to be 2.64dB.cm^{-1} at 0.96MHz using linear extrapolation. The remaining acoustic and thermal properties for VeroClear are listed in Table 2.3, where the density is obtained from the manufacture datasheet [228], and thermal properties were based on average values for acrylic [177].

Three acoustic lens designs were produced in total, the first being a four-sector mode 2 lens (M2) and the second an eight-sector mode 4 lens (M4) as described in Chapter 4. The thickness required to generate an alternating phase difference of π radians with uniform surface amplitude across all sectors was calculated to be 2.03mm using Equation 4.5, with a uniform base thickness of 1.58mm. The third lens (T60) was

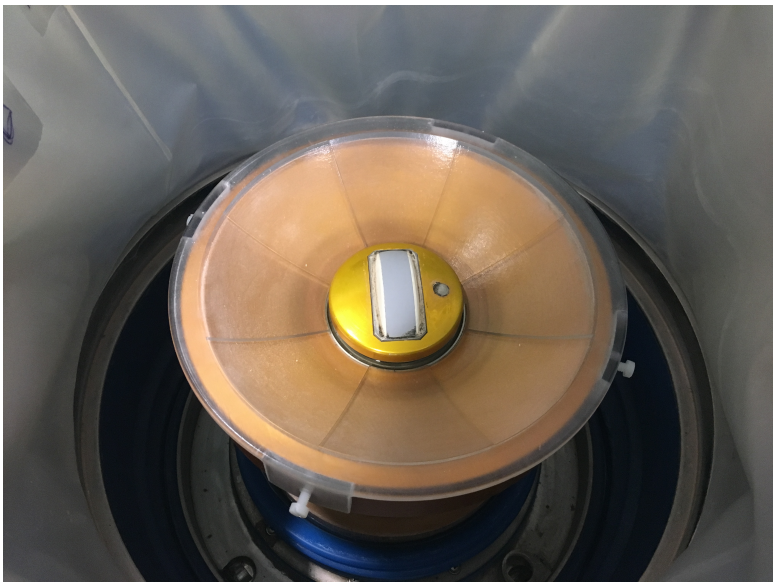


Fig. 6.1 Image of a 3D printed eight-sector mode 4 acoustic lens mounted onto the JC200 clinical transducer.

designed with a constant thickness of 12.01mm in order to provide a uniform acoustic transmission coefficient of 0.60 without significantly altering the shape or location of the focal field. All lenses were designed in AutoCAD 2016, and an image of the mode 4 printed lens mounted onto the JC200 is shown in Figure 6.1.

The purpose of the third lens was to reduce the acoustic pressure at the focus to minimise the likelihood of generating acoustic cavitation, which could potentially damage the FOH, as well as result in unwanted cavitation-enhanced heating artefacts during thermal monitoring within tissue-mimicking phantoms. This was a necessary precaution since the minimum power setting of the JC200 system is fixed at 32W, which from linear Fresnel approximation simulations in water result in a peak negative focal pressure of approximately 6.2MPa. Recall from Chapter 2 section 2.3.2 that the nonlinearity of the acoustic field at the focus can be roughly determined by the length of the shock formation distance $\bar{x}$ as defined in Equation 2.20. For a peak focal pressure of 6.2MPa and using the acoustic properties for water as listed in Table 2.3, $\bar{x}$ is estimated to be 26.7mm, while the peak focal pressure with a 60% transmission

lens is estimated to be 3.7MPa, yielding a shock formation distance of 44.7mm. The longer shock formation distance of 44.7mm is sufficiently far away from the focus to enable the assumption that waves will exhibit predominantly linear behaviour and can be compared to linear simulations.

To verify the performance of the lenses on the JC200, the acoustic field at the focus was measured using a 0.2mm diameter needle hydrophone (HNC-0200, Onda Corporation) and recorded using a digital oscilloscope (Wavesurfer, LeCroy). The hydrophone was attached to a portable two-axis positioning system which comprised of two linear actuators (850G, Newport Corporation), which were secured onto the metal railing of the JC200 bed for a stable reference point as shown in Figure 6.2. The linear actuators were controlled through a MATLAB laptop interface, and configured perpendicular to each other on a metal sliding plate (M-Series, Newport Corporation) to provide two degrees of movement. The accuracy of the transducer positioning system is to the nearest millimetre, therefore the existing 3D mechanical positioning system of the JC200 was used to initially move the focus of the transducer into the central working range of the actuators (6cm), and fine positioning was performed thereafter using the two linear actuators which have a nominal accuracy to the nearest 0.1% of travel and an error of <1 micron. The calibration uncertainty of the acoustic hydrophone is documented as ±1.5dB at 1MHz.

Previously with the H102 transducer, acoustic field measurements were obtained by exciting the transducer with repeated tone bursts from a function generator with the sync connected to the oscilloscope to enable accurate data acquisition windowing. However, the JC200 clinical device is a closed system with no electrical access to easily acquire a reference signal to trigger data acquisition. In order to overcome this, a second hydrophone was fixed to a position in the nearfield of the transducer in order to record the source waveform for manual triggering as shown in Figure 6.2.

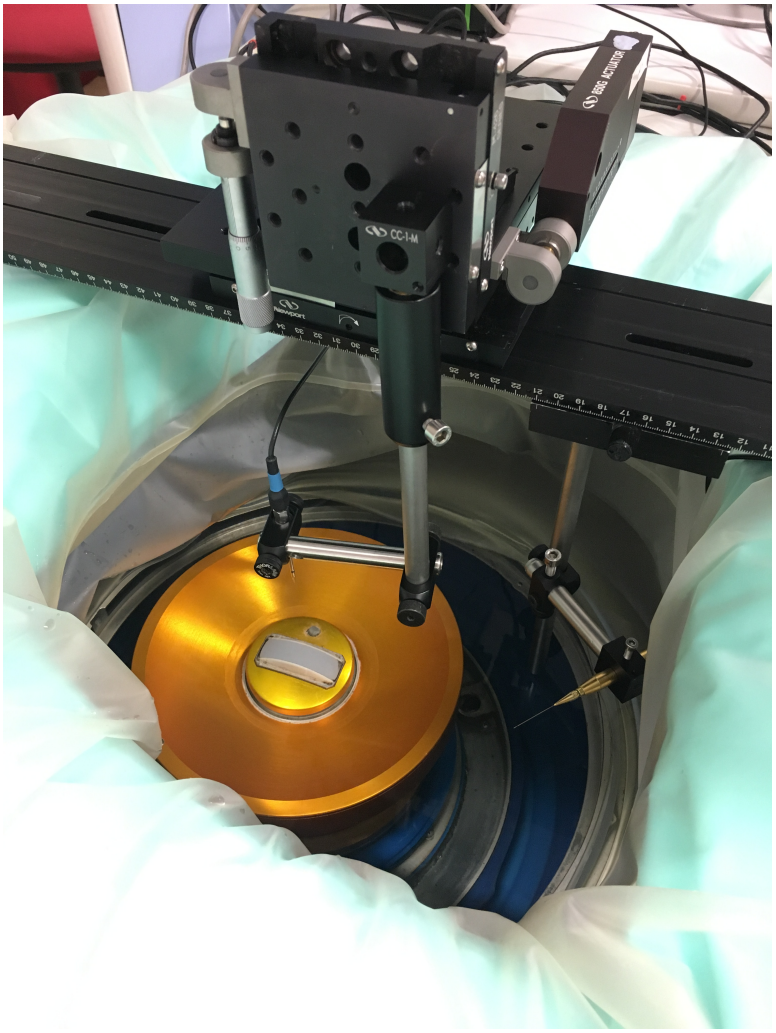


Fig. 6.2 Image of the 2D positioning system setup on the JC200 device with acoustic hydrophone placement prior to water filling. An acoustic absorber (not shown) was secured behind the vertically oriented hydrophone in order to minimise the acoustic reflections from the air-water interface.

Since the JC200 is estimated to produce a peak pressure of 3.7MPa with the T60 lens when operating at the minimum acoustic power of 32W, the transducer excitation was limited to three pulse trains (1s on, 1s off) with a duty cycle of 25% and a pulse repetition frequency (PRF) of 10Hz in order to minimise the risk of causing cavitation damage to the hydrophone, and reduce the likelihood of heat build-up within the acoustic lens. Pulse trains of one second in duration enabled enough time to perform manually triggered data acquisition, where the signal from the hydrophone next to the source was then used to identify the timing of the HIFU source excitation. A window length of 200ms was chosen in order to ensure that the acoustic wave was given enough time to propagate to the far-field hydrophone located near the focus, and a sampling rate of 2.5GHz was employed in order to capture the burst waveform with sufficient accuracy.

Typical source waveforms recorded by the pre-focal hydrophone are shown in Figures 6.3A and 6.3B, where short duration high amplitude spikes in pressure can be seen in both example recordings. These short spikes (which are of the same order in amplitude as the source waveform) made electrical triggering impractical, therefore manual triggering with a long sampling window was necessary. The source of these spikes are suspected to be caused by electrical or acoustical interference from the central imaging transducer, or from the system. In addition, both traces show a burst length of 32ms rather than the requested length of 25ms, which could be due to additional ringing of the transducer, or inaccuracies in the HIFU system.

To find the location of the focus, the far-field hydrophone was approximately aligned to the focal depth of the JC200 and centred visually by using the central b-mode imaging probe. For fine tuning, manually triggered signal acquisition was performed for several field positions, and the raw peak hydrophone signal from each waveform was compared until the position of the focus was determined to the nearest 0.2mm in

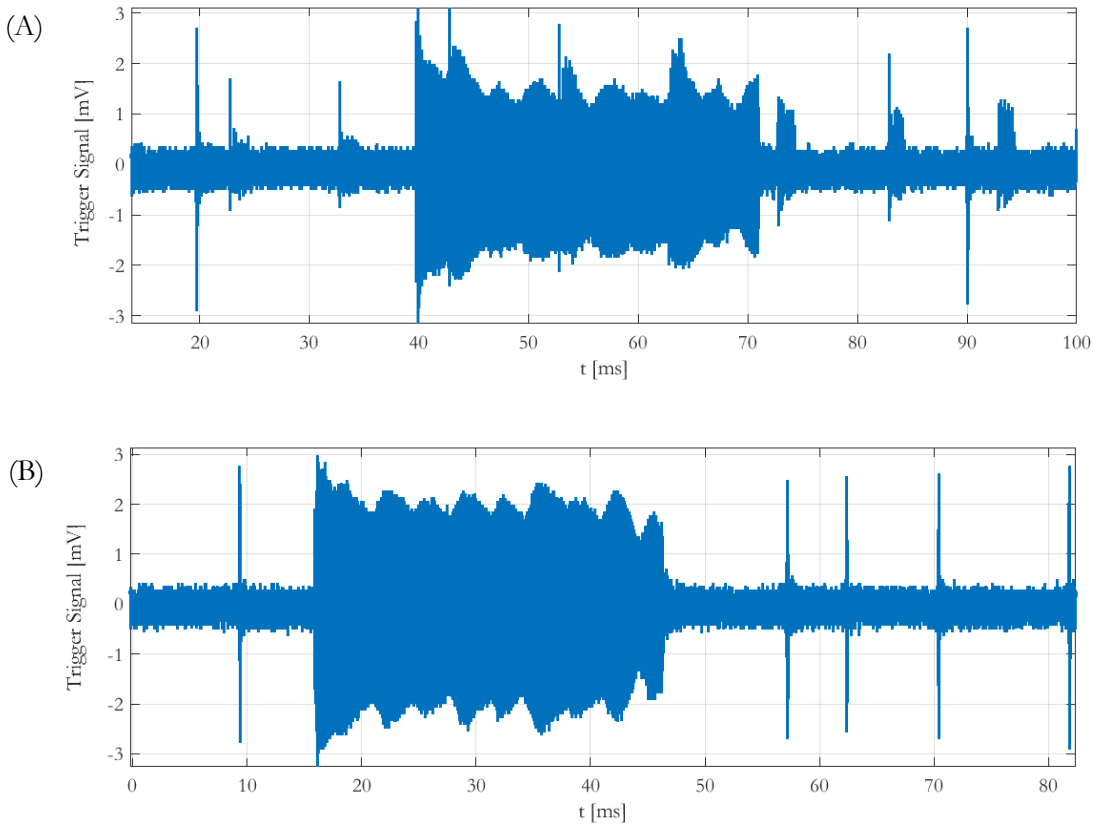


Fig. 6.3 Two typical source waveforms recorded by an acoustic hydrophone situated in the nearfield of the JC200 transducer with the T60 lens while operating at 32W, 25% duty cycle, and 10Hz pulse repetition frequency. A pulse length of 32ms rather than the requested length of 25ms can be seen, and very short duration high amplitude spikes are present in both traces, which are suspected to be due to acoustical or electrical interference from the central imaging transducer. A total window length of 200ms was used in order to ensure that each burst was given adequate time to reach the far-field hydrophone, and a sampling frequency of 2.5GHz was employed.

both x and y directions, and to the nearest 1mm in the z axial direction. Two radial line scans in the y-axis were obtained for each of the three lenses, beginning from -1mm to 5mm in increments of 0.2mm, with the centre of the focus assumed to be at the origin in x and y. Pressure amplitude values were extracted from each recorded burst by converting the RMS value from the central 16ms of the 32ms burst waveform, and a comparison between the simulated and measured radial pressure profiles for the three lenses are shown in Figures 6.4A, 6.4B and 6.4C, with the first being the T60 lens, followed by the M2 lens, and the M4 lens. Simulated radial pressure profiles were produced by the Fresnel approximation, where uniform surface amplitude scaling was applied in order to take into account the calculated transmission coefficient of each lens obtained through Equation 4.4.

Beginning with the 60% transmission lens (Figure 6.4A), the shape of the experimentally acquired scans differ significantly from the Fresnel simulation, where the shape of the focus appears skewed to the right, with no presence of the first sidelobe. The peak simulated pressure was calculated to be 3.7MPa located at $r = 0$mm, while the peak pressures measured in scans 1 and 2 were 1.95±0.37MPa located at $r = 0.2$mm, and 2.93±0.55MPa located at $r = 0.4$mm. The predicted peak pressure is underestimated in scans 1 and 2 by 1.75MPa and 0.77MPa, and the location of the peaks were offset by 0.2mm and 0.4mm which is within the uncertainty of the initial scan position.

Similarly, the shape of the recorded scans for the mode 2 lens (Figure 6.4B) do not agree well with the Fresnel simulation. The peak simulated pressure was calculated to be 2.78MPa located at $r = 1.6$mm, and the measured peak pressures for scans 1 and 2 were 1.81±0.34MPa located at $r = 1.8$mm, and 1.75±0.33MPa located at $r = 1.8$mm. The amplitude of the simulated radial peak pressure is underestimated by 1.0MPa, and a peak pressure of 0.8MPa was measured at $r = 0$mm, which is supposed to be the location of the central pressure null as indicated by the Fresnel simulation.

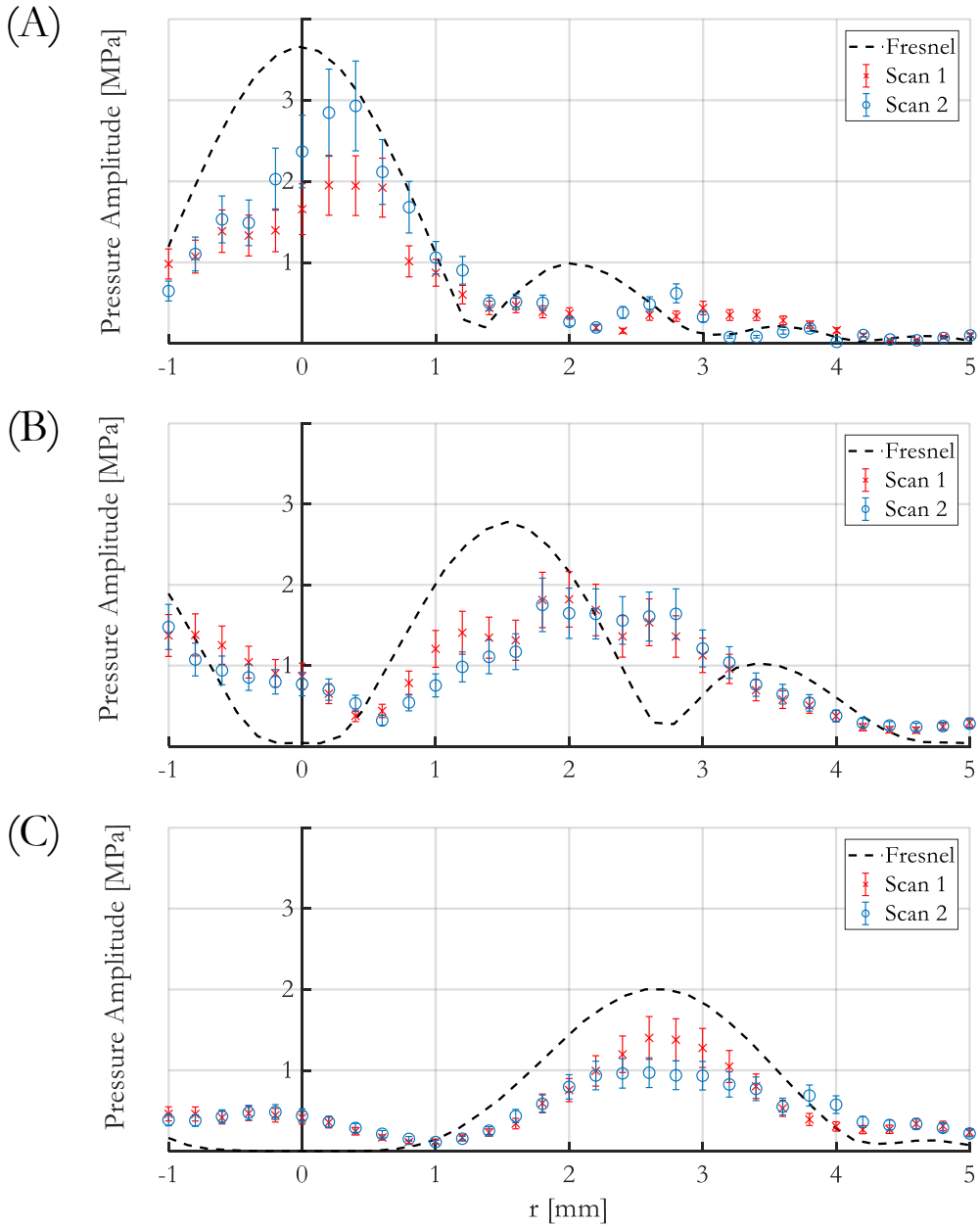


Fig. 6.4 Free-field radial line pressure measurements in the focal plane of the JC200 system operating at 32W, 25% duty cycle and 10Hz PRF with the T60 (60% transmission) lens (A), the M2 (four-sector mode 2) lens (B), and the M4 (eight-sector mode 4) lens (C). Simulated radial pressure profiles shown by the dashed black lines were obtained from the Fresnel approximation where the centre of the geometrical focus is located at $r = 0$mm, and the red and blue data points show the two radial scans where error bars indicate the ± 1.5dB uncertainty of the hydrophone.

Finally, the mode 4 lens scans shown in Figure 6.4C show agreement between the location of the simulated and measured radial peak, where the simulated peak pressure of 2.0MPa is located at $r = 2.7$mm, with measured peak values of 1.4±0.26MPa located at $r = 2.6$mm, and 0.97±0.18MPa located at $r = 2.6$mm. The experimentally measured peak pressure falls short of the simulated amplitude by up to 1.0MPa, and a pressure of 0.4MPa is observed at $r = 0$mm which is expected to be the location of a pressure null according to the Fresnel simulation.

Possible reasons for the consistent underestimation in measured peak pressure for all three lenses could firstly be due to an error in the original alignment of the hydrophone relative to the focus of the transducer. A translational error of the hydrophone would lead to consistent misalignment of the acoustic field for all three lens scans since the same hydrophone reference point was used in subsequent measurements. Secondly, a consistent underestimation in the peak pressure of $1.0-1.75$MPa for all three cases could be due to an underestimation of the pressure transmission coefficient of the lenses. The acoustic properties of the lens material (VeroClear, Stratasys Ltd.) were obtained from a previously reported value in literature [182], and the attenuation coefficient (specified at 2MHz) was linearly extrapolated to 0.97MHz, which is the centre frequency of the JC200 transducer.

Furthermore, the difference in measured peak pressure amplitude for the T60 lens is approximately 1MPa, which suggests that the source itself displays high variability. Variation in the source amplitude is also seen in the two example source waveforms recorded by the prefocal hydrophone shown in Figure 6.3, where the source waveform in Figure 6.3A indicates an initial burst amplitude of ±3MPa, which subsequently reduces to below ±2MPa with fluctuations of $\pm 0.5 - 1$MPa. Using the same acoustic settings, a subsequently recorded source waveform is shown in Figure 6.3B, which begins with an initial burst amplitude of ±3MPa, and subsequently oscillates between

±2.5MPa and ±1.8MPa. The peak pressure values presented in the scans shown in Figure 6.4 were obtained by converting the RMS signal from the central 16ms of a single 32ms recorded burst signal captured by the far-field hydrophone, and therefore would also be subject to the variations observed in the source waveforms.

Despite these discrepancies, the overall observed shift in peak focal pressure away from the central axis increased with increasing operational mode, and a reduction in the observed amplitude of the radial peak pressure suggests that the M2 and M4 lenses have successfully achieved radial spreading of the focal field. Cavitation damage to the hydrophone was avoided during the measurements of the JC200 with the T60 lens, which suggests that the lens had successfully attenuated the focal pressure of the transducer to a safe magnitude for acoustic field characterisation.

6.2.2 Generation of Mild Hyperthermia in an Agar Phantom

The thermal fields produced by a lensed JC200 were investigated by heating an agar-silica phantom and measuring the temperature at several radial positions in the focal plane. The phantom described in Chapter 4 (2%w/v agar fine powder, 3%w/v silica microspheres) was cast in a clear perspex phantom holder with internal dimensions of $100 \times 100 \times 100$mm, and a 1mm diameter hole through the centre of one of the surfaces enabled the insertion of a coaxial needle housing a 0.15mm diameter fibre-optic hydrophone (FOH). The needle and hydrophone were inserted into the centre of the phantom at a depth of 60mm in the axial direction of the transducer. Once the insertion of the coaxial needle achieved the correct depth, the needle was retracted (taking care not to disturb the position of the FOH relative to the phantom) in order to expose the FOH tip.

An illustration of the setup for the following phantom heating experiments is shown in Figure 6.5, and an image of the physical experimental setup is shown in Figure

6.6. As shown in the schematic diagram, the phantom is placed directly above the JC200 source with the top and bottom faces of the phantom holder removed to expose the phantom to the degassed water and provide an acoustic window. White acrylic stoppers (shown in Fig. 6.6) were attached in order to secure the phantom in place, and an acoustic absorber was placed above the phantom in order to minimise reflections from the top surface. The phantom mould was attached to a 3-axis positioning stage comprising of two manually adjustable micromanipulators and two linear actuators. Finally, the 3-axis positioning system was secured to the railing of the JC200 system to ensure a stable fixed reference position relative to the transducer.

In order to obtain measurements in the focal plane at several radial positions from the centre, the entire phantom was manually repositioned until the focus of the transducer was confirmed to the nearest 0.2mm through observation of the maximum temperature rise produced by a short three-second insonation. Thermal alignment was chosen over comparison of the pressure amplitude due to the large variation seen in the radial pressure scans shown in Figure 6.4. Radial measurement positions of 0mm, 1.6mm, and 2.8mm were chosen since these were the locations at which the radial peaks occur from free-field simulations of the three acoustic lenses. The phantom was translated using the linear actuators in order to move the FOH to each radial location, and for each position, insonations were repeated three times with a cooling time interval of at least two minutes to enable the phantom to cool to a relatively steady-state temperature ($dT/dt \leq 0.25°\text{C.min}^{-1}$).

6.2.3 Spot Heating Results

Figure 6.7 shows the simulated (solid lines) and measured (shaded regions) temperature profiles generated by a ten-second insonation with the JC200 operating at an acoustic power of 32W (system minimum), 25% duty cycle, and 10Hz PRF with the T60 lens

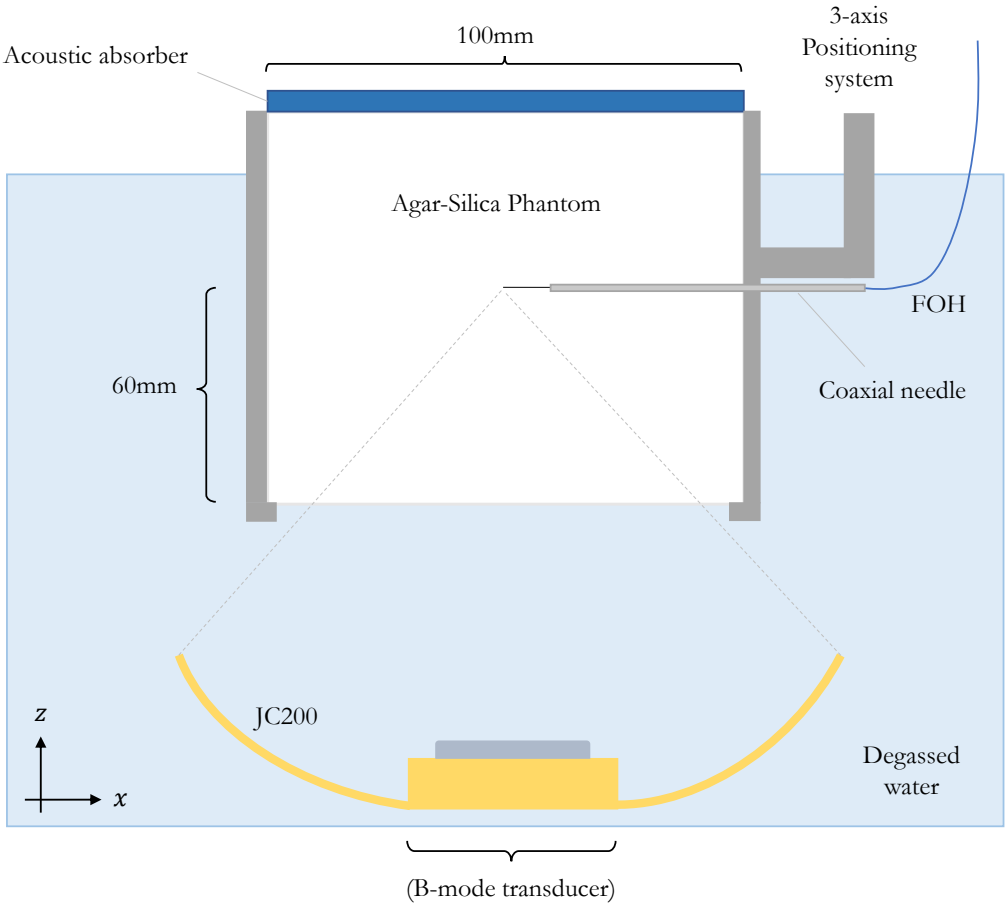


Fig. 6.5 Schematic cross-sectional view of the JC200 agar-heating experiment setup. The transducer (yellow) is focused onto the tip of a FOH embedded at a depth of 60mm into the phantom. The top and bottom faces of the phantom holder were removed to create an acoustic window, and an acoustic absorber (blue) was placed on the top surface in order to minimise acoustic reflections. The phantom holder was connected to a 3-axis positioning system comprising of two computer-controlled linear actuators and two micromanipulators, and the central B-mode imaging transducer was used to locate and align the FOH.

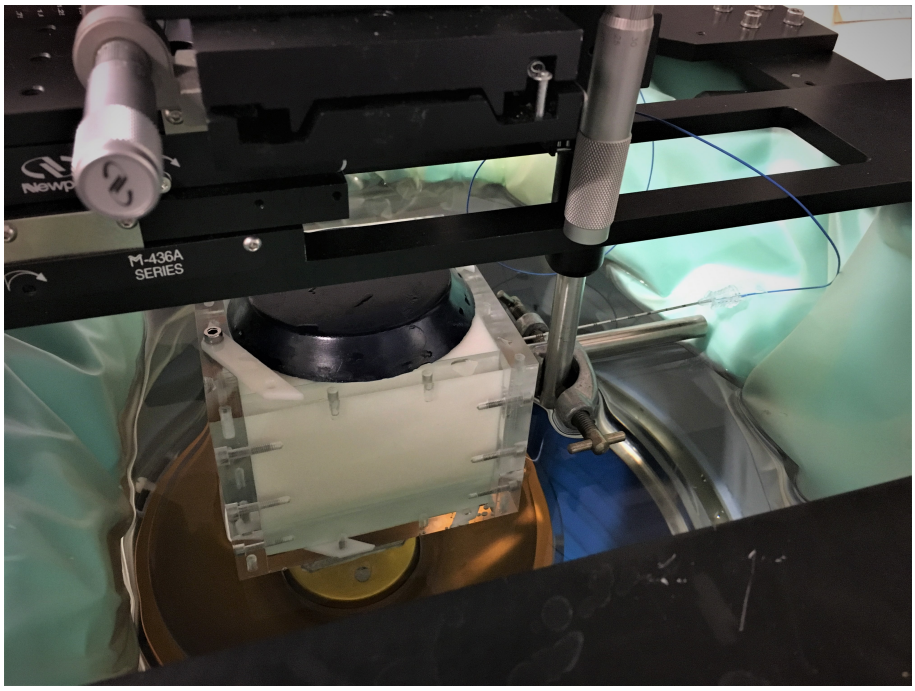


Fig. 6.6 Setup of the phantom placement above the JC200 system. The phantom is connected to a linear positioning system comprising of two manually adjustable axes via micromanipulators, and one computer-controlled axis through the use of two linear actuators. A blue sound absorber was placed on the top phantom surface in order to minimise reflections from the air-phantom interface.

(6.7A), the M2 lens (6.7B), and the M4 lens (6.7C). Shaded regions indicate the range depicted by one standard deviation of the measured temperature curves at each radial location ($n = 3$), and the small step-changes in the measured range are due to the unavoidable automated channel switching of the FOH system which is used to select the recording channel with highest sensitivity. Simulations were performed by the Fresnel approximation with surface amplitude scaling to account for the acoustic transmission coefficient of each acoustic lens. The acoustic power for thermal simulations were adjusted to take into account the extended burst duration of 32ms as observed by the pre-focal hydrophone signals shown in Figure 6.3, and the thermal properties of the phantom were assumed to be equal to water.

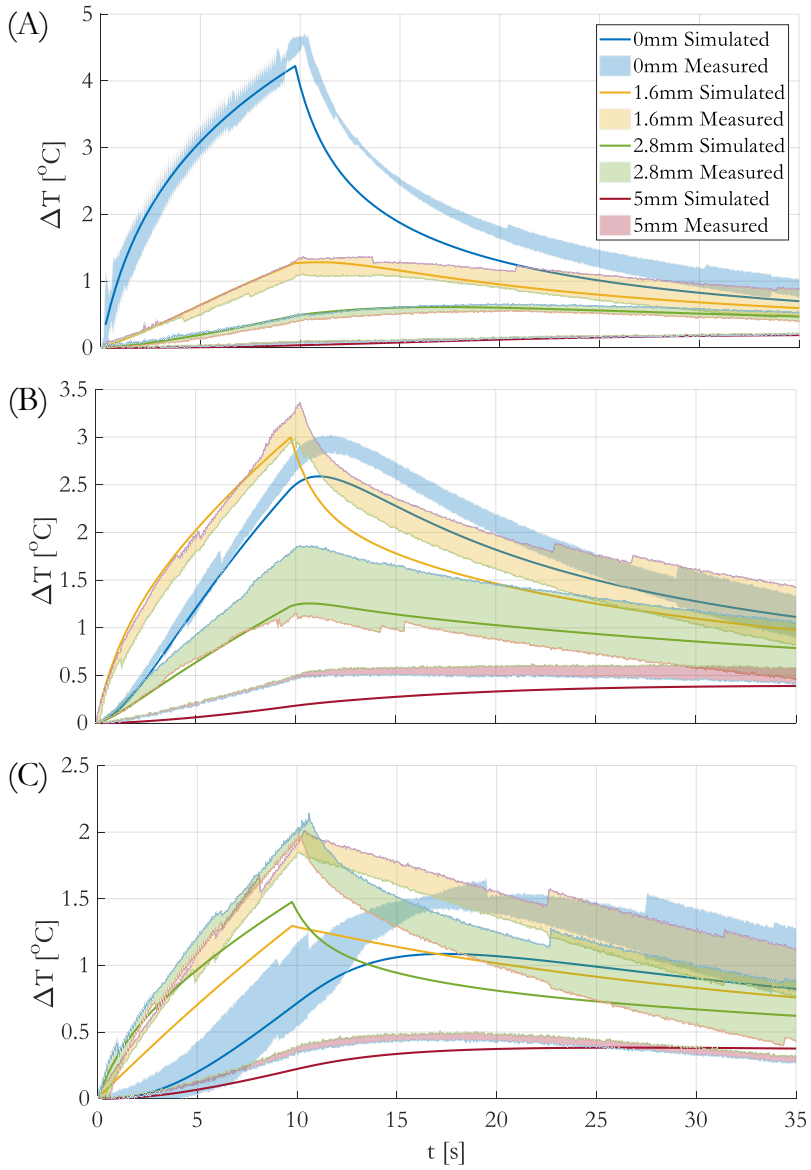


Fig. 6.7 Measured and simulated temperature curves in an agar-silica phantom produced by a 10-second insonation from the JC200 operating at 32W, 25% duty cycle, and 10Hz PRF with the T60 lens (A), M2 lens (B), and the M4 lens (C). Simulated temperature curves (solid lines) were generated by the Fresnel approximation at 32% duty cycle to take into account the 32ms recorded burst lengths shown in Figure 6.3. The FOH was positioned in the focal plane at radial offsets of 0mm (blue), 1.6mm (yellow), 2.8mm (green), and 5mm (red), where shaded regions indicate the standard deviation of the measured temperature rise ($n = 3$). Small jumps seen in the FOH recordings are due to unavoidable automated channel switching of the FOH system.

For the T60 lens (6.7A), the maximum temperature rise is observed on the central axis (blue) with a value of 4.5°C, with progressively lower peak temperature rises of 1.2°C, 0.6°C and 0.2°C observed at radial locations 1.6mm, 2.8mm and 5mm away from the centre (yellow, green and red curves) respectively. There is very good agreement with the simulated temperature rises, with peak values of 4.22°C, 1.3°C, 0.6°C and 0.2°C respectively. For the M2 lens (Figure 6.7B), a peak average temperature rise of 3.2°C is measured at 1.6mm away from the centre (yellow traces) as expected, with the central (blue) curve showing a similar peak average temperature rise of 2.9°C at a delayed point in time due to thermal conduction from the surrounding radial peaks. The maximum average temperature rises measured at 2.8mm and 5mm were 1.5°C and 0.5°C respectively, and the shape and amplitude of the simulated curves show good agreement, with values of 2.6°C, 3.0°C, 1.5°C, and 0.4°C at $r = 0$mm, 1.6mm, 2.8mm and 5mm respectively. Finally for the M4 lens (Figure 6.7C), the maximum temperature rise is measured at a radial observation position of 2.8mm (green) which agrees with the location of the radial peak from simulations and is reflected by the sharp rise and fall in the temperature curve. The M4 lens produced the broadest acoustic field, which is verified by comparable temperature rises of 1.5°C, 1.9°C, 2.0°C and 0.45°C measured at $r = 0$mm, 1.6mm, 2.8mm and 5mm, with simulated peak temperature rises of 1.1°C, 1.3°C, 1.5°C and 0.4°C respectively.

There is very good agreement between the shape of the simulated and measured average temperature curves for all three lenses, with simulations agreeing with measurements to within 0.82°C, 0.45°C, and 0.64°C for the T60, M2 and M4 lenses respectively. Since the shape of the simulated and measured curves match, this suggests that in general, good alignment was achieved between the FOH observation locations relative to the radial peak in the acoustic field. Simulated temperature curves tended to be under-

estimations rather than overestimations for all cases except for the radial measurements in the T60 lens, where only the central location showed an underestimation.

Possible causes for the higher measured values could be due to a small viscous heating artefact caused by the presence of the FOH thermocouple [209], an underestimation of the acoustic transmission coefficient of the lens, or variation in the thermal properties of the phantom. Temperature curves which showed cavitation enhanced heating artefacts in the T60 lens case were observed occasionally (and omitted), however since the FOH is only located at one position, peripheral acoustic cavitation activity may not be detectable and can also result in an increase in the measured temperature rise through thermal conduction.

6.2.4 Repeated Line Scan Results

The measured thermal profile for the M4 lens in Figure 6.7C showed a relatively uniform heating profile produced up to 2.8mm away from the centre, however even this is still not broad enough to encompass a typical clinical mild-hyperthermia treatment volume which can span several centimetres in width. To investigate the effect of the acoustic lenses on the thermal volume produced by mechanical scanning, a programmed repeated line scan spanning a width of 20mm in the x lateral direction was explored. A scan path beginning at the location $x = -10$mm and finishing at $x = 10$mm was defined using the JC200 clinical software, where $x = 0$mm is the centre of the phantom at a propagation depth of 60mm. In order to produce a therapeutic temperature rise of up to 6°C, the JC200 was operated at 32W, 50% duty cycle, 10Hz PRF, and programmed to repeatedly scan along the 20mm path using a movement speed of 3mm.s^{-1} with a three-second pause in between each completed round trip at the position $x = -10$mm. Line scan exposures were repeated three times for each lens in order to record the temperature with the FOH at three scan path locations ($x = 0$mm,

5mm and 10mm). Coupled acoustic-thermal simulations were performed using the Fresnel approximation for the acoustic field, and the ADI method for the thermal simulation. To approximate mechanical scanning at a speed of 3mm.s^{-1}, the acoustic heat source was translated between each simulated time step in the thermal simulation by 0.75mm, where $\Delta t = 0.25$s. A comparison between the simulated and measured temperature curves for the repeated line scan performed by the JC200 with each of the three acoustic lenses are shown in Figure 6.8, where the 60% transmission lens is shown in 6.8A, the mode 2 lens is shown in 6.8B, and the mode 4 lens is shown in 6.8C.

Beginning with the T60 lens shown in Figure 6.8A, the sharp peaks seen in the simulated (yellow) curves which reflect the location of the focus relative to the observed location are not apparent in the measured curves (blue), which suggests that there is probable misalignment between the position of the FOH relative to the scan path. In both measured and simulated cases, the temperature rises at $x = 0$mm and $x = 5$mm are higher than at $x = 10$mm which is expected since the focus will pass through these observation points twice for each line scan, while only passing through the distal end once. The simulated and measured peak temperature rises agreed to within 1°C, where the peak temperature rises measured at $x = 0$mm, 5mm and 10mm were 4.24°C, 4.28°C and 2.63°C, and the simulated peak temperature rises at these locations were lower at 4.02°C, 3.75°C, and 2.47°C respectively.

For the M2 lens (Figure 6.8B), the shape of the simulated and measured temperature curves match well, with each line scan producing a staggered double peak followed by a cooling tail period due to the fact that the focus has two radial peaks which are aligned with the scan path. The maximum temperature rises measured at $x = 0$mm, 5mm and 10mm were 4.80°C, 4.65°C and 2.9°C, while the simulated peak temperature rises were 6.09°C, 5.51°C and 3.46°C respectively. Both the simulated and measured temperature curves at $x = 10$mm show a lower peak value than the other two locations due to it

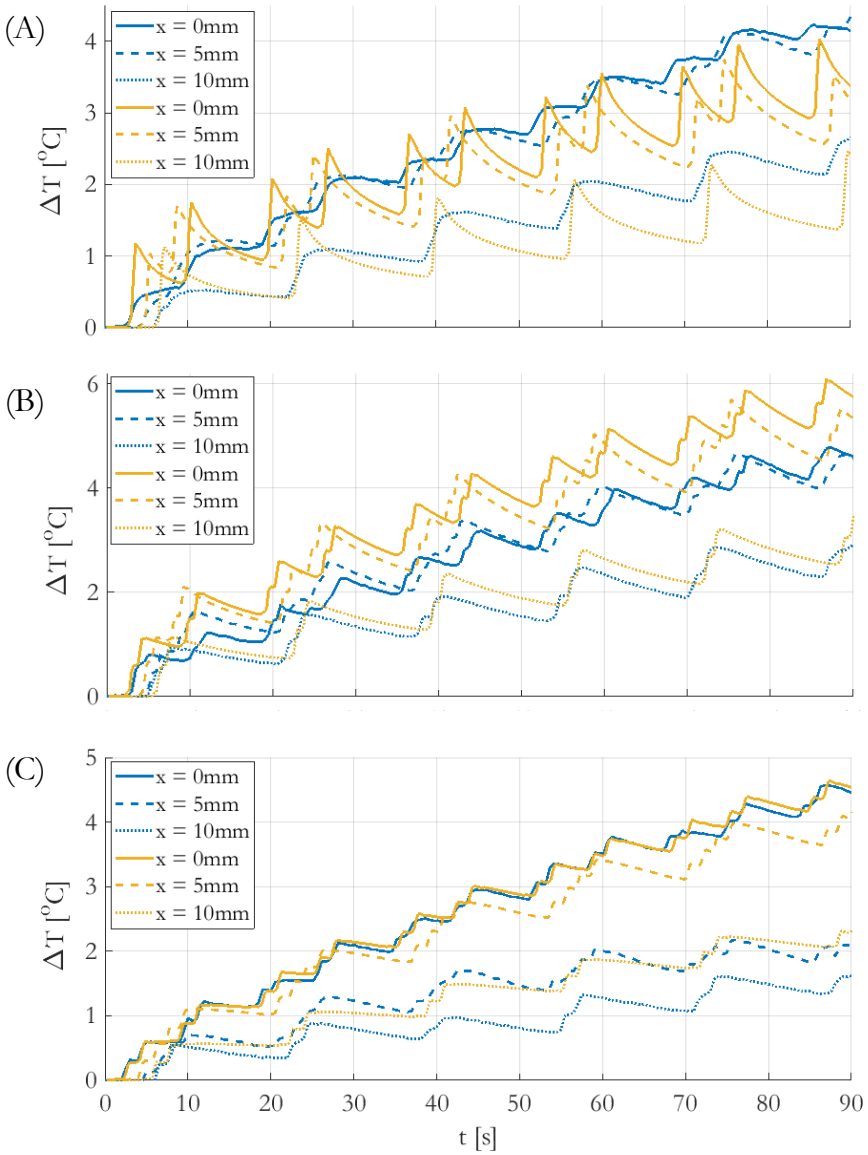


Fig. 6.8 Measured (blue) and simulated (yellow) temperature curves in an agar-silica phantom produced by the JC200 performing repeated line scans (±10mm) operating at 32W, 50% duty cycle, and 10Hz PRF with the T60 lens (A), M2 lens (B), and the M4 lens (C). Simulated temperature curves were generated by the Fresnel approximation also at 50% duty cycle since ringing of the JC200 at this duty cycle was not observed. The FOH was positioned in the focal plane at radial offsets of 0mm, 5mm, and 10mm, where 0mm is the centre of the line path, and 10mm is the distal position of the line path. The predefined line scan was programmed to start at $x = -10$mm and move to the position $x = 10$mm before returning back to $x = -10$mm with a movement speed of 3mm.s^{-1}, with a 3 second pause at $x = -10$mm before repeating the scan again.

being at the end distal location of the line scan, and the final peak temperature rises agree to within 1°C.

Looking at the M4 lens (Figure 6.8C), the more defocused acoustic field resulted in staggered peaks which were smaller in amplitude, resulting in an overall smoother temperature rise over the course of the exposure compared to the other two lenses. The peak temperature rise measured at $x = 0$mm, 5mm and 10mm were 4.47°C, 2.10°C and 1.60°C, while simulated peak temperature rises were 4.54°C, 4.15°C and 2.32°C respectively. Again, the temperature rise observed at the distal end position ($x = 10$mm) showed the smallest temperature rise, however the temperature measured at $x = 5$mm also showed a temperature rise of similar magnitude, unlike in the simulation which suggests higher temperature curves for both $x = 0$mm and $x = 5$mm locations. This discrepancy is possibly due to an alignment error with the scan path relative to the centre of the focal field.

In summary, the agreement between simulated and experimentally measured results from both the spot heating and linear heating regimes have verified that the method described to design and manufacture 3D printed acoustic lenses for the JC200 can be reliably employed and modelled. The T60 lens successfully reduced the amplitude of the focal pressure of the JC200, which minimised the likelihood of generating acoustic cavitation and subsequently reduced the risk of damage to the acoustic hydrophones, which enabled the free-field characterisation of the acoustic field shown in Figure 6.4. In addition, the agreement between simulated and measured spot heating temperature curves verifies the application of linear acoustic modelling to the JC200 for the lensed acoustic fields when operating at the minimum acoustic power setting of 32W.

6.3 Simulation of the JC200 in PZFlex

6.3.1 Model Reduction Strategy to Simulate a Larger Transducer

The size of PZFlex simulations licensed to a particular CPU are limited by the available system RAM memory (192GB for the workstation used in this thesis)[1]. For 3D simulations, PZFlex required approximately 1GB RAM per $4{\times}10^6$ elements. Using this value as a guide, if the JC200 transducer were to be simulated in one sitting, it would require a total simulation volume of at least $210 \times 210 \times 200$mm to include the entire source and the focal region of interest. At a grid resolution of 0.104mm ($dx = \lambda/15$), this would result in a simulation requiring up to 2TB of RAM to perform. Modelling the JC200 source alone (in full 3D, excluding the therapy domain) would require a minimum simulation domain of roughly $210 \times 210 \times 50$mm in size, and require approximately one quarter of the full 3D equivalent (490GB of RAM), which still greatly exceeds the 192GB RAM limitation of the existing workstation.

In order to reduce the computational demand of simulating a transducer of this size, the simulation domain was divided into smaller subregions, each with more manageable memory requirements. The criteria for determining the domain size for each subregion includes the incorporation of a 5mm boundary outside of the geometrical cone to ensure that clipping of the acoustic field was minimised, and secondly a region of at least 20mm past the geometric focus of the transducer was included in order to ensure the entire focal volume was captured. Given these two criteria and the available RAM of 192GB, the maximum 3D propagation length which could be simulated at a resolution of 15 elements per wavelength was calculated to be a volume spanning

[1]The transition of PZFlex LLC to OnScale Inc. in April 2018 enabled the use of cloud services which are capable of performing larger simulations, however the existing software package remained licensed to single CPU workstations and therefore were limited by physical RAM.

$65 \times 65 \times 85$mm, which equated to a focal depth of approximately 65mm into the tissue. Similar calculations were performed for additional subregions building up to the transducer surface.

Acoustic propagation between adjoining subregions were performed through the use of the 'free-field' boundary condition in PZFlex, which involved saving the velocity time-history data of elements located on an entire plane for subsequent loading as a source boundary condition. This way, acoustic propagation can be performed over distances greater than what can be normally modelled in a single simulation, at the cost of additional simulation time and hard disk memory for each free-field history file generated. In order to minimise the size of the free-field history file as well as the model domain size, axisymmetry or quarter symmetry boundary conditions were applied to subregions where possible. For example, the lensed sources could be approximated by a quarter symmetry boundary condition model, which reduced the simulation domain of the source alone (excluding the rest of the acoustic field) to $105 \times 105 \times 50$mm, resulting in a simulation size of 123GB RAM.

An axial plane illustration depicting how the JC200 simulation domain was divided is shown in Figure 6.9, where region (a) is the axisymmetric or quarter-symmetric source model in water, (b) is an axisymmetric or quarter-symmetric propagation model in water, and (c) is the full 3D simulation comprising of water and the segmented CT dataset. The JC200 source is indicated by the yellow curves, and the location of the geometric focus is shown by the red circle within region (c). A thick red line indicates the free-field elements recorded in simulation region (a) used as the source boundary condition in region (b). Similarly, the thick pale blue line indicates the free-field elements recorded in simulation (b) used as the source boundary condition for region (c). The size of each simulation domain was determined by the geometrical cone

diameter of the JC200 transducer for a given propagation depth, which is indicated by the dashed blue line.

To demonstrate the free-field boundary method, the normalised acoustic field produced by an axisymmetric simulation of the JC200 source in water is shown by the top half of Figure 6.10, while the bottom half displays the equivalent axisymmetric acoustic field produced by a free-field source boundary condition located at a depth of $x = 50$mm (recorded from the axisymmetric model). A comparison of the two acoustic fields verifies that they are in good agreement, with a difference in peak pressure of 0.014% and no noticeable shift in the location of the focus.

6.3.2 Forward Simulation Model in a Segmented CT Dataset

The same segmented CT dataset modelled in Chapter 5 was employed for the larger scale PZFlex simulations. Two simulation targets in the liver were chosen, with the first case shown in Figure 6.11A indicating a target location in the liver with two ribs obstructing the acoustic window, and the second case shown in Figure 6.11B which indicates a liver target location centred directly behind a rib. The acoustic window in both cases is approximated by a large blue circle of 61.4mm in diameter, which illustrates the beam width calculated from ray theory at the propagation depth of the rib surface.

To simulate the JC200 with a mode 4 acoustic lens, the simulation domains indicated by regions (a) and (b) in Figure 6.9 were modelled with a linear quarter symmetry assumption, taking 10 hours and 18 hours to process respectively, while the full 3D model (region (c) in Figure 6.9) required 32 hours to process. The free-field history files produced by the first and second subregions were on the order of 500GB and 100GB respectively. Acoustic simulations were performed with a time step of 0.0519μs (based on the maximum allowed value to satisfy the Courant-Friedrichs-Lewy stability criteria

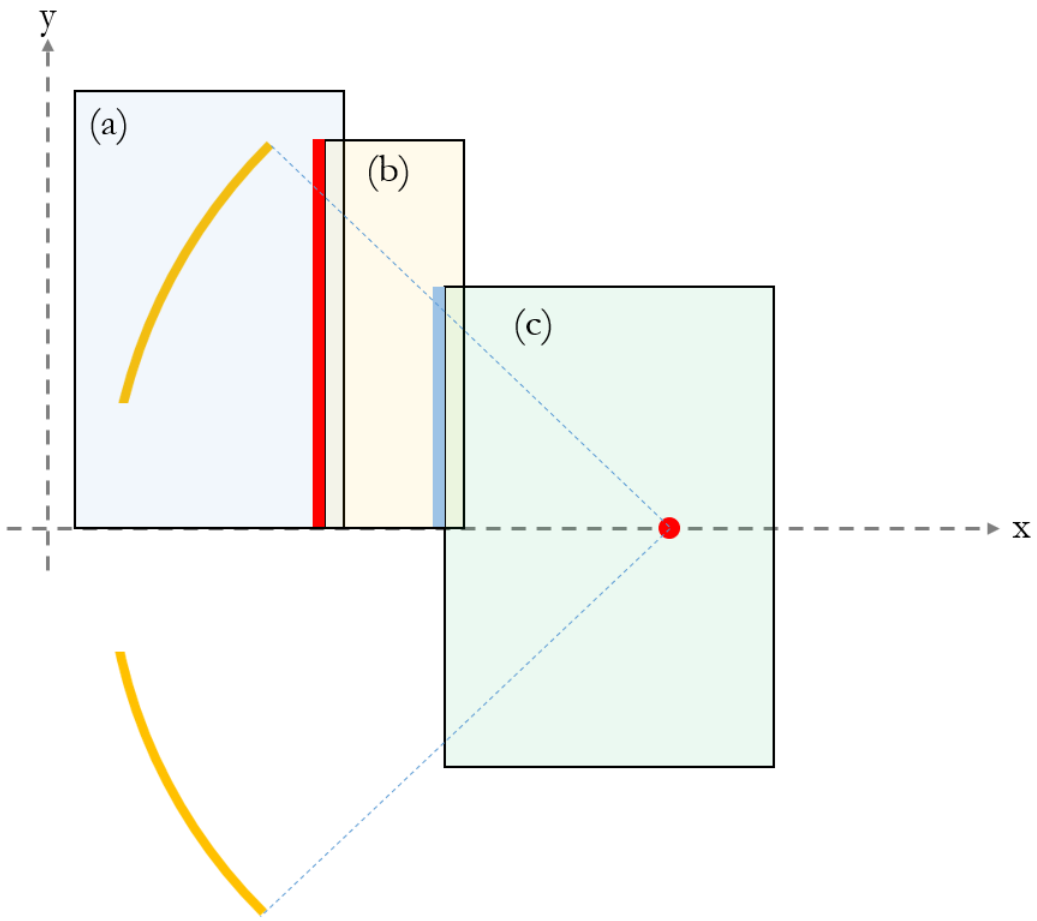


Fig. 6.9 Central axial plane illustration of the multi-model finite-element simulation approach with three example divisions (not to scale). The therapy transducer is illustrated by the two curved yellow lines, where a gap in the centre represents the location of the b-mode imaging probe, and the location of the geometric focus is shown by the red circle. Region (a) indicates the first axisymmetric or quarter-symmetric model comprising of the transducer source (with or without the lens) in water, and the red line indicates the recorded free-field elements used as the source boundary condition for region (b). Region (b) comprises entirely of water and is another axisymmetric or quarter-symmetric model used to receive the free-field boundary from model (a) and produce a second free-field boundary shown by the blue line. Model (c) is the full 3D model which receives the quarter symmetry free-field boundary source from model (b) to calculate acoustic propagation into the segmented CT dataset.

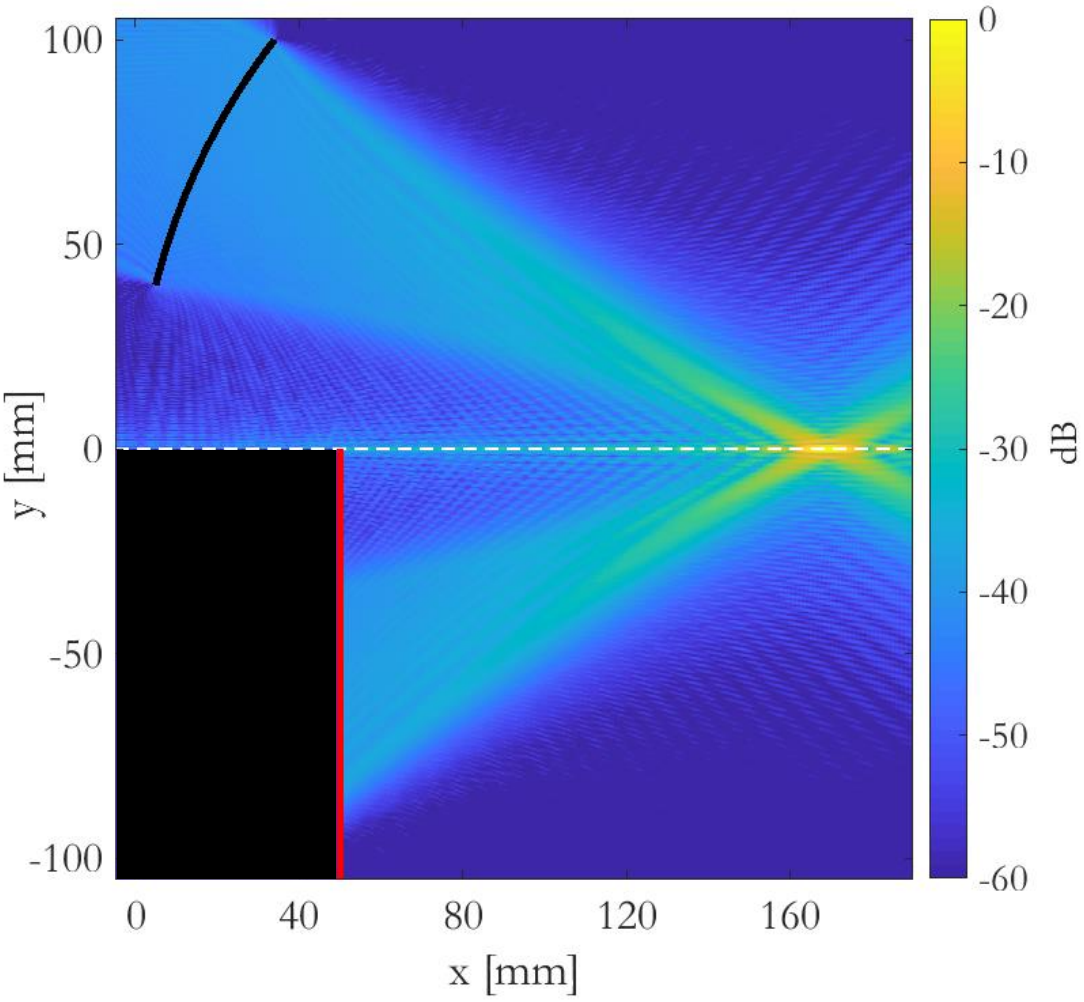


Fig. 6.10 Normalised axisymmetric acoustic simulations of the JC200 transducer in water (top half) compared with an equivalent axisymmetric simulation produced by a free-field boundary source defined at $x = 50$mm (bottom half). The outline of the transducer is shown by the black curve, and the free-field source (recorded from the axisymmetric model) is shown by the red line. The two acoustic fields were in good agreement, with differences in peak acoustic pressure of 0.014% with no noticeable shift in focal volume location.

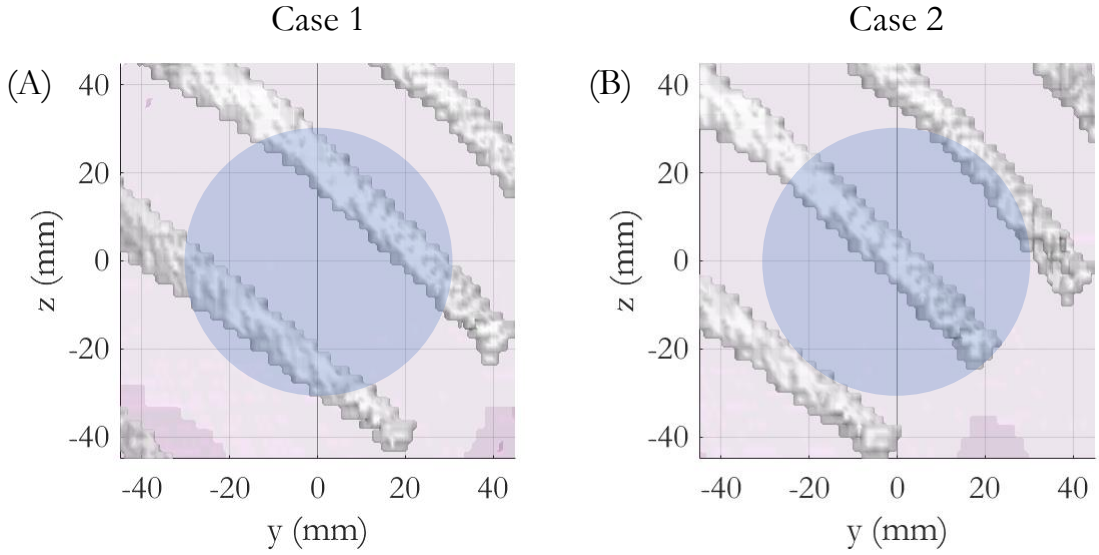


Fig. 6.11 CT volume renderings for two cases, where case 1 shows a target location in the liver centred between two ribs (A), and case 2 directly behind one rib (B). The diameter of the acoustic cone (based on ray theory) at a rib propagation depth of $x = 120$mm is indicated by the two blue circles, both with a diameter of 61.4mm. The transducer is centred at the origin with the axial direction aligned with the x axis, and the tissue surface is locate at approximately $x = 100$mm. In the first case (A), 33.1% of the beam surface area is blocked by the ribs, and in the second case (B) 25.6% is blocked.

[229]), and the source was normalised to a total acoustic power of 1W using Equations 4.6 and 4.7, with subsequent scaling in thermal simulations. In all simulations, the same coordinate system was used in which the transducer was centred at the origin with propagation in the x-axis, and the beginning of the CT dataset was adjusted so that the geometric focus was approximately at a depth of 65mm within the tissue.

The simulated pressure contours produced by the JC200 with no lens in the two liver targets are shown by the blue volume contours in Figure 6.12, and the green sphere centred at the geometric focus indicates the target location with a diameter of 8.8mm, which is the simulated -3dB focal length of the tranducer in water. From top to bottom, the left hand column of Figure 6.12 displays the -3dB, -6dB and -10dB pressure volume contours produced in case 1 (targeting between two ribs), while the right hand column shows the -3dB, -6dB and -10dB pressure volume contours produced in case 2 (targeting directly behind a rib). The shape and location of the -3dB volume contour in cases 1 (6.12A) and 2 (6.12B) both indicate a characteristic elongated ellipsoid shape slightly past the geometric focus, with the case 2 volume being slightly narrower. The peak pressure produced in cases 1 and 2 were found to be 2.58MPa and 3.51MPa, which is equivalent to an acoustic gain of 45.9 and 62.5 respectively, where the lower gain found in case 1 arises from the higher area of rib blocking as indicated in Figure 6.11. Comparing the -6dB contours, a single focal volume is formed in case 1 (Fig 6.12C) however for case 2 (Fig 6.12D) the presence of the rib across the centre of the acoustic window results in splitting of the focal volume into a main lobe, which is accompanied by two additional side lobes which are perpendicular to the alignment of the rib. This focal splitting pattern is characteristic of rib interference and is also reported in literature [97, 163]. The shape and size of the -10dB volume contours follow from the -6dB volume contour shapes, with a larger main lobe in case 1 surrounded by several small sidelobes which extend away from the spherical target volume towards

the transducer. For case 2, the three main lobes are accompanied by several smaller side lobes which are more localised to the spherical target. In both cases, the acoustic gain of the focal field is large enough to ensure the localisation of the -3dB , -6dB, and -10dB contours to within the liver.

The acoustic field produced by the JC200 with a mode 4 lens in target cases 1 and 2 are depicted by the blue focal volumes in the left and right hand columns of Figure 6.13. From top to bottom, the left hand column displays the -3dB, -6dB and -10dB pressure volume contours in case 1, and the right hand column shows the same volume contours produced in case 2. Comparing the -3dB contours (Figs. 6.13A and 6.13B), the total volume is greater in case 1 where more foci are produced, whereas in case 2 only two foci can be seen. For the -6dB contours shown in Figures 6.13C and 6.13D, the total volume for case 1 is greater than that for case 2, however there is an additional elongated pre-focal tail volume which points towards the transducer source between the ribs. In case 2, the -6dB volume is more localised to the liver, with much shorter pre-focal tail volumes. A comparison of the -10dB contours (Figures 6.13E and 6.13F) indicates a significantly greater presence near the ribs and pre-focal area for case 1, while case 2 shows a -10dB volume which is more localised to the focus, with several elongated pre-focal tails pointing towards the transducer and reduced presence in front of the rib. The peak pressures observed in cases 1 and 2 were 1.80MPa and 1.58MPa, which equates to acoustic gains of 32.0 and 28.1 respectively.

The corresponding generation of mild hyperthermia in the two described target cases in the liver were explored through thermal simulations in PZFlex. The acoustic power was kept to the minimum value of 32W in order to minimise the acoustic pressure for linear simulations to remain valid, and duty cycles of 25%, 50% and 100% were explored. Thermal simulations were performed at a resolution of $dx = \lambda/4$, with a time step of $dt = 0.05$s, and executed until a maximum temperature rise of 43 ± 0.1°C

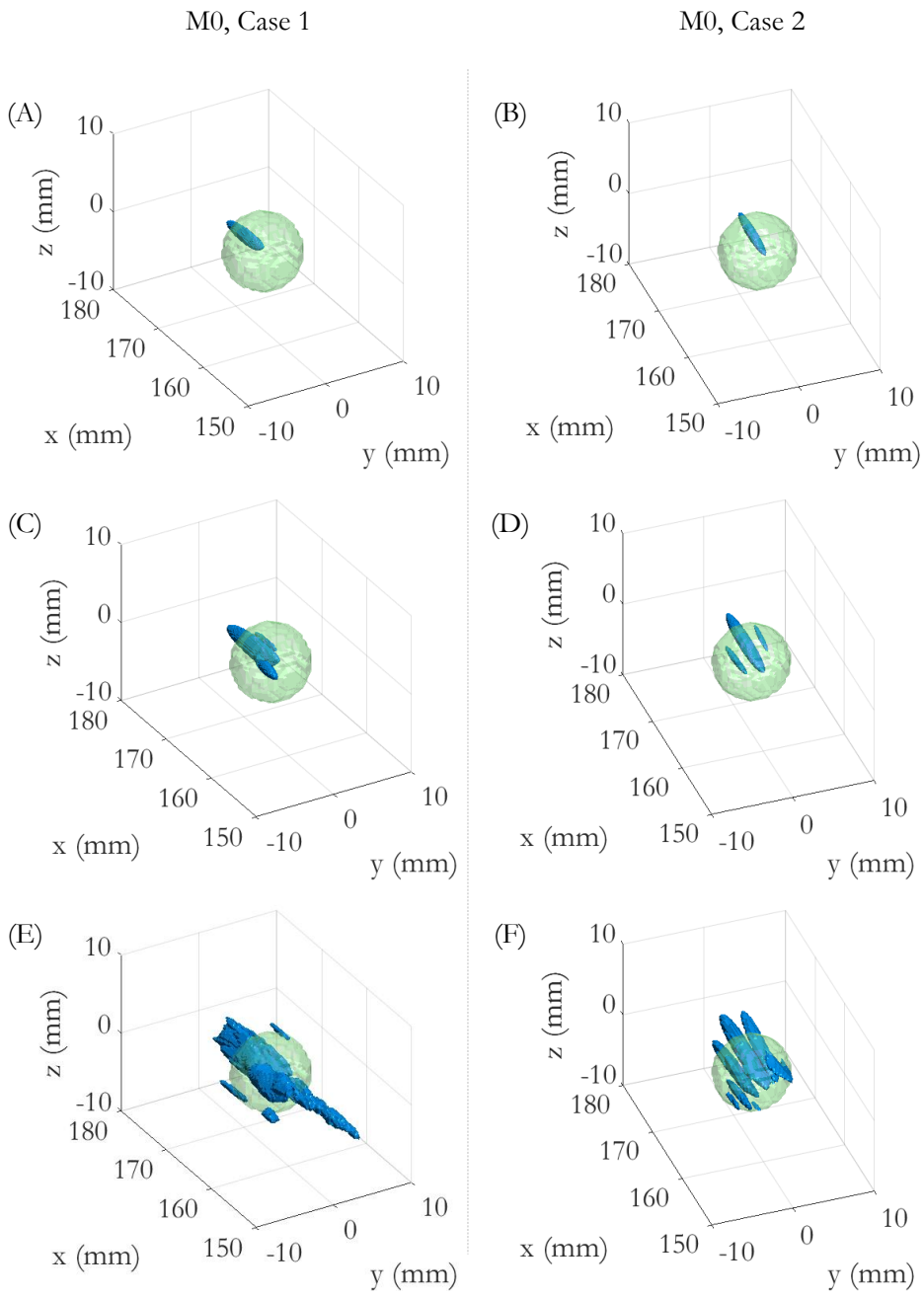


Fig. 6.12 Simulated acoustic pressure volume contours (blue) produced in the liver by the JC200 transducer with no lens in case 1 (left hand column) and case 2 (right hand column). Images (A), (C) and (E) indicate the -3dB, -6dB and -10dB volume contours for case 1 (targeting between ribs), and images (B), (D) and (F) indicate the -3dB, -6dB and -10dB volume contours for case 2 (targeting directly behind a rib). The transducer is located at the origin with axial propagation aligned with the x-axis, the tissue surface is located at $x = 100$mm, and acoustic fields were normalised separately.

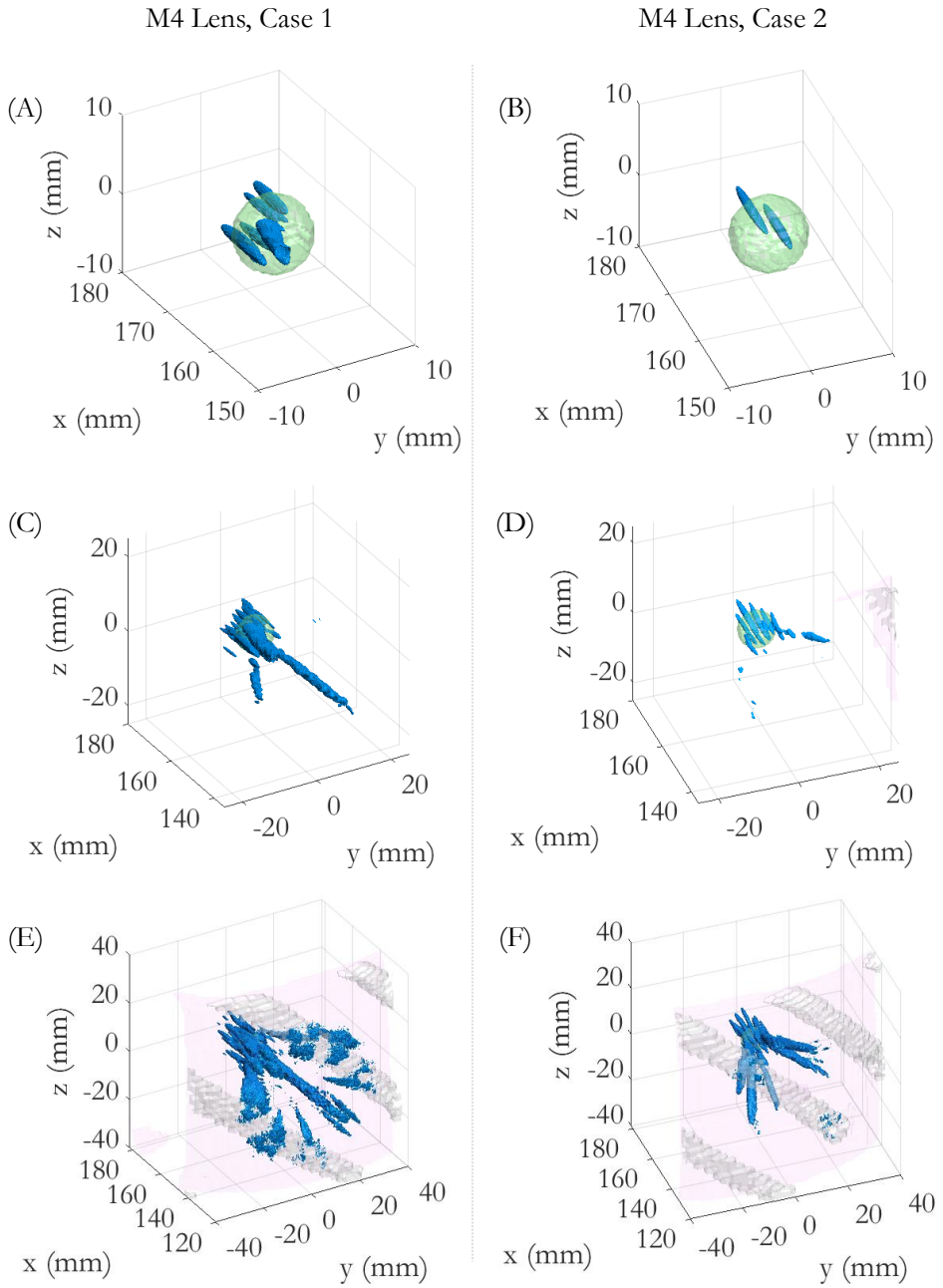


Fig. 6.13 Simulated acoustic pressure volume contours (blue) produced in the liver by the JC200 transducer with a mode 4 acoustic lens in case 1 (left hand column) and case 2 (right hand column). Images (A), (C) and (E) indicate the -3dB, -6dB and -10dB volume contours for case 1 (targeting between ribs), and images (B), (D) and (F) indicate the -3dB, -6dB and -10dB volume contours for case 2 (targeting directly behind a rib). The transducer is located at the origin with axial propagation aligned with the x-axis, the tissue surface is located at $x = 100$mm, and acoustic fields were normalised separately.

was achieved anywhere within the simulation domain in order to prevent thermal damage to tissue. Since a temperature of 39.5°C has therapeutic significance in mild-hyperthermia-mediated drug delivery applications, the resulting 39.5°C therapeutic contours were compared for the JC200 with no lens or with the M4 lens. The thermal simulations for 100% duty cycle cases produced a maximum temperature of 43±0.1°C within one second, therefore the thermal simulation time step was reduced to 0.01s in order to improve simulation accuracy.

Figure 6.14 shows the resulting therapeutic contours for case 1 (left column) and case 2 (right column) produced by the JC200 with no lens, where the top, middle and bottom figures indicate the therapeutic (39.5°C) volume contours produced by duty cycles of 25%, 50% and 100% respectively. Since the peak focal pressure in case 1 was the lower of the two (2.58MPa compared to 3.51MPa), for the 25% duty cycle case (Fig. 6.14A) this resulted in the longest insonation time of 9s until a peak temperature of 43°C was achieved, which resulted in the largest total therapeutic volume (1134mm^3), on target therapeutic volume (52.8mm^3), and therapeutic volume which occurred in bone (986.4mm^3). However, the targeting accuracy of the therapeutic volume was poor, with only 4.6% occurring within the target, and 87% occurring within bone. Operating at higher duty cycle resulted in smaller therapeutic volumes since the maximum simulation temperature of 43°C was reached in a shorter amount of time, however the accuracy was improved, with the best scenario coming from case 2 in 0.33s at 100% duty cycle (Fig. 6.14F), where a total therapeutic volume of 8.4mm^3 was produced, with 59.5% (5.0mm^3) of the total therapeutic volume being on target, and 15.5% (1.3mm^3) occurring in bone. Comparing the 100% duty cycle cases (Figs. 6.14C and 6.14F), a larger total therapeutic volume is produced in case 1 (14.3mm^3), however only 16.8% occurred on target, with 72.7% occurring in bone, which suggests that the obstruction caused by two ribs significantly hindered the targeting accuracy of

Table 6.1 Insonation parameters and therapeutic contour volumes produced by the JC200 transducer with no lens operating at 32W with varying duty cycle in CT cases 1 and 2 (termination criteria: $T_{max} = 43 \pm 0.1°C$). *Based on an 8.8mm diameter spherical target volume in the liver, centred at the geometrical focus of the transducer.

	M0, Case 1			M0, Case 2		
Duty cycle [%]	25	50	100	25	50	100
t [s]	9.00	1.90	0.48	3.30	0.95	0.33
Energy [J]	72.0	30.4	15.2	26.4	15.2	10.4
39.5°C Contour						
Vol. on target* [mm^3]	52.8	8.3	2.4	17.8	9.2	5.0
Vol. in bone [mm^3]	986.4	73.5	10.4	9.4	3.0	1.3
Total vol. [mm^3]	1134	90.4	14.3	35.8	16.6	8.4

the transducer in comparison to the single rib case. A complete list of insonation parameters and therapeutic contour volumes for each simulation in Figure 6.14 can be found in Table 6.1.

Figure 6.15 shows the resulting therapeutic contours produced by the JC200 with the M4 lens in cases 1 (left column) and 2 (right column), where the top, middle and bottom figures indicate the therapeutic volumes produced by duty cycles of 25%, 50% and 100% respectively. The on-target therapeutic volumes produced in both cases were $0mm^3$ for all three duty cycles, with the largest total therapeutic volume of $813.0mm^3$ produced by case 1 at 25% duty cycle, with a therapeutic volume heated in bone of $729.7mm^3$. For the 50% and 100% duty cycle cases, the therapeutic volumes occurring in bone for case 2 were larger than those observed in case 1 despite having a smaller area of bone obstruction, suggesting that the position of the rib in case 2 resulted in a more unfavourable interference on the pre-focal acoustic field. A summary of the thermal contour volumes shown in Figure 6.15 can be found in Table 6.2.

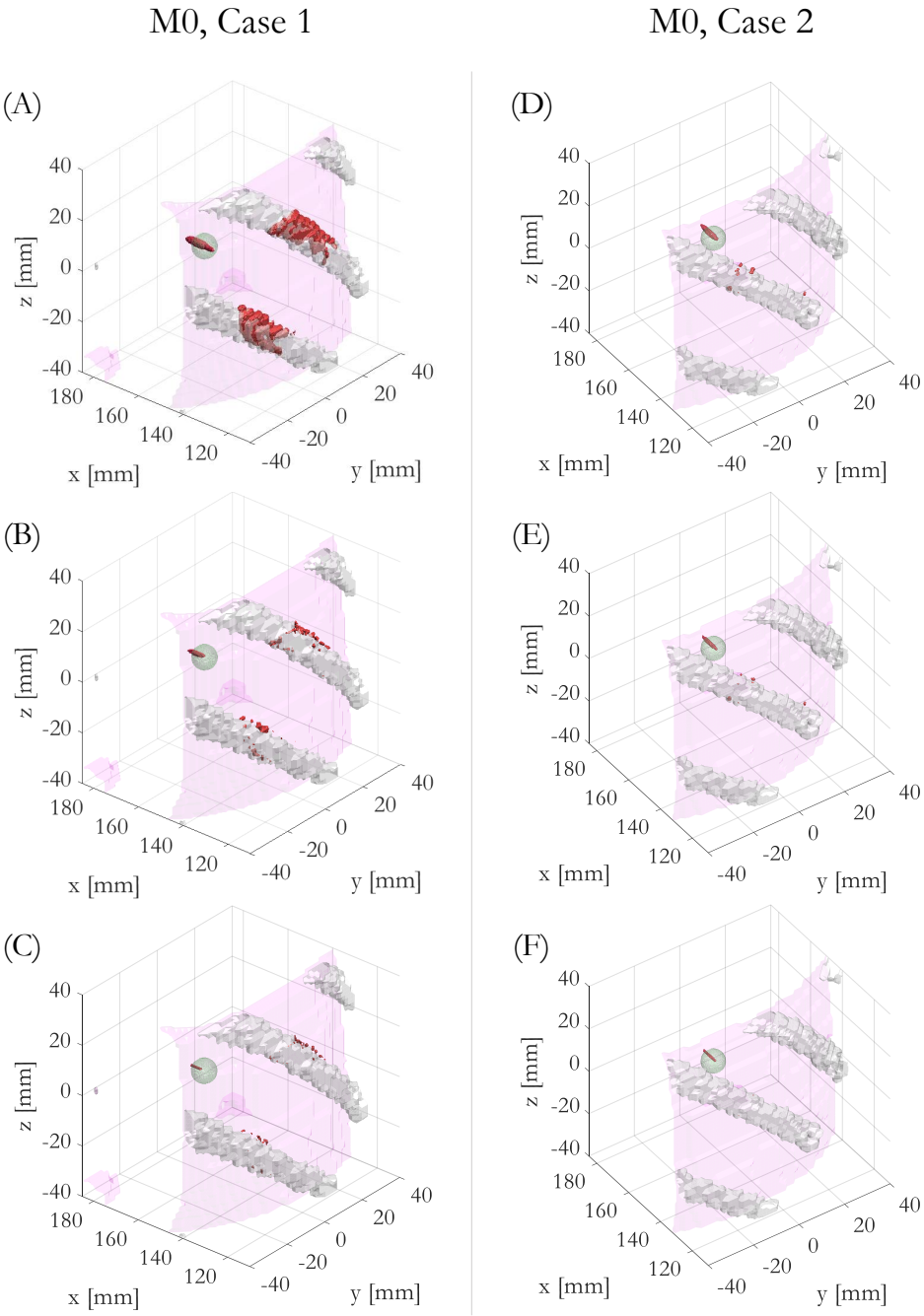


Fig. 6.14 Simulated 39.5°C thermal contours (red) for CT cases 1 (between ribs, left hand column) and 2 (centred over a rib, right hand column) produced by the JC200 transducer with no lens operating at 32W with 25% duty cycle (A, D), 50% duty cycle (B, E), and 100% duty cycle (C, F). Simulations were executed until the maximum temperature reached 43±0.1°C, and individual simulation insonation durations and contour volumes are listed in Table 6.1.

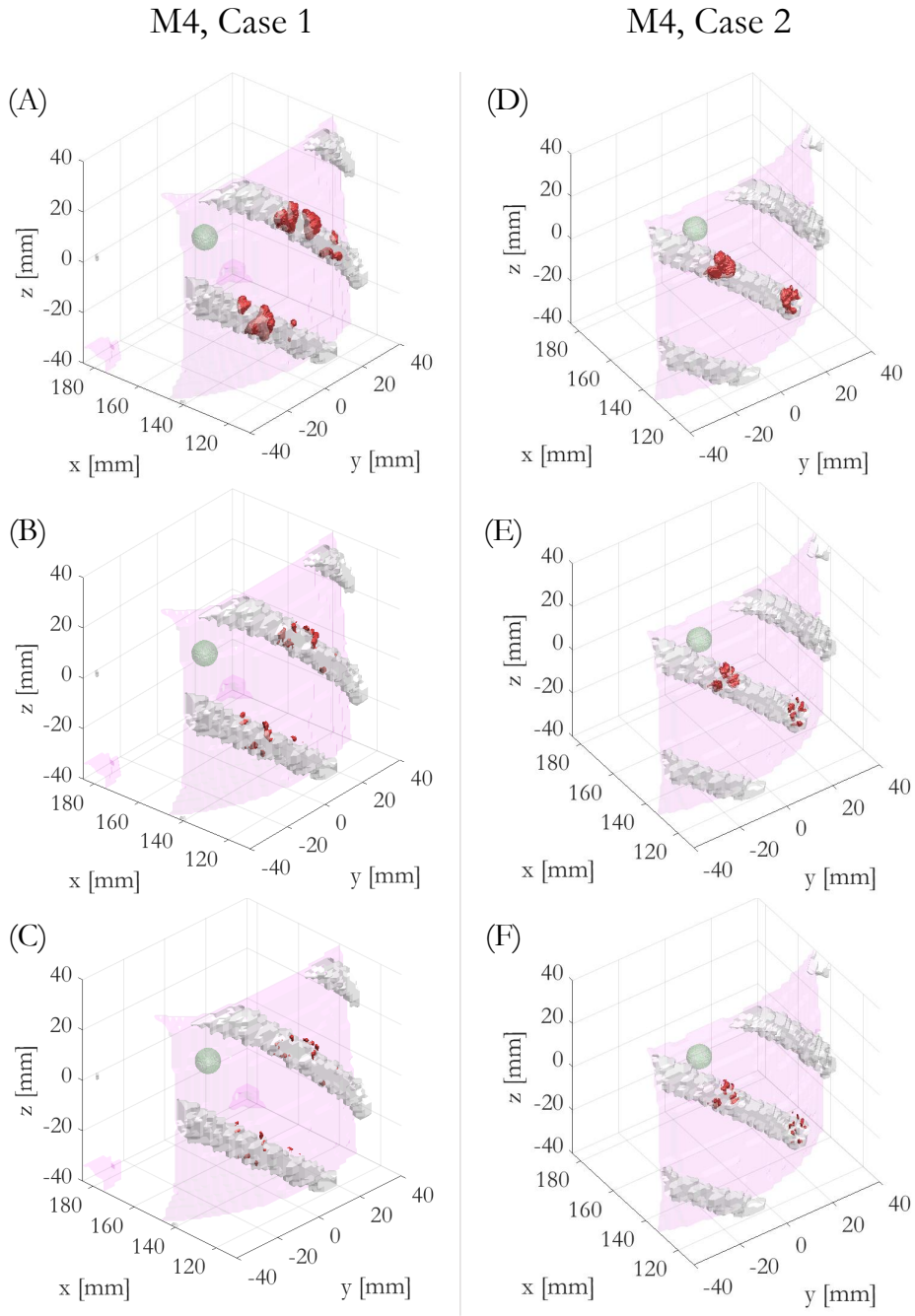


Fig. 6.15 Simulated 39.5°C thermal contours (red) for CT cases 1 (between ribs, left hand column) and 2 (centred over a rib, right hand column) produced by the JC200 transducer with the M4 lens operating at 32W with 25% duty cycle (A, D), 50% duty cycle (B, E), and 100% duty cycle (C, F). Simulations were executed until the maximum temperature reached 43±0.1°C, and individual simulation insonation durations and contour volumes are listed in Table 6.2.

Table 6.2 Insonation parameters and therapeutic contour volumes produced by the JC200 transducer with the M4 lens operating at 32W with varying duty cycle in CT cases 1 and 2 (termination criteria: $T_{max} = 43 \pm 0.1°C$). *Based on an 8.8mm diameter spherical target volume in the liver, centred at the geometrical focus of the transducer.

	M4, Case 1			M4, Case 2		
Duty Cycle [%]	25	50	100	25	50	100
t [s]	12.00	2.20	0.65	10.00	2.80	0.85
Energy [J]	96.0	35.2	20.8	80.0	44.8	27.2
$T_{max,liver}$ [°C]	38.8	38.1	37.8	39.4	39.4	39.1
39.5°C Contour						
Vol. on target* [mm^3]	0	0	0	0	0	0
Vol. in bone [mm^3]	729.7	109.1	30.1	333.9	121.5	47.4
Total vol. [mm^3]	813.0	114.8	31.8	359.9	127.8	49.8

The lack of a therapeutic volume within the target from the M4 lens simulations suggest that the resulting acoustic fields are too defocused and do not have sufficient gain to produce localised heating in the liver. In this heating scenario, a conservative maximum temperature of 43°C has been applied to limit rib heating, however if a higher maximum temperature such as 45°C was chosen instead, the possibility for generating a therapeutic volume in the liver will be increased since the maximum observed temperature values in the liver for case 2 were within 1°C of the therapeutic threshold as indicated in Table 6.2. The risk with using a higher temperature threshold is that if multiple target locations were to be insonated consecutively, there may be a greater amount of pre-focal heat build-up near the ribs.

The position of the focus for the simulations explored here are limited to a maximum a depth of 65mm within the tissue due to the existing RAM of the workstation, which is not much deeper than the H102 simulations presented in Chapter 5. This means the high acoustic gain of the JC200 would not be fully utilised within the tissue, and deeper

targeting may result in a more favourable thermal field since the acoustic pressure in the nearfield can be further reduced.

6.3.3 Virtual Point Source Simulation Model

In order to try to improve the therapeutic volumes observed in the JC200 simulations presented so far, implementation of the phase-conjugate lens and rib masking method presented in Chapter 5 was attempted for the larger model. Taking the more challenging scenario (case 2), a virtual spherical point source situated at the geometrical focus of the transducer in the liver was simulated, and the pressure history on the transducer surface was recorded to determine the influence of tissue inhomogeneity and the ribs on the acoustic field.

Although the multi-model approach described in Fig. 6.9 was a suitable solution to simulate forward acoustic propagation from the JC200, the reverse is significantly more challenging due to the acoustic field no longer having any planes of symmetry to exploit. This means that for regions close to the transducer surface, the size of the model domain must be large enough to encompass the entire transducer surface area. For an acoustic window with dimensions of 210×210mm with a model size limit of 196GB RAM, the maximum propagation depth which can be simulated at a resolution of 15 elements per wavelength ($dx = 0.104$mm) is a distance of 19.6mm. In the JC200 simulation cases shown, the tissue surface is located at $x = 100$mm with the transducer surface centred at the origin. Based on the time and memory requirements of the forward model, modelling a time-domain 3D acoustic field across a total propagation distance of 100mm with consecutive large free-field boundary method simulations of this size would take several weeks to process, with each individual simulation generating very large pressure history files on the order of hundreds of gigabytes or up to one terabyte at each step.

To minimise the number of 3D simulations required, the Rayleigh-Sommerfeld integral described by Equation 3.2 was used instead to calculate the acoustic field on the transducer surface by treating the recorded pressure field from the water plane at $x = 84$mm (close to the surface of the water-tissue boundary) as a time harmonic planar source. This approach is possible since the acoustic medium occupying the space between the transducer surface and the extrapolation plane outside of the CT dataset is homogeneous (water).

Firstly, a virtual point source centred at the geometrical focus of the JC200 in the liver was simulated in PZFlex, which emitted a single cycle sinusoidal pulse with an amplitude of 1MPa and frequency of 0.96MHz. Although the pressure field recorded from a single cycle pulse may not be representative of the continuous wave situation, this was employed in order to minimise the memory requirements of the pressure history file size. The acoustic pressure time history across all elements on the plane $x = 84$mm in water (outside of the tissue model) were recorded from the full 3D multi-tissue layer simulation, taking approximately 16 hours to complete. The required size of the recorded plane was established to be 50×50mm wide based on the geometry of the transducer, and pressure histories were recorded with a sampling rate equal to the simulation time step.

The peak amplitude field map extracted from the recorded pressure history at the plane $x = 84$mm produced by a spherical point source located in the liver for case 2 (targeting between ribs) is shown in Figure 6.16, where darker regions indicate a low recorded amplitude and correspond to the shape and location of the two obstructing ribs as expected.

Surface maps of the recorded arrival time and relative phase are shown in Figures 6.17A and 6.17B respectively, where phase was calculated by looking at the arrival time, using the first zero crossing in pressure as a reference point. The arrival time is shortest

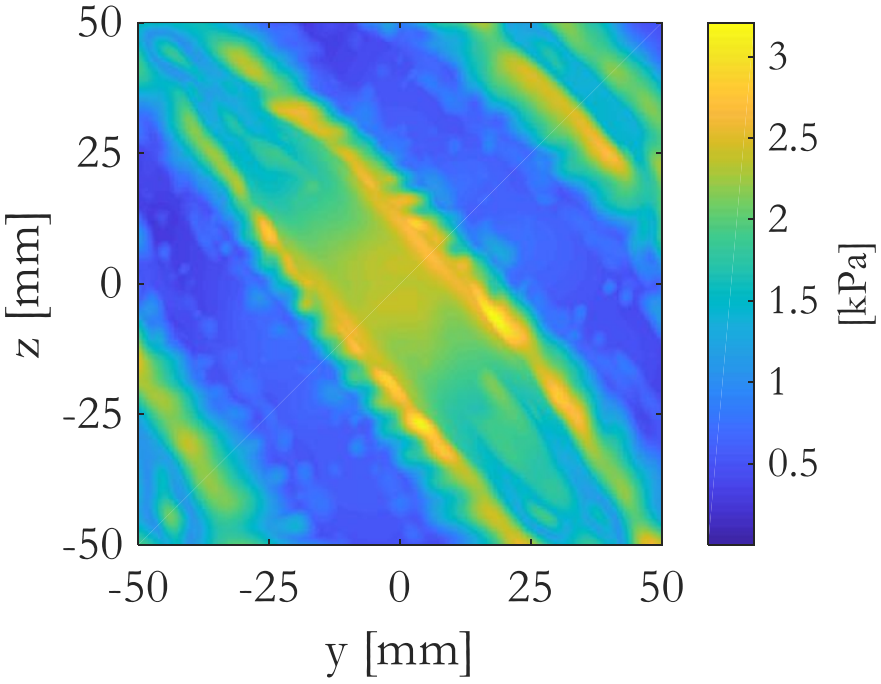


Fig. 6.16 Recorded peak acoustic pressure amplitude at the plane $x = 84$mm produced by a spherical point source centred at the geometrical focus of the JC200 in the liver. Acoustic pressure history locations were sampled at a resolution of $dx = 0.31$mm ($\lambda/5$), the tissue surface is located at $x = 100$mm, the geometrical focus of the transducer is at (164mm, 0, 0), and a one-cycle sinusoidal wave with an amplitude of 1MPa was emitted from the source in order to minimise the duration and size of the pressure time-history file.

in the centre and increases in the radial direction as expected from a spherical point source. Similarly in Figure 6.17B, circular patterns in phase are observed with the phase oscillating between $-\pi$ and π radians in the radial direction. Slight distortions can be seen in the arrival time and phase maps due to the presence of the ribs since the speed of sound in bone is significantly faster than in soft tissue, which are presented as darker shaded regions in arrival time, and as discontinuities in the phase map at the edge of the ribs, as well as a shift in phase for regions obstructed by the ribs in comparison to unobstructed regions.

The acoustic pressure at locations corresponding to the transducer surface were numerically calculated using a discretised form of the Rayleigh-Sommerfeld integral in MATLAB, based on the assumption that the pressure history plane recorded at $x = 84$mm acted as a time-harmonic plane source. The amplitude for each individual source element used in the Rayleigh-Sommerfeld integral was established as the peak amplitude of the recorded pressure history waveform from the multi-tissue model shown in Figure 6.16, and the phase was determined by the arrival time of the pressure waveform at each element as indicated by Figure 6.17B. Figures 6.18A and 6.18B show the resulting extrapolated pressure amplitude and phase on the JC200 surface obtained from numerical implementation of the Rayleigh-Sommerfeld integral, where queried field points on the JC200 transducer surface were defined with a spatial resolution of 1mm in both the y and z axes.

6.3.4 Phase-Conjugate Lens and Model Simulation

In the same way as shown in Chapter 5, a phase-conjugate acoustic lens was designed based on the amplitude and phase maps shown in Figures 6.18A and 6.18B. To determine the regions obstructed by the ribs, the surface amplitude map was smoothed with a 2D Gaussian filter in MATLAB and subsequently thresholded based on the

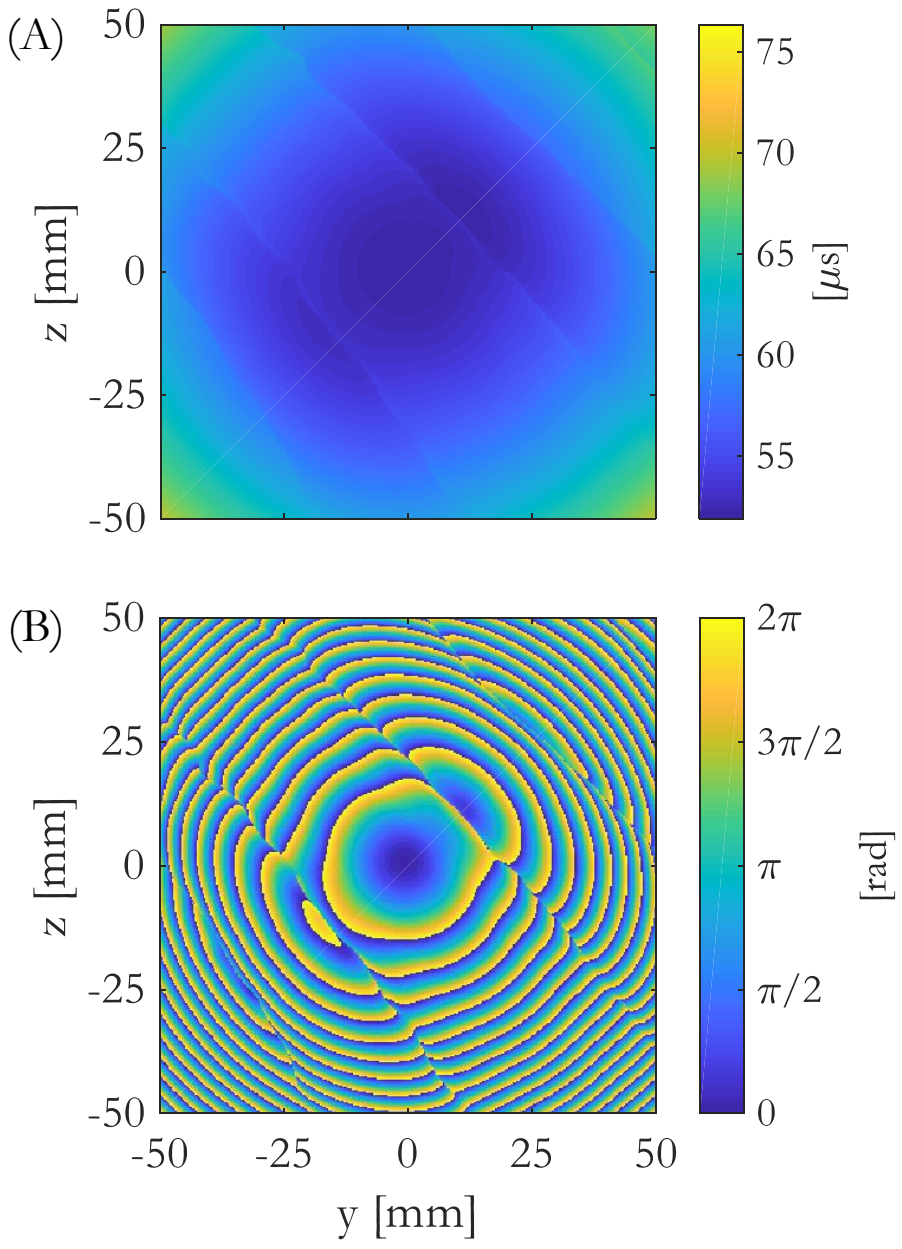


Fig. 6.17 Recorded arrival time (A) and relative phase (B) at the plane $x = 84$mm in water produced by a spherical point source centred at the geometrical focus of the JC200 in the liver. Acoustic pressure history locations were sampled at a resolution of $dx = 0.31$mm ($\lambda/5$), the tissue surface is located at $x = 100$mm, and a spherical point source located at the geometrical focus of the transducer (164mm, 0, 0) was excited with a single cycle sinusoidal wave with an amplitude of 1MPa.

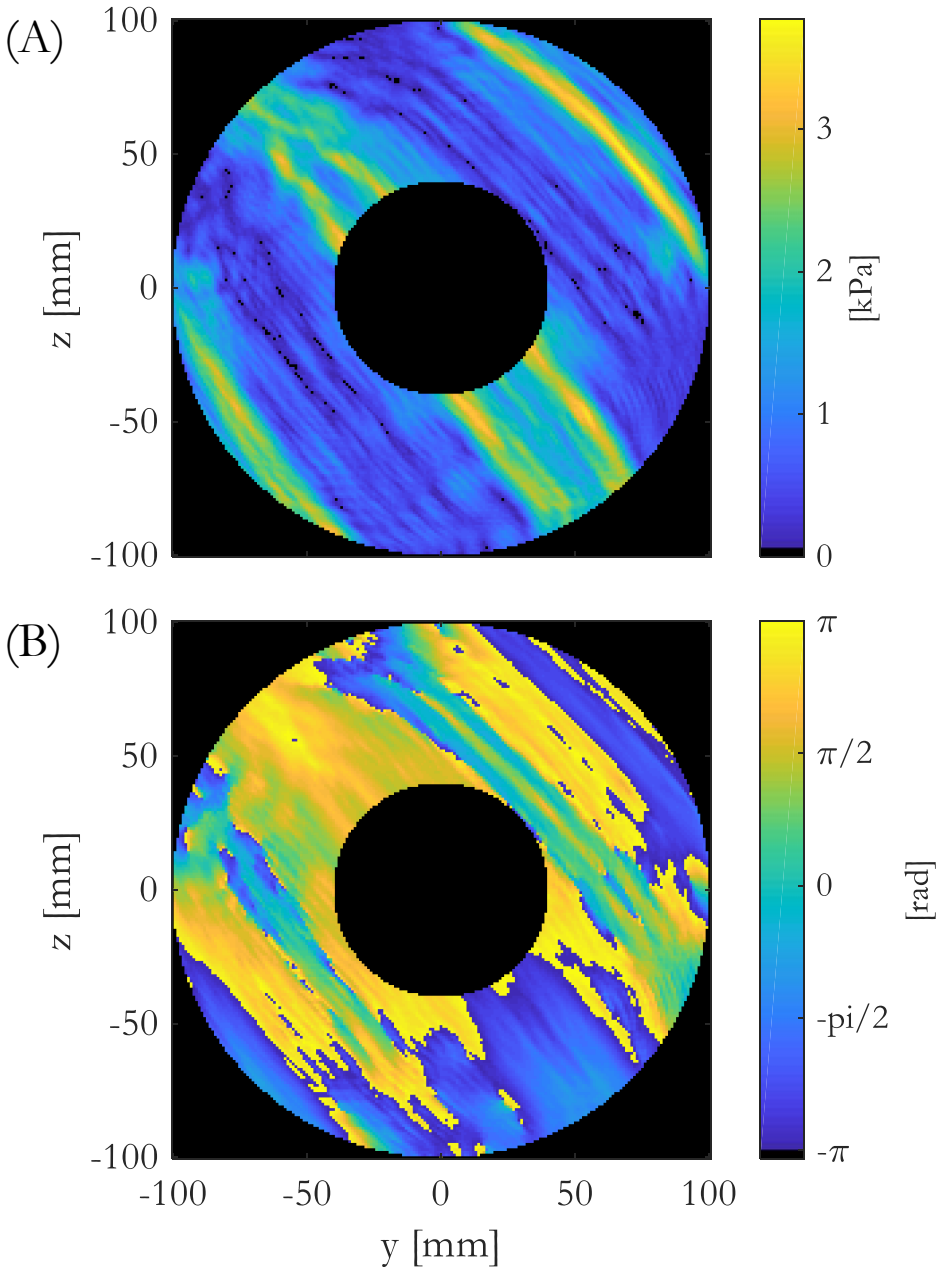


Fig. 6.18 2D amplitude (A) and phase (B) projection maps on the JC200 transducer surface using the recorded source plane at $x = 84$mm as shown in Figure 6.17. The projection was performed using a discretised form of the the Rayleigh-Sommerfeld integral method.

histogram of the recorded surface pressure amplitude. The effect of Gaussian smoothing on the formation of clearly defined rib boundaries was investigated for sigma values of 3mm, 5mm, and 7mm as shown in Figure 6.19, where column (A) indicates the filtered amplitude maps with thresholded regions shown in white, and column (B) corresponds to the respective histogram of the filtered amplitude maps. A red arrow in each histogram indicates the pressure amplitude threshold value (1kPa in this case), and white thresholded regions in each amplitude map indicate the rib obstructed areas. Row (1) is produced without any filtering, and rows (2), (3) and (4) were obtained after application of a Gaussian filter with a sigma value of 3mm, 5mm, and 7mm respectively. The white thresholded regions indicated in Figure 6.19(A1) do not have a clearly defined border, which would not be suitable for the production of a smooth acoustic lens. A Gaussian smoothing filter with $\sigma = 5$mm was selected since the shape of the thresholded region did not differ greatly with increasing values of σ.

To determine the correct lens thickness to provide phase conjugation, the rib obstructed regions were first omitted from the phase map as shown by the white masked regions in Figure 6.20A. Several regions with large jumps in phase from $-\pi$ to π can be seen, which if left alone, may result in large step changes in lens thickness which can cause unwanted reflection and refraction. 2D phase unwrapping was applied using an existing open source MATLAB function [230, 231] which resulted in Figure 6.20B. Although the resulting phase profile is much smoother, the top right region of Figure 6.20B shows a dark blue region close to -2π radians, in contrast to the rest of the phase distribution which is in the range of 0 to 3π, and there is a small unwrapping artefact shown as a yellow spot in the bottom right region of the surface. Again, this could lead to a large difference in lens thickness (and possibly acoustic transmission), therefore manual phase correction was applied to minimise the range by adding or subtracting 2π radians to these areas, which resulted in Figure 6.20C. Finally, the

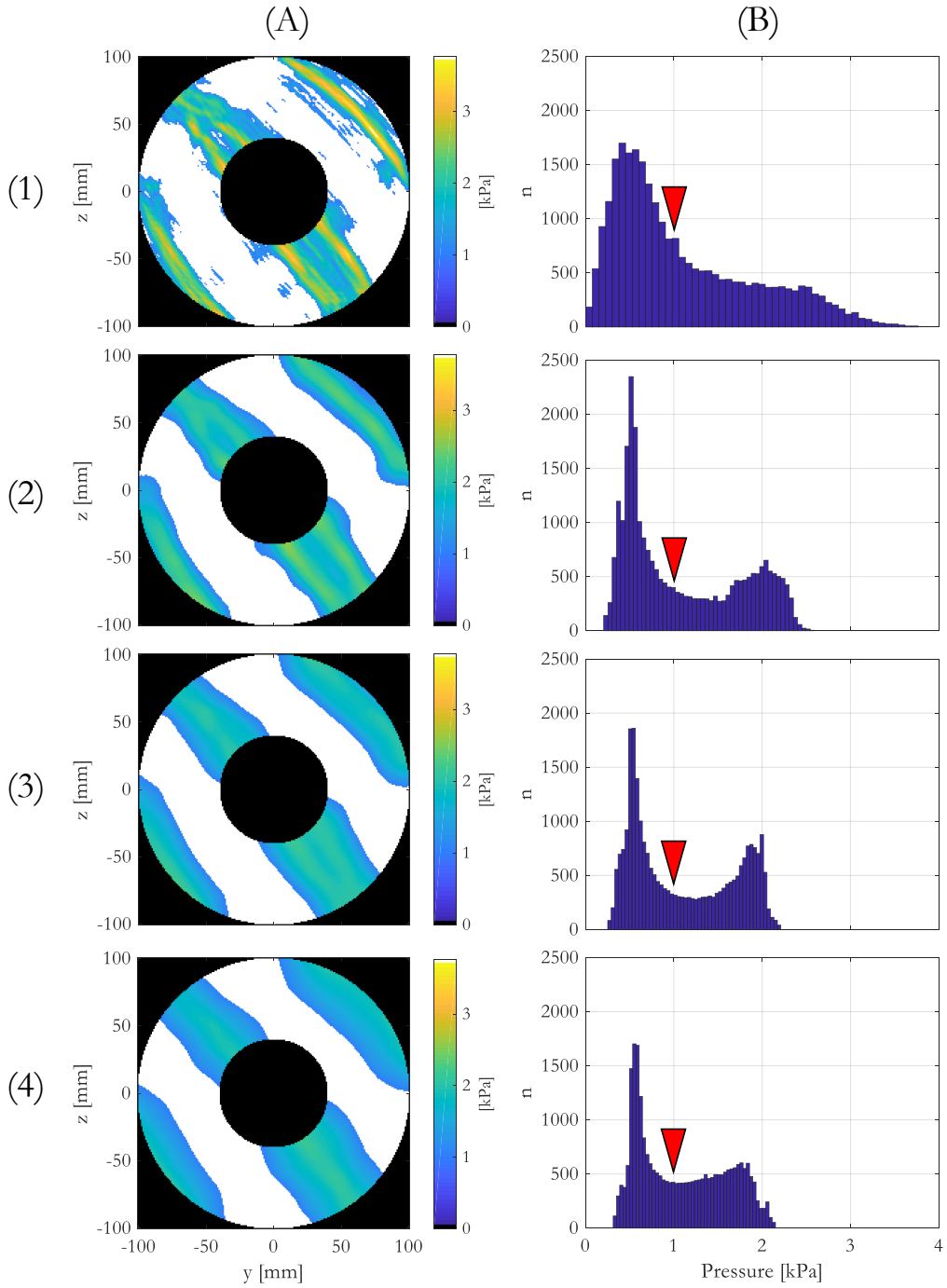


Fig. 6.19 Thresholded amplitude maps (A1-A4) based on the surface amplitude histogram with no filtering (B1), and histograms from amplitude maps with applied Gaussian smoothing filters of $\sigma = 3$mm (B2), 5mm (B3) and 7mm (B4) respectively. White regions on the surface pressure maps indicate areas obstructed by the ribs, and the threshold pressure for each case is indicated by the red marker at a value of 1kPa.

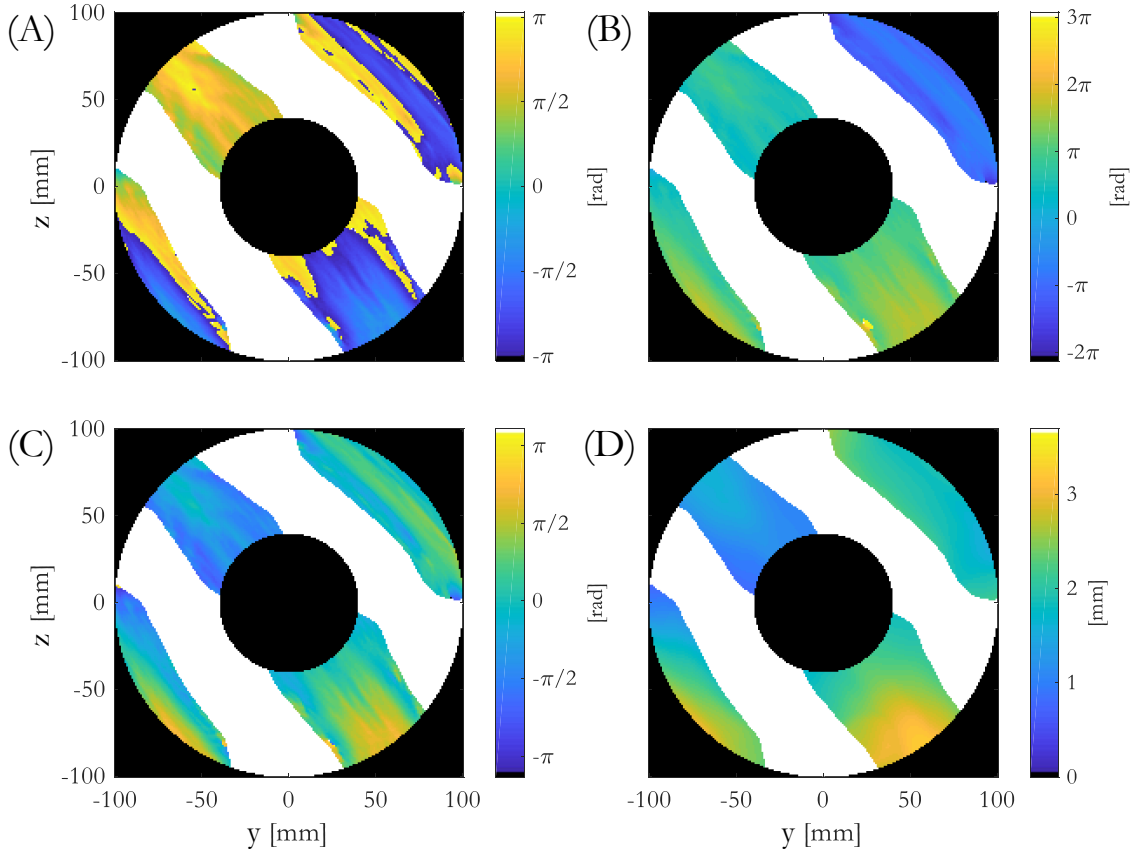


Fig. 6.20 (A) Thresholded surface phase regions. (B) Initial 2D phase unwrapping. (C) Manual correction to minimise the range. (D) Smoothed equivalent lens thickness to provide phase conjugation.

phase map was converted into an appropriate lens thickness using Equation 4.5 and smoothed using a Gaussian smoothing filter in MATLAB in order to produce a profile suitable for printing as shown in Figure 6.20D. Similarly to Figure 5.4E in Chapter 5, smoothing was applied in order to ensure that the surface profile of the lens did not have jumps which exceeded 0.025mm (typical 3D printing resolution).

As discussed earlier in this chapter, the simulation of a patient-specific lens is not currently possible at a resolution of 15 elements per wavelength since this would require over 4TB of RAM memory. Instead, the Rayleigh-Sommerfeld integral method was implemented in MATLAB to numerically calculate the acoustic field produced by the

patient specific lens, where the effect of the lens was translated to an equivalent point source location with amplitude and phase calculated from the three layer transmission model described by Equation 4.4 in Chapter 4, with rib masked source regions omitted (setting the amplitude to 0). The resulting acoustic field on the plane $x = 84$mm was saved as a text file in order for it to be read by PZFlex and applied as a boundary source condition for full 3D simulation in the CT dataset.

The resulting acoustic pressure field on the plane $x = 84$mm produced by the approximated RS-integral time-harmonic source with a total surface acoustic power of 32W is shown in Figure 6.21, where 6.21A indicates the amplitude, and 6.21B indicates the phase. The spatial locations were calculated for locations at the same resolution as the simulation resolution in PZFlex ($dx = 15$ elements per wavelength) in order to enable direct acoustic source loading for each simulated element.

PZFlex was employed to simulate acoustic propagation into the CT dataset by applying a surface boundary source using the pressure amplitude and phase distributions shown in Figure 6.21. To shorten the simulation time, the simulation domain was further split into two subregions, where the first region consisted of water and the various different tissue layers including liver, and the second subregion was smaller and consisted of only liver. The free-field boundary method described previously was employed to link the two acoustic models together at the plane $x = 128$mm.

The resulting pressure field simulated in the CT dataset is shown in Figure 6.22, where the -3dB, -6dB and -10dB pressure contour volumes are indicated in blue in Figures 6.22A, 6.22B and 6.22C. The location of the -3dB and -6dB pressure contours is mainly limited to the pre-focal region outside of the liver, with no -3dB volume contour occurring in the liver, and only a very small portion of the -6dB contour can be seen in the distal end of the green spherical target volume. The -10dB volume contour shows some presence in the target sphere, however the main bulk of the volume is

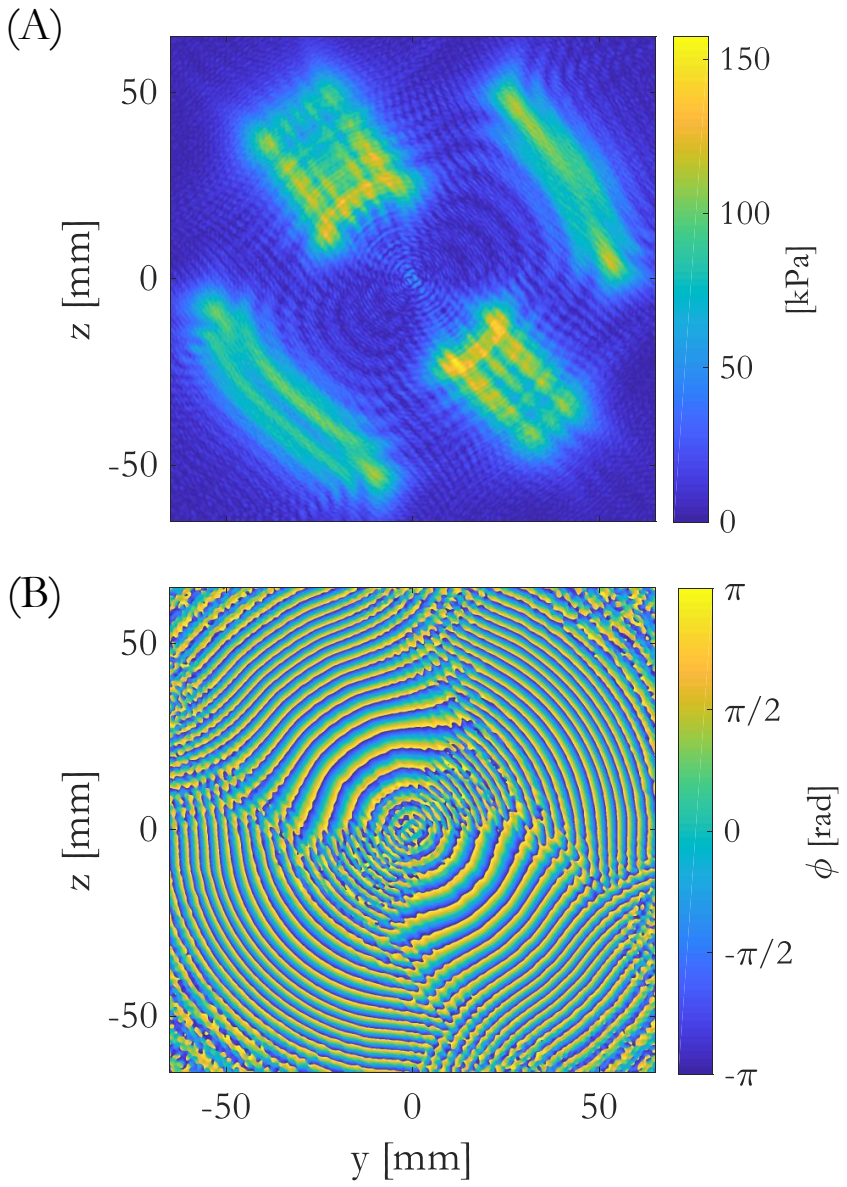


Fig. 6.21 Numerically calculated acoustic pressure amplitude (A) and phase (B) maps at the plane $x = 84$mm produced by the JC200 with a phase-conjugate lens and rib masking. The acoustic power was fixed at 32W, and numerical calculations were performed using the discretised form of the Rayleigh-Sommerfeld Integral.

situated between the ribs in the pre-focal tissue in front of the liver. The maximum pressure in each plane along the axial direction (x) is shown in Figure 6.22D, where the blue contour indicates the acoustic pressure from the first subregion, and the orange contour indicates the acoustic pressure obtained from the second subregion (liver only).

The simulation of the JC200 operating at 32W with no lens in case 1 as shown in Figure 6.12 resulted in a peak pressure of 2.58MPa, however the peak pressure observed in the phase-conjugate lens with rib masking approach only resulted in a peak focal pressure of 0.22MPa, as shown in Figure 6.22D. This suggests that the reduction in the area of the source due to rib masking as well as the transmission loss due to the introduction of an acoustic lens has resulted in excessive reduction in acoustic energy, which is unable to form a useful focal volume in the liver. The introduction of a sectored acoustic lens would also result in a similar manner since the simulation shown in Figure 6.22 is for the mode 0 case, and thermal simulations are not required in order to show that pre-focal heating will dominate, with little or no heating produced in the liver target.

6.4 Conclusions

In this chapter, the design and verification of three 3D printed acoustic lenses were validated on the JC200 clinical focused ultrasound system through the comparison of simulated and measured hydrophone measurements of the acoustic field at the focus, and good agreement was found between the simulated and measured temperature data acquired at the focus of the transducer using a fibre optic hydrophone. The use of a 60% transmission lens enabled the acoustic field of the JC200 to be measured without damaging the hydrophone (presumably cavitation-induced damage), and measurements from the mode 2 and mode 4 lenses successfully demonstrated broadening of the focal volume which resulted in wider temperature heating profiles in the radial direction.

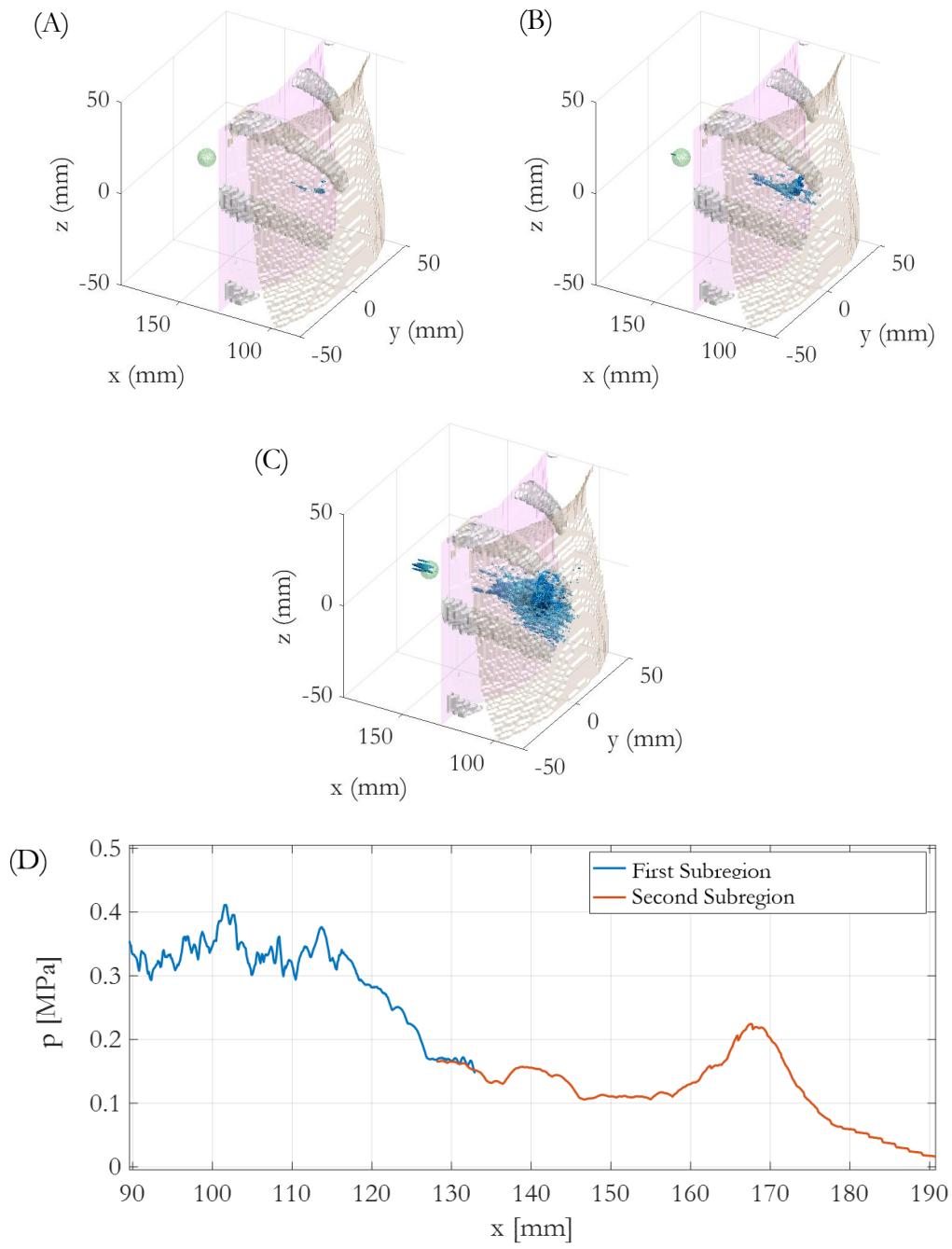


Fig. 6.22 Simulated -3dB (A), -6dB (B), and -10dB (C) pressure contours (blue) generated in the CT dataset using PZFlex produced by a time-harmonic plane source based on the acoustic pressure and phase shown in Figures 6.21A and 6.21B. The maximum pressure at each axial plane is plotted in (D), where blue indicates the pressure simulated in the first subregion consisting of water, fat, muscle, ribs and liver, and the orange line indicates the pressure observed in the second subregion (liver only).

Successful forward simulation of the JC200 transducer source in a segmented CT dataset was performed in PZFlex by dividing the model domain into three smaller subregions, and by utilising the effect of symmetry in the water path leading to the tissue surface. Initial simulations have shown that for the generation of mild hyperthermia in the liver at depth of 65mm, the JC200 alone was able to achieve localised heating in the liver with minor rib heating (reduced by operating with a higher duty cycle for a shorter duration), while the mode 4 lens was unable to produce localised heating in the liver and resulted in significant pre-focal heating especially in the ribs, which suggests that a mode 4 lens cannot be used.

An attempt to correct for the impact of the ribs was investigated through a phase-conjugate lens with masking for the locations of ribs. In order to design the lens, the reverse propagation problem had to be addressed, which posed a greater challenge since the use of symmetry to reduce the model size was no longer possible. Instead, the free-field extrapolation method in PZFlex combined with the use of the Rayleigh-Sommerfeld integral method enabled the acoustic field produced by a spherical point source in the liver to be extrapolated to the transducer surface, where a phase-conjugate lens could be derived. Forward simulation of the JC200 with a patient-specific phase-conjugate lens was not possible in PZFlex due to excessive memory requirements. Instead, the lens was approximated as a collection of amplitude-scaled time-harmonic point sources and numerical calculation of the acoustic field for a plane in water close to the tissue surface was performed using the Rayleigh-Sommerfeld integral. This resulted in an acoustic window small enough to enable the simulation of the water plane in PZFlex for further propagation into the CT dataset.

Initial results for the phase-conjugate lens suggest that it did not result in an improvement in the focal gain. Although the formation of acoustic pressure contour volumes in front of the ribs were avoided due to the masking, the remaining active

surface area of the transducer source seemed to be insufficient to overcome both the acoustic transmission loss of the lens and the acoustic attenuation in the tissue. Further investigation into the targeting depth, degree of rib obstruction, and simulation accuracy of the RS-integral method in combination with PZFlex would be required in order to verify and expand on the current findings to determine a suitable targeting scenario for acoustic lenses with the clinical transducer.

7 Summary and Future Directions

7.1 Summary

The main drive for the work presented in this thesis has been to explore 3D printed acoustic lenses as a possible low-cost solution to increase the focal volume of existing single-element therapeutic transducers, and investigate whether this improves the ability of the transducer to generate useful volumes of mild hyperthermia. Studies of phased arrays in literature have demonstrated that flexibility and control over the focal volume can be achieved by using arrays with a high number of elements [86, 186], however a sector-vortex array design was chosen as a basis due to the ability of this transducer to produce annular multi-foci patterns with minimal additional complexity to the system [197–199]. Acoustic lenses based on the sector-vortex design coupled to a single-element transducer have also been shown to produce similar multi-foci acoustic fields, and at a fraction of the cost of an array [83].

The work presented in Chapter 3 began with the investigation of multi-foci acoustic fields produced by an eight-element sector-vortex array (based on the size and fundamental frequency of the H101 transducer), where the acoustic field was simulated using a fast numerical technique based on the Fresnel approximation [115]. The increase in radial spreading of the focus by using a higher operational mode as described by literature was verified through simulation, where modes 1, 2 and 4 yielded annular focal patterns with radial peaks at ±1mm, ±1.6mm and ±2.8mm respectively. The corresponding simulated thermal profiles generated in a homogeneous attenuating medium

with fixed perfusion resulted in heat distributions with greater radial spreading and uniformity in comparison to the temperature fields produced by the original H101 focused transducer. Alternative acoustic field patterns not defined by a particular mode were also investigated through an automated optimisation process, however the optimised sources resulted in thermal fields with similar performance to that produced by the predefined operational modes of the sector-vortex array described in literature, therefore use of the predefined sector-vortex modes was deemed sufficient.

Chapter 4 explored the production of a mode 2 and mode 4 3D printed sectored acoustic lens for the H102 single-element spherically focused transducer, where the focal volume of the transducer was widened with radial peaks occurring at ±1.6mm and ±2.8mm respectively. Acoustic and thermal simulations using PZFlex were compared with freefield hydrophone scans, as well as thermocouple measurements of heat generation in a tissue-mimicking phantom produced by a short insonation. The tissue-mimicking phantom was based on an existing recipe from the literature [206], and a phantom formula which exhibited an attenuation coefficient of 0.86dB.cm^{-1} at 1.1MHz was used since this value fell within the reported range of human liver tissue. Both acoustic and thermal simulations showed good agreement with experimental results, which justified PZFlex as a reliable simulation method to model the effect of 3D printed lenses on the acoustic and thermal fields.

In Chapter 5, the sectored acoustic lenses described in Chapter 4 were investigated for the H102 transducer focused into a liver target derived from a segmented CT dataset, where the previous verification of PZFlex simulations motivated the use of this method to simulate acoustic propagation and heat generation in inhomogeneous media. Abberation of the acoustic field due to tissue inhomogeneity has previously been reported to result in splitting and distortion of the focal volume [140, 213], and in addition, the presence of ribs pose a significant challenge in transcostal targets

such as the liver due to the high acoustic reflectivity of the tissue-bone interface [166]. Notable strategies to address the aberration caused by tissue inhomogeneity include the time-reversal and phase-conjugation approaches for phased arrays [142, 224, 225], and the approach used in this work involved the design of a phase-conjugate acoustic lens as similarly demonstrated by Maimbourg *et al* (2018) [217]. To overcome rib blocking, suggested strategies reported in the literature include switching off obstructed elements in the case of a phased array [164, 211, 218–221] , introducing sound absorbing structures in front of the ribs to minimise rib heating [222], or partial rib resection [223]. In this work, source locations obstructed by the ribs were masked in simulations to emulate the introduction of a sound absorbing structure. The simulations presented in this chapter have shown that the presence of the ribs hindered both the mode 2 and mode 4 lensed cases in producing a useful therapeutic volume in the liver, and significant pre-focal heating was observed. The incorporation of a phase-conjugate lens with masking of obstructed source regions resulted in therapeutic volumes which were more localised to the liver target, and simulations of the mode 0, mode 2 and mode 4 phase-conjugate lenses with rib masking have shown that a successful compromise between retention of focal gain and defocusing of the acoustic field could be achieved, with the mode 2 lens outperforming the other cases. However, shifts of $\pm$1mm or $\pm5^{\circ}$ led to an 18-24% reduction in total therapeutic volume, which highlights the high sensitivity of this approach to the alignment of the source to the tissue dataset.

The application of the work presented in Chapter 5 to a clinical HIFU system (JC200) is shown in Chapter 6. Good agreement between the simulated and experimentally measured temperature rises produced in an agar-silica phantom verified the application of the mode 0 (60% transmission), mode 2, and mode 4 3D printed acoustic lenses on the clinical transducer, where the mode 2 lens resulted in a measured radial temperature peak at 1.6mm, and the mode 4 lens resulted in a peak at 2.8mm. The mode 0 lens

was designed to exhibit an acoustic transmission coefficient of 60%, which successfully reduced the peak focal pressure to prevent cavitation-based damage to the acoustic hydrophones during free-field measurements at the focus. Performing large scale 3D finite element simulations of the JC200 source in a segmented CT dataset proved to be quite challenging due to the large size of the simulation domain, and a modelling approach which divided the simulation domain into more manageable sub-regions was presented and demonstrated. The use of the Rayleigh-Sommerfeld integral method for acoustic simulations in subregions consisting of a homogeneous medium in combination with the finite element approach for acoustic and thermal simulations in inhomogeneous media is presented as a possible solution to perform large scale modelling. Initial acoustic simulations of the JC200 in two liver target scenarios with differing degree of rib obstruction demonstrated significant splitting and distortion of the focal volume, where heat generation in the liver by the JC200 with no lens was accompanied by slight rib heating in both target cases, and the mode 4 lens failed to produce a meaningfully heated therapeutic volume in the liver due to significant rib heating in both targets. The simulation of a phase-conjugate lens with rib masking for the mode 0 case was also performed, however a useful focal volume in the liver was unable to be produced due to the large reduction in surface area of the source from rib masking. Since even the focused (mode 0) case was unable to generate a useful focal volume in this particular liver target, further spreading of the focus from a sectored lens would also not be of any use. If given more time, it would be useful to investigate the relationship between the amount of rib obstruction and the point where excessive blocking is established, as well as the use of lower operational mode sectored lenses which retain greater focal gain. Furthermore, rather than using a virtual spherical point source which produced a single cycle, a simulated source condition using a short burst of 10-15 cycles would be more representative of the steady-state case. This could be an appropriate compromise

to increase the accuracy of the recorded pressure and phase distributions on the source surface without significantly increasing the size of the pressure history file and RAM requirements.

Based on the resources of a standard high-performance workstation, patient-specific 3D full-wave acoustic modelling has been shown to be possible, where deeper target regions can be modelled if given more RAM. However, a computational approach which uses fewer points per wavelength would be significantly more advantageous, since a factor of 2 reduction in sampling would result in a factor of 8 reduction in volume, and 16 in calculations.

7.2 Future Directions

The use of an acoustic lens has been shown to be able to successfully produce multi-foci focal patterns from a single-element focused ultrasound source, however the drawbacks are that there will be some transmission loss at the transducer-lens and lens-water interfaces due to acoustic impedance mismatch, and attenuation in the acoustic lenses will also result in the build-up of heat within the lens. Heat build-up in the lens is an undesirable effect since excessive heating may damage the lens and the transducer source, and heating of the lens will also change the local sound speed within the material, which may result in unwanted distortion of the acoustic field. Further work to investigate the rate of heat generation in the lenses as a function of acoustic insonation parameters would be useful in order to determine the performance of an acoustic lens when exposed to the insonation conditions of a clinical procedure. The acoustic lens materials investigated in this thesis were limited to two 3D printable clear resins, however many other materials can also be used. The investigation of alternative printable materials would be useful to establish which materials will ensure the most efficient energy transfer through the lens to consequently minimise lens heating. The

addition of active water cooling surrounding the lens would also ensure that heating of the transducer and the lens is minimised.

The biggest challenge when comparing simulations to actual treatment would be deformation of the patient geometry between the simulated model profile and the acoustic field presented to the therapy transducer in practice. Simulations in Chapter 5 have shown that the phase conjugate lens approach is highly sensitive to patient alignment, where a shift in alignment of 1mm was enough to reduce the total therapeutic volume by up to 24%. An imaging method where the patient is laid in the same position for the imaging procedure as for the ultrasound therapy would be the ideal case to minimise deformation of patient geometry. Coupling this with the use of additional imaging guidance would improve the chances of achieving good registration, however taking into account the uncertainty from patient deformation, positioning of the transducer source, imaging resolution, and location of patient fiducial markers, the registration error may be on the same order of 1mm if not more. Achieving transducer alignment to an accuracy of less than 1mm would be very challenging in clinical practice since factors such as patient respiration movement or spontaneous movement may have a significant effect, however compensating for respiratory motion has been shown to be possible for phased arrays [232]. Further investigation to identify whether the sensitivity of the lens is primarily due to the presence of ribs, or if it is also apparent for soft tissues in general would therefore be of significant importance for treatment planning, as well as identifying the required tolerance in registration accuracy for this approach to be effective.

Although the presented finite element approach is able to model the acoustic field and resulting thermal profiles produced in a patient-specific model, only a single target location was considered. Similarly, the proposed phase-conjugate lens would only provide aberration correction for the specific acoustic field modelled. In clinical

practice, the target volume is often much larger than the focal volume of the lensed therapeutic transducers presented in this thesis, and if the lensed approach is to be applied, this would require several target locations to be predefined for treatment planning. 3D finite element modelling of shallow targets of up to 65mm in depth have been shown to require several days to process depending on the size of the acoustic source, and if patient-specific modifications to an acoustic lens are desired, this may take significantly longer. The production of an acoustic lens for the H102 transducer required up to 8 hours to print, and the time needed to outsource an acoustic lens for the JC200 clinical transducer was a minimum of 3 days. Clinical implementation of this would most likely result in the printing of lenses on-site, however repeating this process for multiple acoustic targets would require a significant amount of time (on the order of weeks) which would not be a practical solution in clinical practice. In these situations, the use of a phased array would be more convenient.

Another aspect of treating a larger target volume which needs to be addressed is the use of mechanical scanning of the focal volume. The ability to model a scanned propagation path in a patient-specific dataset using a finite-element approach is still a difficult task to achieve since this would require multiple forward simulations to be solved and would be impractical to simulate for a linearly moving source. A simplification can be made by reducing the number of scan locations (i.e. performing consecutive spot heating), and the capability of an acoustic lens to produce a larger therapeutic volume by targeting several consecutive locations in a patient-specific scenario would be a useful avenue to explore. Other ways to streamline the simulation process would be to use a workstation with larger system RAM, performing simulations on a cloud computing service, or by using a simulation method which requires fewer points per wavelength such as k-Wave. Alternative simulation methods such as geometrical ray tracing can perhaps provide a faster solution to derive the location of bone obstructed

regions and derive a suitable phase conjugate lens, however for forward simulation acoustic modelling and subsequent heat generation in inhomogeneous media, full-wave techniques will still need to be employed.

The approach used to minimise rib heating in the patient-specific simulations presented in Chapters 5 and 6 were to mask source locations which were obstructed by the ribs. One possible way to implement this in physical practice would be to introduce a highly absorbing material (cut or printed to the correct contour) on the patient with sufficient insulation to protect the patient from heat conduction from the material during ultrasound exposure. This would enable masked regions to be less sensitive to patient movement since they would be fixed relative to the patient geometry. Alternatively, sound absorbing material could be placed over the source, however factors to consider with this approach would be potential reverberation effects within the material and on the acoustic field, possible obstruction of some acoustic propagation angles for nearby source regions, and heat conduction from the material to the source. To minimise heat conduction from the attenuating material in both cases, one solution could be to maintain a small water gap or provide insulation between the absorbing material and the patient skin surface or source, and apply active water cooling during the treatment process.

Challenges to consider during physical implementation of a lensed approach would be the replacement and alignment of multiple acoustic lenses during therapy, and whether this can be performed without altering the position of the patient relative to the transducer. For the JC200 system, the water bath which couples the acoustic field to the patient is not large enough to allow convenient access to the transducer when a patient is lying on the therapy bed, therefore only a single lens would be able to be implemented, and the generation of mild hyperthermia over a larger target volume would rely solely on the use of mechanical scanning. An automated lens changing

system would be one possible idea, however the available space within the water bed is limited for most clinical systems. Most recently, some degree of steering has been shown to be possible using a single acoustic lens with a focused source targeting through the skull [233], however, steering with multi-foci acoustic fields for large volume mild hyperthermia has yet to be explored. The natural approach would be to use a phased array transducer instead, where element switch-off and surface phase can be adjusted electronically without waiting for an acoustic lens to be manufactured or installed. Whether lenses can be implemented in clinical practice has yet to be established, and further work would be necessary to determine the optimum acoustic lens design for a specific target depth and therapeutic purpose. The sensitivity of the lens to alignment suggests that perhaps rib masking alone may be the most practical solution, and the investigation of rib masking in a patient-specific model for multiple target locations with and without a fixed acoustic lens could be a useful direction for future work.

The simulations and experiments presented in this thesis have all been based on existing therapeutic transducers which exhibit a similar centre frequency (1.1MHz and 0.97MHz). Amongst numerous other parameters which can be optimised such as the transducer size and shape, the material of the lens, and the acoustic window of the target site, the exploration of transducers which operate at a lower centre frequency may also be advantageous. Transducers designed for transcranial applications often utilise a lower centre frequency in order to minimise bone heating and to increase the amount of acoustic energy transmitted through the skull [118, 234, 235]. This could also be potentially applied to reduce the onset of prefocal rib heating, however the challenge presented would then be to determine whether large focal volumes can be achieved at depth with sufficient focusing gain to produce adequate localisation and heating in the target volume.

References

[1] M. L. Immordino, F. Dosio, and L. Cattel, "Stealth liposomes: review of the basic science, rationale, and clinical applications, existing and potential," *International Journal of Nanomedicine*, vol. 1, no. 3, pp. 297–315, 2006.

[2] M. B. Yatvin, J. N. Weinstein, W. H. Dennis, and R. Blumenthal, "Design of liposomes for enhanced local release of drugs by hyperthermia," *Science*, vol. 202, no. 4374, pp. 1290–1293, 1978.

[3] M. B. Yatvin, H. Mühlensiepen, W. Porschen, L. E. Feinendegen, and J. N. Weinstein, "Selective Delivery of Liposome-associated cis-Dichlorodiammineplatinum(ii) by Heat and Its Influence on Tumor Drug Uptake and Growth," *Cancer Research*, vol. 41, no. 5, pp. 1602–1607, 1981.

[4] A. M. Ponce, Z. Vujaskovic, F. Yuan, D. Needham, and M. W. Dewhirst, "Hyperthermia mediated liposomal drug delivery.," *International Journal of Hyperthermia*, vol. 22, no. 3, pp. 205–213, 2006.

[5] L. Li, T. L. M. Ten Hagen, M. Hossann, R. Süss, G. C. Van Rhoon, A. M. M. Eggermont, D. Haemmerich, and G. A. Koning, "Mild hyperthermia triggered doxorubicin release from optimized stealth thermosensitive liposomes improves intratumoral drug delivery and efficacy," *Journal of Controlled Release*, vol. 168, no. 2, pp. 142–150, 2013.

[6] A. Kheirolomoom, C. Y. Lai, S. M. Tam, L. M. Mahakian, E. S. Ingham, K. D. Watson, and K. W. Ferrara, "Complete regression of local cancer using temperature-sensitive liposomes combined with ultrasound-mediated hyperthermia," *Journal of Controlled Release*, vol. 172, no. 1, pp. 266–273, 2013.

[7] N. M. Bleehen, "Hyperthermia in the treatment of cancer.," *British Journal of Cancer*, vol. 45, p. 96, 1982.

[8] P. Lyon, M. Gray, C. Mannaris, L. Folkes, M. Stratford, L. Campo, D. Chung, S. Scott, M. Anderson, R. Goldin, R. Carlisle, F. Wu, M. Middleton, F. Gleeson, and C. Coussios, "Safety and feasibility of ultrasound-triggered targeted drug delivery of doxorubicin from thermosensitive liposomes in liver tumours (TARDOX): a single-centre, open-label, phase 1 trial," *Lancet Oncology*, vol. 19, no. 8, pp. 1027–1039, 2018.

[9] K. F. Chu and D. E. Dupuy, "Thermal ablation of tumours: biological mechanisms and advances in therapy," *Nature Reviews Cancer*, vol. 14, pp. 199–208, mar 2014.

[10] Cancer Research UK, "Cancer Statistics for the UK." http://www.cancerresearchuk.org/health-professional/cancer-statistics, Accessed: December 2018.

[11] World Health Organization, "Cancer - NMH Fact Sheet January 2010." http://www.who.int/nmh/publications/fact_sheet_cancers_en.pdf, Accessed: December 2018.

[12] D. E. Gerber, "Targeted Therapies: A New Generation of Cancer Treatments," *American Family Physician*, vol. 77, no. 3, pp. 311–319, 2008.

[13] A. C. Begg, F. A. Stewart, and C. Vens, "Strategies to improve radiotherapy with targeted drugs.," *Nature Reviews Cancer*, vol. 11, no. 4, pp. 239–253, 2011.

[14] H. Kobayashi, B. Turkbey, R. Watanabe, and P. L. Choyke, "Cancer drug delivery: Considerations in the rational design of nanosized bioconjugates," *Bioconjugate Chemistry*, vol. 25, no. 12, pp. 2093–2100, 2014.

[15] T. Lammers, F. Kiessling, W. E. Hennink, and G. Storm, "Drug targeting to tumors: Principles, pitfalls and (pre-) clinical progress," *Journal of Controlled Release*, vol. 161, no. 2, pp. 175–187, 2012.

[16] H. Maeda, "Tumor-selective delivery of macromolecular drugs via the EPR effect: Background and future prospects," *Bioconjugate Chemistry*, vol. 21, no. 5, pp. 797–802, 2010.

[17] K. Maruyama, "Intracellular targeting delivery of liposomal drugs to solid tumors based on EPR effects," *Advanced Drug Delivery Reviews*, vol. 63, no. 3, pp. 161–169, 2011.

[18] K. J. Chen, E. Y. Chaung, S. P. Wey, K. J. Lin, F. Cheng, C. C. Lin, H. L. Liu, H. W. Tseng, C. P. Liu, M. C. Wei, C. M. Liu, and H. W. Sung, "Hyperthermia-Mediated Local Drug Delivery by a Bubble-Generating Liposomal System for Tumor-Specific Chemotherapy," *ACS Nano*, vol. 8, no. 5, pp. 5105–5115, 2014.

[19] S. C. McBain, H. H. P. Yiu, and J. Dobson, "Magnetic nanoparticles for gene and drug delivery," *International Journal of Nanomedicine*, vol. 3, no. 2, pp. 169–180, 2008.

[20] C. A. Robertson, D. H. Evans, and H. Abrahamse, "Photodynamic therapy (PDT): A short review on cellular mechanisms and cancer research applications for PDT," *Journal of Photochemistry and Photobiology B: Biology*, vol. 96, no. 1, pp. 1–8, 2009.

[21] W. G. Pitt, G. A. Husseini, and B. J. Staples, "Ultrasonic Drug Delivery – A General Review," *Expert Opinion On Drug Delivery*, vol. 1, no. 1, pp. 37–56, 2004.

[22] P. C. Lyon, L. F. Griffiths, J. Lee, D. Chung, R. Carlisle, F. Wu, M. R. Middleton, F. V. Gleeson, and C. C. Coussios, "Clinical trial protocol for TARDOX: A phase I study to investigate the feasibility of targeted release of lyso-thermosensitive liposomal doxorubicin (ThermoDox®) using focused ultrasound in patients with liver tumours," *Journal of Therapeutic Ultrasound*, vol. 5, no. 1, pp. 1–8, 2017.

[23] J. P. May and S. D. Li, "Hyperthermia-induced drug targeting," *Expert Opinion on Drug Delivery*, vol. 10, no. 4, pp. 511–527, 2013.

[24] C. J. Diederich and K. Hynynen, "Ultrasound Technology for Hyperthermia," *Ultrasound in Medicine & Biology*, vol. 25, no. 6, pp. 871–887, 1999.

[25] G. M. Hahn, J. Braun, and I. Har-Kedar, "Thermochemotherapy: Synergism Between Hyperthermia (42-43 degrees) and Adriamycin (or Bleomycin) in Mammalian Cell Inactivation," *Proceedings of the National Academy of Sciences of the United States of America*, vol. 72, no. 3, pp. 937–940, 1975.

[26] C. W. Song, H. Park, and R. J. Griffin, "Improvement of Tumor Oxygenation by Mild Hyperthermia," *Radiation Research*, vol. 155, no. 4, pp. 515–528, 2001.

[27] M. W. Dewhirst, Z. Vujaskovic, E. Jones, and D. Thrall, "Re-setting the biologic rationale for thermal therapy.," *International Journal of Hyperthermia*, vol. 21, no. 8, pp. 779–90, 2005.

[28] M. Mallory, E. Gogineni, G. C. Jones, L. Greer, and C. B. Simone, "Therapeutic hyperthermia: The old, the new, and the upcoming," *Critical Reviews in Oncology/Hematology*, vol. 97, pp. 56–64, 2016.

[29] P. R. Stauffer and S. N. Goldberg, "Introduction: Thermal Ablation Therapy," *International Journal of Hyperthermia*, vol. 20, no. 7, pp. 671–677, 2004.

[30] D. Haemmerich and P. F. Laeseke, "Thermal tumour ablation: Devices, clinical applications and future directions," *International Journal of Hyperthermia*, vol. 21, no. 8, pp. 755–760, 2005.

[31] J. E. Kennedy, "High-intensity focused ultrasound in the treatment of solid tumours," *Nature Reviews Cancer*, vol. 5, no. 4, pp. 321–327, 2005.

[32] S. A. Sapareto and W. C. Dewey, "Thermal dose determination in cancer therapy," *International Journal of Radiation Oncology, Biology, Physics*, vol. 10, no. 6, pp. 787–800, 1984.

[33] W. C. Dewey, "Arrhenius relationships from the molecule and cell to the clinic," *International Journal of Hyperthermia*, vol. 10, no. 4, pp. 457–483, 1994.

[34] P. S. Yarmolenko, E. J. Moon, C. Landon, A. Manzoor, D. W. Hochman, B. L. Viglianti, and M. W. Dewhirst, "Thresholds for thermal damage to normal tissues: An update," *International Journal of Hyperthermia*, vol. 27, no. 4, pp. 320–343, 2011.

[35] S. A. Sapareto, L. E. Hopwood, W. C. Dewey, M. R. Raju, and J. W. Gray, "Effects of Hyperthermia on Survival and Progression of Chinese Hamster Ovary Cells," *Cancer Research*, vol. 38, pp. 393–400, 1978.

[36] D. Sinden and G. ter Haar, "Dosimetry implications for correct ultrasound dose deposition: uncertainties in descriptors, planning and treatment delivery," *Translational Cancer Research*, vol. 3, no. 5, pp. 459–471, 2014.

[37] G. C. van Rhoon, "Is CEM43 still a relevant thermal dose parameter for hyperthermia treatment monitoring?," *International Journal of Hyperthermia*, vol. 32, no. 1, pp. 50–62, 2016.

[38] T. G. Leighton and R. O. Cleveland, "Lithotripsy," *Proceedings of the Institution of Mechanical Engineers, Part H: Journal of Engineering in Medicine*, vol. 224, no. 2, pp. 317–342, 2010.

[39] E. P. Stride and C. C. Coussios, "Cavitation and contrast: the use of bubbles in ultrasound imaging and therapy," *Proceedings of the Institution of Mechanical Engineers, Part H: Journal of Engineering in Medicine*, vol. 224, no. 2, pp. 171–191, 2010.

[40] W. L. Nyborg, "Ultrasonic microstreaming and related phenomena.," *The British Journal of Cancer. Supplement*, vol. 5, pp. 156–160, 1982.

[41] A. P. Sarvazyan, O. V. Rudenko, and W. L. Nyborg, "Biomedical applications of radiation force of ultrasound: historical roots and physical basis," *Ultrasound in Medicine and Biology*, vol. 36, no. 9, pp. 1379–1394, 2010.

[42] C. C. Coussios and R. A. Roy, "Applications of Acoustics and Cavitation to Noninvasive Therapy and Drug Delivery," *Annual Review of Fluid Mechanics*, vol. 40, no. 1, pp. 395–420, 2008.

[43] Z. Xu, L. Y. Eun, T. L. Hall, B. C. Tran, B. Fowlkes, and C. A. Cain, "Controlled Ultrasound Tissue Erosion," *Ultrasound in Medicine and Biology*, vol. 51, pp. 726–736, jun 2004.

[44] Y. N. Wang, T. Khokhlova, M. Bailey, J. H. Hwang, and V. Khokhlova, "Histological and Biochemical Analysis of Mechanical and Thermal Bioeffects in Boiling Histotripsy Lesions Induced by High Intensity Focused Ultrasound," *Ultrasound in Medicine & Biology*, vol. 39, no. 3, pp. 424–438, 2013.

[45] P. M. Corry, B. Barlogie, E. J. Tilchen, and E. P. Armour, "Ultrasound-induced hyperthermia for the treatment of human superficial tumors," *International Journal of Radiation Oncology, Biology, Physics*, vol. 8, no. 7, pp. 1225–1229, 1982.

[46] W. J. Fry, W. H. Mosberg, J. W. Barnard, and F. J. Fry, "Production of Focal Destructive Lesions in the Central Nervous System With Ultrasound," *Journal of Neurosurgery*, vol. 11, no. 5, pp. 471–478, 1954.

[47] S. R. Sirsi and M. A. Borden, "Advances in ultrasound mediated gene therapy using microbubble contrast agents," *Theranostics*, vol. 2, no. 12, pp. 1208–1222, 2012.

[48] H. Pan, X. Ma, M. Li, J. Chen, and H. Jiang, "Ultrasound assistant chemotherapy may be a novel modality for solid tumors," *Medical Hypotheses*, vol. 73, no. 4, pp. 526–527, 2009.

[49] S. Y. Chae, Y. S. Kim, M. J. Park, J. Yang, H. Park, M. S. Namgung, H. Rhim, and H. K. Lim, "High-Intensity Focused Ultrasound-Induced, Localized Mild Hyperthermia to Enhance Anti-Cancer Efficacy of Systemic Doxorubicin: An Experimental Study," *Ultrasound in Medicine & Biology*, vol. 40, no. 7, pp. 1554–1563, 2014.

[50] S. Mo, C. C. Coussios, L. Seymour, and R. Carlisle, "Ultrasound-enhanced drug delivery for cancer," *Expert Opinion on Drug Delivery*, vol. 9, pp. 1525–1538, dec 2012.

[51] J. J. Rassweiler, T. Knoll, K. U. Köhrmann, J. A. McAteer, J. E. Lingeman, R. O. Cleveland, M. R. Bailey, and C. Chaussy, "Shock Wave Technology and Application: An Update," *European Urology*, vol. 59, no. 5, pp. 784–796, 2011.

[52] S. Vaezy, R. W. Martin, U. Schmiedl, M. Caps, S. Taylor, K. Beach, S. Carter, P. Kaczkowski, G. Keilman, S. Helton, W. Chandler, P. Mourad, M. Rice, R. Roy, and L. Crum, "Liver hemostasis using high-intensity focused ultrasound," *Ultrasound in Medicine and Biology*, vol. 23, no. 9, pp. 1413–1420, 1997.

[53] T. R. Porter and F. Xie, "Ultrasound, microbubbles, and thrombolysis," *Progress in Cardiovascular Diseases*, vol. 44, no. 2, pp. 101–110, 2001.

[54] C. Wright, K. Hynynen, and D. Goertz, "In Vitro and In Vivo High Intensity Focused Ultrasound Thrombolysis," *Investigative Radiology*, vol. 47, no. 4, pp. 217–225, 2012.

[55] Q. Wang, A. A. O. Carneiro, C. Acosta, S. Wang, E. E. Konofagou, H. A. S. Kamimura, H. Chen, and C. Aurup, "Focused ultrasound neuromodulation of cortical and subcortical brain structures using 1.9 MHz," *Medical Physics*, vol. 43, no. 10, pp. 5730–5735, 2016.

[56] S. Wang, V. Zderic, and V. Frenkel, "Extracorporeal, low-energy focused ultrasound for noninvasive and nondestructive targeted hyperthermia," *Future Oncology*, vol. 6, no. 9, pp. 1497–1511, 2010.

[57] L. Zhang and Z. B. Wang, "High-intensity focused ultrasound tumor ablation: Review of ten years of clinical experience.," *Frontiers of Medicine in China*, vol. 4, no. 3, pp. 294–302, 2010.

[58] G. ter Haar and C. Coussios, "High intensity focused ultrasound: past, present and future," *International Journal of Hyperthermia*, vol. 23, no. 2, pp. 85–87, 2007.

[59] M. F. Hamilton, V. A. Khokhlova, and O. V. Rudenko, "Analytical method for describing the paraxial region of finite amplitude sound beams," *The Journal of the Acoustical Society of America*, vol. 101, no. 3, pp. 1298–1308, 1997.

[60] David. T. Blackstock, "Fundamentals of Physical Acoustics." John Wiley and Sons, Inc., 2000.

[61] J. Pohlhammer and W. D. O'Brien Jr., "Dependence of the ultrasonic scatter coefficient on collagen concentration in mammalian tissues," *The Journal of the Acoustical Society of America*, vol. 69, no. 1, pp. 283–285, 1981.

[62] F. A. Duck, *Physical Properties of Tissue, A Comprehensive Reference Book*. Academic Press Ltd., 1990.

[63] B. E. Treeby and B. T. Cox, "k-Wave: MATLAB toolbox for the simulation and reconstruction of photoacoustic wave fields," *Journal of Biomedical Optics*, vol. 15, no. 2, 2010.

[64] W. L. Nyborg, "Heat generation by ultrasound in a relaxing medium," *The Journal of the Acoustical Society of America*, vol. 70, no. 2, pp. 310–312, 1981.

[65] H. Pennes, "Analysis of tissue and arterial blood temperatures in the resting human forearm," *Journal of Applied Physiology*, vol. 1, no. 2, pp. 93–122, 1948.

[66] A. Kotte, G. Van Leeuwen, J. De Bree, J. Van Der Koijk, H. Crezee, and J. Lagendijk, "A description of discrete vessel segments in thermal modelling of tissues," *Physics in Medicine and Biology*, vol. 41, no. 5, pp. 865–884, 1996.

[67] A. N. Kotte, G. M. Van Leeuwen, and J. J. Lagendijk, "Modelling the thermal impact of a discrete vessel tree," *Physics in Medicine and Biology*, vol. 44, no. 1, pp. 57–74, 1999.

[68] E. Sassaroli, K. C. Li, and B. E. O'Neill, "Modeling focused ultrasound exposure for the optimal control of thermal dose distribution," *The Scientific World Journal*, vol. 2012, pp. 1–11, 2012.

[69] M. M. Chen and K. R. Holmes, "Microvascular Contributions in Tissue Heat Transfer," *Annals of the New York Academy of Sciences*, vol. 335, no. 1, pp. 137–150, 1980.

[70] H. Arkin, L. X. Xu, and K. R. Holmes, "Recent Developments in Modeling Heat Transfer in Blood Perfused Tissues," *IEEE Transactions on Biomedical Engineering*, vol. 41, no. 2, pp. 97–107, 1994.

[71] W. D. O'Brien Jr., "Ultrasound-biophysics mechanisms," *Progress in Biophysics and Molecular Biology*, vol. 93, no. 1-3, pp. 212–255, 2007.

[72] G. ter Haar and C. Coussios, "High intensity focused ultrasound: Physical principles and devices," *International Journal of Hyperthermia*, vol. 23, no. 2, pp. 89–104, 2007.

[73] R. E. Beard, R. L. Magin, L. A. Frizzell, and C. A. Cain, "An annular focus ultrasonic lens for local hyperthermia treatment of small tumors.," *Ultrasound in Medicine & Biology*, vol. 8, no. 2, pp. 177–184, 1982.

[74] N. P. K. Ellens, B. B. C. Lucht, S. T. Gunaseelan, J. M. Hudson, and K. H. Hynynen, "A novel, flat, electronically-steered phased array transducer for tissue ablation: preliminary results," *Physics in Medicine and Biology*, vol. 60, no. 6, pp. 2195–2215, 2015.

[75] J. Vincenot, D. Melodelima, F. Chavrier, A. Vignot, A. Kocot, and J. Y. Chapelon, "Electronic Beam Steering Used with a Toroidal HIFU Transducer Substantially Increases the Coagulated Volume," *Ultrasound in Medicine and Biology*, vol. 39, no. 7, pp. 1241–1254, 2013.

[76] D. R. Daum and K. Hynynen, "A 256-element ultrasonic phased array system for the treatment of large volumes of deep seated tissue," *IEEE Transactions on Ultrasonics, Ferroelectrics and Frequency Control*, vol. 46, no. 5, pp. 1254–1268, 1999.

[77] K. Hynynen, G. T. Clement, N. McDannold, N. Vykhodtseva, R. King, P. J. White, S. Vitek, and F. A. Jolesz, "500-Element ultrasound phased array system for noninvasive focal surgery of the brain: A preliminary rabbit study with ex vivo human skulls," *Magnetic Resonance in Medicine*, vol. 52, no. 1, pp. 100–107, 2004.

[78] C. M. C. Tempany, N. J. McDannold, K. Hynynen, and F. A. Jolesz, "Focused Ultrasound Surgery in Oncology: Overview and Principles," *Radiology*, vol. 259, no. 1, pp. 39–56, 2011.

[79] E. Maloney and J. H. Hwang, "Emerging HIFU applications in cancer therapy," *International Journal of Hyperthermia*, vol. 31, no. 3, pp. 302–309, 2014.

[80] P. Fessenden, E. R. Lee, T. L. Anderson, J. W. Strohbehn, J. L. Meyer, T. V. Samulski, and J. B. Marmor, "Experience with a multitransducer ultrasound system for localized hyperthermia of deep tissues.," *IEEE Transactions on Biomedical Engineering*, vol. 31, no. 1, pp. 126–135, 1984.

[81] E. Seppi, E. Shapiro, L. Zitelli, S. Henderson, A. Wehlau, G. Wu, and C. Dittmer, "A Large Aperture Ultrasonic Array System for Hyperthermia Treatment of Deep-Seated Tumors," *IEEE 1985 Ultrasonics Symposium*, pp. 942–948, 1985.

[82] R. Lalonde, A. Worthington, and J. W. Hunt, "Hyperthermia: Field Conjugate Acoustic Lenses for Deep Heating," *Annual International Conference of the IEEE Engineering in Medicine and Biology Society*, vol. 12, no. 1, pp. 264–265, 1990.

[83] T. Fjield, V. Sorrentino, H. Cline, and K. Hynynen, "Design and experimental verification of thin acoustic lenses for the coagulation of large tissue volumes.," *Physics in Medicine and Biology*, vol. 42, no. 12, pp. 2341–2354, 1997.

[84] S. I. Umemura, K. R. Holmes, L. A. Frizzell, and C. A. Cain, "Insonation of fixed porcine kidney by a prototype sector-vortex-phased array applicator," *International Journal of Hyperthermia*, vol. 8, no. 6, pp. 831–842, 1992.

[85] E. S. Ebbini, *Deep localized hyperthermia with ultrasound-phased arrays using the pseudoinverse pattern synthesis method.* PhD thesis, University of Illinois at Urbana-Champaign, 1990.

[86] E. S. Ebbini and C. A. Cain, "Multiple-focus ultrasound phased-array pattern synthesis: optimal driving-signal distributions for hyperthermia," *IEEE Transactions on Ultrasonics, Ferroelectrics and Frequency Control*, vol. 36, no. 5, pp. 540–548, 1989.

[87] K. Hynynen, "MRI-guided focused ultrasound treatments," *Ultrasonics*, vol. 50, no. 2, pp. 221–229, 2010.

[88] E. S. Ebbini and G. ter Haar, "Ultrasound-guided therapeutic focused ultrasound: Current status and future directions," *International Journal of Hyperthermia*, vol. 31, no. 2, pp. 77–89, 2015.

[89] Y. Ishihara, A. Calderon, H. Watanabe, K. Okamoto, Y. Suzuki, K. Kuroda, and Y. Suzuki, "A precise and fast temperature mapping using water proton chemical shift.," *Magnetic Resonance in Medicine*, vol. 34, no. 6, pp. 814–823, 1995.

[90] N. Hijnen, S. Langereis, and H. Grüll, "Magnetic resonance guided high-intensity focused ultrasound for image-guided temperature-induced drug delivery," *Advanced Drug Delivery Reviews*, vol. 72, pp. 65–81, 2014.

[91] Y. S. Kim, "Advances in MR image-guided high-intensity focused ultrasound therapy," *International Journal of Hyperthermia*, vol. 31, no. 3, pp. 225–232, 2015.

[92] M. Pernot, M. Tanter, J. Bercoff, K. R. Waters, and M. Fink, "Temperature Estimation Using Ultrasonic Spatial Compound Imaging," *IEEE Transactions on Ultrasonics, Ferroelectrics and Frequency Control*, vol. 51, no. 5, pp. 606–615, 2004.

[93] D. Liu and E. S. Ebbini, "Real-Time 2-D Temperature Imaging Using Ultrasound," *IEEE Transactions on Biomedical Engineering*, vol. 57, no. 1, pp. 12–16, 2010.

[94] Y. F. Zhou, "High intensity focused ultrasound in clinical tumor ablation," *World Journal of Clinical Oncology*, vol. 2, no. 1, pp. 8–27, 2011.

[95] M. A. Lewis, R. M. Staruch, and R. Chopra, "Thermometry and ablation monitoring with ultrasound," *International Journal of Hyperthermia*, vol. 31, no. 2, pp. 1–19, 2015.

[96] R. T. Beyer, *Nonlinear Acoustics*. AIP-Press, 1 ed., 1974.

[97] P. V. Yuldashev, S. M. Shmeleva, S. A. Ilyin, O. A. Sapozhnikov, L. R. Gavrilov, and V. A. Khokhlova, "The role of acoustic nonlinearity in tissue heating behind the rib cage using high intensity focused ultrasound phased array," *Physics in Medicine and Biology*, vol. 58, no. 8, pp. 2537–2559, 2013.

[98] C. Rossmanna and D. Haemmerich, "Review of Temperature Dependence of Thermal Properties, Dielectric Properties, and Perfusion of Biological Tissues at Hyperthermic and Ablation Temperatures," *Critical Reviews in Biomedical Engineering*, vol. 42, no. 6, pp. 467–492, 2014.

[99] E. A. Neppiras, "Acoustic cavitation," *Physics Reports*, vol. 61, no. 3, pp. 159–251, 1980.

[100] A. D. Maxwell, C. A. Cain, T. L. Hall, J. B. Fowlkes, and Z. Xu, "Probability of Cavitation for Single Ultrasound Pulses Applied to Tissues and Tissue-Mimicking Materials," *Ultrasound in Medicine and Biology*, vol. 39, no. 3, pp. 449–465, 2013.

[101] Y. A. Pishchalnikov, J. A. McAteer, M. R. Bailey, I. V. Pishchalnikova, J. C. Williams, and A. P. Evan, "Acoustic shielding by cavitation bubbles in Shock Wave Lithotripsy (SWL)," *AIP Conference Proceedings*, vol. 838, pp. 319–322, 2006.

[102] W. W. Roberts, "Development and translation of histotripsy: Current status and future directions," *Current Opinion in Urology*, vol. 24, no. 1, pp. 104–110, 2014.

[103] J. J. Kwan, R. Myers, C. M. Coviello, S. M. Graham, A. R. Shah, E. Stride, R. C. Carlisle, and C. C. Coussios, "Ultrasound-Propelled Nanocups for Drug Delivery," *Small*, vol. 11, no. 39, pp. 5305–5314, 2015.

[104] H. L. Liu, W. S. Chen, J. S. Chen, T. C. Shih, Y. Y. Chen, and W. L. Lin, "Cavitation-enhanced ultrasound thermal therapy by combined low- and high-frequency ultrasound exposure," *Ultrasound in Medicine and Biology*, vol. 32, no. 5, pp. 759–767, 2006.

[105] C. Coviello, R. J. Kozick, J. J. Choi, M. Gyongy, J. Collin, C. Jensen, P. Probert Smith, and C. C. Coussios, "Passive acoustic mapping using optimal beamforming for real-time monitoring of ultrasound therapy," *The Journal of the Acoustical Society of America*, vol. 137, no. 5, pp. 2573–2585, 2015.

[106] J. Gu and Y. Jing, "Modeling of wave propagation for medical ultrasound: a review," *IEEE Transactions on Ultrasonics, Ferroelectrics, and Frequency Control*, vol. 62, no. 11, pp. 1979–1992, 2015.

[107] k-Wave, "Alternative Acoustics Software." http://www.k-wave.org/acousticsoftware.php, Accessed: December 2018.

[108] IEEE Ultrasonics, Ferroelectrics and Frequency Control Society, "Ultrsonics Software." https://ieee-uffc.org/ultrasonics/software/, Accessed: December 2018.

[109] J. W. Goodman, *Introduction to Fourier Optics*. The McGraw-Hill Companies, Inc., 1996.

[110] P. R. Stepanishen, "Transient Radiation from Pistons in an Infinite Planar Baffle," *The Journal of the Acoustical Society of America*, vol. 49, no. 5, pp. 1629–1638, 1970.

[111] G. E. Tupholme, "Generation of acoustic pulses by baffled plane pistons," *Mathematika*, vol. 16, no. 2, pp. 209–224, 1969.

[112] J. A. Jensen, "A new approach to calculating spatial impulse responses," in *IEEE Ultrasonics Symposium Proceedings. An International Symposium (Cat. No.97CH36118)*, pp. 1755–1759, 1997.

[113] P. R. Stepanishen and K. C. Benjamin, "Forward and backward projection of acoustic fields using FFT methods," *The Journal of the Acoustical Society of America*, vol. 71, no. 4, pp. 803–812, 1982.

[114] P. Alais and P. Y. Hennion, "Etude par une méthode de Fourier de l'interaction non linéaire de deux rayonnements acoustiques dans un milieu absorbant. Cas particulier de l'émission paramétrique," *Acta Acustica*, vol. 43, no. 1, pp. 1–11, 1979.

[115] T. D. Mast, "Fresnel approximations for acoustic fields of rectangularly symmetric sources," *The Journal of the Acoustical Society of America*, vol. 121, no. 6, pp. 3311–3322, 2007.

[116] M. E. Schafer, P. A. Lewin, and J. M. Reid, "Propagation Through Inhomogeneous Media Using The Angular Spectrum Method," in *IEEE Ultrasonics Symposium*, pp. 943–946, 1987.

[117] X. Fan and K. Hynynen, "The effect of wave reflection and refraction at soft tissue interfaces during ultrasound hyperthermia treatments," *The Journal of the Acoustical Society of America*, vol. 91, no. 3, pp. 1727–1736, 1992.

[118] J. Sun and K. Hynynen, "Focusing of therapeutic ultrasound through a human skull: A numerical study," *The Journal of the Acoustical Society of America*, vol. 104, no. 3, pp. 1705–1715, 1998.

[119] I. M. Hallaj and R. O. Cleveland, "FDTD simulation of finite-amplitude pressure and temperature fields for biomedical ultrasound," *The Journal of the Acoustical Society of America*, vol. 105, no. 5, pp. L7–L12, 1999.

[120] X. Yuan, D. Borup, J. Wiskin, M. Berggren, and S. A. Johnson, "Simulation of Acoustic Wave Propagation in Dispersive Media with Relaxation Losses by Using FDTD Method with PML Absorbing Boundary Condition," *IEEE Transactions on Ultrasonics, Ferroelectrics and Frequency Control*, vol. 46, no. 1, pp. 14–23, 1999.

[121] C. Vanhille, C. Conde, and C. Campos-Pozuelo, "Finite-difference and finite-volume methods for nonlinear standing ultrasonic waves in fluid media," *Ultrasonics*, vol. 42, pp. 315–318, apr 2004.

[122] E. Bossy, M. Talmant, and P. Laugier, "Three-dimensional simulations of ultrasonic axial transmission velocity measurement on cortical bone models," *The Journal of the Acoustical Society of America*, vol. 115, no. 5, pp. 2314–2324, 2004.

[123] Treeby, B. and Cox, B. and Jaros, J., "k-Wave User Manual Version 1.1." http://www.k-wave.org/manual/k-wave_user_manual_1.1.pdf, Accessed: December 2018.

[124] E. Bossy, "SimSonic Suite, User's guide for SimSonic3D, November 20, 2012." http://www.simsonic.fr/, Accessed: December 2018.

[125] B. E. Treeby and B. T. Cox, "Modeling power law absorption and dispersion for acoustic propagation using the fractional Laplacian.," *The Journal of the Acoustical Society of America*, vol. 127, no. 5, pp. 2741–48, 2010.

[126] S. Qiao, E. Jackson, C. C. Coussios, and R. Cleveland, "Simulation of nonlinear propagation of biomedical ultrasound using PZFlex and the KZK Texas code," *The Journal of the Acoustical Society of America*, vol. 140, no. 3, pp. 2039–2046, 2016.

[127] S. J. Scott, V. Salgaonkar, P. Prakash, E. C. Burdette, and C. J. Diederich, "Interstitial ultrasound ablation of vertebral and paraspinal tumours: parametric and patient-specific simulations.," *International Journal of Hyperthermia*, vol. 30, no. 4, pp. 228–244, 2014.

[128] PZFlex, LLC, ""Short Course: Finite Element Modeling for Ultrasonic Applications: Part 1: FEA Basics," IEEE Ultrasonics Symposium, 2005." https://pzflex.com/wp-content/uploads/2017/11/Section_1_Finite_Element_Modelling_For_Ultrasound_Applications.pdf, Accessed: December 2018.

[129] T. Fjield and K. Hynynen, "The combined concentric-ring and sector-vortex phased array for MRI guided ultrasound surgery," *IEEE Transactions on Ultrasonics, Ferroelectrics, and Frequency Control*, vol. 44, no. 5, pp. 1157–1167, 1997.

[130] X. Fan and K. Hynynen, "Ultrasound surgery using multiple sonications–treatment time considerations.," *Ultrasound in Medicine & Biology*, vol. 22, no. 4, pp. 471–482, 1996.

[131] R. J. Dickinson, "An ultrasound system for local hyperthermia using scanned focused transducers.," *IEEE Transactions on Biomedical Engineering*, vol. 31, no. 1, pp. 120–125, 1984.

[132] A. Zolfaghari, M. Maerefat, "Bioheat Transfer." http://www.intechopen.com/books/developments-in-heat-transfer/bioheat-transfer, Accessed: December 2018.

[133] M. S. Ibbini and C. A. Cain, "The concentric-ring array for ultrasound hyperthermia: Combined mechanical and electrical scanning," *International Journal of Hyperthermia*, vol. 6, no. 2, pp. 401–419, 1990.

[134] C. M. Moran, N. L. Bush, and J. C. Bamber, "Ultrasonic propagation properties of excised human skin," *Ultrasound in Medicine and Biology*, vol. 21, no. 9, pp. 1177–1190, 1995.

[135] Y. G. Lv and J. Liu, "Effect of transient temperature on thermoreceptor response and thermal sensation," *Building and Environment*, vol. 42, no. 2, pp. 656–664, 2007.

[136] R. B. Roemer, W. Swindell, S. T. Clegg, and R. L. Kress, "Simulation of Focused, Scanned Ultrasonic Heating of Deep-Seated Tumors: The Effect of Blood Perfusion," *IEEE Transactions on Sonics and Ultrasonics*, vol. 31, no. 5, pp. 457–466, 1984.

[137] T. D. Mast, "Empirical relationships between acoustic parameters in human soft tissues," *Acoustics Research Letters Online*, vol. 1, no. 2, pp. 37–42, 2000.

[138] C. W. Connor and K. Hynynen, "Patterns of thermal deposition in the skull during transcranial focused ultrasound surgery," *IEEE Transactions on Biomedical Engineering*, vol. 51, no. 10, pp. 1693–1706, 2004.

[139] T. L. Szabo, *Diagnostic Ultrasound Imaging: Inside Out.* Elsevier Academic Press, 2004.

[140] V. Suomi, J. Jaros, B. Treeby, and R. Cleveland, "Nonlinear 3-D simulation of High-Intensity Focused Ultrasound Therapy in the Kidney," *38th Annual International Conference of the IEEE Engineering in Medicine and Biology Society (EMBC)*, vol. 70, no. 12, pp. 773–779, 2016.

[141] M. Tabei, T. D. Mast, and R. C. Waag, "Simulation of ultrasonic focus aberration and correction through human tissue," *The Journal of the Acoustical Society of America*, vol. 113, no. 2, pp. 1166–1176, 2003.

[142] J. L. Thomas and M. A. Fink, "Ultrasonic beam focusing through tissue inhomogeneities with a time reversal mirror: application to transskull therapy," *IEEE Transactions on Ultrasonics, Ferroelectrics, and Frequency Control*, vol. 43, no. 6, pp. 1122–1129, 1996.

[143] P. Gélat, G. ter Haar, and N. Saffari, "Modelling of the acoustic field of a multi-element HIFU array scattered by human ribs," *Physics in Medicine and Biology*, vol. 56, no. 17, pp. 5553–5581, 2011.

[144] S. A. Goss, R. L. Johnston, and F. Dunn, "Comprehensive compilation of empirical ultrasonic properties of mammalian tissues," *The Journal of the Acoustical Society of America*, vol. 64, no. 2, pp. 423–457, 1978.

[145] R. Kuc and K. J. W. Taylor, "Variation of Acoustic Attenuation Coefficient Slope Estimates for In Vivo Liver," *Ultrasound in Medicine and Biology*, vol. 8, no. 4, pp. 403–412, 1982.

[146] S. B. Sherriff, R. C. Smart, and I. Taylor, "Clinical study of liver blood flow in man measured by 133Xe clearance after portal vein injection.," *Gut*, vol. 18, no. 12, pp. 1027–31, 1977.

[147] L. R. Williams and R. W. Leggett, "Reference values for resting blood flow to organs of man," *Clinical Physics and Physiological Measurement*, vol. 10, no. 3, pp. 187–217, 1989.

[148] J. Feely, G. R. Wilkinson, and A. J. J. Wood, "Reduction of liver blood flow and propanolol metabolism by cimetidine," *The New England Journal of Medicine*, vol. 304, no. 12, 1981.

[149] H. A. Wynne, L. H. Cope, E. Mutch, M. D. Rawlins, K. W. Woodhouse, and O. F. W. James, "The effect of age upon liver volume and apparent liver blood flow in healthy man.," *Hepatology*, vol. 9, no. 2, pp. 297–301, 1989.

[150] A. M. Seifalian, G. P. Stansby, K. E. Hobbs, D. J. Hawkes, and A. C. Colchester, "Measurement of liver blood flow: a review," *HPB Surgery*, vol. 4, pp. 171–186, 1991.

[151] H. Taniguchi, A. Oguro, K. Takeuchi, K. Miyata, T. Takahashi, T. Inaba, and H. Nakahashi, "Difference in regional hepatic blood flow in liver segments–non-invasive measurement of regional hepatic arterial and portal blood flow in human by positron emission tomography with H2(15)O," *Annals of Nuclear Medicine*, vol. 7, no. 3, pp. 141–145, 1993.

[152] J. Burggraaf, H. C. Schoemaker, and A. F. Cohen, "Assessment of changes in liver blood flow after food intake - Comparison of ICG clearance and echo-Doppler," *British Journal of Clinical Pharmacology*, vol. 42, no. 4, pp. 499–502, 1996.

[153] H. Kojima, N. Tanigawa, A. Komemushi, S. Kariya, and S. Sawada, "Computed tomography perfusion of the liver: Assessment of pure portal blood flow studied with CT perfusion during superior mesenteric arterial portography," *Acta Radiologica*, vol. 45, no. 7, pp. 709–715, 2004.

[154] D. K. Molina and V. J. DiMaio, "Normal Organ Weights in Men," *The American Journal of Forensic Medicine and Pathology*, vol. 33, no. 4, pp. 362–367, 2012.

[155] R. C. Chivers and R. J. Parry, "Ultrasonic velocity and attenuation in mammalian tissues.," *The Journal of the Acoustical Society of America*, vol. 63, no. 3, pp. 940–953, 1978.

[156] F. T. D'Astous and F. S. Foster, "Frequency Dependence of Ultrasound Attenuation and Backscatter in Breast Tissue," *Ultrasound in Medicine & Biology*, vol. 12, no. 10, pp. 795–808, 1986.

[157] O. A. Larsen, N. A. Lassen, and F. Quaade, "Blood flow through human adipose tissue determined with radioactive xenon.," *Acta Physiologica Scandinavica*, vol. 66, no. 3, pp. 337–345, 1966.

[158] F. Karpe, B. A. Fielding, V. Ilic, I. A. Macdonald, L. K. M. Summers, and K. N. Frayn, "Impaired Postprandial Adipose Tissue Blood Flow Response Is Related to Aspects of Insulin Sensitivity," *Diabetes*, vol. 51, pp. 2467–2473, 2002.

[159] K. N. Frayn and F. Karpe, "Regulation of human subcutaneous adipose tissue blood flow," *International Journal of Obesity*, vol. 38, no. 8, pp. 1019–1026, 2014.

[160] D. K. Nassiri, D. Nicholas, and C. R. Hill, "Attenuation of ultrasound in skeletal muscle," *Ultrasonics*, vol. 17, no. 5, pp. 230–232, 1979.

[161] I. H. Heinonen, J. Kemppainen, K. Kaskinoro, J. E. Peltonen, R. Borra, M. Lindroos, V. Oikonen, P. Nuutila, J. Knuuti, R. Boushel, and K. K. Kalliokoski, "Regulation of human skeletal muscle perfusion and its heterogeneity during exercise in moderate hypoxia," *AJP: Regulatory, Integrative and Comparative Physiology*, vol. 299, no. 1, pp. R72–R79, 2010.

[162] I. Heinonen, B. Saltin, J. Kemppainen, S. T. Hannu, V. Oikonen, P. Nuutila, J. Knuuti, K. Kalliokoski, and Y. Hellsten, "Skeletal muscle blood flow and oxygen uptake at rest and during exercise in humans: a pet study with nitric oxide and cyclooxygenase inhibition," *American Journal of Physiology: Heart and Circulatory Physiology*, vol. 300, pp. H1510–H1517, 2011.

[163] S. Bobkova, L. Gavrilov, V. Khokhlova, A. Shaw, and J. Hand, "Focusing of high-intensity ultrasound through the rib cage using a therapeutic random phased array," *Ultrasound in Medicine and Biology*, vol. 36, no. 6, pp. 888–906, 2010.

[164] S. Qiao, G. Shen, J. Bai, and Y. Chen, "Transcostal high-intensity focused ultrasound treatment using phased array with geometric correction," *The Journal of the Acoustical Society of America*, vol. 134, no. 2, pp. 1503–1514, 2013.

[165] H. L. Liu, H. Chang, W. S. Chen, T. C. Shih, J. K. Hsiao, and W. L. Lin, "Feasibility of transrib focused ultrasound thermal ablation for liver tumors using a spherically curved 2D array: A numerical study," *Medical Physics*, vol. 34, no. 9, pp. 3436–3448, 2007.

[166] J. F. Aubry, M. Pernot, F. Marquet, M. Tanter, and M. Fink, "Transcostal high-intensity-focused ultrasound: Ex vivo adaptive focusing feasibility study," *Physics in Medicine and Biology*, vol. 53, no. 11, pp. 2937–2951, 2008.

[167] E. Cochard, C. Prada, J. F. Aubry, and M. Fink, "Ultrasonic focusing through the ribs using the DORT method," *Medical Physics*, vol. 36, no. 8, pp. 3495–3503, 2009.

[168] P. J. White, K. Hynynen, and G. T. Clement, "Longitudinal and shear mode ultrasound propagation in human skull bone," *AIP Conference Proceedings*, vol. 829, no. 7, pp. 251–255, 2006.

[169] B. E. Treeby and B. T. Cox, "Modeling power law absorption and dispersion in viscoelastic solids using a split-field and the fractional Laplacian," *The Journal of the Acoustical Society of America*, vol. 136, no. 4, pp. 1499–1510, 2014.

[170] D. H. Copp and S. S. Shim, "Extraction Ratio and Bone Clearance of Sr85 As a Measure of Effective Bone Blood Flow," *Circulation Research*, vol. 16, pp. 461–467, 1965.

[171] T. Lahtinen, P. Karjalainen, and E. M. Alhava, "Measurement of bone blood flow with a 133Xe washout method," *European Journal of Nuclear Medicine*, vol. 4, pp. 435–439, 1979.

[172] M. A. Morris and P. J. Kelly, "Use of tracer microspheres to measure bone blood flow in conscious dogs," *Calcified Tissue International*, vol. 32, no. 1, pp. 69–76, 1980.

[173] P. H. Martiat, A. Ferrant, M. Cogneau, and G. Sokal, "Assessment of bone marrow blood flow using positron emission tomography : no relationship with bone marrow cellularity," *British Journal of Haemotology*, vol. 66, pp. 307–310, 1986.

[174] B. D. Kahn, J. Weiner, S. Ben-haim, L. L. B. Ponto, T. Madsen, D. L. Bushnell, G. L. Watkins, E. A. Argenyi, and R. D. Hichwa, "Positron Emission Tomographic Measurement of Bone Marrow Blood Flow to the Pelvis and Lumbar Vertebrae in Young Normal Adults," *Blood*, vol. 83, no. 4, pp. 958–963, 1994.

[175] Y. K. Tu, A. T. Bishop, T. Kato, M. L. Adams, and M. B. Wood, "Experimental carpal reverse-flow pedicle vascularized bone grafts. Part II: Bone blood flow measurement by radioactive-labeled microspheres in a canine model," *Journal of Hand Surgery*, vol. 25, no. 1, pp. 46–54, 2000.

[176] I. Heinonen, J. Kemppainen, K. Kaskinoro, H. Langberg, J. Knuuti, R. Boushel, M. Kjaer, and K. K. Kalliokoski, "Bone blood flow and metabolism in humans: Effect of muscular exercise and other physiological perturbations," *Journal of Bone and Mineral Research*, vol. 28, no. 5, pp. 1068–1074, 2013.

[177] Engineering ToolBox, (2003), "Thermal Conductivity of common Materials and Gases. [online]." https://www.engineeringtoolbox.com/thermal-conductivity-d_429.html, Accessed: December 2018.

[178] S. Biyikli, M. F. Modest, and R. Tarr, "Measurements of thermal properties for human femora," *Journal of Biomedical Materials Research*, vol. 20, no. 9, pp. 1335–1345, 1986.

[179] J. W. Valvano, J. R. Cochran, and K. R. Diller, "Thermal conductivity and diffusivity of biomaterials measured with self-heated thermistors," *International Journal of Thermophysics*, vol. 6, no. 3, pp. 301–311, 1985.

[180] A. H. Frucht, "Die Schallgeschwindigkeit in menschlichen und tierischen Geweben," *Zeitschrift fur Die Gesamte Experimentelle Medizin*, vol. 120, no. S, pp. 526–557, 1953.

[181] J. Ophir, N. F. Maklad, and R. H. Bigelow, "Ultrasonic attenuation measurements of in vivo human muscle," *Ultrasonic Imaging*, vol. 4, no. 3, pp. 290–295, 1982.

[182] K. Melde, A. G. Mark, T. Qiu, and P. Fischer, "Holograms for acoustics," *Nature*, vol. 537, no. 7621, pp. 518–522, 2016.

[183] A. Partanen, M. Tillander, P. S. Yarmolenko, B. J. Wood, M. R. Dreher, and M. O. Kohler, "Reduction of peak acoustic pressure and shaping of heated region by use of multifoci sonications in MR-guided high-intensity focused ultrasound mediated mild hyperthermia.," *Medical Physics*, vol. 40, no. 1, 2013.

[184] W. L. Lin, Y. Y. Chen, S. Y. Lin, J. Y. Yen, M. J. Shieh, and T. S. Kuo, "Optimal configuration of multiple-focused ultrasound transducers for external hyperthermia.," *Medical Physics*, vol. 26, no. 9, pp. 2007–2016, 1999.

[185] K. Hynynen, R. Roemer, D. Anhalt, C. Johnson, Z. X. Xu, W. Swindell, and T. Cetas, "A scanned, focused, multiple transducer ultrasonic system for localized hyperthermia treatments.," *International Journal of Hyperthermia*, vol. 26, no. 1, pp. 1–11, 2010.

[186] E. S. Ebbini and C. A. Cain, "A spherical-section ultrasound phased array applicator for deep localized hyperthermia," *IEEE Transactions on Biomedical Engineering*, vol. 38, no. 7, pp. 634–643, 1991.

[187] L. Wu, D. Chen, X. Zeng, K. Khurshid, and R. J. McGough, "Sector-vortex scanning for hyperthermia with large square ultrasound phased array aperture," in *IEEE International Conference on Electro/Information Technology*, pp. 635–640, 2006.

[188] J. W. Hand, A. Shaw, N. Sadhoo, S. Rajagopal, R. J. Dickinson, and L. R. Gavrilov, "A random phased array device for delivery of high intensity focused ultrasound.," *Physics in Medicine and Biology*, vol. 54, no. 19, pp. 5675–5693, 2009.

[189] X. Ji, G. F. Shen, J. F. Bai, D. H. Li, Y. Yu, S. Qiao, and Y. Z. Chen, "Multi-element ultrasound phased array applicator for the ablation of deep-seated tissue," *Journal of Shanghai Jiaotong University (Science)*, vol. 16, no. 1, pp. 55–60, 2011.

[190] R. J. Lalonde and J. W. Hunt, "Optimizing ultrasound focus distributions for hyperthermia.," *IEEE Transactions on Biomedical Engineering*, vol. 42, no. 10, pp. 981–90, 1995.

[191] O. S. Haddadin and E. S. Ebbini, "Ultrasonic focusing through inhomogeneous media," *The Journal of the Acoustical Society of America*, vol. 104, no. 1, pp. 313–325, 1998.

[192] X. Fan and K. Hynynen, "A study of various parameters of spherically curved phased arrays for noninvasive ultrasound surgery," *Physics in Medicine and Biology*, vol. 41, pp. 591–608, 1996.

[193] M. Lu, M. Wan, F. Xu, X. Wang, and H. Zhong, "Focused beam control for ultrasound surgery with spherical-section phased array: sound field calculation and genetic optimization algorithm," *IEEE Transactions on Ultrasonics, Ferroelectrics and Frequency Control*, vol. 52, no. 8, pp. 1270–1290, 2005.

[194] R. J. McGough, E. S. Ebbini, and C. A. Cain, "Direct Computation of Ultrasound Phased-Array Driving Signals from a Specified Temperature Distribution for Hyperthermia," *IEEE Transactions on Biomedical Engineering*, vol. 39, no. 8, pp. 825–835, 1992.

[195] Jerome Gateau, L. Marsac, M. Pernot, J. F. Aubry, M. Tanter, and M. Fink, "Transcranial ultrasonic therapy based on time reversal of acoustically innduced cavitation bubble signature," *IEEE Transactions on Biomedical Engineering*, vol. 57, no. 1, pp. 134–144, 2010.

[196] J. F. Aubry, M. Pernot, F. Marquet, M. Tanter, and M. Fink, "High power transcranial beam steering for ultrasonic brain therapy," *Physics in Medicine and Biology*, vol. 48, pp. 2577–2589, 2003.

[197] C. Cain and S. Umemura, "Concentric-Ring and Sector-Vortex Phased-Array Applicators for Ultrasound Hyperthermia," *IEEE Transactions on Microwave Theory and Techniques*, vol. 34, pp. 542–551, 1986.

[198] S. Umemura and C. A. Cain, "Acoustical evaluation of a prototype sector-vortex phased-array applicator.," *IEEE Transactions on Ultrasonics, Ferroelectrics and Frequency Control*, vol. 39, no. 1, pp. 32–38, 1992.

[199] S. Umemura and C. A. Cain, "The sector-vortex phased array: acoustic field synthesis for hyperthermia.," *IEEE Transactions on Ultrasonics, Ferroelectrics and Frequency Control*, vol. 36, no. 2, pp. 249–257, 1989.

[200] S. Umemura and C. A. Cain, "Analysis of temperature responses to diffused ultrasound focal fields produced by a sector-vortex phased array," *International Journal of Hyperthermia*, vol. 6, no. 3, pp. 641–654, 1990.

[201] H. Wang, *Adaptive Ultrasound Phased Arrays for Deep Hyperthemia.* PhD thesis, University of Michigan, 1999.

[202] Sonic Concepts Inc., "H-Transducer Series D64mm [online]." http://sonicconcepts.com/wp-content/uploads/2017/07/H-%C3%9864-Rev.-B.pdf, Accessed: December 2018.

[203] Y. Hertzberg and G. Navon, "Bypassing absorbing objects in focused ultrasound using computer generated holographic technique," *Medical Physics*, vol. 38, no. 12, pp. 6407–6415, 2011.

[204] C. Bing, J. Nofiele, R. Staruch, M. Ladouceur-Wodzak, Y. Chatzinoff, A. Ranjan, and R. Chopra, "Localised hyperthermia in rodent models using an MRI-compatible high-intensity focused ultrasound system," *International Journal of Hyperthermia*, vol. 2, no. 2, pp. 813–822, 2015.

[205] X. Wu, *Theoretical Evaluation of Moderately Focused Spherical Transducers and Multi-focus Acoustic Lens/Transducer Combinations for High Intensity Focused Ultrasound Thermal Therapy.* PhD thesis, University of Toronto, 2001.

[206] A. Partanen, C. Mougenot, and T. Vaara, "Feasibility of Agar-Silica Phantoms in Quality Assurance of MRgHIFU," *AIP Conference Proceedings*, vol. 1113, pp. 296–300, 2009.

[207] P. Morris, A. Hurrell, A. Shaw, E. Zhang, and P. Beard, "A Fabry-Perot fiber-optic ultrasonic hydrophone for the simultaneous measurement of temperature and acoustic pressure.," *The Journal of the Acoustical Society of America*, vol. 125, no. 6, pp. 3611–3622, 2009.

[208] J. Huang, R. G. Holt, R. O. Cleveland, and R. A. Roy, "Experimental validation of a tractable numerical model for focused ultrasound heating in flow-through tissue phantoms," *The Journal of the Acoustical Society of America*, vol. 116, no. 4, pp. 2451–2458, 2004.

[209] H. Morris, I. Rivens, A. Shaw, and G. ter Haar, "Investigation of the viscous heating artefact arising from the use of thermocouples in a focused ultrasound field," *Physics in Medicine and Biology*, vol. 53, no. 17, pp. 4759–4776, 2008.

[210] J. Georgii, C. V. Dresky, S. Meier, D. Demedts, C. Schumann, and T. Preusser, "Focused Ultrasound-Efficient GPU Simulation Methods for Therapy Planning," in *Proc. of Workshop on Virtual Reality Interaction and Physical Simulation (VRIPHYS)*, pp. 119–128, 2011.

[211] R. J. McGough, "Treatment planning for hyperthermia with ultrasound phased arrays," *IEEE Transactions on Ultrasonics, Ferroelectrics, and Frequency Control*, vol. 43, no. 6, pp. 1074–1084, 1996.

[212] T. D. Mast, L. M. Hinkelman, M. J. Orr, V. W. Sparrow, and R. C. Waag, "Simulation of ultrasonic pulse propagation through the abdominal wall," *The Journal of the Acoustical Society of America*, vol. 102, no. 2, pp. 1177–1190, 1997.

[213] H. L. Liu, N. McDannold, and K. Hynynen, "Focal beam distortion and treatment planning in abdominal focused ultrasound surgery," *AIP Conference Proceedings*, vol. 829, no. 2005, pp. 191–195, 2006.

[214] P. Gélat, G. ter Haar, and N. Saffari, "Scattering of the field of a multi-element phased array by human ribs," *Journal of Physics: Conference Series*, vol. 353, no. 1, 2012.

[215] M. Burtnyk, R. Chopra, and M. J. Bronskill, "Quantitative analysis of 3-D conformal MRI-guided transurethral ultrasound therapy of the prostate: Theoretical simulations," *International Journal of Hyperthermia*, vol. 25, no. 2, pp. 116–131, 2009.

[216] D. Pajek and K. Hynynen, "The design of a focused ultrasound transducer array for the treatment of stroke: a simulation study," *Physics in Medicine and Biology*, vol. 57, no. 15, pp. 4951–4968, 2012.

[217] G. Maimbourg, A. Houdouin, T. Deffieux, and M. Tanter, "3D-printed adaptive acoustic lens as a disruptive technology for transcranial ultrasound therapy using single-element transducers," *Physics in Medicine and Biology*, vol. 63, 2018.

[218] F. Marquet, J. F. Aubry, M. Pernot, M. Fink, and M. Tanter, "Optimal transcostal high-intensity focused ultrasound with combined real-time 3D movement tracking and correction," *Physics in Medicine and Biology*, vol. 56, no. 22, pp. 7061–7080, 2011.

[219] B. Quesson, M. Merle, M. O. Köhler, C. Mougenot, S. Roujol, B. D. de Senneville, and C. T. Moonen, "A method for MRI guidance of intercostal high intensity focused ultrasound ablation in the liver," *Medical Physics*, vol. 37, no. 6, pp. 2533–2540, 2010.

[220] M. Almekkawy, D. McMahon, H. Alqarni, and J. He, "Optimization of transcostal phased-Array refocusing using iterative sparse semidefinite relaxation method," in *39th Annual International Conference of the IEEE Engineering in Medicine and Biology Society (EMBC)*, pp. 1449–1452, IEEE, 2017.

[221] J. Civale, R. Clarke, I. Rivens, and G. ter Haar, "The use of a segmented transducer for rib sparing in HIFU treatments," *Ultrasound in Medicine and Biology*, vol. 32, no. 11, pp. 1753–1761, 2006.

[222] Y. T. Chao, C. J. Hsu, Y. L. Yu, J. Y. Yen, M. C. Ho, Y. Y. Chen, H. C. Chang, and F. L. Lian, "A novel sound-blocking structure based on the muffler principle for rib-sparing transcostal high-intensity focused ultrasound treatment," *International Journal of Hyperthermia*, vol. 31, no. 5, pp. 507–527, 2015.

[223] H. Zhu, K. Zhou, L. Zhang, C. Jin, S. Peng, W. Yang, K. Li, H. Su, W. Chen, J. Bai, F. Wu, and Z. Wang, "High intensity focused ultrasound (HIFU) therapy for local treatment of hepatocellular carcinoma: Role of partial rib resection," *European Journal of Radiology*, vol. 72, no. 1, pp. 160–166, 2009.

[224] M. Fink, C. Prada, F. Wu, and D. Cassereau, "Self focusing in inhomogeneous media with "time reversal" acoustic mirrors," *Proceedings., IEEE Ultrasonics Symposium*, pp. 681–686, 1989.

[225] M. Fink, "Time Reversal of Ultrasonic Fields – Part I: Basic Principles," *IEEE Transactions on Ultrasonics, Ferroelectrics and Frequency Control*, vol. 39, no. 5, pp. 555–566, 1992.

[226] E. Mylonopoulou, C. D. Arvanitisa, M. Bazan-Peregrinoa, M. Arora, and C. C. Coussios, "Ultrasonic Activation of Thermally Sensitive Liposomes," *AIP Conference Proceedings*, vol. 1215, no. May 2016, pp. 83–87, 2010.

[227] Sonic Concepts Inc., "H-Transducer Series D64mm with D20mm Opening [online]." http://sonicconcepts.com/wp-content/uploads/2017/07/H-%C3%9864-with-20.0-mm-Central-Opening-Rev-B..pdf, Accessed: December 2018.

[228] Stratasys Ltd., "PolyJet Materials Data Sheet [online]." http://usglobalimages.stratasys.com/Main/Files/Material_Spec_Sheets/MSS_PJ_PJMaterialsDataSheet.pdf?v=635785205440671440, Accessed: December 2018.

[229] R. Courant, K. Friedrichs, and H. Lewy, "Über die partiellen Differenzengleiehungen der Physik," *Mathematische Annalen*, vol. 100, no. 1, pp. 32–74, 1928.

[230] M. A. Herraez, D. R. Burton, M. J. Lalor, and M. A. Gdeisat, "Fast two-dimensional phase-unwrapping algorithm based on sorting by reliability following a noncontinuous path," *Applied Optics*, vol. 41, no. 35, pp. 7437–7444, 2002.

[231] M. F. Kasim, "Fast 2D phase unwrapping implementation in MATLAB." https://github.com/mfkasim91/unwrap_phase/, Accessed: December 2018.

[232] M. Tanter, M. Pernot, J. F. Aubry, G. Montaldo, F. Marquet, and M. Fink, "Compensating for bone interfaces and respiratory motion in high-intensity focused ultrasound.," *International Journal of Hyperthermia*, vol. 23, no. 2, pp. 141–151, 2007.

[233] G. Maimbourg, A. Houdouin, T. Deffieux, M. Tanter, and J. F. Aubry, "Steering capabilities of an acoustic lens for transcranial therapy: numerical and experimental studies," *IEEE Transactions on Biomedical Engineering*, 2019.

[234] M. Pernot, J. F. Aubry, M. Tanter, J. L. Thomas, and M. Fink, "High power transcranial beam steering for ultrasonic brain therapy," *Physics in Medicine and Biology*, vol. 48, no. 16, pp. 2577–2589, 2003.

[235] X. Yin and K. Hynynen, "A numerical study of transcranial focused ultrasound beam propagation at low frequency.," *Physics in Medicine and Biology*, vol. 50, no. 8, pp. 1821–1836, 2005.

A Appendix

Acoustic Wave Steepening Script

The following MATLAB script is used to numerically solve Equation 2.19, which is derived from the Poisson's solution to the second order nonlinear wave equation (also known as the Westervelt Equation in literature). The propagation distance x can be varied in order to study the steepening of a forward propagating nonlinear monochromatic wave in one dimension based on the retarded time frame τ.

```
%% Wave Steepening Script
% Written by Brian Chu
% University of Oxford
% April 2018

rho = 997;                          % Density [kg/m3]
f = 1.1e6;                          % Frequency [Hz]
c0 = 1482;                          % Small signal sound speed [m/s]
w = 2*pi*f;                         % Angular frequency [Hz]
BA = 5.0;                           % Nonlinearity parameter
p0 = 1;                             % Source pressure amplitude [Pa]
beta = 1 + 0.5*BA;                  % Coefficient of nonlinearity
xbar = rho*(c0^3)/(beta*p0*w);      % Shock formation distance [m]
T = 1/f;                            % Period [s]

% Vary 'x' to change the observation (propagation) distance:
x = xbar*0.8;                       % Observation distance [m]

% Higher sampling rate at the beginning and end to capture the sharp
% turning point of the curve:
t1 = 0:0.005*T:(T/6);
t2 = (T/6)+0.01*T:0.01*T:(5*T/6);
t3 = (5*T/6):0.005*T:T;
t = [t1 t2 t3]; % Time stamps (in retarded time)

solpall = [];
syms p;
for i = 1:length(t)
    % Poisson's solution (1808):
    eqn = p == p0*sin(w*t(i) + beta*w*p*x/(rho*c0^3));
    solp = solve(eqn,p); % Implements MATLAB's inbuilt numerical solver
    solpall = [solpall; eval(solp)];
```

```
end

% Plot the waveform:
plot(t*1e6,solpall/p0);
axis tight; grid on;
title(['\sigma = ',num2str(x/xbar)]);
xlabel('\tau/T');
ylabel('p/p_0');
set(gca,'FontSize',24,'FontName','Garamond');
axis([0 T*1e6 -1 1]);
```

Fresnel Approximation Function

The MATLAB function 'f8SegPres.m' approximately evaluates the Rayleigh-Sommerfeld integral for 2D rectangularly symmetric, baffled, time-harmonic sources by implementing a Fresnel approximation [115]. This method is extended to incorporate geometric focusing and surface apodisation to approximate a sector-vortex spherically-focused transducer with eight sectors.

```
function [P,P0,px,py,pz] = f8SegPres(M,Pow,Elem,XYZLims,Attn,Zattn,Pplot,L,MAmp)
% ========================================================================
% 8-Segment Focused Transducer Pressure Simulation - Fresnel Approximation
% ========================================================================
% Written by Brian Chu
% University of Oxford
% Last modified: September 2018
% ========================================================================
%
% [P,P0,px,py,pz] = f8SegPres(M,Pow,Elem,XYZLims,Attn,Zattn,Pplot,L,MAmp)
%
% Definitions:
% ============
% P             3D Simualted Pressure field [Pa].
%
% XYZLims       Coordinate limits for pressure field calculation in [m].
%               XYZLims = [xmin xmax ymin ymax zmin zmax]
%
% M             [1x8] Array containing the relative phase angle of each of
%               the eight transducer segments [radians]
%
% Pow           Acoustic power given to the transducer [Watts].
%
% Elem          # of elements per wavelength (Source and sample resolution).
%
% Attn          Attenuation coefficient [Np/m].
%
% Zattn         Depth of focus in attenuating medium [m].
%
% Pplot         Flag to plot graphs during processing, 1 = plot.
%
% L             Multiplication factor to increase FFT length (N = R0*L)
```

```
33 %
34 % MAmp        Surface amplitude multiplier (default = 1).
35 %
36 % Function Description:
37 % =====================
38 % f8SegPres calculates the pressure field for a given acoustic power 'Pow'
39 % and arrangement of phases 'M' describing each of the eight segments for
40 % an eight segment focused bowl transducer. (Inner and outer radii can be
41 % specified through the variables 'RI' and 'RO').
42 %
43 %   The pressure 'P' is calculated using the Fresnel approximation and 2D
44 % fast Fourier transform for computational efficiency. The location of each
45 % element in 'P' is described by the co-ordinate system contained in the
46 % variables px, py, and pz.
47 %
48 %   Default media set as water(c = 1482 m/s, rho = 997 kg/m^3). A
49 % homogeneous attenuating medium can be introduced by specifying the
50 % attenuation value 'Attn' in [Np/m] and the depth of the focus in the
51 % attenuating medium through 'Zattn'. The attenuating medium has the same
52 % density and speed of sound as the initial propagation medium.
53 % ========================================================================
54
55 % Simulation parameters:
56 c = 1482;          % Speed of sound [m/s]
57 rho = 997;         % Density [kg/m3]
58 f = 1.1e6;         % Frequency [Hz]
59 wl = c/f;          % Wavelength [m]
60 k = 2*pi/wl;       % Wavenumber [m]
61 Foc = 62.6e-3;     % Focal length [m]
62
63 if Attn > 0
64     alpha = Attn;
65 else
66     alpha = 0;
67 end
68
69 res = wl/Elem;
70 RO = 32e-3;                    % Outer radius [m]
71 RI = 10e-3;                    % Inner radius [m]
72 SA = pi*(RO^2) - pi*(RI^2);    % Transducer surface area [m2]
73 I = Pow/SA;                    % Average intensity [W/m2]
74 P0 = sqrt(I*2*rho*c);          % Peak surface pressure amplitude [Pa]
75
76 % Surface simulation region:
77 if isempty(L)
78     Ln = 5;
79 else
80     Ln = L;
81 end
82 LimX = RO*Ln;                          % FT x limits [m]
83 Xstep = res;
84 LimY = RO*Ln;                          % FT y limits [m]
85 Ystep = res;
86 x = -LimX:Xstep:LimX;                  % x-axis [m]
87 Lx = length(x);
88 y = -LimY:Ystep:LimY;                  % y-axis [m]
89 Ly = length(y);
90 [xx,yy] = meshgrid(x,y);
91 rr = sqrt(xx.^2 + yy.^2);              % Radial position [m]
92
93 % Circular geometry mask
94 mask = (rr <= RO) & (rr >= RI);
95
96 % Assigning the desired phase to mask elements for each segment:
97 SegAng = atan2(xx,yy) + pi;
98 Bmask = double(mask);
```

```
for n = 1:8                                 % Segment number (8 in total)
    phs2 = n*pi/4;
    phs1 = phs2 - pi/4;
    mask2 = (SegAng >= phs1) == (SegAng <= phs2);
    Bmask(mask & mask2) = exp(1i*M(n));  % Obtaining phase from M(n)
end
mask = Bmask;

% Plotting the Magnitude and Phase of the Mask:
if Pplot == 1
    figure;
    subplot(1,2,1);
    imagesc(x*1000,y*1000,abs(mask)); cb = colorbar;
    title('|mask|');
    cb.Label.String = '|M|';
    axis equal; xlabel('x [mm]'); ylabel('y [mm]');
    set(gca,'FontSize',24,'FontName','Garamond');
    axis([-R0*1000 R0*1000 -R0*1000 R0*1000]);

    subplot(1,2,2); imagesc(x*1000,y*1000,angle(mask)); cb = colorbar;
    title('angle(mask)');
    cb.Label.String = '[rad]';
    axis equal; xlabel('x [mm]'); ylabel('y [mm]');
    set(gca,'FontSize',24,'FontName','Garamond');
    axis([-R0*1000 R0*1000 -R0*1000 R0*1000]);
end

% Pressure Field Calculation:
% ===========================
if length(XYZLims) == 6
    Px1 = XYZLims(1);
    Px2 = XYZLims(2);
    Py1 = XYZLims(3);
    Py2 = XYZLims(4);
    Pz1 = XYZLims(5);
    Pz2 = XYZLims(6);
else
    Px1 = -30.e-3;
    Px2 = 30.e-3;
    Py1 = -30.e-3;
    Py2 = 30.e-3;
    Pz1 = 30.e-3;
    Pz2 = 80.e-3;
end
Z = Pz1:res:Pz2;                % Z locations to calculate [m]
Nz = length(Z);
Pxs = Px1:res:Px2;
Nx = length(Pxs);
Pys = Py1:res:Py2;
Ny = length(Pys);
P = zeros(Nx,Ny,Nz);            % Array to store resampled pressure slices

if isempty(Zattn)
    ZattFoc = 40.e-3;
else
    ZattFoc = Zattn;            % z-distance of focal point travelled in agar.
end
ZattStart = Foc - ZattFoc;      % Z location to start attenuation

% Surface coordinates:
rr0 = rr;
rr0(~abs(mask)) = 0;
rrTheta = atand(rr0./Foc);
mask = double(mask).*MAmp;

disp('Running pressure simulation...  ');
```

```
for z = 1:Nz                    % For each z-distance point Z(z)

    % Attenuation:
    Zat = Z(z) - ZattStart;
    if Zat > 0
        Adx = Zat./cosd(rrTheta);
        attn = exp(-alpha.*Adx);
    else
        attn = 1;
    end

    A = exp(1i*k*(rr.^2)/(2*Z(z))).*double(mask).*exp(-1i*k*(rr.^2)/(2*Foc));
    C = -1i*k*P0*attn*exp(1i*k*Z(z))/(2*pi*Z(z));
    Pp = C.*fft2(A);            % 2D FFT
    Pp = Xstep*Ystep.*Pp;       % Scaling the FT image
    Pp = abs(fftshift(Pp));     % Re-centering the image

    % Converting spatial frequency Fx and Fy to x and y:
    Fx = (1:Lx) - (Lx/2);
    Fx = Fx/(Lx*Xstep);
    Fx = Fx - (Fx(2)-Fx(1));
    Fy = (1:Ly) - (Ly/2);
    Fy = Fy/(Ly*Ystep);
    Fy = Fy - (Fy(2)-Fy(1));

    X = Fx*wl*Z(z);
    Y = Fy*wl*Z(z);

    % Cropping and resampling to simualtion limits defined in XYZLims:
    X2 = (X>=Px1) & (X<=Px2);
    X0 = X2==0;
    X2 = X(X2);
    Y2 = (Y>=Py1) & (Y<=Py2);
    Y0 = Y2==0;
    Y2 = Y(Y2);
    Pp(X0,:) = [];
    Pp(:,Y0) = [];

    [XX,YY] = meshgrid(X2,Y2);
    [XXs,YYs] = meshgrid(Pxs,Pys);
    PResamp = interp2(XX,YY,Pp,XXs,YYs,'cubic',0);
    P(:,:,z) = abs(PResamp);
    clear XX YY XXs YYs;

    clc;
    disp(['Pressure simulation: ',num2str(round(z*100/length(Z))),'[%]']);
    pause(0.001);
end

px = Pxs;
py = Pys;
pz = Z;

end
```

Optimisation Runscript

```
% Transducer Optimisation Runscript
% Written by Brian Chu
% University of Oxford
% September 2016

clear variables; close all; clc;
global T0 R_pow R_M R_MSE Nit;  %#ok<NUSED>
global OptRuns;
for OptRuns = 1:3
    Nit = 1;
    tic;
    disp(['Optimisation run number: ',num2str(OptRuns)]);
    Mopt = rand(1,8)*2*pi - pi;     % Initial radomised phase [rad]
    Pow = 8*rand(1);               % Initial power guess [W]
    Mini = [Pow Mopt];              % Initial input parameters.
    T0 = 0;                         % Initialised temperature field.

    % Boundary conditions:  -pi <= Mopt <= pi
    lbphase = -pi*ones(1,8) - 0.1;  % Lower bound for phase [rad]
    lbpow = 0;                      % Lower bound for power [W]
    ubphase = pi*ones(1,8) + 0.01;   % Upper bound for phase [rad]
    ubpow = 8;                      % Upper bound for power [W]

    lb = [lbpow lbphase];       % Lower bounds
    ub = [ubpow ubphase];       % Upper bounds
    Fopt = optimoptions('fmincon','Display','iter');

    OptmRes = fmincon(@f8SegEmse_Print,Mini,[],[],[],[],lb,ub,[],Fopt);

    dtotal = toc;
    disp(['Total runtime = ',num2str(round(dtotal/60)),' minutes.']);
    disp(['Power =',num2str(OptmRes(1)),'[Watts]']);
    disp('Phases = ');
    disp(OptmRes(2:end));
    Opow = OptmRes(1);
    Ophase = OptmRes(2:end);
    Omins = num2str(round(dtotal/60));
    save(['Results.',num2str(OptRuns),'.mat'],'Opow','Omins','Ophase');
end
```

Optimisation Function

```
function Emse = f8SegEmse_Print(M_in)
% ========================================================================
% 8-Segment Focused Transducer Error Function
% ========================================================================
% Written by Brian Chu
% University of Oxford
% September 2016
% ========================================================================
%
% Emse = f8SegEmse(M_in)
%
% Definitions:
% ============
% Emse        Mean squared error between desired and simulated temperature.
%
% M_in        Input parameters in the form [power phase] with 'power' in
%             watts, and 'phase' is a 1 by 8 array containing the surface
%             phase distribution of an 8-element sectored array in radians.
%
% Function Description:
% =====================
% f8SegPres simulates the pressure field of an 8-segment focused
% transducer with properties as described in the function script
% 'f8SegPres'. The pressure field is then imported into the thermal
% simulation function 'f8SegBHTE' which is based on the thermal ADI code
% (Prof. Robin Cleveland, University of Oxford), and the mean squared
% error between the reference temperature profile 'T_ref' and the
% simulated temperature profile 'T' is returned in 'Emse'.
% ========================================================================

global R_pow R_M R_MSE Nit OptRuns T0;

Nit = Nit + 1;
R_pow = [R_pow; M_in(1)];
R_M = [R_M; M_in(2:end)];
% Run Pressure Simulation using mode 'M' and Acoustic power 'Pow':
Pow = M_in(1); disp(['Power = ',num2str(Pow),' [W]']);
M = M_in(2:end); disp(['Phase = {',num2str(M),'} [rad]']);
Pplot = 0;
Elem = 6;
XYZLims = [-30 30 -30 30 20 85]/1000;
AdB = 0.79;
Attn = AdB*100/8.686;
Zattn = 40e-3;
L = 4;
[P,~,px,py,pz] = f8SegPres(M,Pow,Elem,XYZLims,Attn,Zattn,Pplot,L);
P(1,:,:) = [];
P(end,:,:) = [];
P(:,1,:) = [];
P(:,end,:) = [];
P(:,:,1) = [];
P(:,:,end) = [];
px(1) = []; px(end) = [];
py(1) = []; py(end) = [];
pz(1) = []; pz(end) = [];

% Run Thermal Simulation from pressure field 'P':
T0 = 0;
```

```
59 Tplot = 1; probe = 0; ss = 1;
60 [T,~,~,~,~] = f8SegBHTE(P,px,py,pz,Tplot,probe,ss,1);
61
62 % Generate 'Tideal': 2cm diameter sphere centred at (0,0,164)mm
63 r_ref = 0.01;
64 xx = repmat(px,length(px),1,length(pz));
65 yy = repmat(px',1,length(px),length(pz));
66 zz = ones(length(px),length(py),length(pz));
67 for i = 1:length(pz)
68     zz(:,:,i) = zz(:,:,i).*pz(i);
69 end
70 rr = sqrt(xx.^2 + yy.^2 + (zz-0.0626).^2);
71
72 % Exclusion zone:
73 Xcld = (rr>r_ref) & (rr<(r_ref+0.01));
74 Targ = rr<=r_ref;
75
76 %T_ref(xbin,ybin,zbin) = 5;  % 5 degree temperature rise from 37 to 42.
77 T_ref = 0.*(Xcld);
78 T_ref(Targ) = 5;
79
80 % Mask for locations with a temperature rise less than 1C:
81 %T1C = (T < 1);
82 %Xcld = Xcld | T1C;
83 Incld = Xcld.*(-1)+1;
84 Incld = logical(Incld);
85 N = sum(sum(sum(Incld)));
86
87 % Calcualte MSE for locations with DT > 1C and outside of exclusion zone,
88 % normalised against the number of elements that met this criteria:
89 Emse = sum(sum(sum((T_ref(Incld)-T(Incld)).^2)))/N;
90 R_MSE = [R_MSE; Emse];
91 save(['Current_results_',num2str(OptRuns),'.mat'],'R_MSE','R_pow','R_M',...
92     'Nit','-v7.3');
93 pause(0.01);
94
95 end
```